1-15-2014

Synthesis And Characterization Of New Gd3+-Containing Complexes As Potential Targeted Contrast Agents For Magnetic Resonance Imaging

Sashiprabha Manjari Vithanarachchi
Wayne State University,

SYNTHESIS AND CHARACTERIZATION OF NEW Gd^{3+}-CONTAINING COMPLEXES AS POTENTIAL TARGETED CONTRAST AGENTS FOR MAGNETIC RESONANCE IMAGING.

by

SASHIPRABHA MANJARI VITHANARACHCHI

DISSERTATION

Submitted to the Graduate School

of Wayne State University,

Detroit, Michigan

in partial fulfillment of the requirements

for the degree of

DOCTOR OF PHILOSOPHY

2014

MAJOR: CHEMISTRY (Inorganic)

Approved by:

_____

Advisor Date

_____

_____

_____

DEDICATION

This dissertation is dedicated to my parents, grandma, punchi, and sudu punchi who have been the first teachers of my life.

ACKNOWLEDGMENTS

I would like to offer my sincere and profound gratitude to my advisor Dr. Matthew J. Allen for his great guidance and support during my graduate career. I appreciate and am inspired by his knowledge, kindness, patience, and willingness to help his students to meet their goals. His encouragement and positive perspectives always directed me to find solutions when I struggled with my research. Under his outstanding mentorship I learned to communicate and present my work effectively as a scientist. I think I am very fortunate to have one of the best advisors in the world as my graduate advisor.

I would like to thank my committee members Dr. Claudio Verani, Dr. Sarah Trimpin, Dr. Matthew P. Galloway, Dr. Stanislav Groysman, and Dr. Parastoo Hashemi for their valuable time, suggestions, and advice.

I would like to thank my collaborators and their lab members for the support they provided during my graduate work. Thank you, Dr. Tiffany A. Mathews, Brooke Newman, and Aaron Apaw for allowing me to use the vibrotome and microscope, and for providing me with mouse brain tissue. Thank you, Dr. Mi Hee Lim for inviting me to work in your lab. Thank you, Akiko Kochi for helping me with gel electrophoresis and letting me stay in your place during my visit to the University of Michigan. Thank you, Dr. Sarah Trimpin and Lorelie F. Imperial for performing mass spectrometry imaging. Thank you, Dr. Meser M. Ali and Dr. James R. Ewing for helping me with MR imaging of mouse brains. I would also like to thank Dr. Alana Conti and Jennifer Lowing for providing mouse brains for my studies.

It wouldn’t be easy to work in the same place for five years if the people around were not friendly. I am very fortunate to work with a very talented group who are very friendly,

supportive, and caring like a family. I would like to thank Prabani, Nipuni, and Jeremy for helping me with setting up my place and getting familiar with instruments in the lab during my first year. Special thank goes to my hood mate Jeremy Moore for teaching me how to engineer things to use for my research, helpful discussions of chemistry, and helping me to expand my vocabulary. I would like to thank my batch mates Buddhima and Joel for their friendly and insightful talks about research and MRI theory, and I would like to thank Buddhima for giving me rides whenever I needed to attend a group party or any other function. I would like to thank Derek and Lauren for proof reading chapters of my dissertation. Thank you, Lauren for always helping in arranging group events and showing me the Rain Forest cafe. I would like to thank Akhila for helping me with cyclic voltametry and Jin for helping me with ^{17}O NMR measurements. I would also like to thank Samantha, Chamika, Nikhil, and Levi for sharing their views about science with me.

I would like to extend my thanks to the staff of Lumigen Instrument Center, business office, and science store of the department of chemistry for their time and support. I thank Melissa Barton and all the other members of the chemistry department for their support during these five years. I thank Sanofar and Salim, and all the members of Sri Lankan student association for helping me when I first came to Detroit.

Finally, I would like to thank my mother, father, brother, uncles and aunts, and all my cousins for their encouragement, love, and not letting me feel that I am far away from them during these five years.

TABLE OF CONTENTS

LIST OF TABLES

LIST OF FIGURES

LIST OF SCHEMES

LIST OF ABBREVIATIONS

Abbreviation	Term
2-NPG	2-nitrophloroglucinol
BBB	blood–brain barrier
BnSCN	benzyl isothiocyanate
cc	corpus callossum
CPu	caudate putamen
DIEA	diisopropylethylamine
DLS	dynamic light scattering
DMSO	dimethylsulfoxide
DOTA	1,4,7,10-tetraazacyclododecane-*N*,*N´*,*N´´*,*N´´´*-tetraacetic acid
DTPA	diethylenetriaminepentaacetic acid
f	fornix
fi	fimbria
HDL	high-density lipoprotein
HER2	human epidermal growth factor receptor type 2
HPLC	high-performance liquid chromatography
HRESIMS	high-resolution electrospray ionization mass spectra
ic	internal capsule
ICP–MS	inductively coupled plasma mass spectrometry
ICP–OES	inductively coupled plasma optical emission spectroscopy
K_i	binding inhibition constant
LFB MBS	luxol fast blue MBS
LSIV	laser spray ionization vacuum mass spectrometry
MALDI	matrix-assisted laser desorption ionization
mmt	mammillothalamic tract
MRI	magnetic resonance imaging
ot	optic tract
PAMAM	polyamidoamine
PBS	phosphate buffered saline
PET	positron emission tomography
r_1	longitudinal relaxivity
R_1	longitudinal relaxation rate
RES	reticuloendothelial system
RT	room temperature
SPIO	superparamagnetic iron oxide
T_1	longitudinal relaxation time
T_2	transverse relaxation time
TBS	tris buffered saline
TE	echo time
TEM	transmission electron microscopy
TLC	thin-layer chromatography
Tris	tris(hydroxymethyl)aminomethane
uPA	urokinase-type plasminogen activator

CHAPTER 1. Strategies to obtain target-specific metal complexes as imaging agents

Portions of this chapter are reprinted or adapted with permission from Vithanarachchi, S. M.; Allen, M. J. *Current Molecular Imaging* **2012,** *1,* 12–25.

Introduction

Imaging techniques play a vital role in diagnostic medicine and medical research by aiding with the detection of diseases as well as the monitoring of disease progression and treatment. These imaging modalities include single photon emission computed tomography, positron emission tomography, ultrasound, magnetic resonance imaging (MRI), photoacoustic tomography, and fluorescence imaging, and reviews describing the advantages and limitations of each modality have been published elsewhere.[1–6] This thesis focuses on MRI because my research explored the utility of Gd^{III}-containing complexes to achieve targeted imaging with MRI. MRI is a powerful, non-invasive imaging technique that does not use ionizing radiation and has the capability to generate three-dimensional images of deep tissue with good spatial resolution (25–100 μm).[6]

Conventional MRI images are produced by mapping either the relaxation rates or densities of the nuclear spins of water protons in a magnetic field. Differences in relaxation rates are due in part to the chemical composition of the surrounding environment; however, the inherent levels of signal intensity that result from the differences in relaxation rates of water protons are often not sufficient to produce satisfactory contrast. Therefore, chemicals known as contrast agents are used in MRI to catalytically accelerate the relaxation rate of water protons to obtain contrast-enhanced images. Paramagnets including Gd^{III}, Mn^{II}, and Mn^{III} are referred to as "T_1-shortening agents" because of their influence on longitudinal (T_1) relaxation rates, and superparamagnetic iron oxide (SPIO) particles are referred to as "T_2-shortening agents" because

of their influence on transverse (T_2) relaxation rates.[7] The ability of a contrast agent to influence contrast is measured in terms of relaxivity, and relaxivity changes in response to changes in physical parameters including magnetic field strength, temperature, and solvent composition. This dependence of relaxivity on measurement conditions often prevents a meaningful direct comparison of agents in different studies. Hence, in this chapter, physical parameters are reported for each example to avoid misinterpretation that could arise due to direct comparison of agents measured under different conditions (**Table 1.1**).

In current clinical MRI (1.5–3 T), Gd^{III}-based complexes are the most commonly used contrast agents, and these agents are non-specific; they do not accumulate in particular tissues or organs of interest. Non-specific contrast agents are useful in the imaging of pathologies like tumors, lesions, and inflammation because these agents aid in the differentiation of healthy and diseased tissues based on vascular volume, vascular perfusion, and vascular permeability.[8] While these non-specific contrast agents are used in ~35% of clinical scans,[9] their utility in the early detection of disease and imaging of specific biological regions is limited. This limitation arises because diseases often do not display changes in vasculature, and if observable changes in vasculature occur, they are likely to occur in later stages of diseases. One method to address the limitation of non-specificity is the use of targeted contrast agents. Since the first descriptions of targeted contrast agents,[10,11] this topic has become a focus in the field of MRI and contrast agent research because of the potential to enable molecular imaging in addition to anatomical imaging. The importance of targeted contrast agents has been described in several recent reviews.[8,3,12–18] These reviews discuss the development and properties of T_1- and T_2-shortening agents and the use of different biomarkers as targets. In this chapter, targeted contrast agents are described for proton MRI that were developed during the last ten years using two different synthetic strategies

with a focus on agents that have been tested both *in vitro* and *in vivo* to emphasize limitations that must be overcome to enable the clinical use of targeted contrast agents.

The design of target-specific contrast agents involves two types of strategies: the most common strategy is to conjugate a contrast agent with an antibody, peptide, or a small organic molecule that enables interactions with a target. A second strategy is to transform a contrast agent directly into the targeting moiety by mimicking the structure of a molecule that naturally interacts with a desired target. The development of targeted contrast agents with these two strategies has led to successful targeting *in vitro*, and some agents have been successfully translated to enable *in vivo* visualization of targets. The remainder of this chapter is organized into these two strategies: conjugation and mimicking.

The conjugation strategy

Direct conjugation of derivatives of clinically approved contrast agents to peptides, antibodies, or small organic molecules is a popular and relatively simple method of achieving target specificity. All directly conjugated contrast agents contain three parts: a targeting moiety, a contrast-enhancing unit, and a linker that connects the other two parts (**Figure 1.1**). When linking the contrast-enhancing unit and targeting moiety, either metalate-then-conjugate or conjugate-then-metalate methods can be used,[19] and conjugation generally results in the formation of biologically stable amides, ethers, thioesters, or triazoles. Low molecular weight (≤30 kDa) targeted contrast agents are desirable because their small size enables diffusion to small areas and facile clearance, but this type of targeted contrast agent faces the challenge of low sensitivity: with small Gd^{III}-based contrast agents, micromolar or greater concentrations are needed to achieve satisfactory contrast *in vivo*.[20, 21] Therefore, contrast agents that possess both

high relaxivity and long circulation times are desirable to lower the dose of contrast agent. To increase sensitivity, targeting moieties and Gd^{III}-containing complexes are conjugated to macromolecules including dendrimers, polymers, proteins, liposomes, and nanoparticles. These agents obtain high relaxivity by slowing the molecular tumbling rate, by combining several contrast-enhancing units per targeting moiety, or both. In the following section, the use of the conjugation strategy is described in the synthesis of targeted imaging agents using both a single contrast-enhancing unit (monomeric) and multiple contrast-enhancing units (multimeric), and the selectivity and sensitivity of the resulting agents is described for *in vitro* and *in vivo* experiments.

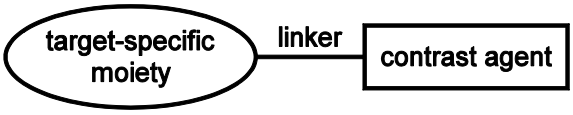

Figure 1.1. Schematic representation of the basic units of targeted contrast agents synthesized using the conjugation strategy.

Monomeric target-specific contrast agents

Monomeric targeted contrast agents contain one contrast-enhancing unit per targeting moiety; therefore, to achieve satisfactory contrast enhancement with these agents, targets with high expression levels need to be selected. Examples of such highly expressed targets include biomarkers associated with tumors; consequently, many monomeric tumor-targeted contrast agents are reported. Conjugation of steroids with contrast agents enables targeting of receptors on tumor cells because hormone receptors are over-expressed by various tumors. 21-Hydroxyprogesterone and 17β-estradiol are steroids that interact with progesterone receptors and estrogen receptors that are over-expressed by uterine, breast, ovarian, and prostate carcinomas. These two steroids were conjugated with Gd^{III}-containing complexes to produce monomeric contrast agents **1.2a** and **1.2b**, respectively (**Figure 1.2**).[22,23] The relaxivity of **1.2a** is 5.35 mM^{-}

$^{1}s^{-1}$ (1.41 T, 37 °C, and 1% dimethylsulfoxide in water), and the relaxivity of **1.2b** is 6.8 $mM^{-1}s^{-1}$ (9.4 T and phosphate buffered saline (PBS)). Because these relaxivity values are similar to those of clinically used non-specific agents,[20,24] doses similar to those used for non-specific agents are needed to enable good contrast (0.15 mmol/kg for **1.2a** and 0.075 mmol/kg for **1.2b**). *In vivo* imaging of xenograft mice using intraperitoneal or subcutaneous injections of **1.2a** at 7.05 T resulted in contrast enhancement of progesterone-receptor-positive tumors with respect to progesterone-receptor-negative tumors (**Figure 1.3**). Furthermore, agent **1.2a** labels tissues that express progesterone receptors including the uterus and ovaries.[22] Imaging of xenograft mice using **1.2b** (tail-vein injection at 9.4 T) demonstrated the targeting efficiency of this agent toward estrogen-receptor-positive tumors by enhancing contrast relative to estrogen-receptor-negative tumors.[23] The success of these two agents in enhancing contrast in tumors relies on the over expression of receptors in tumors relative to normal tissues.

Integrins are other receptors targeted for imaging. Integrin-targeted contrast agents have the potential to enable the detection of angiogenesis and thrombosis. The cyclic peptide cRGD is a widely used targeting moiety for integrins.[25–27] An $\alpha_{IIb}\beta_3$ integrin-receptor-targeted agent reported by Fayad and co-workers to detect thrombosis demonstrates the importance of high receptor concentration to obtain good contrast enhancement with monomeric agents.[25] Their contrast agent, **1.2c**, consists of cRGD conjugated to Gd^{III} 1,4,7,10-tetraazacyclododecane-*N*,*N*′,*N*′′,*N*′′′-tetraacetic acid (DOTA). This agent has a relaxivity of 9 $mM^{-1}s^{-1}$ (1.41 T and 40 °C) and binds with the $\alpha_{IIb}\beta_3$ receptor as well as the $\alpha_V\beta_3$ receptor. *In vivo* studies with mouse models of thrombosis demonstrated the ability of **1.2c** to increase contrast of activated platelets with a 0.1 mmol/kg dose injected in the tail-vein. The reason for the success of **1.2c** as a thrombosis-targeted contrast agent is the high expression of the $\alpha_{IIb}\beta_3$ receptor (40,000 per

platelet) in platelets relative to $\alpha_V\beta_3$ (~1,500 per platelet).[28] When the expression level of a target is low, larger amounts of monomeric agents are needed to achieve contrast enhancement. For example, cRGD-conjugated contrast agent **1.2d** (**Figure 1.2**) was studied as a means to selectively image the $\alpha_V\beta_3$ integrin receptor that is over-expressed in hepatocelluler carcinomas.[27] The relaxivity of contrast agent **1.2d** is 7.4 $mM^{-1}s^{-1}$ (1.5 T and 25 °C), and *in vivo* imaging of H-ras12V transgenic mice bearing hepatocellular carcinomas at 1.5 T (tail-vein injection of 1.43 mmol/kg of **1.2d**) enhanced contrast of the tumor region. Tumor cells used in this study have a low concentration of $\alpha_V\beta_3$ receptors, and the contrast agent has a moderate specificity for these receptors; thus, the high dose used in this study was needed to saturate the receptors.

Table 1.1. Conditions used for relaxivity measurements and MR imaging

contrast agent	field strength (T)		temperature for relaxivity (°C)	medium for relaxivity measurements	relaxivity (T_1) ($mM^{-1}s^{-1}$) [a]	relaxivity (T_2) ($mM^{-1}s^{-1}$)[a]	*in vivo* imaging dose	*in vitro* imaging concentrations	reference
	relaxivity measurements	*in vivo*/*in vitro* studies							
1.2a	4.7	7.05	21	NR	4.73	NR	0.15 mmol/kg	NR	22
1.2a	1.41	7.05	37	1% DMSO in water	5.35	6.14	0.15 mmol/kg	NR	22
1.2b	9.4	9.4	NR	PBS	6.8	NR	0.075 mmol/kg	NR	23
1.2c	1.41	9.4	40	NR	9	NR	0.1 mmol/kg	NR	25
1.2d	1.5	1.5	25	NR	7.4	4	1.43 mmol/kg	NR	27
1.2e	9.4	9.4	NR	PBS	4.7	NR	0.075 mmol/kg	NR	23
1.2f	4.7	4.7	NR	aqueous	1.28	NR	0.2 µmol/mouse	0.5 mM	29
1.2g	1.41	2	37	water	21	30	0.03 mmol/kg	NR	30
1.2h	1.41	4.7	37	Tris buffer, pH 7	21	30	0.24 µmol/mouse	NR	31
1.2i	0.47	NR	25	pH 7.4	7.7	NR	NR	NR	33
1.2j	4.7	NR	37	water	5.5	6.9	NR	NR	24
1.2j	3	NR	37	water	5.3	6.1	NR	NR	24
1.2j	1.5	NR	37	water	5.2	5.9	NR	NR	24
1.2k	0.47	NR	37	water	5.6	NR	NR	NR	26
1.2l	3	3	RT	NR	4.22	4.45	0.1 mmol/kg	NR	34

1.2m	NR	7	NR	NR	NR	NR	0.4–2 mg/mouse[b]	NR	35
1.2n	9.4	9.4	21	water	5.2	NR	1.14 μmol/kg	0.1 mM	38, 39
1.2n	1.41	9.4	40	water	5.1	NR	1.14 μmol/kg	0.1 mM	38, 39
1.2n	0.47	9.4	40	water	5.8	NR	1.14 μmol/kg	0.1 mM	38, 39
1.4a	1.41	1.5	37	TBS, pH 7.4	10.1, 40.3[c]	12.8, 51.1[c]	4 μmol/kg	NR	40, 41
1.4a	0.47	1.5	37	TBS, pH 7.4	11.1, 44.4[c]	NR	4 μmol/kg	NR	40, 41
1.4b	4.7	4.7	25	PBS, pH 7.4	5.4, 16.2[c]	NR	0.025 mmol/kg	NR	43, 44
1.4b	1.41	4.7	37	PBS, pH 7.4	16.1, 48.4[c]	NR	0.025 mmol/kg	NR	43, 44
1.4b	0.47	4.7	37	PBS, pH 7.4	18.7, 56.2[c]	NR	0.025 mmol/kg	NR	43, 44
1.4c	3	3	NR	water	9.7	NR	5 μmol Gd/kg	NR	45
1.4d	1.5	9.4	NR	water	20.6	NR	0.03 mmol Gd/kg	NR	46
1.4e	0.6	7	25	water, pH 7	29.1	NR	NR	≥50 μM	47
1.4f	3	3	NR	water	64.88	NR	0.05 mmol Gd/kg	NR	49
1.4g	2	2	20	NR	26, 598[c]	NR	0.029 mmol Gd/kg	0.01 mM	50
1.4h	0.47	1.5	40	NR	~20, 1,800,000[c]	NR	2.7 μmol Gd/kg	NR	54
1.4i	3	3	25	water	8.2, 353[c]	16.1, 692[c]	0.03 mmol Gd/kg	NR	56
1.4j	4.7	1.5	NR	NR	NR	NR	3.3 μmol /kg	NR	58
1.4k	0.47	4.7	40	NR	1.04	NR	0.2 mmol Gd/kg	NR	59
1.4l	3	3	RT	water	3.13, 131[c]	8.74, 367[c]	0.03mmol Mn/kg	NR	60
1.4m	3	3	25	NR	4.1, ~91,127[c]	18.9, ~441,120[c]	NR	NR	61
1.4n	3	3	25	NR	14.6, ~423,420[c]	70.7, ~2,135,482[c]	NR	NR	61
1.4o	NR	1.5	NR	NR	NR	NR	30 μmol particles/kg	0.54 mM	63
1.4p	1.41	9.4	NR	NR	NR	89	0.18 mmol Fe/kg	2.68 mM	64
1.4q	3	3	NR	NR	3.6	124	NR	NR	65
1.4r	NR	7	NR	NR	NR	NR	NR	0.03 mg/mL	66
1.4s	NR	4.7	NR	NR	NR	NR	10–16 mg/kg	NR	67, 68
1.7a	4.7	4.7	25	aqueous	8.9	NR	0.05 mmol Mn/kg	NR	70
1.7b	NR	9.4	NR	NR	~ 3.1[d]	NR	0.017–0.02 μmol/kg	NR	71
1.7c	7	7	23	aqueous	16.3	20	0.1 mmol/kg	NR	72
1.7d	7	7	23	aqueous	31.7	38.2	0.1 mmol/kg	NR	72
1.7e	1.2	1.5	25	aqueous saline	18	NR	0.017 mmol/kg	NR	82, 84
1.7f	4.7	4.7, 14	NR	ethanol	0.15	NR	NR	1 % w/v	81
1.7f	14	4.7, 14	NR	ethanol	0.12	NR	NR	1 % w/v	81
1.7f	4.7, 14	4.7,	NR	aqueous	0.09	NR	NR	1 % w/v	81

		14							
1.7g	1.5	9.4	25	water, pH 7.4	10.4[c]	NR	3.25–4.36 µmol/kg	NR	75
1.7h	1.41	9.4	40	NR	8.9[c]	94.2[c]	0.54 mmol Fe/kg	0.072 mM Fe	76
1.7i	1.5	1.5	NR	Dulbecco's PBS	8.4[c] (for 5000Fe)	93[c] (for 5000Fe)	NR	3 mM Fe	78
1.7j	NR	11.7	NR	NR	NR	1–10	0.089 mmol Fe/kg[e]	NR	79
1.7k	9.4	3, 9.4	NR	NR	6	50	~2.4 µmol Gd/kg	NR	86
1.7k	3	3, 9.4	NR	NR	48	88	~2.4 µmol Gd/kg	NR	86
1.7k	1.5	3, 9.4	NR	NR	117	129	~2.4 µmol Gd/kg	NR	86

NR = not reported RT = room temperature

[a] relaxivity per ion is reported except for those that denoted [b] *ex vivo* imaging

[c] relaxivity per molecule or particle [d] estimated *in vivo* [e] five doses used

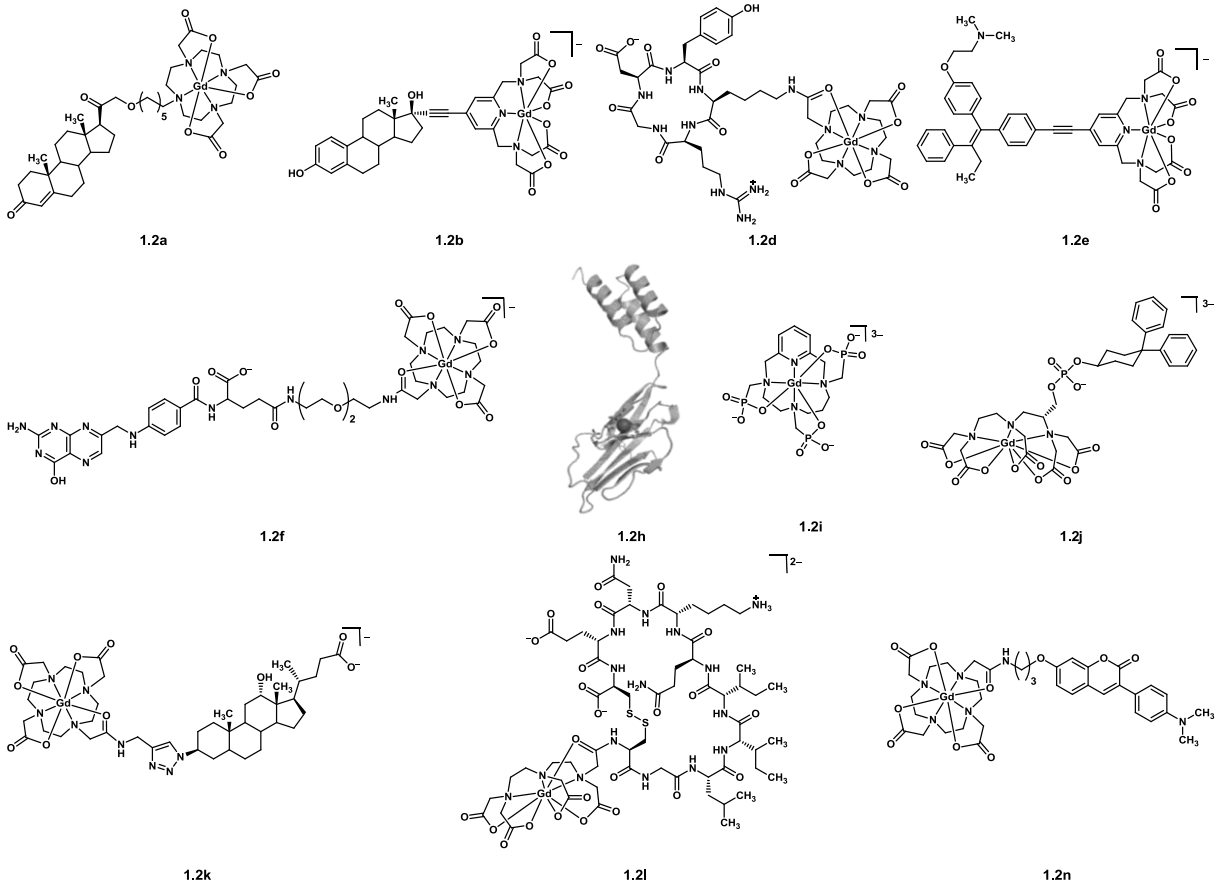

Figure 1.2. Monomeric targeted contrast agents synthesized using the conjugation strategy. Contrast agent **1.2h** is adapted with permission from reference 31. Copyright 2011 Qiao *et al*.

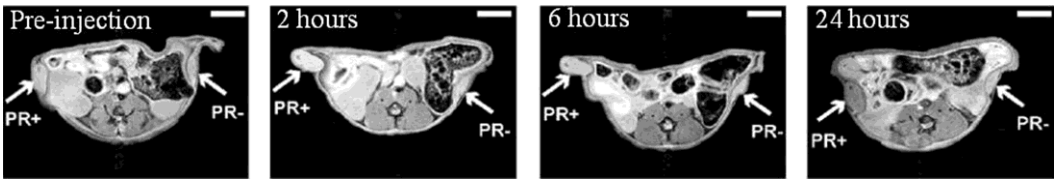

Figure 1.3. Representative *in vivo* images of targeted contrast agents: contrast enhancement of progesterone-receptor (PR)-positive and PR-negative tumors using monomeric conjugated contrast agent **1.2a**. Scale bars represent 5 mm, and arrows point to tumors. Adapted with permission from reference 22. Copyright 2011 American Chemical Society.

The integrin-receptor-targeted examples **1.2c** and **1.2d** demonstrate the importance of biomarker expression level for targeted imaging. However, *in vitro* success is often difficult to translate *in vivo* even with biomarkers expressed at high levels and high-affinity targeting moieties. For example, the estrogen-receptor-targeted contrast agent **1.2e** (**Figure 1.2**) reported by Degani and co-workers has a relaxivity of 4.7 $mM^{-1}s^{-1}$ (9.4 T and PBS). However, agent **1.2e** (using same dose as **1.2b**) was not able to produce significant enhancement *in vivo* despite a higher *in vitro* binding affinity with a binding inhibition constant, K_i, of 0.13 μmol/L for estrogen receptors than **1.2b** (K_i = 0.97 μmol/L).[23] This discrepancy likely was due to the accumulation of **1.2e** in muscle tissues causing a reduction in the effective dose for estrogen-receptor-positive tumors.

Further highlights of the inconsistencies that are often observed between *in vitro* and *in vivo* systems are exemplified by two studies that target the folate receptor, which is found in high concentrations in tumors. Folate-conjugated monomeric contrast agent **1.2f** (**Figure 1.2**) has a low relaxivity of 1.28 $mM^{-1}s^{-1}$ (4.7 T and aqueous solution).[29] *In vitro* studies of **1.2f** with human folate-receptor-positive ovarian carcinoma (IGROV-1) cell lines did not produce signal enhancement; however, inductively coupled plasma-mass spectrometry results with competitive binding experiments confirmed the uptake of **1.2f** by the cells. Despite the negative imaging results of the *in vitro* studies, *in vivo* studies at the same field strength demonstrated increased contrast of tumors in xenograft mouse models using a micromolar dose of **1.2f** delivered intravenously. Conversely, the folate-related agent **1.2g** reported by Wang and co-workers containing a dimeric Gd^{III} chelate conjugated to folate has a high relaxivity of 21 $mM^{-1}s^{-1}$ per Gd^{III} ion (1.41 T, 37 °C, and water).[30] *In vitro* studies with IGROV-1 cells confirmed the uptake of **1.2g** through folate receptors. While contrast agent **1.2g** was unable to enhance contrast in

tumors implanted in rat models *in vivo* at 2 T (0.03 mmol/kg dose), the relaxation rate in the tumor increased and ΔR_1 (the difference between the T_1 relaxation rates before and 1 h after contrast enhancement) was 0.214 s^{-1} for **1.2g** relative to non-targeted agents (0.112 s^{-1}), suggesting that the agent was retained in the tumor. Hence, the poor enhancement obtained in this study likely is not related to the selectivity of the contrast agent.

Conjugating a high relaxivity agent to a targeting moiety often is advantageous because it leads to an increase in contrast with lower doses of agent. Recently, Yang and co-workers reported contrast agent **1.2h** targeted to human epidermal growth factor receptor type 2 (HER2) (**Figure 1.2**) using a designed protein chelator for Gd^{III}, and agent **1.2h** has a high relaxivity (21 $mM^{-1}s^{-1}$, 1.41 T, 37 °C, and tris(hydroxymethyl)aminomethane (Tris) buffer at pH 7).[31] The contrast agent is conjugated to a HER2 affibody as the targeting moiety, a fluorescent dye to enable tracking by fluorescence microscopy, and polyethylene glycol moieties to achieve biocompatibility. Agent **1.2h** demonstrated increased *in vivo* enhancement of tumors in xenograft mice using a tail vein injection of 100 fold lower dose (0.24 μmol per mouse) than is used commonly with clinical contrast agents for routine MR imaging experiments.

Although, a protein was used as the chelating moiety in the previous example, more often proteins are used as targets. There are several contrast agents that label human serum albumin, including Gd^{III} 3,6,10,16-tetraazabicyclo[10.3.1]hexadecane-3,6,10-tris(methanephosphonates) **1.2i**, MS-325 **1.2j**, and Gd^{III}DOTA-deoxycholic acid **1.2k** (**Figure 1.2**).[26,32,33] These agents bind to albumin leading to increased circulation times; consequently, they are used as blood pool imaging agents. Fibrin and collagen are other well explored proteins for targeted imaging because they are found in high concentrations in angiogenesis, thrombosis, atherosclerosis, and other wound-healing processes. The cyclic decapeptide cCGLIIQKNEC (CLT1) conjugated to

Gd^{III} diethylenetriaminepentaacetic acid (DTPA), **1.2l**, (**Figure 1.2**) is a fibrin–fibronectin-labeling agent with a relaxivity of 4.22 $mM^{-1}s^{-1}$ (3 T and room temperature).[34] *In vivo* tumor imaging of human colon cancer xenografts in mice showed enhancement of tumors using a 0.1 mmol/kg dose because of the high concentration of fibrin–fibronectin associated with the neovascularization of tumors.

Imaging diseases in the brain is more challenging than in other parts of the body because of the tight regulation in transportation of compounds across the blood–brain barrier (BBB). Some diseases like brain tumors disrupt the BBB allowing contrast agents to accumulate in the interstitial spaces that outline the tumor region. However, many other abundant neuropathologies including Alzheimer's disease and multiple sclerosis do not disrupt the BBB during early stages of the diseases. Hence, the synthesis of targeting biomarkers to image neuropathology with MRI is an active area of research because of the current lack of *in vivo* detection methods. β-Amyloid peptides and myelin are two components that have been investigated as targets.[35–39]

β-Amyloid plaques are potential biomarkers for imaging Alzheimer's disease.[35–37] A derivative of amyloid peptide conjugated with Gd^{III}-containing complexes, **1.2m**, was found to label amyloid plaques *in vivo*.[35] MRI imaging at 7 T of brains removed from transgenic mice (APP-PS1) that were injected intravenously with **1.2m** demonstrated contrast enhancement of plaques. This result implies that **1.2m** has the ability to cross the BBB. However, *in vivo* imaging was not reported; hence, the applicability of **1.2m** for *in vivo* imaging cannot be predicted without further research.

Myelin is another biomarker for various neurodegenerative diseases including multiple sclerosis, leukodystrophies, and schizophrenia because these neuropathological disorders cause

either the degradation of myelin or the formation of defective myelin. Wang and co-workers reported myelin-targeted contrast agent **1.2n** (**Figure 1.2**).[38,39] Contrast agent **1.2n** contains a coumarine derivative as the targeting unit conjugated to Gd^{III}DOTA, and this agent has a relaxivity of 5.2 $mM^{-1}s^{-1}$ (9.4 T, 21 °C, and water). *Ex vivo* T_1 mapping of mouse brains incubated with **1.2n** demonstrated the specificity of **1.2n** for myelin.[38] Subsequent *in vivo* studies were carried out with intracerebroventricular infusions (~1 mg (1.14 μmol)/kg) because of the poor BBB penetration of **1.2n**. These studies demonstrated the specificity for myelin and the ability of **1.2n** to highlight demyelination with T_1 mapping at 9.4 T.[39] However, conventional MR imaging was not reported with this agent, which likely was due to low sensitivity that needs to be improved for clinical translations of **1.2n**.

While monomeric agents are desirable because of their low molecular weight, in general, studies of monomeric targeted agents reveal the need for biomarkers with high local concentrations or for the use of large doses of contrast agents to achieve enhancement of targets due to the low sensitivity of these agents. Therefore, it is essential to increase the sensitivity of target-specific agents to image biomarkers with relatively low expression levels.

Multimeric target-specific contrast agents

Compared to monomeric agents, multimeric contrast agents can be used to image biomarkers that have relatively low expression levels. Also, the blood circulation of multimeric contrast agents tends to be longer than that of monomeric agents because the large size of multimeric agents prevents rapid clearance via the kidneys; hence, multimeric agents often have a longer time to interact with targets. Furthermore, high molecular weights result in slow tumbling rates that increase relaxivity, and multimeric targeted contrast agents contain up to

thousands of contrast-enhancing units and targeting moieties that also increase relaxivity. The long circulation times and high relaxivities of multimeric agents enable the use of smaller doses than monomeric agents for *in vivo* imaging.

Fibrin-targeted agent **1.4a** (**Figure 1.4**) contains four Gd^{III}DOTA complexes conjugated to an 11-amino-acid fibrin-targeting peptide. The relaxivity of this tetrameric contrast agent is 10.1 $mM^{-1}s^{-1}$ per Gd^{III} ion in the absence of fibrin and increases to 17.8 $mM^{-1}s^{-1}$ per Gd^{III} ion upon binding to fibrin (1.41 T, 37 °C, and Tris buffered saline (TBS)).[40] The effectiveness of **1.4a** as a targeted contrast agent *in vivo* was demonstrated by imaging pulmonary emboli and cerebral venous sinus thrombosis.[41,42] Both studies were performed using swine models containing engineered human blood clots, and contrast enhancement was reported at 1.5 T after intravenous injection of 4 μmol/kg of **1.4a**. These studies reveal the specificity of **1.4a** for fibrin and the applicability of **1.4a** to the detection of fibrin-associated diseases *in vivo* with low doses.

A structurally similar agent to **1.4a** is collagen-targeted contrast agent **1.4b** (**Figure 1.4**). Agent **1.4b** was synthesized by conjugating three Gd^{III}DTPA complexes to a 16-amino-acid peptide.[43] Contrast agent **1.4b** has a relaxivity of 16.1 $mM^{-1}s^{-1}$ per Gd^{III} ion (1.41 T, 37 °C, and PBS) or 5.4 $mM^{-1}s^{-1}$ per Gd^{III} ion (4.7 T, 25 °C, and PBS). *In vivo* imaging with **1.4b** (tail-vein injection of 0.025 mmol/kg) in mouse models enabled specific imaging of myocardial fibrosis at 4.7 T.[43,44] The higher dose used for **1.4b** relative to **1.4a**, is likely necessary due to the large amounts of collagen present in many organs and low relaxivity reported for **1.4b** at 4.7 T field strength. With agents **1.4a** and **1.4b**, three or four Gd^{III}-containing units were conjugated to the targeting peptide via functional groups present in the amino acid side chains resulting in increased efficiency.

To increase relaxivity by increasing Gd^{III}-loading, macromolecules including polymers, dendrimers, nanoparticles, and liposomes are used.[45–60] These macromolecules act as carriers to transport large numbers of contrast agents and targeting moieties. The expectation with this method is that contrast enhancement will be observed even if only a small number of target molecules are labeled. Conjugation of several Gd^{III}-containing complexes and targeting moieties to poly(L-glutamic acid)cystamine or *N*-(2-hydroxypropyl)methacrylamide produced contrast agents **1.4c** and **1.4d** (**Figure 1.4**) for targeting integrins.[45,46] Agent **1.4c** has a relaxivity of 9.7 $mM^{-1}s^{-1}$ per Gd^{III} ion (3 T and water) and **1.4d** has a relaxivity of 20.6 $mM^{-1}s^{-1}$ per Gd^{III} ion (1.5 T and water). Both agents effectively bind $\alpha_V\beta_3$ intergrin *in vitro*, and quantitative T_1 mapping demonstrated that polymers **1.4c** and **1.4d** interact with integrins in the tumors of xenograft mice using tail-vein injections of 5 μmol Gd^{III}/kg and 0.03 mmol Gd^{III}/kg, respectively. However, a contrast enhancement was not observed with **1.4c** or **1.4d**, which likely was due to insufficient loading of Gd^{III}-containing complexes onto the polymers.[45,46]

Another type of macromolecular targeting agent uses proteins as scaffolds for targeting moieties and Gd^{III}-containing chelates. Maleylated bovine serum albumin conjugated to Gd^{III}DOTA, **1.4e**, was studied as a macrophage-scavenger-receptor-targeted contrast agent *in vitro*.[47] The maleyl groups acted as the targeting moieties and up to 22 Gd^{III}-chelates were linked to the protein. The relaxivity of **1.4e** is 29.1 $mM^{-1}s^{-1}$ per Gd^{III} ion (0.61 T, 25 °C, and water at pH 7), and *in vitro* cell imaging demonstrated increased contrast for macrophages after incubation with **1.4e**.

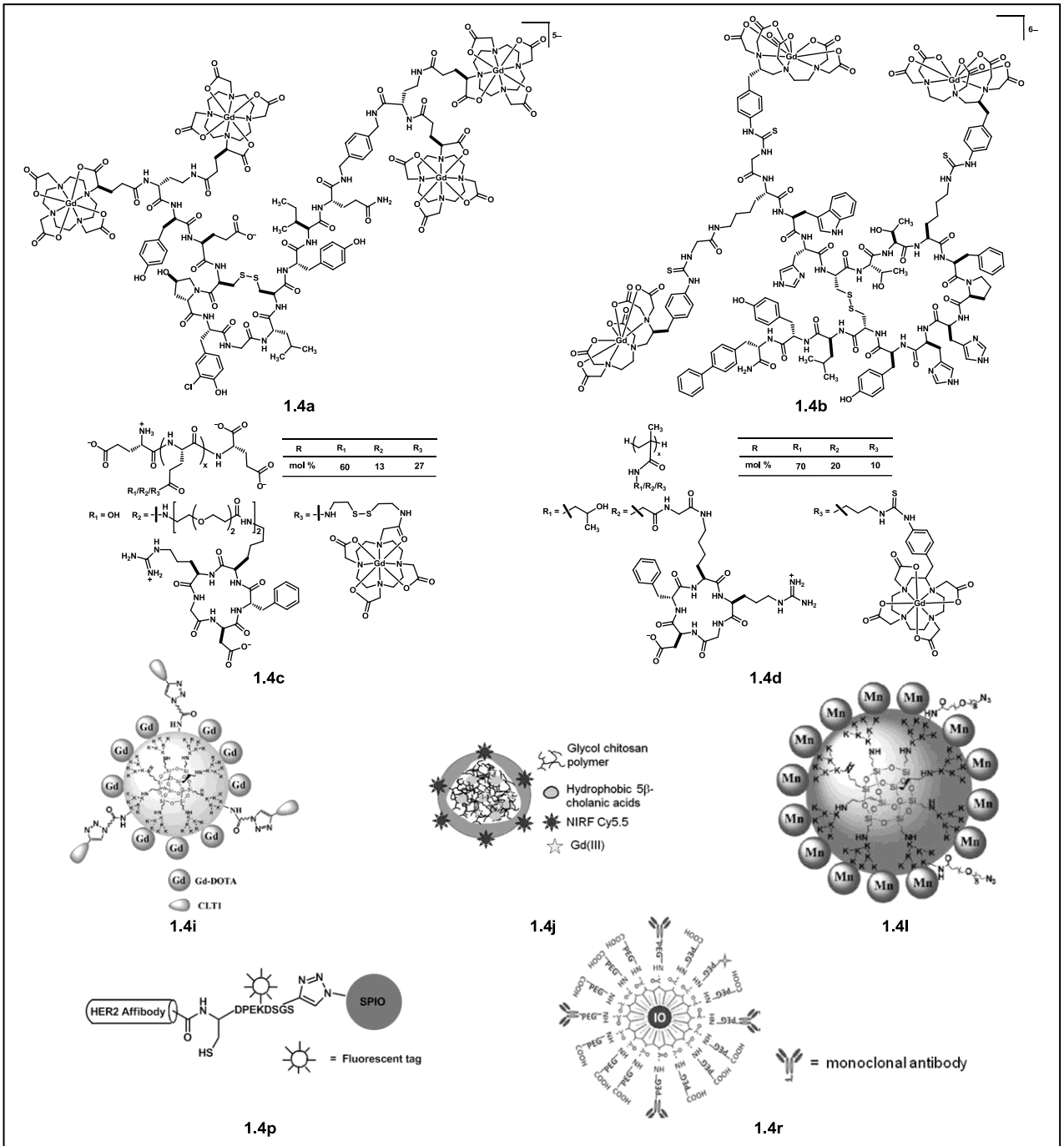

Figure 1.4. Multimeric targeted contrast agents synthesized using the conjugation strategy. Contrast agents **1.4i**, **1.4j**, **1.4l**, **1.4p**, and **1.4r** were adapted with permission from references 56, 58, 60, 66. Copyright 2010 American Chemical Society; and 64. Copyright 2010 Wiley-VCH verlag GmbH & Co. KGaA, Weinheim, respectively.

Dendrimers are also used as carriers for multimeric agents. Polyamidoamine (PAMAM) dendrimers are widely used as a macromolecular delivery system because they can be functionalized easily and are biocompatible.[48–50] *In vivo* imaging using agents **1.4f** and **1.4g** composed of folic acid and Gd^{III}-containing chelates conjugated to PAMAM dendrimers enabled contrast enhancement of human epidermoid carcinomas in xenograft mice.[49,50] The relaxivity of these contrast agents is higher than monomeric agents, for example 64.88 $mM^{-1}s^{-1}$ per Gd^{III} ion (3 T and water) for **1.4f** and 26.0 $mM^{-1}s^{-1}$ per Gd^{III} ion (2 T and 20 °C) for **1.4g**. These high relaxivities enable low-dose imaging (tail-vein injections of 0.05 mmol Gd^{III}/kg and 0.029 mmol Gd^{III}/kg for **1.4f** and **1.4g**, respectively).

Nanoparticles and liposomes that contain Gd^{III} chelates are other classes of multimeric targeted contrast agents. These systems enable the incorporation of different types of imaging, therapeutic, and targeting agents to the same carrier without great synthetic burden. Tens to thousands of Gd^{III} or Mn^{II} ions have been loaded into nanoparticles for use as targeted contrast agents for *in vitro* and *in vivo* studies.[54,56,57] Lanza and co-workers reported integrin-targeted contrast agents for tumor imaging using Gd^{III}-containing nanoparticles.[54,55] These nanoparticles, **1.4h**, containing an $\alpha_V\beta_3$ integrin antagonist and Gd^{III}DTPA, were used to visualize early tumor angiogenesis in xenograft mice using intravenous injections of 0.5 mL/kg (~0.03 nmol particles/kg or 2.7 μmol Gd^{III}/kg based on data in [54]). Each nanoparticle contained ~90,000 Gd^{III} ions with a relaxivity of 1,800,000 $mM^{-1}s^{-1}$ per particle (~20 $mM^{-1}s^{-1}$ per Gd^{III} ion, 0.47 T, and 40 °C). Nanoparticle **1.4h** produced a 173% contrast enhancement in melanoma xenografts at 1.5 T.[54] Lu and co-workers recently reported a nanoglobular system **1.4i** (**Figure 1.4**) containing the decapeptide CLT1 and Gd^{III}DOTA to target fibrin–fibronectin.[56] The generation 3 nanoglobular system with a molecular relaxivity of 353 $mM^{-1}s^{-1}$ (8.2 $mM^{-1}s^{-1}$ per Gd^{III} ion) (3

T, 25 °C, and water) was used for *in vivo* imaging of tumor-bearing mice. A tail-vein injection of 0.03 mmol Gd^{III}/kg of **1.4i** produced image enhancement in the area of the tumor (**Figure 1.5**). The nanoparticles were excreted via the renal pathway, which is important for the translation of these contrast agents into clinical applications.

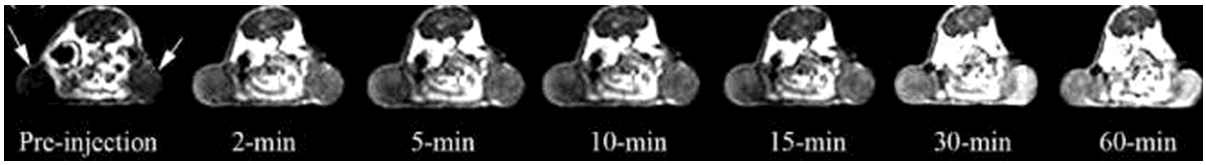

Figure 1.5. Representative *in vivo* images of targeted contrast agents: contrast enhancement of fibronectin–fibrin complex in tumor tissues using multimeric conjugated contrast agent **1.4i**. Arrows point to tumors. Reprinted with permission from reference 56. Copyright 2010 American Chemical Society.

Although, nanoparticles are potential carriers to increase the local concentration of contrast agent at sites of interest, maintaining a size smaller than the renal excretion threshold (~8 nm) and a high relaxivity is needed to enable the clinical application of these agents. To achieve high relaxivity with nanoparticles, attachment of Gd^{III}-containing chelates to the surface of nanoparticles is more desirable than encapsulation[57] because encapsulation decreases relaxivity of nanoparticles. For example, Gd^{III}DOTA encapsulated in chitosan nanoparticles **1.4j** (**Figure 1.4**) and Gd^{III}DTPA encapsulated in liposomes **1.4k** have lower relaxivities (1.04 $mM^{-1}s^{-1}$ per Gd^{III} ion, 0.47 T, and 40 °C for **1.4k**) than Gd^{III}DOTA and Gd^{III}DTPA, respectively.[58,59] These low relaxivities resulted from the reduced accessibility of water molecules to the Gd^{III} ions due to the encapsulation inside of the hydrophobic nanosystems. Attaching Gd^{III}-containing chelates on particle surfaces enables facile access of water molecules to Gd^{III} ions; however,

attaching a large number of Gd^{III}-containing chelates on the nanoparticle surface increases the risk of leaching Gd^{III} ions.

Because of the toxicity of unchelated Gd^{III} ions, several research groups have studied Mn^{II}-containing nanosystems for targeted imaging.[60,61] Although, Mn^{II} (spin 5/2) has a lower relaxivity than Gd^{III} (spin 7/2), nanosystems with large Mn^{II} loadings can produce contrast enhancement of targets. Lu and co-workers reported a nanoglobular system **1.4l** (**Figure 1.4**) that contained the fibrin-targeted decapeptide CLT1 and Mn^{II}DOTA monoamide.[60] This Mn^{II} nanosystem has a relaxivity of 3.13 $mM^{-1}s^{-1}$ per Mn^{II} ion and 131 $mM^{-1}s^{-1}$ per nanoglobule (3 T and room temperature). *In vivo* imaging of breast carcinoma xenograft mice that were injected (tail-vein) with 0.03 mmol Mn^{II}/kg of **1.4l** produced contrast enhancement of tumor with respect to non-targeted controls, and the contrast agents were excreted through the kidneys. Manganese oxide nanocolloidal systems also were reported to target fibrin.[61] Mn^{II} oxide nanocolloide **1.4m** and Mn^{II} oleate nanocolloide **1.4n** both labeled fibrin clots *in vitro*. The relaxivities of **1.4m** and **1.4n** were 4.1 and 14.6 $mM^{-1}s^{-1}$ per Mn^{II} ion (91,127 and 423,420 $mM^{-1}s^{-1}$ per particle at 3T, 25 °C), respectively. These high relaxivity values and *in vitro* studies suggest that Mn^{II} oxide nanocolloides could be useful for *in vivo* fibrin detection.

Superparamagnetic target-specific contrast agents using the conjugation strategy

Superparamagnetic iron oxide (SPIO) nanoparticles coated with polymers are another class of contrast agents for MRI. These agents enhance the contrast of images by decreasing signal intensity in T_2- and T_2^*-weighted imaging and, consequently, darkening the target area relative to surrounding tissues. Although, the darkening effect (negative contrast) is not ideal for anatomical imaging, many SPIO-based target-specific contrast agents are reported with T_2-

weighted imaging because they can be used for target detection in post-injection images when compared to pre-injection images. Additionally, SPIO-based images can be converted to positive imaging agents using different pulse sequences and post-processing positive-contrast techniques.[62] Although, these new positive imaging techniques with SPIO nanoparticles have been reported with cell labeling and tracking studies, we have limited our discussion on SPIO-based target-specific contrast agents in this section to conventional T_2- or T_2^*-weighted imaging.

SPIO nanoparticles are used in MRI because of the biocompatibility of iron oxide nanoparticles and high T_2 relaxivity for contrast enhancement. These biocompatible SPIO nanoparticles are taken up by the reticuloendothelial system (RES) in cells; hence, in early studies, SPIO nanoparticles were used to detect lesions in RES-rich organs including the liver, spleen, and lymph nodes without the use of a conjugated targeting moiety.[17] However, recent research has focused on conjugating targeting moieties to the nanoparticle surface to achieve selectivity to areas other than hepatic lesions. Conjugation of targeting moieties to the iron oxide core is possible because of the polymeric coatings used to stabilize the SPIO nanoparticles. Rajabi and Tsourkas and co-workers reported the use of targeted SPIO nanoparticles for selective detection of tumors *in vivo*.[63,64] The contrast agents reported by these groups target the HER2 receptor in tumor tissues and consisted of magnetic nanoparticles modified with the monoclonal antibody Trastuzumab, **1.4o**, or with a HER2-affibody, **1.4p** (**Figure 1.4**). To synthesize particle **1.4o**, the targeting antibody was conjugated to the nanoparticle using an amine-containing linker incorporated into a dextran coating.[63] Whereas, in particle **1.4p**, the azide–alkyne Huisgen cycloaddition (often referred to as "click" chemistry) was used to conjugate an alkynated linker containing the HER2-targeted affibody to a polymer coating functionalized with azides.[64] Agent **1.4o** enhanced the tumor regions in mouse models relative to

surrounding tissues with 30 μmol/kg (tail-vein injections). For agent **1.4p**, a 10 mg (0.18 mmol) Fe/kg dose was used (retro-orbital injection) to enhance contrast of tumors (**Figure 1.6**). Iron oxide nanoparticles conjugated with urokinase-type plasminogen activator (uPA) peptide, **1.4q**, used carboxylates on the polymer coating to conjugate with targeting moieties.[65] The uPA peptide was engineered to contain an amine that enables conjugation with nanoparticles via amide linkages. Contrast agent **1.4q** has relaxivity (T_2) value of 124 $mM^{-1}s^{-1}$ (3 T) and targets uPA receptors that are over-expressed in tumors. *In vivo* imaging with intravenous injections of **1.4q** at 3 T using mammary carcinoma bearing mouse models demonstrated enhanced contrast in the tumor region, but contrast enhancement within the tumor was heterogeneous. This heterogeneous distribution of **1.4q** in tumor tissue and the resultant decrease in signal intensity enabled an understanding of receptor distribution in addition to tumor detection. Another cancer-cell-targeted SPIO-nanopartcle-based contrast agent, **1.4r** (**Figure 1.4**), acts as a drug delivery vehicle as well as an imaging probe.[66] In this study, SPIO nanoparticles were labeled with a monoclonal antibody, a fluorescent probe, and four anticancer drugs that release from the SPIO nanoparticle in response to changes in pH. Although, *in vivo* imaging was not performed, *in vitro* studies of this potential theranostic agent using human colon cancer cells (LS174T) demonstrated a reduction of T_2 in cells incubated (0.03 mg/mL and 37 °C) with **1.4r** (55.5 ms) with respect to untreated control cells (117.3 ms) at 7 T.

Figure 1.6. Representative *in vivo* images of targeted contrast agents: contrast enhancement of HER2-positive tumors using conjugated SPIO nanoparticle **1.4p**. Arrows point to tumors. Adapted with permission from reference 64. Copyright 2010 Wiley-VCH Verlag GmbH & Co. KGaA, Weinheim.

Other than tumor imaging, SPIO nanoparticles are reported to detect renal inflammations. Thurman and co-workers reported the use of SPIO nanoparticles, **1.4s**, conjugated with a recombinant protein that targets the complement receptor type 2 in kidneys for *in vivo* studies of glomerulonephritis. A dose of 10–16 mg of particles/kg enhanced contrast of the kidneys of diseased mice and demonstrated the potential for selective visualization of renal inflammation without the need for invasive renal biopsies.[67,68]

The direct conjugation of targeting moieties with contrast agents or carrier molecules containing contrast agents is synthetically a simple approach to achieve selectivity. Therefore, both *in vitro* and *in vivo* imaging are reported for many targeted agents synthesized with this strategy. Monomeric targeted agents interact with or are internalized by targeted cells and can clear from the body easily because of their small size. But, monomeric agents often have low sensitivity. Multimeric agents that bear up to thousands of contrast-enhancing units and targeting moieties have high relaxivities because of their large size and the number of conjugated contrast agents. However, large size can result in difficulties in clearance. Therefore, while each class of targeted agents has potential niche uses, multimeric agents of intermediate size that have high

relaxivities but remain within the renal-clearance threshold likely will be the agents with more potential for *in vivo* applications in the future.

Target-specific contrast agents designed with the structure-mimicking strategy

Transforming contrast agents into structural mimics of molecules that interact with specific tissues and receptor molecules is a targeting strategy that converts contrast agents directly into targeting moieties. However, the synthesis of contrast agents that mimic the structure of biologically active molecules can be synthetically challenging. Several attempts to synthesize targeted biomimetic contrast agents have been reported and include porphyrin-, high-density-lipoprotein-, and ferritin-based agents.[69–79]

Porphyrins selectively accumulate in necrotic tissues and interact with neurons;[69,80,81] porphyrins also form stable complexes with some metal ions and possess optical properties that are advantageous for imaging studies. Consequently, several porphyrin-based contrast agents have been reported for tumor targeting. Mn^{III}-containing porphyrin–dextran system **1.7a** (**Figure 1.7**) was used to visualize tumors *in vivo*. Porphyrin agent **1.7a** has a relaxivity of 8.90 $mM^{-1}s^{-1}$ (4.7 T and aqueous solution) and enhances tumor contrast in mice bearing hepatoma tumors using a 0.05 mmol Mn^{III}/kg dose (intravenous injection).[70] Another Mn^{III}-based porphyrin, **1.7b** (**Figure 1.7**), was reported as a brain-tissue-specific contrast agent that is cell permeable and labels neuronal cell bodies in the hippocampus.[71] However, the introduction of contrast agent **1.7b** to rat brains (0.017–0.02 μmol/kg dose) using direct injection and the long retention time reported in brain tissues ($t_{1/2} \approx 10$ days) suggest areas for future research with this contrast agent.

Although, Mn^{III}-containing porphyrins have higher relaxivities than clinical contrast agents, they have lower relaxivities than Gd^{III}-containing porphyrins.[70,72] Two Gd^{III}-containing

porphyrins **1.7c** and **1.7d** (**Figure 1.7**) were reported for *in vivo* melanoma imaging (relaxivities of 16.3 and 31.7 $mM^{-1}s^{-1}$ at 7 T, 23 °C, and aqueous solutions for **1.7c** and **1.7d** respectively).[72,73] *In vivo* imaging of xenograft nude mice using 0.1 mmol/kg of **1.7c** and **1.7d** (intravenous bolus injections) showed contrast enhancement in tumors due to specific accumulation.[72] However, Gd^{III}-containing porphyrins are kinetically unstable in solution because of the size disparity between the cation and porphyrin cavity.[74,82] Hence, expanded porphyrin systems, such as texaphyrins, are used to form stable complexes with Gd^{III}. Like porphyrins, Gd^{III}-containing texaphyrins accumulate in tumors and enhance contrast.[83] The relaxivity of Gd^{III}-containing texaphyrin **1.7e** (**Figure 1.7**) is 18 $mM^{-1}s^{-1}$ (1.2 T, 25 °C, and aqueous saline).[84] Because of the specific accumulation of texaphyrins in tumors and the optical properties of these molecules, texaphyrins are used as radiation sensitizers for tumor therapy and as tumor-specific imaging probes.[85]

Another porphyrin structural mimic used as a targeted contrast agent is the copper phthalocyanine dye Luxol fast blue MBS (LFB MBS) **1.7f** (**Figure 1.7**). Complex **1.7f** is a histology stain for myelinated neurons that was studied as a contrast agent for MRI in *ex vivo* brain tissues.[81] The relaxivity of this agent is low (0.15 $mM^{-1}s^{-1}$, 4.7 T, and ethanol) partially because the Cu^{II} ion has a spin of 3/2. Heavily myelinated regions appeared brighter in images when stained with LFB MBS with respect to control experiments, but to attain good contrast enhancement, similar molecules containing metals with higher spin values need to be synthesized.

Synthetic high-density lipoprotein (HDL) nanoparticles are another class of targeted contrast agents that mimic natural molecular entities to achieve selectivity. HDL particles are made into contrast agents by incorporating chelated Gd^{III} into the outer phospholipid coating or

by loading the core of the HDL particle with iron oxide.[75,76] Synthetic HDL nanoparticles **1.7g** and **1.7h** (**Figure 1.7**) target atherosclerosis. *In vivo* imaging of genetically engineered hyperlipidemic (ApoE KO) mice with tail-vein injections of 3.25 and 4.36 μmol/kg doses of **1.7g** (relaxivity (T_1) of 10.4 $mM^{-1}s^{-1}$ per particle, 1.5 T, 25 °C, and water at pH 7.4) demonstrated contrast enhancement of plaques (**Figure 1.8**).[75] *In vivo* imaging of ApoE KO mice with **1.7h** (relaxivity (T_2) of 94.2 $mM^{-1}s^{-1}$, 1.41 T, and 40 °C) also demonstrated contrast enhancement of plaques using 30 mg (0.54 mmol) Fe/kg.[76]

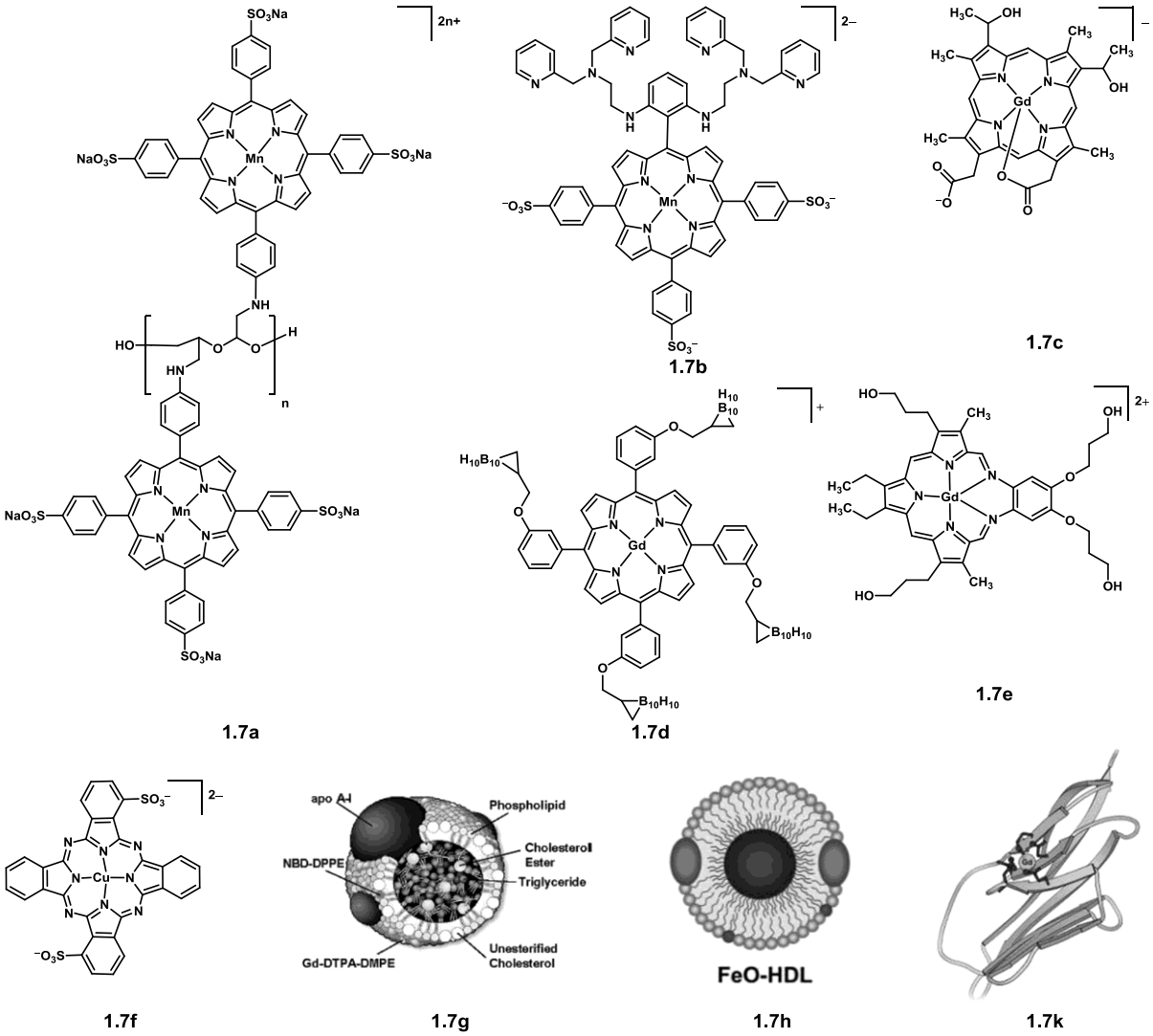

Figure 1.7. Targeted contrast agents synthesized using the structure mimicking strategy. Contrast agents **1.7g**, **1.7h**, and **1.7k** were adapted with permission from references 75, 78, and 86. Copyright 2004 and 2008 American Chemical Society.

Another iron-oxide-containing biomimetic used as a targeted agent is ferritin. Ferritin is a protein that stores iron and regulates levels of iron in the body. Consequently, endogenous ferritin can be used to recognize some ferritin-related diseases using MRI.[77] Thus, ferritin provides a template to generate SPIO-based contrast agent mimics. Recombinant human H chain

ferritin, **1.7i**, was used *in vitro* as a macrophage-targeted contrast agent, and these studies showed selective uptake of **1.7i** by macrophages (incubated with 165 μg (3 μmol) Fe/mL of **1.7i**) resulting in contrast enhancement at 1.5 T.[78] In another study, cationic ferritin **1.7j** was used as a basement-membrane-selective contrast agent to detect glomerulosclerosis.[79] Both *ex vivo* and *in vivo* imaging using **1.7j** in rat models at 11.7 T detected disruptions of basement membranes; however, five intravenous injections of a relatively high dose (~5 mg (0.089 mmol) Fe/kg) was required to detect cationic ferritin accumulation in glomeruli *in vivo*: this high dose is a challenge for translation into clinical applications.

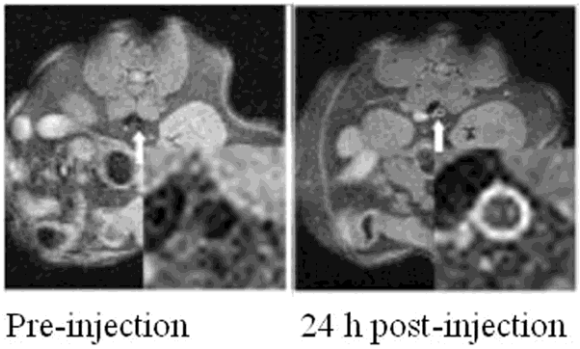

Figure 1.8. Representative *in vivo* images of targeted contrast agents: contrast enhancement of atherosclerotic plaques using high-density lipoprotein mimic **1.7g**. Arrows point to abdominal aorta. Adapted with permission from reference 75. Copyright 2004 American Chemical Society.

Recently, Yang and co-workers reported engineered proteins that chelate Gd^{III} ions to produce stable high relaxivity contrast agents for MRI.[86] An example is a contrast agent containing an engineered cell adhesion protein **1.7k** (**Figure 1.7**) with a domain to chelate Gd^{III} ions. Agent **1.7k** has a relaxivity of 117 $mM^{-1}s^{-1}$ (1.5 T) enabling doses as low as 2.4 μmol Gd^{III}/kg for contrast-enhanced imaging. Using this approach, endogenous proteins can be mimicked to synthesize targeted contrast agents with higher efficiency.

While the structure-mimicking strategy enables the use of endogenous interactions to deliver agents, synthesizing targeted agents with the structure-mimicking strategy is challenging and not generalizable like the conjugation strategy. Therefore, the scope of targets and number of examples are limited relative to agents synthesized with the conjugation strategy. Some of these agents have high relaxivities and enhance contrast *in vivo*; however, more research is needed in this area to improve current mimetic agents and to find new biomimetics that form stable paramagnetic complexes and are specific for various tissues and diseases.

Summary

Targeted contrast agents enable the visualization of structural changes in organs or the expression of biological molecules, and these agents have the potential to aid in the diagnosis of diseases at early stages. In general, targeting ability is achieved by conjugating a targeting moiety to a contrast agent or by mimicking the structural features of targeting moieties with contrast agents. A large number of targeted agents have been synthesized with the conjugation strategy, and while conjugation of a single contrast-enhancing unit per targeting moiety enables selective imaging in the presence of high local concentrations of targets, many such contrast agents suffer from low sensitivity and require large doses to achieve contrast enhancement. The use of multiple contrast-enhancing units in multimeric agents overcomes the limitation of sensitivity, but the large size of multimeric agents can cause difficulties with excretion. Synthesis of macromolecules smaller than the renal excretion threshold is a strategy to avoid this problem, but this strategy also influences relaxivity. Also, polydispersity of these systems can lead to difficulties with reproducibility. Relatively few examples of the mimicking strategy are reported for the design of targeted contrast agents because of the limited availability of biomimetics that form stable complexes with paramagnetic cations; however, recent advances in nanochemistry

and biotechnology will likely lead to more opportunities for mimicking biologically important structures with contrast agents.

Except for one or two target-specific contrast agents that are clinically approved (MS-325) or in clinical-trials (texaphyrins), the majority of target-specific agents are in pre-clinical levels of research; however, successful *in vivo* imaging was reported with many pre-clinical studies, and these results shine positive light onto the future of the field. An area of where extra attention to detail will likely aid the field is the inclusion of as many experimental details as possible: the direct comparison of different studies is difficult because the conditions used for relaxivity measurements and imaging experiments are different (**Table 1.1**), and improper comparisons could lead to misinterpretations of the efficiency of one agent compared to another. Finally, improvements to the selectivity, sensitivity, and biocompatibility of target-specific agents and the selection of new molecular targets using both the conjugation and mimicking strategies will likely enable translation into clinical applications for MRI.

Focus and layout of this thesis

The focus of the research described in this thesis is the exploration of the utility of Gd^{III}-containing complexes to achieve targeted imaging with MRI. The two targets that were selected were myelin and β-amyloid plaques, which are important markers for detection of neurological disease as described earlier in this chapter. The ability to detect neurological disease without ambiguity is important for clinical imaging where early detection is essential for better treatment, and also for the advancement of related research. The findings of the research in this thesis would be mostly important for pre-clinical research related to neurological disease because these

studies lead to ex vivo and in vitro targeted imaging of myelin and β-amyloid aggregates, respectively.

To achieve the target specificity with Gd^{III}-containing complexes, both the conjugation and structure mimicking synthetic strategies that introduced previously in this chapter were used. The Gd^{III}-containing complex that was used to achieve the targeting of β-amyloid aggregates was synthesized using conjugation strategy, and the Gd^{III}-containing complexes for targeting myelin were synthesized using structure mimicking strategy. In Chapter 2, the design and synthesis of each metal complex is detailed including a discussion of the features of the new designed complexes that are important to achieve target specificity. In Chapters 3 and 4, the experiments are described that establish the ability of these complexes to act as target-specific contrast agents. In Chapter 5, the results reported in Chapters 2–4 are summarized in the context of other reported contrast agents and includes a discussion of suggested future directions for this research.

CHAPTER 2. Ligand design and synthesis

Introduction

Target-specific metal complexes can be achieved using two synthetic strategies, either conjugation or structure mimicking, as described in Chapter 1. To obtain efficient targeting and imaging, these metal complexes need to fulfill several requirements regardless of the synthetic strategy that is being used, including (1) enabling interaction with the target, (2) maintaining kinetic stability under the conditions of imaging, (3) having no interference of function between the targeting and imaging components, and (4) being synthetically feasible. Thus, addressing these requirements is an essential step in ligand design to achieve efficient target-specific contrast agents. The metal complexes presented in this thesis as contrast agents for magnetic resonance imaging (MRI) were designed to fulfill these four requirements. The following sections describe the design, synthesis, and the characterization of the metal complexes.

Design and synthesis of a β-amyloid-targeted metal complex.

The β-amyloid-targeted metal complex **2.1** was designed to be synthesized using the conjugation strategy, specifically by conjugating a small molecule known to have affinity for β-amyloid plaques to a derivative of a Gd^{III}-based contrast agent. The β-amyloid-plaque-selective small molecule that was chosen is curcumin, 1,7-bis-(4-hydroxy-3-methoxyphenyl)-1,6-heptadiene-3,5-dione (**Figure 2.1a**). Curcumin is a compound found in the rhizomes of the plant *Curcuma longa*, and it is a relatively hydrophobic, fluorescent molecule that is non-toxic at gram dosages.[87] Curcumin is known to interact with amyloid fibrils, and the planar hydrophobic aromatic structure of the molecule is considered to be the key feature for its interaction with β-amyloid fibrils.[88]

The β-pleated structure of aggregated amyloid protein allows small planar hydrophobic molecules to intercalate among β-pleated sheets and aromatic residues in the protein, leading to specific retention of these molecules in amyloid plaques. Therefore, curcumin is a good candidate for a targeting moiety for β-amyloid aggregates with its planar, hydrophobic, and non-toxic properties. Furthermore, synthetic curcumin is commercially available, and there are several functional groups found in curcumin including phenols and a β-ketoenol that can be used for conjugation reactions.

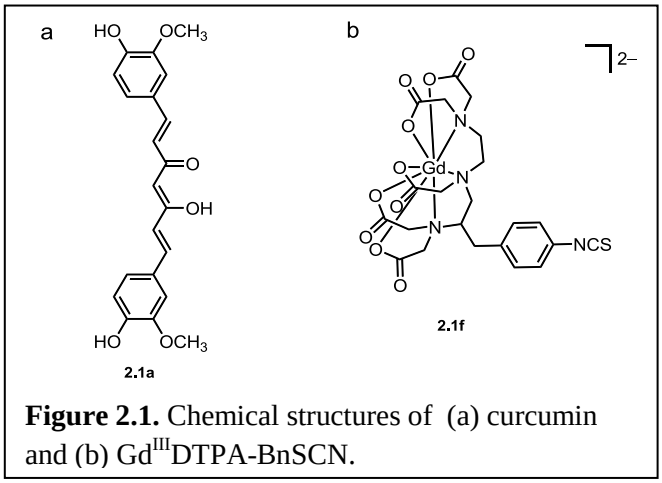

Figure 2.1. Chemical structures of (a) curcumin and (b) Gd^{III}DTPA-BnSCN.

The contrast agent that was chosen for the conjugation is a Gd^{III}-containing complex of diethylenetriaminepentaacetic acid functionalized with an isothiocyanate group (Gd^{III}DTPA-BnSCN) (**Figure 2.1b**). Gd^{III}DTPA is a clinically approved contrast agent for MRI, and the isothiocyanate group imparts the ability to conjugate to various nucleophilic functionalities. Furthermore, benzyl-isothiocyanate-containing DTPA is commercially available.

Initial design of the metal conjugate included a direct conjugation of the isothiocyanate group to the activated α-carbon of the β-ketoenol. To synthesize the conjugate, the phenols were first protected with benzoyl chloride and then two different sets of reaction conditions were tried to accomplish the desired reaction. The first attempt included the reaction of benzoyl-protected curcumin with Gd^{III}DTPA-BnSCN in dimethylsulfoxide in the presence of KOH following published procedures for the conjugation of similar functional groups.[89] The second attempt included the reaction of benzoyl-protected curcumin with sodium ethoxide to form the sodium

salt of enolate of **2.1a** and subsequent reaction of with Gd^{III}DTPA-BnSCN in pyridine. These reaction conditions did not result in the desired conjugate based on mass spectrometric analysis. The reason that avoided the occurrence of the reaction assumed to be the steric hindrance caused by DTPA molecule. Because direct conjugation of the curcumin molecule to the isothiocyante group in Gd^{III}DTPA-BnSCN was not successful, the targeted complex was redesigned by introducing an amine containing arm to the curcumin molecule.

The rationale behind the introduction of an amine linker included facilitating the reaction of Gd^{III}DTPA-BnSCN with curcumin and incorporating space between the targeting moiety and the imaging unit to avoid potential interference of function. The amine linker was synthesized using a published procedure[90] and was introduced to one of the phenol groups using sodium methoxide in methanol. The isolated amine-linker-containing curcumin was conjugated to Gd^{III}DTPA-BnSCN in the presence of diisopropylethylamine (DIEA) in aqueous acetonitrile (**Scheme 2.1**).

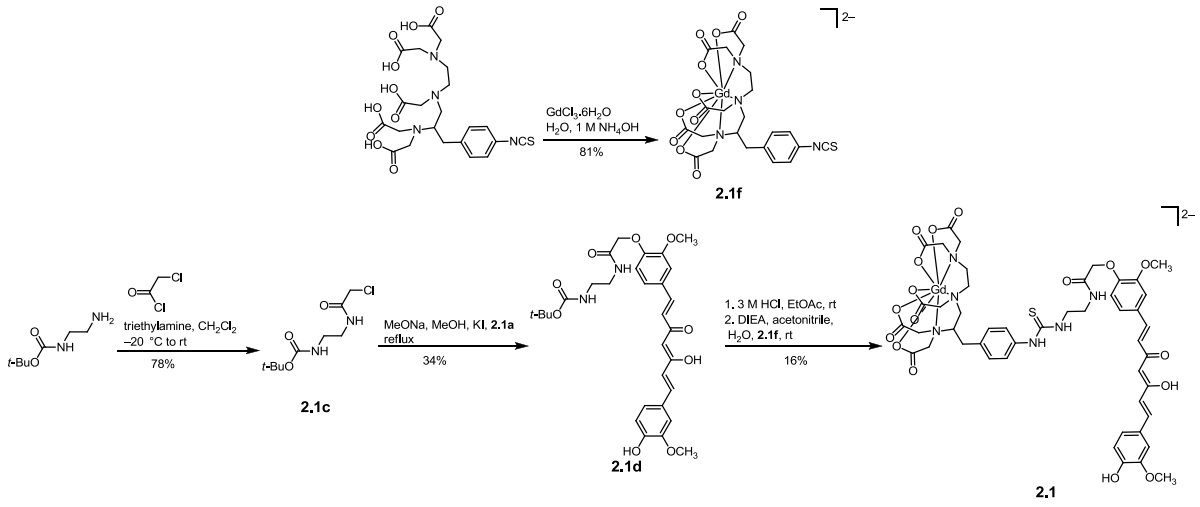

Scheme 2.1. Synthetic route to β-amyloid-targeted curcumin-conjugated Gd^{III}-containing complex **2.1**.

Design and synthesis of myelin-targeted metal complexes

Myelin-targeted metal complexes were designed to be synthesized using the structure mimicking strategy. A known myelin-specific histology stain, luxol fast blue MBS (LFB MBS), was selected as the template molecule (**Figure 2.2**). LFB MBS was found to be a stain for myelin in 1953 by Klüver and Barrera based on the knowledge that porphin derivatives are able to bind with myelin and that the phthalocyanine ring is similar in structure to porphyrins.[91] Although it is known that LFB MBS is capable of staining myelin, the site of interaction and nature of the interaction is unknown. However, several potential sites of interaction have been suggested: phospholipids, neurokeratin, proteolipid proteins, lipoproteins, and myelin basic proteins.[81] From these potential sites, the acid–base type of interaction between LFB MBS and myelin basic protein is more accepted due to the removal of ditolylguanidinium cation from stain upon interaction.[92] The planar non-polar structure of the LFB MBS is assume to facilitate the diffusion of LFB MBS into the myelinated regions in tissue, thus facilitating the interaction between the sulfonate groups of LFB MBS and the basic proteins containing cationic amino acids such as arginine. Despite functional knowledge of the myelin–LFB MBS interaction being limited, LFB MBS was used as the template molecule to design a myelin-targeted contrast agent in this research because its structure includes a macrocyclic ligand coordinated to a metal, and this motif is amenable to adaptation into a contrast agent for MRI. The texaphyrin ligand (**Figure 2.3**) was selected to design a

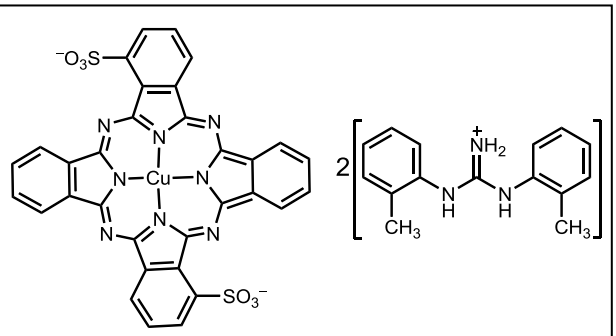

Figure 2.2. Structure of LFB MBS stain

complex containing the Gd^{III} ion by mimicking the structural features of the phthalocyanine ligand of LFB MBS. Of the chelating ligands for trivalent lanthanide cations that have been reported in the literature, the texaphyrin macrocycle shows a good potential to mimic the LFB MBS ligand fulfilling the requirements mentioned at the beginning of this chapter, namely, the ability to form a stable complex with Gd^{III}, good relaxivity that is essential for imaging, and synthetic feasibility. Structural similarities of phthalocyanine and texaphyrins include 22π Hückel aromatic systems, pyrrolic nitrogen donor atoms, and a planar macrocyclic structure. Additionally, the potential to introduce functional groups to the side chains of texaphyrins allows further mimicking of the LFB MBS structure. Using the texaphyrin ligand core, six different paramagnetic metal complexes, **2.2**–**2.7**, were designed to study the effect of charge and acid functional groups on myelin binding (**Figure 2.4**).

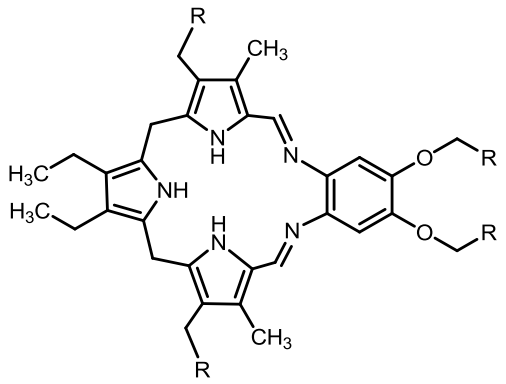

Figure 2.3. General structure of texaphyrin ligands. R can include a variety of different functional groups.

The functional groups incorporated in these designed molecules include esters, sulfonates, and carboxylates. All these functional groups have oxygen donor atoms, and sulfonates and carboxylates carry negative charges. Sulfonates were chosen to exactly mimic the functional group in LFB MBS, and carboxylates were chosen to investigate if the acid group needs to be sulfonates. Methyl esters were chosen to study the need for acid functional groups. Additionally, the methyl ester containing texaphyrin is an intermediate in the synthesis of the carboxylate-containing texaphyrin. Sessler and coworkers have intensively studied texaphyrin

complexes with different functional groups including alcohol, ether, ethyleneglycol, amine, and chloro groups;[93–95] however, functional groups of complexes **2.2–2.7** have not been reported previously with the texaphyrin motif.

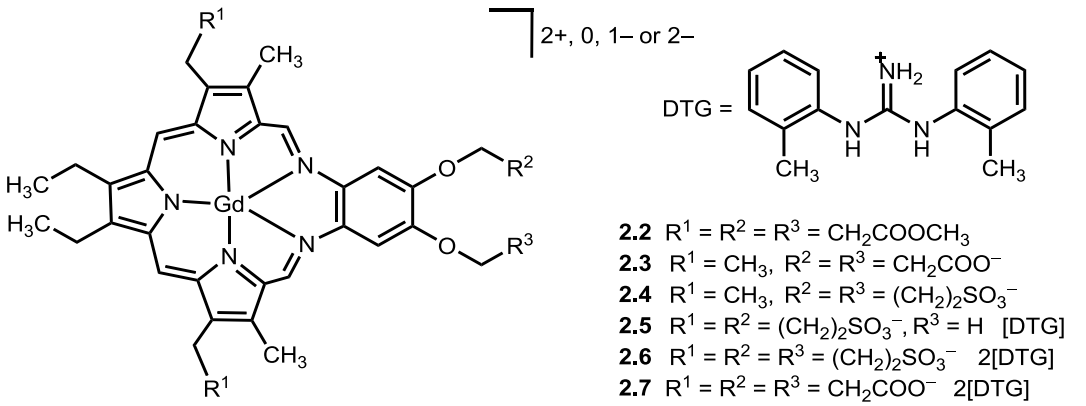

Figure 2.4. Target texaphyrin complexes

The overall charge of complex **2.2** is +2, and it does not have acidic functional groups; thus, it was designed to use as a control if negative charge or acidic functional groups are crucial for myelin-specific interactions. Complexes **2.4**–**2.6** have sulfonic acid groups and charges of 0, –1, and –2, respectively, and they were designed to use to study the necessity of sulfonate groups and the effect of the number of sulfonate groups on interaction with myelin. Complexes **2.3** and **2.7** have carboxylate groups with charges of 0 and –2, respectively, representing the carboxylate analogues of sulfonate texaphyrin complexes. All six of these complexes were designed to study with ex vivo mouse brain samples to investigate the important features for effective myelin-specific binding. Syntheses of metal complexes **2.2**–**2.6** were achieved as outlined in **Scheme 2.2**.

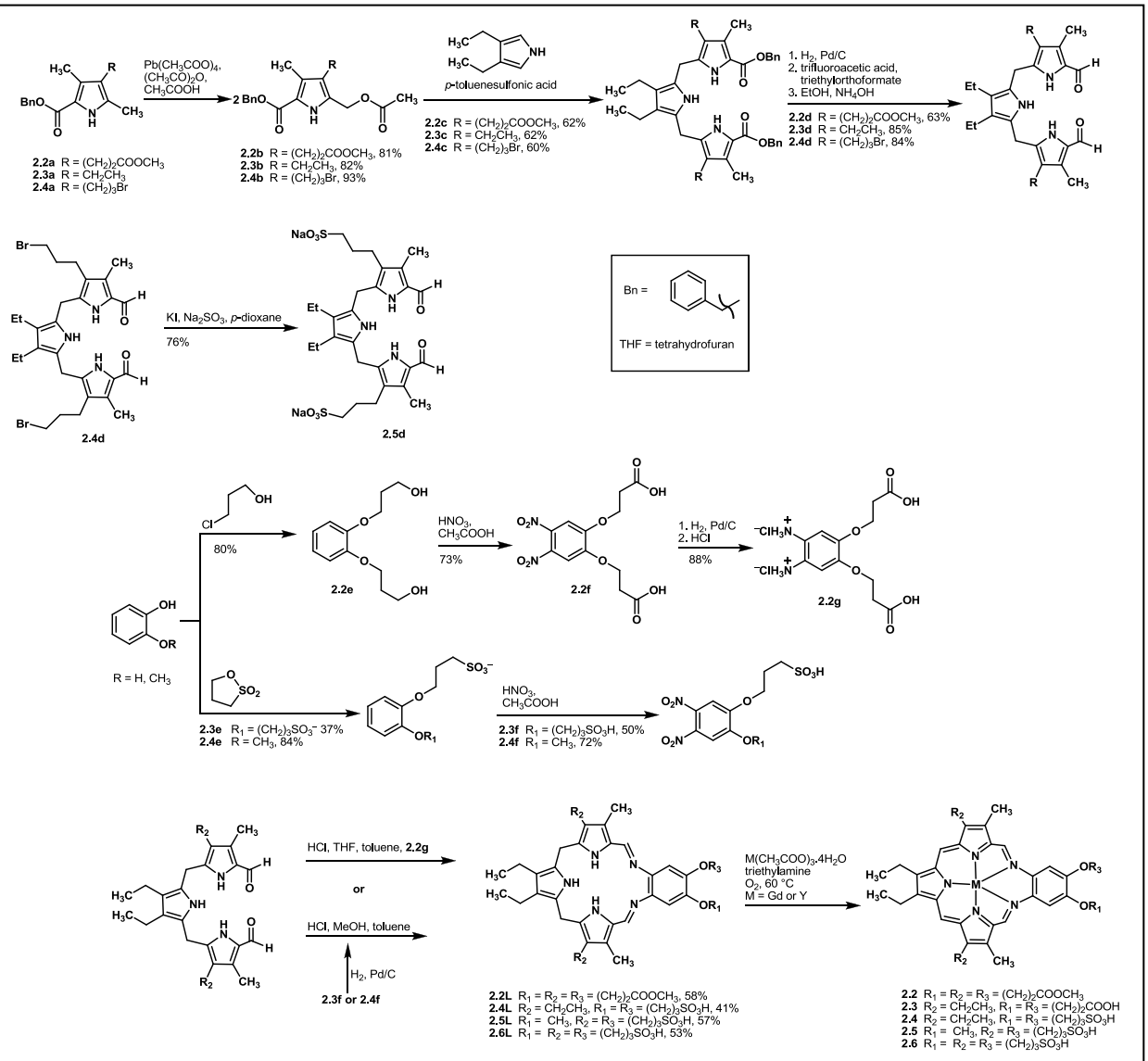

Scheme 2.2. Synthetic route to Gd^{III}-containing texaphyrin complexes **2.2–2.6**.

The synthesis of complex **2.7** was not confirmed by any characterization technique—including mass spectrometry, NMR spectroscopy, and UV–vis spectroscopy—despite the employment of a variety of synthetic conditions (**Table 2.1**). Hence, the synthesis of complex **2.7** was not

achieved. However, this set back did not affect the studies of myelin binding because complexes **2.2**–**2.6** contain all of the necessary variables to complete the planned studies.

Table 2.1. Synthetic conditions attempted toward the synthesis of complex **2.7**

Starting material	Reaction type and reaction conditions	Observations
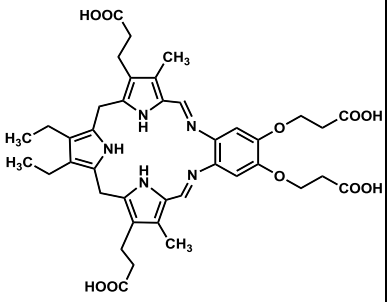	metallation $Gd(OAc)_3 \cdot 4H_2O$, triethylamine, methanol, air, reflux	A precipitate formed from the reaction mixture. UV–vis spectrum did not show the formation of metallated complex.
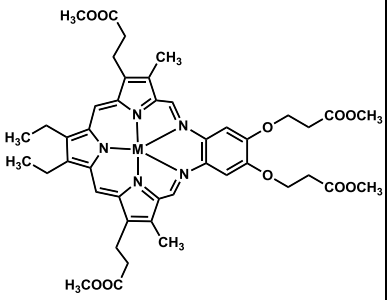	Sapponification of esters 1. LiOH, THF, H_2O 2. NaOH, MeOH, H_2O 3. NH_4OH (aq) 4. Me_3SnOH, $C_2H_4Cl_2$, 80 °C 5. $NaOSi(CH_3)_3$, THF 6. DOWEX 8×50W-100, H_2O, reflux	Conditions 1 and 2 resulted in depletion of metal-complex-specific absorptions at 474 and 740 nm. The resulting residue was insoluble in water and other common organic solvents. With conditions 3–6 the metal-complex-specific absorptions were present. However, they also produced an insoluble residue and the only identifiable peak in mass spectra was starting material.
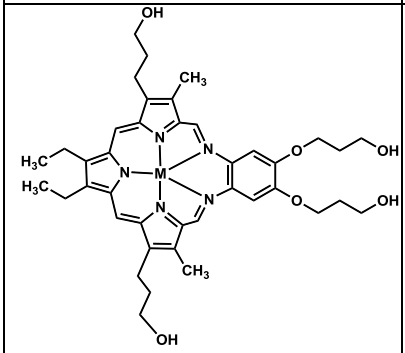	Oxidation of alcohols 1. Pyridiniumdichlorochromate, dimethylformamide 2. 2,2,6,6-tetramethylpiperidine-1-oxyl, $PhI(OAc)_2$, H_2O, acetonitrile 3. $KMnO_4$, NaOH	1. Depletion of metal-complex-specific absorptions at 474 and 740 nm 2. Alcohols oxidized to aldehydes 3. Depletion of metal complex specific absorption and appearance of a new peak in the 300–400 nm regions.

Experimental procedures for Gd^{III}-containing target-specific metal complexes.

Commercially available chemicals were of reagent-grade purity or better and were used without purification unless otherwise noted. Water was purified using a PURELAB Ultra Mk2 water purification system (ELGA). Compounds **2.1c**,[90] **2.1f**,[19] **2.2b**,[96] **2.2c**,[95] **2.3c**,[94] and **2.2f**[95] were synthesized using previously published procedures. Compounds **2.3a** and **2.3b** were synthesized following a similar procedure to reference 97. Compound **2.2e** was synthesized following the procedure in reference 98 with some modifications to purification.

Analytical thin-layer chromatography (TLC) was carried out on ASTM TLC plates precoated with silica gel 60 F_{254} (250 μm layer thickness). Visualization of TLC was accomplished using a UV lamp followed by charring with potassium permanganate stain (3 g $KMnO_4$, 20 g K_2CO_3, 5 mL 5% w/v aqueous NaOH, 300 mL H_2O) or by charring with ceric ammonium molybdate stain (4 g cerium(IV) sulfate hydrate complex with sulfuric acid, 100 g ammonium molybdate tetrahydrate, 900 mL H_2O, 100 mL concentrated H_2SO_4). Flash chromatography was performed using silica gel 60, 230–400 mesh (EMD Chemicals) or aluminum oxide, activated, acidic, Brockmann I, standard grade, ~150 mesh, 58 Å (Sigma Aldrich). Preparative reverse-phase chromatography was performed using RP-tC18 SPE Sep-Pak columns (Waters) and a high-performance liquid chromatography (HPLC) system (Shimadzu) equipped with a C18 column (Restek International, Viva C18, 5 μm, 250 × 10.0 mm). Analytical HPLC analyses were performed with a C18 column (Restek International, Viva C18, 5 μm, 250 × 4.6 mm). Both preparative and analytical HPLC used a binary gradient method (pump A: water, pump B: acetonitrile; 5% B for 5 min, 5–30% B over 1 min, 30% B for 10 min, 30–95% B over 1 min, 95% B for 2 min) for complex **2.1**, and (pump A: water, pump B: acetonitrile; 5% B for 5 min, 5–95% B over 7 min, 95% B for 1 min, 95–5% B over 1 min) for

complexes **2.2–2.6**. The flow rates used for preparative and analytical columns were 5 and 1 mL/min, respectively. Detection was carried out with a photodiode array detector and fluorescence detector (λ_{ex} = 395 nm, and λ_{em} = 521 nm).

^{1}H NMR spectra were obtained using a Varian Mercury 400 (400 MHz) spectrometer, Agilent 400 (400 MHz), Varian 500 (500 MHz), or Agilent 600 (600 MHz) spectrometers, and ^{13}C NMR spectra were obtained using a Varian Mercury 400 (101 MHz), Agilent 400 (101 MHz), Varian 500 (126 MHz), or Agilent 600 (151 MHz) spectrometers. Chemical shifts are reported relative to residual solvent signals unless otherwise noted ($CDCl_3$: ^{1}H: δ 7.27, ^{13}C: δ 77.16; dimethylsulfoxide-d_6: ^{1}H: 2.50, ^{13}C: 39.52; D_2O: ^{1}H: 4.79, ^{13}C: 49.00 for an internal standard of methanol-d_4 or 39.52 for an internal standard of dimethyl sulfoxide-d_6; CD_3OD/D_2O mixture, ^{1}H: 4.79, ^{13}C: 49.00). NMR data are assumed to be first order, and the apparent multiplicity is reported as "s" = singlet, "d" = doublet, "dd" = doublet of doublets, "t" = triplet, "q" = quartet, "m" = multiplet, or "brs" = broad singlet. Italicized elements are those that are responsible for the chemical shifts. High-resolution electrospray ionization mass spectra (HRESIMS) were obtained on an electrospray time-of-flight high-resolution Waters Micromass LCT Premier XE mass spectrometer. UV−vis spectra were obtained on Shimadzu UVmini-1240 UV−vis spectrophotometer. Data are reported as UV−vis (solvent) λ_{max}, nm (ε). Abbreviations: λ_{max} is the wavelength of maximum absorption in nanometers; ε is the molar absorption coefficient; and sh is the shoulder. Fluorescence spectra were obtained using a HORIBA Jobin Yvon Fluoromax-4 spectrofluorometer.

Sonication was performed using a FS60H sonicator (Fisher Scientific). Centrifugation was performed using a mini-centrifuge (05-090-100, Fisher Scientific) at 6600 rpm or Centrific™ Centrifuge at 7000 rpm (04-978-50, Fisher Scientific). Vortexing was done using a

vortex mixer (Fisher Scientific). Freeze drying was performed using a Freezone 2.5 freeze dryer (LABCONCO). Elemental analyses were performed by Midwest Microlab LLC, Indianapolis, Indiana, USA.

β-amyloid-targeted metal complex

***tert*-Butyl-2-(2-(4-((1E,4Z,6E)-5-hydroxy-7-(4-hydroxy-3-methoxyphenyl)-3-oxohepta-1,4,6-trienyl)-2-methoxyphenoxy)acetamido)ethylcarbamate (2.1d):**

To a solution of commercially available curcumin, **2.1a**, (205 mg, 0.557 mmol, 1 equiv) in anhydrous methanol (7 mL) at 50 °C was added a solution of sodium methoxide (0.81 mmol, 0.54 M, 1.5 equiv) in anhydrous methanol (1.5 mL) dropwise over a period of 20 min under Ar. The resulting reaction mixture was stirred for 40 min at 50 °C under Ar. A mixture of amine linker **2.1c** (323 mg, 1.36 mmol, 2.5 equiv) and KI (186 mg, 1.12 mmol, 2 equiv) in anhydrous methanol (1 mL) was added to the reaction mixture dropwise over 15 min. Anhydrous toluene (3 mL) was added, and the resulting reaction mixture was stirred at 80 °C under Ar for 22 h in the dark. Volatiles were removed under reduced pressure, and the resulting solid was purified using silica gel column chromatography (stepwise gradient of 2:3→4:1→1:0 ethyl acetate/hexanes) to yield **2.1d** (0.11 g, 34%) as an orange oil. ^{1}H NMR (400 MHz, $CDCl_3$, δ): 1.43 (s, C*H*$_3$, 9H), 3.18–3.58 (m, C*H*$_2$, 4H), 3.95 (s, C*H*$_3$, 6H), 4.57 (s, C*H*$_2$, 2H), 4.87 (brs, N*H*, 1H), 5.83 (s, C*H*, 1H), 5.96 (brs, O*H*, 1H), 6.49 (d, *J* = 15.98 Hz, C*H*, 1H), 6.52 (d, *J* = 15.58 Hz, C*H*, 1H), 6.80–7.19 (m, Ar*H*, 6H), 7.22 (brs, N*H*, 1H), 7.59 (d, *J* = 15.58 Hz, C*H*, 1H), 7.61 (d, *J* = 15.98 Hz, C*H*, 1H), 16.01 (brs, O*H*, 1H); ^{13}C NMR (101 MHz, $CDCl_3$, δ): 28.5 (*C*H_3), 39.6 (*C*H_2), 40.6 (*C*H_2), 56.1 (*C*H_3), 56.2 (*C*H_3), 69.2 (*C*H_2), 79.8, 101.6 (*C*H), 109.8 (*C*H), 110.9 (*C*H), 114.9 (*C*H), 115.1 (*C*H), 121.9 (*C*H), 122.2 (*C*H), 123.2 (*C*H), 123.3 (*C*H), 127.7, 130.3, 139.8 (*C*H),

141.1 (*C*H), 147.0, 148.2, 148.8, 149.9, 156.5, 169.1, 182.6, 184.2; TLC: R_f = 0.23 (4:1 ethylacetate/hexanes); HRESIMS (*m*/*z*): $[M + H]^+$calcd for $C_{30}H_{37}N_2O_9$, 569.2499; found, 569.2504.

Curcumin-conjugated Gd^{III}DTPA complex (2.1):

Compound **2.1d** (34 mg, 0.060 mmol) was added to a solution of HCl (3 M) in ethyl acetate (2.5 mL), and the resulting mixture was stirred at ambient temperature for 30 min. Solvents were removed under reduced pressure, and the product was triturated with diethyl ether (2 × 3 mL) to obtain a brown solid (26 mg, 0.056 mmol, 1 equiv) that was dissolved in water (0.2 mL). To the resulting solution was added a solution of DIEA (39 μL, 0.22 mmol, 4 equiv) in acetonitrile (0.2 mL) dropwise over 5 min while stirring. At the end of the addition, water (0.2 mL) was added to the reaction mixture followed by complex **2.1f** (55 mg, 0.079 mmol, 1.4 equiv) as a solid in 4 equal portions. Upon complete addition of **2.1f**, water (1.1 mL) was added to the reaction mixture that was subsequently sonicated (1 min). The reaction mixture was stirred in the dark at ambient temperature for 6.5 h then purified by reverse-phase chromatography using RP-tC18 SPE Sep-Pak (stepwise gradient of 3:7→1:1 acetonitrile/water) followed by HPLC. Volatiles were removed under reduced pressure, and the resulting residue was dissolved in water (1 mL) and freeze dried to obtain **2.1** (0.010 g, 16%) as a fluffy yellow powder. HRESIMS (*m*/*z*): $[M]^{2-}$ calcd for $C_{47}H_{51}N_6O_{17}SGd$, 579.1129; found, 579.1102. HPLC chromatograms on page 115 in Appendix B.

Myelin-targeted metal complexes

Benzyl 4-ethyl-3,5-dimethyl-1*H*-pyrrole-2-carboxylate (2.3a):

To a vigorously stirring suspension of diethylaminomalanoate hydrochloride salt (3.0 g, 14 mmol, 1 equiv) in CH_2Cl_2 (30 mL) was added a saturated solution of $NaHCO_3$ (22.5 mL) dropwise over 20 min, and stirring was continued for 20 min. The aqueous layer was decanted. The organic layer was dried over anhydrous $MgSO_4$, filtered, and the solvent was removed under reduced pressure to yield 2.5 g (95%) of diethylaminomalanoate as a colorless liquid. To refluxing glacial acetic acid (12 mL) was added a mixture of diethylaminomalanoate (2.0 g, 11 mmol, 1 equiv) and 3-ethyl-2,4-pentanedione (1.5 g, 11 mmol, 1 equiv) dropwise over 30 min. The reaction mixture was heated at reflux for 3 h and poured into ice. The resulting precipitate was filtered and the solvent was removed under reduced pressure to yield 1.2 g (60%) of ethyl 4-ethyl-3,5-dimethyl-1H-pyrrole-2-carboxylate as an off white crystalline solid. ^{1}H NMR (400 MHz, $CDCl_3$, δ): 1.06 (t, J = 7.6 Hz, CH_3, 3H), 1.35 (t, J = 7.2 Hz, CH_3, 3H), 2.21 (s, CH_3, 3H), 2.29 (s, CH_3, 3H), 2.39 (q, J = 7.6 Hz, CH_2, 2H), 4.30 (q, J = 7.2 Hz, CH_2, 2H), 8.70 (brs, N*H*, 1H); ^{13}C NMR (101 MHz, $CDCl_3$, δ): 10.6 (*C*H_3), 11.5 (*C*H_3), 14.7 (*C*H_3), 15.5 (*C*H_3), 17.3 (*C*H_2), 59.7 (*C*H_2), 116.8, 124.0, 126.9, 129.2, 161.9.

To a gradually heating (from ambient temperature to 200 °C over 2 h) solution of 4-ethyl-3,5-dimethyl-1H-pyrrole-2-carboxylate (1.25 g, 6.41 mmol, 1 equiv) in benzyl alcohol (6 mL) was added a mixture of sodium (14.8 mg, 0.641 mmol, 0.1 equiv) dissolved in benzyl alcohol (1.2 mL) portionwise over 2 h. After the addition of sodium, the reaction mixture was stirred for 5 min at 200 °C, and the hot solution was poured into a cooled mixture of ethanol/water/glacial acetic acid (0 °C, 1:0.75:0.01, 14.1 mL). The resulting mixture was cooled at 0 °C for 20 min. The resulting precipitate was filtered, and washed with cold ethanol (0 °C, 2 mL). Solvent was

removed under reduced pressure to yield 1.18 g (72%) of **2.3a** as a white fluffy solid. ^{1}H NMR (400 MHz, $CDCl_3$, δ): 1.05 (t, *J* = 7.6 Hz, C*H*$_3$, 3H), 2.20 (s, C*H*$_3$, 3H), 2.30 (s, C*H*$_3$, 3H), 2.39 (q, *J* = 7.6 Hz, C*H*$_2$, 2H), 5.30 (s, C*H*$_2$, 2H), 7.30–7.45 (m, C*H*, 5H), 8.54 (brs, N*H*, 1H); ^{13}C NMR (101 MHz, $CDCl_3$, δ): 10.7 (*C*H_3), 11.5 (*C*H_3), 15.5 (*C*H_3), 17.3 (*C*H_2), 65.5 (*C*H_2), 124.2, 128.1 (*C*H), 128.2 (*C*H), 128.7 (*C*H), 129.5, 136.8.

Benzyl 4-(3-bromopropyl)-3,5-dimethyl-1*H*-pyrrole-2-carboxylate (2.4a):

Compound **2.2a** (1.5 g, 4.7 mmol, 1 equiv) was cooled to 0 °C, and to it was added BH_3-THF (1 M, 24 mL, 24 mmol, 5 equiv) dropwise while stirring. The reaction mixture was allowed to warm to ambient temperature and stirred for 5 h. Excess BH_3-THF was quenched with CH_3OH (20 mL), and the solvent was removed under reduced pressure. The resulting residue was dissolved in CH_2Cl_2 and washed with HCl (0.5 M, 2 × 20 mL). The organic layer was dried with anhydrous K_2CO_3, and the solvent was removed under reduced pressure to yield 1.34 g (98%) of reduced **2.2a** as a white powder. ^{1}H NMR (400 MHz, $CDCl_3$, δ): 1.49 (brs, O*H*, 1H), 1.64–1.86 (m, C*H*$_2$, 2H), 2.20 (s, C*H*$_3$, 3H), 2.30 (s, C*H*$_3$, 3H), 2.47 (t, *J* = 7.4 Hz, C*H*$_2$, 2H), 3.64 (t, *J* = 5.6 Hz, C*H*$_2$, 2H), 5.30 (s, C*H*$_2$, 2H), 7.29–7.56 (m, C*H*, 5H), 8.79 (brs, N*H*, 1H); ^{13}C NMR (101 MHz, $CDCl_3$, δ): 10.8 (*C*H_3), 11.6 (*C*H_3), 20.3 (*C*H_2), 33.6 (*C*H_2), 62.5 (*C*H_2), 65.6 (*C*H_2), 116.6, 121.5, 127.8, 128.1 (*C*H), 128.2 (*C*H), 128.6 (*C*H), 130.2, 136.7, 161.5; HRESIMS (*m*/*z*): $[M + H]^+$ calcd for $C_{17}H_{22}NO_3$, 288.1600; found, 288.1641.

To a solution of reduced **2.2a** (0.90 g, 3.2 mmol, 1 equiv) in anhydrous CH_2Cl_2 was added CBr_4 (1.6 g, 4.8 mmol, 1.5 equiv). The resulting mixture was cooled to 0 °C and stirred for 10 min under Ar in the dark. To this mixture was added PPh_3 (1.3 g, 4.8 mmol, 1.5 equiv), and the mixture was stirred for 1.5 h at ambient temperature under Ar in the dark. Solvent was

removed under reduced pressure, and the resulting viscous oil was purified by silica gel chromatography (1:5 ethyl acetate/hexanes) to obtain 0.83 g (74%) of **2.4a** as an off white powder. ^{1}H NMR (400 MHz, $CDCl_3$, δ): 1.92–2.12 (m, C*H*$_2$, 2H), 2.23 (s, C*H*$_3$, 3H), 2.32 (s, C*H*$_3$, 3H), 2.55 (t, *J* = 8.0 Hz, C*H*$_2$, 2H), 3.40 (t, *J* = 8.0 Hz, C*H*$_2$, 2H), 5.32 (s, C*H*$_2$, 2H), 7.31–7.51 (m, C*H*, 5H), 8.99 (brs, N*H*, 1H); ^{13}C NMR (101 MHz, $CDCl_3$, δ): 10.9 (*C*H_3), 11.6 (*C*H_3), 22.4 (*C*H_2), 33.5 (*C*H_2), 33.6 (*C*H_2), 65.6 (*C*H_2), 116.7, 120.4, 127.7, 128.1 (*C*H), 128.6 (*C*H), 130.6, 136.7, 161.5; HRESIMS (*m*/*z*): $[M + H]^+$ calcd for $C_{17}H_{21}NO_2Br$, 350.0756; found, 350.0941; TLC: R_f = 0.44 (1:5 ethyl acetate/hexanes).

Benzyl 5-(acetoxymethyl)-4-(3-ethyl)-3-methyl-1*H*-pyrrole-2-carboxylate (2.3b):

To a stirring mixture of **2.3a** (1.0 g, 3.9 mmol, 1 equiv) in glacial acetic acid (50 mL) was added acetic anhydride (15 mL) dropwise under Ar at ambient temperature. The reaction mixture was stirred for 15 min; $Pb(OAc)_4$ (2.5 g, 5.6 mmol, 1.4 equiv) was added; and stirring was continued for 195 min. The reaction mixture was poured onto ice, and the resulting precipitate was collected and washed with water (10 × 100 mL). The precipitate was dried under reduced pressure, dissolved in $CHCl_3$ (4 mL), and precipitated using petroleum ether (150 mL) to yield 1.0 g (82%) of **2.3b** as a white fluffy powder. ^{1}H NMR (400 MHz, $CDCl_3$, δ): 1.11(t, *J* = 7.6 Hz, C*H*$_2$, 3H), 2.07 (s, C*H*$_3$, 3H), 2.32 (s, C*H*$_3$, 3H), 2.49 (q, *J* = 7.6 Hz, C*H*$_2$, 2H), 5.05 (s, C*H*$_2$, 2H), 5.33 (s, C*H*$_2$, 2H), 7.31–7.48 (m, C*H*, 5H), 9.26 (brs, N*H*, 1H); ^{13}C NMR (101 MHz, $CDCl_3$, δ): 10.5 (*C*H_3), 16.0 (*C*H_3), 17.2 (*C*H_2), 21.0 (*C*H_3), 57.0 (*C*H_2), 65.8 (*C*H_2), 119.0, 126.6, 127.0, 127.1, 128.2 (*C*H), 128.6 (*C*H), 136.5, 161.4, 171.6.

Benzyl 5-(acetoxymethyl)-4-(3-bromopropyl)-3-methyl-1*H*-pyrrole-2-carboxylate (2.4b):

To a stirring mixture of **2.4a** (0.44 g, 1.2 mmol, 1 equiv) in glacial acetic acid (17 mL) was added acetic anhydride (5 mL) dropwise under Ar at ambient temperature. The reaction mixture was stirred for 15 min; $Pb(OAc)_4$ (1.1 g, 2.5 mmol, 2 equiv) was added; and stirring was continued for 1 h. The reaction mixture was poured on to ice, and the resulting precipitate was collected and washed with water (10 × 50 mL). The precipitate was dried under reduced pressure, dissolved in CH_2Cl_2 (2 mL), and filtered. The filtrate was precipitated using petroleum ether (100 mL) to yield 0.45 g (93%) of **2.4b** as a white fluffy powder. ^{1}H NMR (400 MHz, $CDCl_3$, δ): 1.98–2.06 (m, C*H*$_2$, 2H), 2.06 (s, C*H*$_3$, 3H), 2.30 (s, C*H*$_3$, 3H), 2.62 (t, *J* = 7.4 Hz, C*H*$_2$, 2H), 3.39 (t, *J* = 6.4 Hz, C*H*$_2$, 2H), 5.05 (s, C*H*$_2$, 2H), 5.31 (s, C*H*$_2$, 2H), 7.31–7.50 (m, C*H*, 5H), 9.23 (brs, N*H*, 1H); ^{13}C NMR (101 MHz, $CDCl_3$, δ): 10.7 (*C*H$_3$), 21.1 (*C*H$_3$), 22.2 (*C*H$_2$), 33.3 (*C*H$_2$), 33.8 (*C*H$_2$), 57.0 (*C*H$_2$), 65.9 (*C*H$_2$), 119.3, 123.3, 126.8, 127.8 (*C*H), 128.3 (*C*H), 128.7 (*C*H), 136.4, 161.2, 171.7; HRESIMS (*m*/*z*): $[M + H]^+$ calcd for $C_{19}H_{23}NO_4Br$, 408.0811 found, 408.0588.

Benzyl-5,5'-(3,4-diethyl-1*H*-pyrrole-2,5-diyl)bis(methylene)bis(4-(3-bromopropyl)-3-methyl-1*H*-pyrrole-2-carboxylate) (2.4c):

Compound **2.4b** (0.39 g, 0.96 mmol, 2 equiv) and 3,4-diethylpyrrole (65 µL, 0.48 mmol, 1 equiv) were suspended in CH_3OH (27 mL) under Ar in the dark and heated at 60 °C for 1 h until a clear solution was obtained. To this clear solution was added *p*-toluene sulfonic acid (7.9 mg, 0.041 mmol, 0.085 equiv) in CH_3OH (1 mL). The resulting reaction mixture was stirred for 1.5 h at 60 °C, at which point the volume was reduced by sparging N_2 through the reaction mixture (5–10 min) until a precipitate started to form. Once precipitation started, N_2 sparging was stopped, and reaction was stirred for 4 h at 60 °C. The reaction mixture was concentrated to

10 mL under reduced pressure and cooled to –20 °C for 2 h to promote precipitation. The precipitate was separated, washed with cold CH_3OH (0 °C, 2 mL) and dried under reduced pressure to yield 0.24 g (60%) of **2.4b** as a pink powder. ^{1}H NMR (400 MHz, $CDCl_3$, δ): 1.19 (t, *J* = 7.4 Hz, C*H*$_3$, 6H), 1.84–2.03(m, C*H*$_2$, 4H), 2.26 (s, C*H*$_3$, 6H), 2.42–2.66 (m, C*H*$_2$, 8H), 3.36 (t, *J* = 6.2 Hz, C*H*$_2$, 4H), 3.62 (brs, C*H*$_2$, 4H), 4.35 (brs, C*H*$_2$, 4H), 6.96–7.10 (m, C*H*, 4H), 7.24–7.39 (m, C*H*, 6H), 8.85 (brs, N*H*, 1H), 11.33 (brs, N*H*, 2H); ^{13}C NMR (101 MHz, $CDCl_3$, δ): 11.3 (*C*H_3), 17.0 (*C*H_3), 17.8 (*C*H_2), 21.9 (*C*H_2), 22.1(*C*H_2), 33.3 (*C*H_2), 33.6 (*C*H_2), 65.2 (*C*H_2), 117.3, 118.8, 119.3, 122.0, 126.2 (*C*H), 126.6, 127.1 (*C*H), 127.9 (*C*H), 133.7, 136.5, 162.5; HRESIMS (*m*/*z*): $[M + H]^+$ calcd for $C_{42}H_{50}N_3O_4Br_2$, 818.2168; found, 818.2140.

Dimethyl-3,3'-(2,2-(3,4-diethyl-1*H*-pyrrole-2,5-diyl)bis(methylene)bis(5-formyl-4-methyl-1*H*-pyrrole-3,2-diyl))dipropanoate (2.2d):

A mixture of tripyrrane **2.2c** (0.38 g, 0.51 mmol, 1 equiv) and Pd/C (10%, 0.070 g, 0.067 mmol) in anhydrous THF (12 mL) was degassed under reduced pressure and then saturated with hydrogen (1 atm), and the resulting reaction mixture was stirred for 6 h at ambient temperature under an atmosphere of hydrogen. The reaction mixture was filtered through celite, and the solvents were removed under reduced pressure to obtain deprotected **2.2c** as a pink powder. To deprotected **2.2c** (0.29 g, 0.51 mmol, 1 equiv) was added trifluoroacetic acid (0.90 mL, 13 mmol, 25 equiv) dropwise under Ar at ambient temperature while stirring. Upon complete addition of trifluoroacetic acid, the resulting solution was stirred for 10 min. The reaction mixture was cooled to –20 °C, and triethylorthoformate (0.96 mL, 5.7 mmol, 11 equiv) was added dropwise. The resulting reaction mixture was stirred at –20 °C for 10 min before allowing the reaction mixture to warm to ambient temperature. Water (3.0 mL) was added dropwise to the stirring

mixture immediately after the temperature warmed above –20 °C, and stirring at ambient temperature was continued for 15 min. A dark red precipitate was collected and washed with water (5 × 5 mL). The precipitate was suspended in a mixture of water/ethanol/ammonium hydroxide (1:2:1 v/v/v, 5.0 mL) and stirred at ambient temperature for 1 h. The resulting yellow precipitate was filtered and washed with water (3 × 3 mL) followed by cold ethanol (0 °C, 2.0 mL). The precipitate was dissolved in a methanol/water mixture (5:1, 3.6 mL), heated to 60 °C for 5 min, cooled to ambient temperature, and concentrated under reduced pressure. The resulting suspension was cooled at –20 °C for 4 h then filtered, and the precipitate was washed with water (4.0 mL). Solvents were removed under reduced pressure to yield 171 mg (63%) of **2.2d** as a light brown solid. ^{1}H NMR (400 MHz, $CDCl_3$, δ): 1.11 (t, *J* = 7.4 Hz, C*H*$_3$, 6H), 2.21 (s, C*H*$_3$, 6H), 2.31 (t, *J* = 7.8 Hz, C*H*$_2$, 4H), 2.45 (q, *J* = 7.4 Hz, C*H*$_2$, 4H), 2.71 (t, *J* = 7.8 Hz, C*H*$_2$, 4H), 3.64 (s, C*H*$_3$, 6H), 3.87 (s, C*H*$_2$, 4H), 9.09 (s, C*H*, 2H), 9.30 (s, N*H*, 1H), 10.52 (s, N*H*, 2H); ^{13}C NMR (101 MHz, $CDCl_3$ δ): 8.9 (*C*H_3), 16.7 (*C*H_3), 17.8 (*C*H_2), 19.3 (*C*H_2), 22.8 (*C*H_2), 34.5 (*C*H_2), 51.7 (*C*H_3), 120.7, 120.9, 121.8, 128.2, 133.0, 138.7, 173.6 (*C*H), 175.6; HRESIMS (*m*/*z*): $[M + H]^+$ calcd for $C_{30}H_{40}N_3O_6$, 538.2917; found, 538.2917.

5,5'-(3,4-Diethyl-1*H*-pyrrole-2,5-diyl)bis(methylene)bis(4-ethyl-3-methyl-1*H*-pyrrole-2-carbaldehyde) (2.3d):

Compound **2.3d** was synthesized according to the procedure in reference 94 with some modifications to the protocol. The modifications included addition and stirring of triflouroacetic acid at ambient temperature, addition and stirring of triethylorthoformate at –20 °C, and purification by precipitation with methanol at –20 °C, instead of extraction to yield 73% of **2.3d** as a light brown solid. ^{1}H NMR (400 MHz, $CDCl_3$, δ): 0.80–1.29 (m, C*H*$_3$, 12H), 2.20 (s, C*H*$_3$,

6H), 2.32–2.56 (m, C*H*$_2$, 8H), 3.84 (s, C*H*$_2$, 4H), 9.14 (s, C*H*, 2H), 9.39 (s, N*H*, 1H), 10.11 (s, N*H*, 2H); ^{13}C NMR (101 MHz, $CDCl_3$, δ): 8.8 (*C*H$_3$), 15.1 (*C*H$_3$), 16.5 (*C*H$_3$), 16.9 (*C*H$_2$), 17.7 (*C*H$_2$), 22.7 (*C*H$_2$), 120.8, 121.5, 124.8, 128.2, 132.9, 138.0, 175.6 (*C*H); HRESIMS (*m*/*z*): $[M + H]^+$ calcd for $C_{26}H_{36}N_3O_2$, 422.2808; found, 422.2808.

5,5'-(3,4-Diethyl-1*H*-pyrrole-2,5-diyl)bis(methylene)bis(4-(3-bromopropyl)-3-methyl-1*H*-pyrrole-2-carbaldehyde) (2.4d):

A mixture of tripyrrane **2.4c** (0.60 g, 0.73 mmol, 1 equiv) and Pd/C (10%, 0.10 g, 0.095 mmol) in anhydrous THF (18 mL) was degassed under reduced pressure and saturated with hydrogen (1 atm), and the reaction mixture was stirred for 6 h at ambient temperature under an atmosphere of hydrogen. The reaction mixture was filtered through celite, and solvent was removed under reduced pressure to obtain deprotected **2.4c** as a pink powder. To deprotected **2.4c** (0.46 g, 0.73 mmol, 1 equiv) was added trifluoroacetic acid (0.67 mL, 8.9 mmol, 12 equiv) dropwise under Ar at ambient temperature while stirring. Upon complete addition of trifluoroacetic acid, the resulting solution was stirred for 10 min. The reaction mixture was cooled at –20 °C, and triethylorthoformate (0.79 mL, 4.8 mmol, 6.5 equiv) was added dropwise over 15 min. The resulting reaction mixture was stirred at –20 °C for 15 min; the cold bath was removed; and water (22 mL) was added dropwise without stirring immediately after the temperature warmed above –20 °C. The reaction mixture was left to stand for 30 min at ambient temperature, and a dark red precipitate was collected and washed with water (5 × 10 mL). The precipitate was suspended in ethanol (8.6 mL), and a mixture of ammonium hydroxide/water (1:3 v/v, 8.5 mL) was added. The reaction mixture was stirred at ambient temperature for 20 min. The resulting precipitate was separated and washed with water (5 × 20 mL) until washings were

neutral as measured by pH paper. The resulting solid was dissolved in CH_2Cl_2 (5 mL) and precipitated using CH_3OH/water (8:1, 45 mL). The resulting suspension was cooled to −20 °C for 24 h, filtered, and washed with water (5.0 mL). Solvents were removed under reduced pressure to yield 371 mg (84%) of **2.4d** as a light brown solid. ^{1}H NMR (400 MHz, $CDCl_3$, δ): 1.12 (t, *J* = 7.4 Hz, C*H*$_3$, 6H), 1.82–1.96 (m, C*H*$_2$, 4H), 2.20 (s, C*H*$_3$, 6H), 2.46 (q, *J* = 7.4 Hz, C*H*$_2$, 4H), 2.54 (t, *J* = 7.2 Hz, C*H*$_2$, 4H), 3.31 (t, *J* = 6.4 Hz, C*H*$_2$, 4H), 3.87 (brs, C*H*$_2$, 4H), 9.07 (s, C*H*, 2H), 9.26 (brs, N*H*, 1H), 10.74 (brs, N*H*, 2H); ^{13}C NMR (101 MHz, $CDCl_3$, δ): 9.2 (*C*H$_3$), 16.8 (*C*H$_3$), 17.9 (*C*H$_2$), 22.3 (*C*H$_2$), 22.9 (*C*H$_2$), 33.3 (*C*H$_2$), 33.4 (*C*H$_2$), 120.6, 121.2, 121.8, 128.2, 133.3, 139.0, 175.5 (*C*H); HRESIMS (*m*/*z*): $[M + H]^+$ calcd for $C_{28}H_{38}N_3O_2Br_2$, 606.1331; found, 606.1338.

Sodium 3,3'-(2,2'-(3,4-diethyl-1H-pyrrole-2,5-diyl)bis(methylene)bis(5-formyl-4-methyl-1H-pyrrole-3,2-diyl))dipropane-1-sulfonate (2.5d):

To a solution of **2.4d** (0.20 g, 0.33 mmol, 1 equiv) in *p*-dioxane (12 mL) was added an aqueous solution of KI (0.14 g, 0.80 mmol, 2.5 equiv, 2.0 mL), and the resulting mixture was stirred for 30 min at 80 °C under Ar. To the resulting mixture was added an aqueous solution of Na_2SO_3 (0.24 g, 1.9 mmol, 6.0 equiv, 2.0 mL), and the mixture was stirred for 24 h under Ar at 80 °C. Solvents were removed under reduced pressure, and the resulting residue was purified by reverse-phase chromatography using RP-tC18 SPE Sep-Pak (stepwise gradient of 1:0→7:3 water/CH_3OH). Volatiles were removed under reduced pressure, and the resulting residue was dissolved in water (2 mL) and freeze dried to yield 0.16 g (76%) of **2.5d** as a brown fluffy powder. ^{1}H NMR (400 MHz, D_2O, δ): 0.91 (t, *J* = 6.6 Hz, C*H*$_3$, 6H), 1.61–1.74 (m, C*H*$_2$, 4H), 2.14 (s, C*H*$_3$, 6H), 2.21–2.44 (m, C*H*$_2$, 8H), 2.70 (t, *J* = 7.4 Hz, C*H*$_2$, 4H), 3.80 (s, C*H*$_2$, 4H), 9.06 (s, C*H*, 2H); ^{13}C NMR (101 MHz, D_2O with dimethylsulfoxide-d_6 internal standard δ): 9.8

(CH_3), 17.4 (CH_3), 18.6 (CH_2), 23.3 (CH_2), 24.3 (CH_2), 26.4 (CH_2), 52.1 (CH_2), 122.7, 123.0, 123.9, 129.0, 137.6, 141.8, 178.7 (*C*H); HRESIMS (*m*/*z*): $[M + H]^+$ calcd for $C_{28}H_{38}N_3O_8S_2$, 608.2100; found, 608.2116.

3,3'-(1,2-Phenylenebis(oxy))dipropan-1-ol (2.2e):

Compound **2.2e** was synthesized according to the procedure in reference 92 with some modifications to the protocol. The modification included purification using silica gel chromatography (stepwise gradient of 2:1→4:1, ethyl acetate/hexanes) to yield 80% of **2.2e** as a white crystalline solid. ^{1}H NMR (400 MHz, $CDCl_3$, δ): 2.01–2.09 (m, C*H*$_2$, 4H), 3.41 (brs, O*H*, 2H), 3.82–3.87 (m, C*H*$_2$, 4H), 4.16 (t, *J* = 5.8 Hz, C*H*$_2$, 4H), 6.80–6.92 (m, C*H*, 4H); ^{13}C NMR (101 MHz, $CDCl_3$, δ): 32.2 (*C*H_2), 61.3 (*C*H_2), 68.0 (*C*H_2), 113.4 (*C*H), 121.7 (*C*H), 148.8; HRESIMS (*m*/*z*): $[M + H]^+$ calcd for $C_{12}H_{18}O_4Na$, 249.1103; found, 249.0938; TLC: R_f = 0.23 (2:1 ethyl acetate/hexanes)

3,3'-(1,2-Phenylenebis(oxy))dipropane-1-sulfonic acid (2.3e):

Catechol (0.72 g, 6.5 mmol, 1 equiv) was dissolved in a mixture of NaOH (0.65 g, 16 mmol, 2.7 equiv) and ethanol (35 mL) under Ar, and the resulting mixture was heated at reflux until a clear solution was obtained. This mixture was added to propane sultone (1.8 g, 15 mmol, 2.5 equiv) dropwise over 30 min under Ar. The reaction mixture was heated at reflux under Ar for 48 h. The reaction mixture was centrifuged while hot; liquid was decanted; and the resulting residue was washed with hot ethanol (60 °C, 3 × 25 mL). The residue was dissolved in water (10 mL) and sparged with gaseous HCl for 3 min. The acid-saturated solution was centrifuged, and the liquid was decanted and concentrated under reduced pressure. The concentrated liquid (3

mL) was precipitated using CH_3OH (47 mL) and cooled to –20 °C. The solid residue was isolated, dissolved in water (5 mL), and purified by re-precipitation using CH_3OH/diethyl ether (8:1 v/v, 45 mL) at –20 °C. The precipitate was separated and washed with diethyl ether (2 × 25 mL). Volatiles were removed under reduced pressure to obtain 0.82 g (37%) of **2.3e** as an off white solid. ^{1}H NMR (400 MHz, D_2O, δ): 2.15–2.30 (m, CH_2, 4H), 3.05–3.17 (m, CH_2, 4H), 4.12 (t, J = 6.4 Hz, CH_2, 4H), 7.03 (s, CH, 4H); ^{13}C NMR (101 MHz, D_2O with internal standard of dimethylsulfoxide-d_6, δ): 25.8 (CH_2), 49.4 (CH_2), 69.2 (CH_2), 116.1 (CH), 123.7 (CH), 149.3; HRESIMS (m/z): $[M –2H + Na]^-$ calcd for $C_{12}H_{16}O_8S_2Na$, 375.0184; found, 375.0247.

Sodium 3-(2-methoxyphenoxy)propane-1-sulfonate (2.4e):

2-Methoxyphenol (0.6 mL, 4 mmol, 1 equiv) was added to a mixture of NaOH (0.24 g, 6.0 mmol, 1.5 equiv) and ethanol (15 mL) under Ar in the dark, and the resulting reaction mixture was heated at reflux until a homogeneous solution was obtained. This mixture was added to propane sultone (0.74 g, 6.0 mmol, 1.5 equiv) dropwise under Ar. The reaction mixture was heated at reflux under Ar for 20 h in the dark. The reaction mixture was centrifuged while hot; liquid was decanted; and the resulting residue was washed with hot ethanol (60 °C, 3 × 20 mL). The residue was dissolved in water (5 mL), precipitated using ethanol (40 mL), and cooled to –20 °C. The solid residue was isolated, and the volatiles were removed under reduced pressure to obtain 0.83 g (84%) of **2.4e** as an off white solid. ^{1}H NMR (400 MHz, D_2O, δ): 2.14–2.27 (m, CH_2, 2H), 3.04–3.15 (m, CH_2, 2H), 3.84 (s, CH_3, 3H), 4.14 (t, J = 6.4 Hz, CH_2, 2H), 6.95–7.14 (m, CH, 4H); ^{13}C NMR (101 MHz, D_2O with an internal standard of dimethylsulfoxide-d_6, δ): 25.6 (CH_2), 49.2 (CH_2), 56.9 (CH_3), 68.6 (CH_2), 113.6 (CH), 114.9

(*C*H), 122.9 (*C*H), 123.2 (*C*H), 148.5, 149.8.; HRESIMS (*m*/*z*): $[M - H]^-$ calcd for $C_{10}H_{13}O_5S$, 245.0484; found, 245.0491.

3,3'-(4,5-Dinitro-1,2-phenylene)bis(oxy)dipropane-1-sulfonic acid (2.3f):

Sulfonic acid **2.3e** (0.24 g, 0.68 mmol, 1 equiv) was dissolved in glacial acetic acid (3.9 mL) and stirred for 15 min at 15 °C. To this mixture was added aqueous HNO_3 (70%, 2.5 mL) dropwise over a period of 15 min while maintaining the temperature of the reaction mixture at 15 °C. After the addition, the reaction mixture was warmed to ambient temperature and stirred for 15 min. The reaction mixture was cooled to 15 °C, and fuming HNO_3 (6.6 mL) was added dropwise over a period of 30 min while the temperature of the reaction mixture was held at 15 °C. After the addition, the reaction mixture was warmed to ambient temperature and stirred for 64 h. The reaction mixture was concentrated under reduced pressure, and cold methanol (0 °C, 2.0 mL) was added to form a precipitate. The precipitate was collected and dried under reduced pressure. Purification was performed using an RP-tC18 SPE Sep-Pak column (stepwise gradient of 1:9→1:4 CH_3OH/water) to yield 151.6 mg (50%) of **2.3f** as a yellow solid. ^{1}H NMR (400 MHz, D_2O, δ): 2.22–2.37 (m, CH_2, 4H), 3.11 (t, J = 7.4 Hz, CH_2, 4H), 4.32 (t, J = 6.4 Hz, CH_2, 4H), 7.60 (s, C*H*, 2H); ^{13}C NMR (101 MHz, D_2O with internal standard of dimethylsulfoxide-d_6, δ): 25.5 (*C*H_2), 49.1 (*C*H_2), 70.2 (*C*H_2), 110.5 (*C*H), 137.6, 152.7; HRESIMS (*m*/*z*): $[M - H]^-$ calcd for $C_{12}H_{15}N_2O_{12}S_2$, 443.0066; found, 443.0062.

3-(2-Methoxy-4,5-dinitrophenoxy)propane-1-sulfonic acid (2.4f):

Sulfonic acid **2.4e** (0.80 g, 3.3 mmol, 1 equiv) was dissolved in glacial acetic acid (19 mL) and stirred for 10 min at 15 °C. To this mixture was added aqueous HNO_3 (70%, 12 mL)

dropwise over a period of 15 min while maintaining the temperature of the reaction mixture at 15 °C. After the addition, the reaction mixture was warmed to ambient temperature and stirred for 15 min. The reaction mixture was cooled to 15 °C, and fuming HNO_3 (30 mL) was added dropwise over a period of 30 min while the temperature of the reaction mixture was held at 15 °C. After the addition, the reaction mixture was warmed to ambient temperature and stirred for 46 h. The reaction mixture was concentrated under reduced pressure, and the resulting residue was dissolved in water (0.5 mL), and precipitated using CH_3OH/diethyl ether (1:1, 50 mL). The precipitate was collected and dried under reduced pressure to yield 0.80 g (72%) of **2.4f** as a yellow solid. ^{1}H NMR (400 MHz, D_2O, δ): 2.22–2.33 (m, CH_2, 2H), 3.09 (t, J = 7.6 Hz, CH_2, 2H), 3.96 (s, CH_3, 3H), 4.24–4.32 (m, CH_2, 2H), 7.51–7.56 (m, C*H*, 2H); ^{13}C NMR (101 MHz, D_2O with internal standard of dimethylsulfoxide-d_6, δ): 25.3 (*C*H_2), 48.8 (*C*H_2), 58.3 (*C*H_3), 69.9 (*C*H_2), 109.0 (*C*H), 109.7 (*C*H), 137.3, 152.2, 153.1; HRESIMS (*m*/*z*): $[M - H]^-$ calcd for $C_{10}H_{11}N_2O_9S$, 335.0185; found, 335.0189.

3,3'-(4,5-Diamino-1,2-phenylene)bis(oxy)dipropanoic acid hydrochloride salt (2.2g):

A mixture of dinitro compound **2.2f** (0.40 g, 1.2 mmol, 1 equiv), Pd/C (10%, 0.11 g, 0.10 mmol), and ethanol (18 mL) was sonicated until **2.2f** was dissolved. The resulting reaction mixture was degassed under reduced pressure, saturated with hydrogen (1 atm), and heated at reflux for 3 h under an atmosphere of hydrogen. Solvent was removed under reduced pressure; HCl (1 M, 10 mL) was added; and the resulting mixture was filtered through a 0.2 μm syringe filter. The filtrate was concentrated by removing solvent under reduced pressure to yield 367.3 mg (88%) of **2.2g** as a purple hygroscopic solid. ^{1}H NMR (400 MHz, D_2O, δ): 2.70 (t, J = 6.0 Hz, CH_2, 4H), 4.15 (t, J = 5.6 Hz, CH_2, 4H), 6.96 (s, C*H*, 2H); ^{13}C NMR (101 MHz, D_2O with

internal standard of dimethylsulfoxide-d_6, δ): 35.4 (*C*H_2), 67.3 (*C*H_2), 111.9 (*C*H), 120.8, 149.1, 176.8; HRESIMS (*m*/*z*): $[M - H]^-$ calcd for $C_{12}H_{15}N_2O_6$, 283.0930; found, 283.0936.

4,5-Diethyl-10,23-dimethyl-9,24-bis(methylpropanoate)-16,17-bis((methylpropanoate)oxy)-13,20,25,26,27-pentaazapentacyclo-[20.2.1.1^{3,6}.1^{8,11,}.0^{14,19}]heptacosa-3,5,8,10,12,14,16,18,20,22,24-undecaene (2.2L):

To a mixture of tripyrrole **2.2d** (0.12 g, 0.22 mmol, 1 equiv) in toluene/CH_3OH (6:1, 140 mL) under Ar was added a solution of diamine salt **2.2g** (0.080 g, 0.22 mmol, 1 equiv) in CH_3OH (4.0 mL). To the resulting reaction mixture was added HCl (11.6 M, 0.05 mL, 0.6 mmol, 3 equiv), and the mixture was heated at 80 °C for 6 h under Ar. The reaction mixture was cooled to ambient temperature; K_2CO_3 (83 mg, 0.60 mmol, 3 equiv) was added; and stirring was continued for 30 min. The reaction mixture was filtered, and the filtrate was concentrated under reduced pressure. Solids were dissolved in methanol (4.0 mL) and cooled at –20 °C for 16 h to promote precipitation. The precipitate was collected, washed with diethyl ether (2.0 mL), and solvents were removed under reduced pressure to yield 76.4 mg (58%) of **2.2L** as a bright red solid. ^{1}H NMR (500 MHz, $CDCl_3$, δ): 1.06 (t, *J* = 7.5 Hz, C*H*$_3$, 6H), 2.27 (s, C*H*$_3$, 6H), 2.38 (q, *J* = 7.5 Hz, C*H*$_2$, 4H), 2.46 (t, *J* = 7.8 Hz, C*H*$_2$, 4H), 2.70–2.91 (m, C*H*$_2$, 8H), 3.71 (s, C*H*$_3$, 6H), 3.73 (s, C*H*$_3$, 6H) 3.96 (dd, J = 15.5, 123.4 Hz, C*H*$_2$, 4H), 4.25 (brs, C*H*$_2$, 4H), 7.16 (s, C*H*, 2H), 8.30 (s, C*H*, 2H), 11.07 (s, N*H*, 1H), 12.25 (s, N*H*, 2H); ^{13}C NMR (126 MHz, $CDCl_3$, δ): 9.8 (*C*H_3), 16.7 (*C*H_3), 17.8 (*C*H_2), 19.5 (*C*H_2), 22.2 (*C*H_2), 34.4 (*C*H_2), 35.2 (*C*H_2), 51.81 (*C*H_3), 51.82 (*C*H_3), 65.2 (*C*H_2), 102.6 (*C*H), 120.3, 120.4, 121.2, 125.3, 131.0, 133.5, 140.2, 141.6 (*C*H), 148.0, 171.5, 173.2; HRESIMS (*m*/*z*): $[M + H]^+$ calcd for $C_{44}H_{56}N_5O_{10}$, 814.4027; found, 814.4015; UV–vis (30% CH_3OH in water) λ_{max}, nm (ε): 364 (48400).

4,5-Diethyl-10,23-dimethyl-9,24-bis(ethyl)-16,17-bis((propanesulfonicacid)oxy)-13,20,25,26,27-pentaazapentacyclo-[20.2.1.1^{3,6}.1^{8,11,}.0^{14,19}]heptacosa-3,5,8,10,12,14,16,18,20,22,24-undecaene (2.4L):

To a mixture of dinitrosulfonic acid **2.3f** (52.8 mg, 0.118 mmol, 1 equiv) in water/CH_3OH (1:2, 3.6 mL) was added Pd/C (10%, 26.8 mg, 0.0252 mmol). The resulting reaction mixture was degassed under reduced pressure and saturated with hydrogen (1 atm). The reaction mixture was heated at reflux for 40 min under an atmosphere of hydrogen until the solution became colorless. The resulting suspension was filtered through a 0.2 μm syringe filter into a mixture of **2.3d** (50.4 mg, 0.118 mmol, 1 equiv) in CH_3OH/toluene/water (25:5:1, 62 mL) and HCl (11.6 M, 0.030 mL, 0.35 mmol, 3 equiv). The reaction mixture was stirred under Ar for 6.5 h. Solvents were removed under reduced pressure, and the resulting residue was precipitated with CH_3OH (5 mL) at –20 °C. The precipitate was isolated and purified by reverse-phase chromatography using an RP-tC18 SPE Sep-Pak (stepwise gradient of 1:1→1:4 water/CH_3OH). Volatiles were removed under reduced pressure to yield 37 mg (41%) of **2.4L** as a red powder. ^{1}H NMR (600 MHz, dimethylsulfoxide-d_6, δ): 1.01 (t, J = 7.5 Hz, CH_3, 6H), 1.11 (t, J = 7.5 Hz, CH_3, 6H), 2.01–2.07 (m, CH_2, 4H), 2.30–2.37 (m, CH_2, CH_3, 10H), 2.50–2.53 (m, CH_2, 4H), 2.58 (t, J = 6.9 Hz, CH_2, 4H), 3.95 (s, CH_2, 4H), 4.26 (t, J = 6.9 Hz, CH_2, 4H), 7.57 (s, CH, 2H), 8.72 (s, CH, 2H), 10.43 (s, NH, 1H), 11.17 (s, NH, 2H); ^{13}C NMR (151 MHz, dimethylsulfoxide-d_6, δ); 8.5 (CH$_3$), 14.4 (CH$_3$), 15.1 (CH$_3$), 15.9 (CH$_2$), 16.1 (CH$_2$), 22.0 (CH$_2$), 23.6 (CH$_2$), 46.7 (CH$_2$), 66.6 (CH$_2$), 101.3 (CH), 119.4, 120.0, 123.5, 125.1, 140.5 (CH), 147.1; HRESIMS (m/z) : [M – H]$^-$ calcd for $C_{38}H_{50}N_5O_8S_2$, 768.3101; found, 768.3099; UV–vis (30% CH_3OH in water) λ_{max}, nm (ε): 368 (38417).

Diethyl-10,23-dimethyl-9,24-bis(propanesulfonicacid)-16-((propanesulfonicacid)oxy)-17-methoxy-13,20,25,26,27-pentaazapentacyclo-[20.2.1.1^{3,6}.1^{8,11}.0^{14,19}]heptacosa-3,5,8,10,12,14,16,18,20,22,24-undecaene (2.5L):

To a mixture of dinitrosulfonic acid **2.4f** (17 mg, 0.050 mmol, 1 equiv) in water/CH_3OH (1:2, 1.8 mL) was added Pd/C (10%, 11 mg, 0.0010 mmol). The resulting reaction mixture was degassed under reduced pressure and saturated with hydrogen (1 atm). The reaction mixture was heated at reflux for 75 min under an atmosphere of hydrogen until the solution became colorless. The resulting suspension was filtered through a 0.2 μm syringe filter into a mixture of **2.5d** in CH_3OH/water (15:1, 32 mL) and HCl (11.6 M, 0.020 mL, 0.23 mmol, 4.6 equiv). The reaction mixture was stirred under Ar for 6 h. Solvents were removed under reduced pressure, and the resulting residue was purified by reverse-phase chromatography using an RP-tC18 SPE Sep-Pak (stepwise gradient of 1:0→7:3 water/CH_3OH). Volatiles were removed under reduced pressure, and the resulting residue was dissolved in water (2 mL) and freeze dried to yield 24 mg (57%) of **2.5L** as a red fluffy powder. ^{1}H NMR (600 MHz, CD_3OD/D_2O (5:2), δ): 0.87 (brs, C*H*$_3$, 6H), 1.90 (brs, C*H*$_2$, 4H), 2.09 (brs, C*H*$_2$, 2H), 2.20–2.36 (m, C*H*$_2$, C*H*$_3$, 10H), 2.65 (brs, C*H*$_2$, 4H), 2.81 (brs, C*H*$_2$, 6H), 3.88 (s, C*H*$_3$, 3H), 4.02 (brs, C*H*$_2$, 4H), 4.18 (brs, C*H*$_2$, 2H), 7.27–7.40 (m, C*H*, 2H), 8.43 (s, C*H*, 2H); ^{13}C NMR (151 MHz, CD_3OD/D_2O (5:2), δ): 10.0 (*C*H_3), 16.8 (*C*H_3), 18.2 (*C*H_2), 23.3 (*C*H_2), 24.2 (*C*H_2), 25.1 (*C*H_2), 26.2 (*C*H_2), 49.8 (*C*H_2), 51.7 (*C*H_2), 57.4 (*C*H_3), 68.9 (*C*H_2), 103.8 (*C*H), 104.6 (*C*H), 121.9, 123.5, 123.7, 124.5, 124.6, 126.1, 126.5, 127.0, 127.2, 142.6 (*C*H), 142.9 (*C*H), 143.6, 149.3, 150.7, 152.5; HRESIMS (*m*/*z*): $[M - H]^-$ calcd for $C_{38}H_{50}N_5O_{11}S_3$, 848.2669; found, 848.2674; UV−vis (30% CH_3OH in water) λ_{max}, nm (ε): 365 (49529), 459 (sh, 15588).

4,5-Diethyl-10,23-dimethyl-9,24-bis(propanesulfonicacid)-16,17-bis((propanesulfonicacid)oxy)-13,20,25,26,27-pentaazapentacyclo-[20.2.1.1^{3,6}.1^{8,11,}.0^{14,19}]heptacosa-3,5,8,10,12,14,16,18,20,22,24-undecaene (2.6L):

To a mixture of dinitrosulfonic acid **2.3f** (23 mg, 0.050 mmol, 1 equiv) in water/CH_3OH (1:2, 1.8 mL) was added Pd/C (10%, 11 mg, 0.0010 mmol). The resulting reaction mixture was degassed under reduced pressure and saturated with hydrogen (1 atm). The reaction mixture was heated at reflux for 35 min under an atmosphere of hydrogen until the solution became colorless. The resulting suspension was filtered through a 0.2 μm syringe filter into a mixture of **2.5d** in CH_3OH/water (15:1, 32 mL) and HCl (11.6 M, 0.020 mL, 0.23 mmol, 4.6 equiv). The reaction mixture was stirred under Ar for 6 h. Solvents were removed under reduced pressure, and the resulting residue was purified by reverse-phase chromatography using an RP-tC18 SPE Sep-Pak (stepwise gradient of 1:0→4:1 water/CH_3OH). Volatiles were removed under reduced pressure, and the resulting residue was dissolved in water (2 mL) and freeze dried to yield 25 mg (53%) of **2.6L** as a red fluffy powder. ^{1}H NMR (600 MHz, CD_3OD/D_2O (5:2), δ): 0.86 (t, *J* = 7.5 Hz, C*H*$_3$, 6H), 1.86–1.94 (m, C*H*$_2$, 4H), 2.05–2.11 (m, C*H*$_2$, 4H), 2.34 (brs, C*H*$_2$, C*H*$_3$, 10H), 2.61–2,68 (m, C*H*$_2$, 4H), 2.78–2.84 (m, C*H*$_2$, 8H), 4.04(s, C*H*$_2$, 4H), 4.15–4.20 (m, C*H*$_2$, 4H), 7.35 (s, C*H*, 2H), 8.45 (s, C*H*, 2H); ^{13}C NMR (151 MHz, CD_3OD/D_2O (5:2), δ): 10.2 (*C*H_3), 16.9 (*C*H_3), 18.2 (*C*H_2), 23.3 (*C*H_2), 24.4 (*C*H_2), 25.1 (*C*H_2), 26.3 (*C*H_2), 49.8 (*C*H_2), 51.8 (*C*H_2), 69.0 (*C*H_2), 105.6 (*C*H), 121.7, 123.8, 124.4, 125.3, 127.7, 142.9 (*C*H), 144.7, 149.8, 153.9; HRESIMS (*m*/*z*): $[M - H]^-$ calcd for $C_{40}H_{54}N_5O_{14}S_4$, 956.2550; found, 956.2527; UV−vis (30% CH_3OH in water) λ_{max}, nm (ε): 363 (57217), 467 (sh, 16283).

Gd^{III} texaphyrin complex 2.2:

To a stirring solution of texaphyrin **2.2L** (0.060 g, 0.074 mmol, 1 equiv) in a mixture of CH_2Cl_2/CH_3OH (1:4, 5 mL) was added triethylamine (99 µL, 0.74 mmol, 10 equiv). To the resulting solution was added $Gd(OAc)_3 \cdot 4H_2O$ (60 mg, 0.15 mmol, 2 equiv), and the reaction mixture was heated at 60 °C while sparging with air until the peak intensity ratio (742 nm/364 nm) become constant (4.5 h). Solvents were removed under reduced pressure, and the resulting residue was purified using silica gel chromatography (stepwise gradient of 1:9→1:4 CH_3OH/CH_2Cl_2). Precipitation from CH_3OH/CH_2Cl_2 (1:2, 0.5 mL) layered with CH_3OH/diethyl ether (1:1, 3 mL) yielded 36.4 mg (45%) of **2.2** as a green solid. HRESIMS (*m*/*z*): $[M + AcO^-]^+$ calcd for $C_{46}H_{53}N_5O_{12}Gd$, 1022.2917; found, 1022.2921; Anal. Calcd for $C_{44}H_{50}N_5O_{10}GdCl_3 \cdot CH_3COOH \cdot 3H_2O$: C, 46.60; H, 5.02; N, 5.91. Found: C, 46.78; H, 4.64; N, 6.10; UV−vis (30% CH_3OH in water) λ_{max}, nm (ε): 742 (32291), 470 (90902), 416 (sh, 52916); TLC: R_f = 0.24 (1:9 CH_3OH/CH_2Cl_2).

Gd^{III} texaphyrin complex 2.3:

To a mixture of tripyrrole **2.3d** (72 mg, 0.16 mmol, 1 equiv) in THF/toluene (5:1 v/v, 90 mL) and HCl (11.6 M, 0.1 mL, 0.8 mmol, 5 equiv) was added a solution of diamine salt **2.2g** (0.060 g, 0.16 mmol, 1 equiv) in water (1.0 mL), and the mixture was heated at 80 °C for 8.5 h under Ar. Solvents were removed under reduced pressure. To the resulting residue (0.10 g, 0.15 mmol, 1 equiv) in CH_3OH (8 mL) was added triethylamine (0.21 mL, 1.5 mmol, 10 equiv). To the resulting solution was added $Gd(OAc_3)_3 \cdot 4H_2O$ (0.30 g, 0.75 mmol, 5 equiv), and the reaction mixture was heated at 60 °C while sparging with air until the peak intensity ratio (740 nm/370 nm) became constant (20 h). Solvents were removed under reduced pressure. The resulting

residue was washed with CH_3OH, dissolved in CH_2Cl_2, and purified by acidic alumina chromatography (stepwise gradient of 1:1:0→0:1:0.01 CH_2Cl_2/CH_3OH/AcOH). Volatiles were removed under reduced pressure to yield 27 mg (22%) of **2.3** as a green powder. HRESIMS (*m*/*z*): $[M - H]^+$ calcd for $C_{38}H_{41}N_5O_6Gd$, 821.2303; found, 821.3124 ; UV−vis (30% CH_3OH in water) λ_{max}, nm (ε): 740 (30004), 474 (80403), 416 (sh, 48902).

Gd^{III} texaphyrin complex 2.4:

To a stirring solution of texaphyrin **2.4L** (22 mg, 0.028 mmol, 1 equiv) in a mixture of CH_2Cl_2/CH_3OH (1:2.5 v/v, 2.8 mL) was added triethylamine (40 µL, 0.28 mmol, 10 equiv). To the resulting solution was added $Gd(OAc_3)_3 \cdot 4H_2O$ (46 mg, 0.11 mmol, 4 equiv), and the reaction mixture was heated at 60 °C while sparging with air until the peak intensity ratio (738 nm/368 nm) became constant (4 h). Solvents were removed under reduced pressure, and purified using silica gel chromatography (stepwise gradient of 1:9→1:4 CH_3OH/CH_2Cl_2). Purification by precipitation from CH_3OH (5 mL) layered with diethyl ether (25 mL) yielded 9.7 mg (37%) of **2.4** as a green solid. HRESIMS (*m*/*z*): $[M + Na]^+$ calcd for $C_{38}H_{44}N_5O_8S_2GdNa$, 940.1755; found, 940.1725; Anal. Calcd for $C_{38}H_{45}N_5O_8GdS_2Na_2 \cdot 3H_2O$: C, 44.69; H, 5.03; N, 6.86. Found: C, 44.86; H, 5.03; N, 6.49; UV−vis (30% CH_3OH in water) λ_{max}, nm (ε): 738 (27878), 473 (88060), 416 (sh, 44727); TLC: R_f = 0.26 (1:4 CH_3OH/CH_2Cl_2).

Gd^{III} texaphyrin complex 2.5:

To a stirring solution of texaphyrin **2.5L** (50 mg, 0.059 mmol, 1 equiv) in CH_3OH (6 mL) was added triethylamine (0.080 mL, 0.59 mmol, 10 equiv). To the resulting solution was added $Gd(OAc_3)_3 \cdot 4H_2O$ (120 mg, 0.29 mmol, 5 equiv), and the reaction mixture was heated at 60 °C

while sparging with air until the peak intensity ratio (742 nm/365 nm) became constant (22 h). Solvents were removed under reduced pressure, and the resulting residue was purified by reverse-phase chromatography using an RP-tC18 SPE Sep-Pak (stepwise gradient of 1:0→7:3 water/CH_3OH). Volatiles were removed under reduced pressure. The resulting residue was dissolved in water (2 mL) and freeze dried to yield 30.2 mg (51%) of **2.5** as a green fluffy powder. HRESIMS (*m*/*z*): $[M - H]^+$ calcd for $C_{38}H_{45}N_5O_{11}S_3Gd$, 1001.1524; found, 1001.2540; Anal. Calcd for $C_{38}H_{43}N_5O_{11}GdS_3Na_5 \cdot 5H_2O$: C, 37.90; H, 4.44; N, 5.82. Found: C, 37.77; H, 3.87; N, 5.82; UV–vis (30% CH_3OH in water) λ_{max}, nm (ε): 742 (34571), 470 (93523), 416 (sh, 46904). HPLC chromatogram on page 116 of Appendix B.

Gd^{III} texaphyrin complex 2.6:

To a stirring solution of texaphyrin **2.6L** (0.048 g, 0.049 mmol, 1 equiv) in CH_3OH (8 mL) was added triethylamine (0.070 mL, 0.49 mmol, 10 equiv). To the resulting solution was added $Gd(OAc_3)_3 \cdot 4H_2O$ (0.10 g, 0.25 mmol, 5 equiv), and the reaction mixture was heated at 60 °C while sparging with air until the peak intensity ratio (743 nm/363 nm) became constant (6 h). Solvents were removed under reduced pressure, and the resulting residue was purified by reverse-phase chromatography using an RP-tC18 SPE Sep-Pak (stepwise gradient of 1:0→7:3 water/CH_3OH). Volatiles were removed under reduced pressure. The resulting residue was dissolved in water (2 mL) and freeze dried to yield 30.7 mg (55%) of **2.6** as a green fluffy powder. HRESIMS (*m*/*z*): $[M - H]^+$ calcd for $C_{40}H_{49}N_5O_{14}S_4Gd$, 1109.1411; found, 1109.2557; Anal. Calcd for $C_{40}H_{46}N_5O_{14}GdS_4Na_8 \cdot 8H_2O$: C, 33.50; H, 4.36; N, 4.88. Found: C, 33.55; H, 3.84; N, 4.85; UV–vis (30% CH_3OH) λ_{max}, nm (ε): 743 (30486), 472(82734), 416 (sh, 43146). HPLC chromatogram on page 117 of Appendix B.

CHAPTER 3. A multimodal, β-amyloid-targeted contrast agent

Portions of this chapter are reproduced by permission of The Royal Society of Chemistry from Vithanarachchi, S. M.; Allen, M. J. *Chem. Commun.* **2013,** *49,* 4148–4150. http://pubs.rsc.org/en/content/articlepdf/2013/cc/c2cc36583a

Introduction

β-Amyloid plaques are a diagnostic marker of Alzheimer's disease, which is one of the most common neurodegenerative diseases in the world;[99] hence, detection of β-amyloid plaques is important in the diagnosis of, in the monitoring of treatments for, and in research related to Alzheimer's disease. The β-amyloid aggregates that comprise plaques are often detected using fluorescent dyes or β-amyloid-targeted radiolabels that interact with β-amyloid aggregates.[100–105] However, fluorescence microscopy has limited tissue penetration, and radiolabels for nuclear imaging use harmful ionizing radiation. Magnetic resonance imaging (MRI) is a non-invasive imaging technique with excellent tissue penetration and high spatial resolution (25–100 mm)[6] that has the potential to overcome the limitations of fluorescence microscopy and nuclear imaging with respect to the detection of β-amyloid aggregates. MRI has been used in several imaging studies of β-amyloid plaques.[35,36,106–110] In these studies, both transverse relaxation time (T_2)-weighted and longitudinal relaxation time (T_1)-weighted imaging methods were reported.[35,36,106–109] The T_1-weighted methods are more desirable because T_1-weighted imaging can distinguish plaques from hemorrhages and blood vessels unlike T_2-weighted methods. Although T_1-weighted imaging is desirable, it suffers from poor contrast enhancement of plaques leading to a widespread interest in the labeling of plaques with target-specific contrast agents. Examples of β-amyloid-targeting groups that have been reported include β-amyloid

peptides,[35,36,107] monoclonal antibodies,[108] and β-amyloid-binding dyes.[109] Agents composed of conjugates of these targeting groups are capable of labeling β-amyloid plaques, but possible amyloidogenesis, toxicity, and the large size of these contrast agents limit their usefulness. These limitations reveal the need for new β-amyloid-targeted contrast agents with higher efficiency, smaller size, and non-amyloidogenic and non-toxic properties to make MRI a useful technique in β-amyloid imaging.

This chapter describes a β-amyloid-targeted contrast agent for MRI that is more efficient than current clinical contrast agents. To target β-amyloid aggregates, a non-toxic small molecule that can be traced with fluorescence microscopy was used; thus, this agent is multi-modal being detectable by both MRI and fluorescence microscopy. The multimodal contrast agent was synthesized using the conjugation strategy for target specific molecules by linking a clinically approved contrast agent to a target-specific moiety.[111] For the target-specific moiety, curcumin, 1,7-bis-(4-hydroxy-3-methoxy-phenyl)-1,6-heptadiene-3,5-dione, was chosen because it is non-toxic, interacts with β-amyloid aggregates, is non amyloidogenic, and inhibits aggregate formation.[37,100–103] Moreover, curcumin is fluorescent and has been used for imaging β-amyloid plaques with fluorescence microscopy.[37,100,101] Curcumin conjugates are often synthesized via the total synthesis of curcumin derivatives[103,112,113] or the direct reaction of linkers with commercially available curcumin.[113,114] Total synthetic routes are tedious and limited to the synthesis of specific derivatives. Alternatively, the direct reaction of commercially available curcumin provides shorter synthetic routes and has been used to synthesize conjugates with reactive functional groups including alkenes, alcohols, esters, amides, cyanide, carboxylic acids, and azides.[113,114] To facilitate conjugation to curcumin, an amine-functionalized linker was introduced at one of the phenolic sites of curcumin. That amine-functionalized curcumin is

expected to be a useful intermediate for other conjugations of curcumin because of the facile synthesis and resistance of amine-derived conjugates including amides, thioureas, ureas, and carbamates, to hydrolysis in enzyme-rich biological environments.[115] The phenolic group was selected as a site of conjugation because conjugations to this position do not inhibit the targeting ability of curcumin.[103] Furthermore, the amine group enabled facile reaction with an isothiocyanate derivative of Gd^{III}diethylenetriaminepentaacetate (Gd^{III}DTPA), which is a clinically approved contrast agent.

In vitro studies of interaction between multimodal contrast agent and β-amyloid aggregates

Conjugate **2.1** was synthesized via the direct reaction of commercially available curcumin with linker **2.1c** to obtain amine linker containing curcumin **2.1d** as described in Chapter 2 (**Scheme 2.1**). The reactions were performed in the dark because of the photoinstability of curcumin.[117] The amine group was deprotected with HCl and reacted with isothiocyanate-containing Gd^{III}DTPA, **2.1f**, to obtain curcumin-conjugated contrast agent **2.1**. After synthesis, the efficiency of conjugate **2.1** as a contrast agent for MRI was determined as described under experimental procedures. The longitudinal relaxivity (r_1) of **2.1** is 13.63 ± 0.03 mM^{-1} s^{-1} [phosphate buffered saline (PBS), pH 7.4, 1.4 T, and 37 °C]. This value is 4.1 times greater than that of clinically approved Gd^{III}DTPA under the same conditions (3.30 ± 0.06 mM^{-1} s^{-1}). The high relaxivity of **2.1** demonstrates that it is an efficient contrast agent. The efficiency is likely caused by a slowing of the molecular reorientation rate upon conjugation to curcumin and potential aggregation in solution.[20] To measure the interaction of **2.1** with β-amyloid aggregates, the T_1 of solutions containing complex **2.1** was measured in the presence and absence of β-amyloid fibrils that were prepared as described in experimental procedures. The formation of fibrils (diameters of 200–600 nm) was confirmed with dynamic light scattering and transmission

electron microscopy. Different stoichiometries (0, 0.5, 1, and 2 equiv relative to **2.1**) of aggregated β-amyloid were incubated with complex **2.1**, and T_1 values were measured at a clinically relevant field strength (1.4 T) at 37 °C in PBS (pH = 7.4). As a non-binding control, T_1 measurements of β-amyloid aggregates at each concentration were measured in the presence of clinically approved Gd^{III}DTPA, and all measurements were replicated with independently prepared samples. The T_1 of samples containing conjugate **2.1** that were incubated with 1 or 2 equiv of β-amyloid aggregates were shorter than the blank of **2.1** that did not contain β-amyloid aggregates (Student *t* test, 99% confidence interval). However, the Gd^{III}DTPA control did not have different T_1 values at any concentration of β-amyloid aggregates (Student *t* test, 99% confidence interval) with respect to Gd^{III}DTPA in the absence of β-amyloid aggregates. To quantify the magnitude of the influence of the interaction of fibrils with **2.1** on relaxation rates, values of $\Delta 1/T_1$ were calculated for samples containing conjugate **2.1**, the Gd^{III}DTPA control, and PBS [eq (3.1)]. In eq (3.1), $\Delta 1/T_1$ is the change in $1/T_1$ due to the interaction with β-amyloid aggregates; $(1/T_1)_n$ is the relaxation rate in the presence of *n* equiv of β-amyloid aggregates where $n = 0$, 0.5, 1, or 2; and $(1/T_1)_0$ is the relaxation rate in the absence of β-amyloid aggregates.

$$\Delta\frac{1}{T_1} = \left(\frac{1}{T_1}\right)_n - \left(\frac{1}{T_1}\right)_0 \qquad (3.1)$$

A plot of $\Delta 1/T_1$ vs equiv of β-amyloid aggregates demonstrates that there is an increase in relaxation rate for **2.1** with increasing amounts of β-amyloid aggregates (**Figure 3.1**). A 67×10^{-3} s^{-1} (9%) change in $1/T_1$ in the presence of 2 equiv of β-amyloid aggregates was observed compared to in the absence of aggregates. The controls of Gd^{III}DTPA with β-amyloid aggregates and the β-amyloid aggregates alone did not show an increase in relaxation rate as a function of β-amyloid concentration. Values of T_1 were expected to decrease upon the interaction of contrast agents to macromolecules, like fibrillar aggregates, due to the reduction in tumbling

rate based on Solomon–Bloembergen–Morgan theory.[20,32,117] Hence, a decrease in T_1 values in the presence of β-amyloid aggregates provides evidence of the interaction of conjugate **2.1** with β-amyloid aggregates.

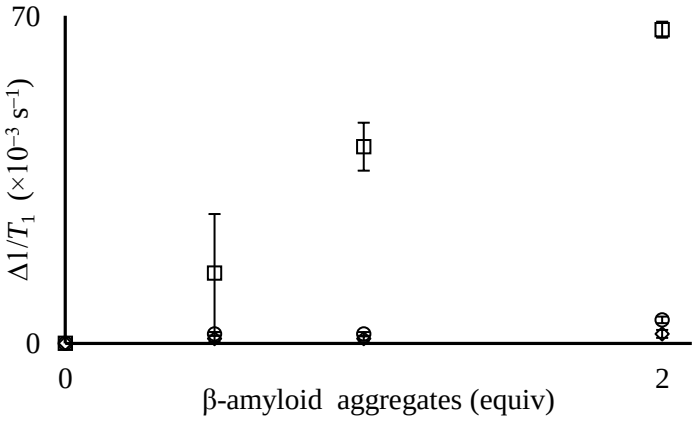

Figure 3.1. Plot showing the change in relaxation rate ($\Delta 1/T_1$) as a function of the amount of β-amyloid (βA) aggregates in PBS. The relaxation rate of **2.1** increases in the presence of βA, and the rate of the control samples do not: **2.1** + βA (□); Gd^{III}DTPA + βA (○); and βA (◊). Error bars represent standard error of the mean.

To explore the multimodal nature of complex **2.1**, the effect of β-amyloid aggregates on the fluorescence emission of conjugate **2.1** was investigated. Emission spectra were acquired at the end of each T_1 measurement (**Figure 3.2**), and the fluorescence emission maximum of conjugate **2.1** (516 nm) was blue shifted 9 nm in the presence of 2 equiv of β-amyloid aggregates. Furthermore, the fluorescence intensity of conjugate **2.1** increased by 43% in the presence of 2 equiv of β-amyloid aggregates relative to **2.1** in the absence of β-amyloid aggregates. Similar observations have been reported for β-amyloid-specific fluorescent dyes due to their interaction with β-amyloid aggregates,[37,104,109,118] thus agreeing with the measurements in this thesis and providing further indication of the presence of an interaction of complex **2.1** with the β-amyloid aggregates. The changes in emission wavelength and intensity make conjugate **2.1**

a multimodal imaging agent for β-amyloid plaques. Importantly, these probes allow for validation of results using orthogonal modalities: The multimodal nature of conjugate **2.1** enables the validation of MRI results with fluorescence studies.

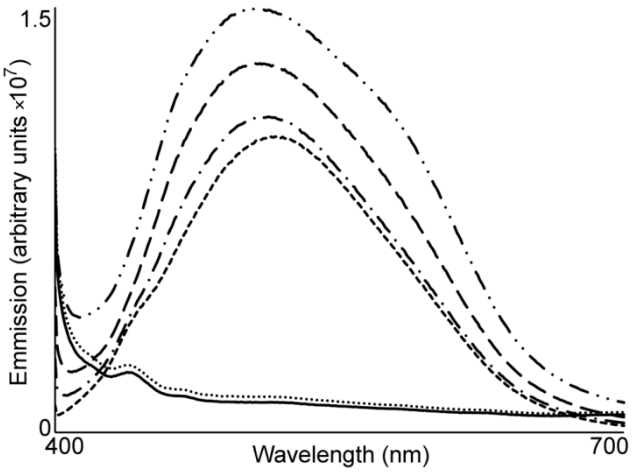

Figure 3.2. Emission spectra (λ_{ex} = 385 nm) of **2.1** and Gd^{III}DTPA incubated with β-amyloid aggregates (βA) in PBS: 2 equiv βA + **2.1** (··—); 1 equiv. βA + **2.1** (— —); 0.5 equiv βA + **2.1** (·-); **2.1** (---), 2 equiv βA + Gd^{III}DTPA (···); and βA (—).The maximum emission of **2.1** undergoes a 9 nm blue shift and 43% increase in intensity upon interaction with 2 equiv of βA.

Experimental procedures

Commercially available chemicals were of reagent-grade purity or better and were used without purification unless otherwise noted. β-Amyloid peptide (1–42) was obtained from American Peptide Company Inc. Gd^{III}diethylenetriaminepentaacetate (Gd^{III}DTPA) was obtained as a 0.5 M aqueous solution from Bayer HealthCare Pharmaceutical Inc. Water was purified using a PURELAB Ultra Mk2 water purification system (ELGA). Phosphate buffered saline (PBS) (1×, 11.9 mM phosphate, 137 mM NaCl, and 2.7 mM KCl, pH = 7.4) was used for amyloid fibril formation and relaxation time measurements.

Dynamic light scattering measurements were obtained on a Zetasizer nanoparticle analyzer equipped with 633 nm helium–neon laser (NanoZS, Malvern Instruments Ltd.).

Transmission electron microscopy (TEM) was performed on a JEOL-2010 FasTEM Transmission Electron Microscope.

Relaxation time (T_1) measurements were obtained on a Bruker mq60 minispec NMR spectrometer at 60 MHz and 37 °C. Fluorescence spectra were obtained using a HORIBA Jobin Yvon Fluoromax-4 spectrofluorometer. Sonication was performed using a FS60H sonicator (Fisher Scientific). Centrifugation was performed using a mini-centrifuge (05-090-100, Fisher Scientific) at 6600 rpm. Vortexing was done using a vortex mixer (Fisher Scientific). Spin filtration of amyloid protein was performed using SpinX 8161 (Costar) spin filters (0.22 μm). Rotating of β-amyloid samples was done using a Thermo Labquake Tube Shaker/Rotator. Inductively coupled plasma mass spectrometry (ICP–MS) analyses were performed by Columbia Analytical Services Inc, Tucson, Arizona, USA.

Relaxivity measurements of 2.1 and Gd^{III}DTPA

Longitudinal relaxation times (T_1) were measured using a standard recovery method with a Bruker Minispec mq 60 at 1.4 T and 37 °C in PBS. The slope of a plot of $1/T_1$ vs concentration of Gd^{III} was used to obtain relaxivity. Measurements were repeated 3 times with independently prepared samples, and Gd concentrations were determined by ICP–MS. T_1 measurements of complex **2.1** are given in the **Tables 3.1–3.3** for six different concentrations of Gd^{III} (0–0.63 mM). Linear plots obtained by plotting $1/T_1$ vs concentration for each trial are shown in **Figures 3.3–3.5**. T_1 measurements of Gd^{III}DTPA are given in the **Tables 3.4–3.6** for four different concentrations of Gd^{III} (0–1 mM). Linear plots obtained by plotting $1/T_1$ vs concentration for each trial are shown in **Figures 3.6–3.8**.

Table 3.1 Relaxivity measurements of **2.1** (trial 1).

Concentration (mM)	T_1 (s)	$1/T_1$ (s^{-1})
0.63	0.1137	8.80
0.32	0.2380	4.20
0.16	0.4959	2.02
0.08	0.8838	1.13
0.04	1.5010	0.67
0.00	3.8600	0.26

Table 3.2 Relaxivity measurements of **2.1** (trial 2).

Concentration (mM)	T_1 (s)	$1/T_1$ (s^{-1})
0.63	0.1141	8.76
0.32	0.2350	4.26
0.16	0.4902	2.04
0.08	0.8915	1.12
0.04	1.4350	0.70
0.00	3.8460	0.26

Table 3.3 Relaxivity measurements of **2.1** (trial 3).

Concentration (mM)	T_1 (s)	$1/T_1$ (s^{-1})
0.63	0.1135	8.81
0.32	0.2450	4.08
0.16	0.4915	2.03
0.08	0.8898	1.12
0.00	3.8650	0.26

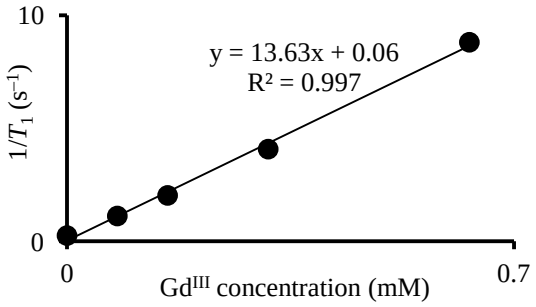

Figure 3.3. Relaxivity plot of complex **2.1** (trial 1).

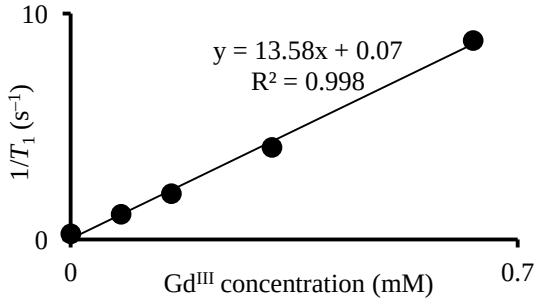

Figure 3.4. Relaxivity plot of complex **2.1** (trial 2).

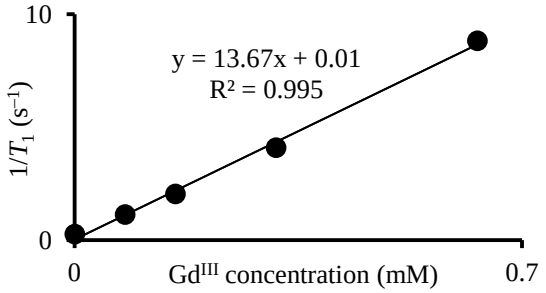

Figure 3.5. Relaxivity plot of complex **2.1** (trial 3).

Table 3.4 Relaxivity measurements of Gd^{III}DTPA (trial 1).

Concentration(mM)	T_1 (s)	$1/T_1$ (s^{-1})
1.00	0.2846	3.51
0.50	0.5315	1.88
0.25	0.9055	1.10
0.00	3.8500	0.26

Table 3.5 Relaxivity measurements of Gd^{III}DTPA (trial 2).

Concentration(mM)	T_1 (s)	$1/T_1$ (s^{-1})
1.00	0.2865	3.49
0.50	0.5384	1.86
0.25	0.9366	1.07
0.00	3.8460	0.26

Table 3.6 Relaxivity measurements of Gd^{III}DTPA (trial 3).

Concentration(mM)	T_1 (s)	$1/T_1$ (s^{-1})
1.00	0.2726	3.67
0.50	0.5373	1.86
0.25	0.9344	1.07
0.00	3.8470	0.26

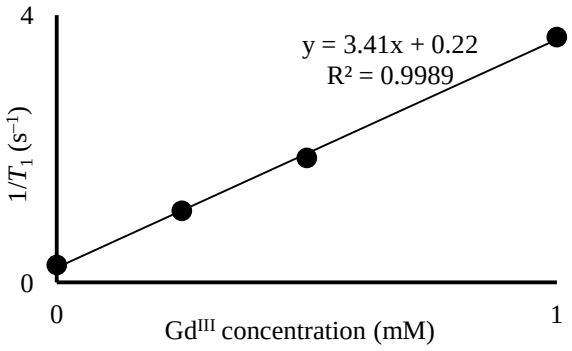

Figure 3.6. Relaxivity plot of Gd^{III}DTPA (trial 1).

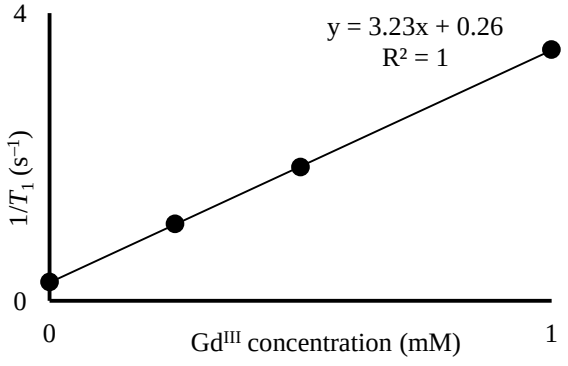

Figure 3.7. Relaxivity plot of Gd^{III}DTPA (trial 2).

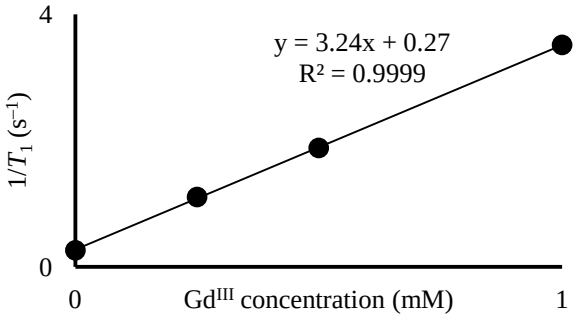

Figure 3.8. Relaxivity plot of Gd^{III}DTPA (trial 3).

Preparation of β-amyloid fibrils

β-Amyloid peptide (1–42) (1 mg, 0.2 μmol) was dissolved in PBS (1 mL) and stirred gently (350 rpm) at 37 ºC for 20 h to obtain a 0.2 mM stock solution of β-amyloid fibrils following published procedures.[100,104,119]

Transmission electron microscopy (TEM) studies

Aggregated β-amyloid peptide was centrifuged (0.2 mM, 100 μL), and the resulting sediment was suspended in water (20 μL) and mixed by vortexing. Aggregated protein solution (5 μL) was applied to a TEM substrate grid (200-mesh copper grid coated with Formvar/carbon film) and incubated for 10 min. Excess solution was removed with a filter paper. Phosphotungstic acid (1% (w/v), 3 μL) was applied to the grid containing protein. After incubation for 3 min, excess stain was washed with water (20–40 μL), and excess water was removed with a filter paper. The resulting sample was air dried for 3 h. TEM was performed at 100 kV (60,000×). The TEM image (**Figure 3.9**) of aggregated fibrils is similar to the appearance of other reported TEM images of aggregated fibrils.[100,119]

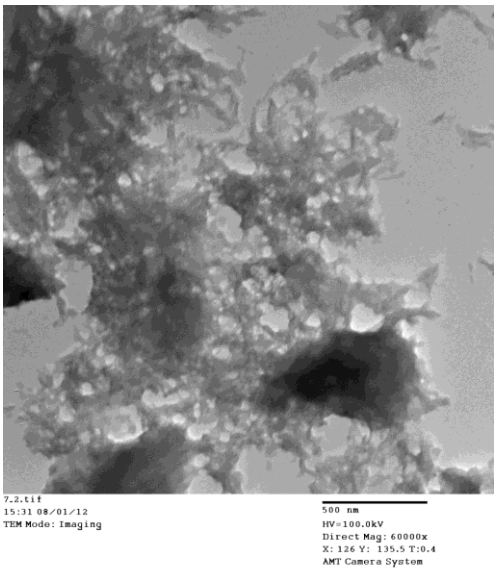

Figure 3.9. TEM image of β-amyloid aggregates.

Dynamic light scattering (DLS) studies of fibril formation

A 100 µL aliquot was taken from the β-amyloid stock while stirring and filtered through a 0.22 µm spin filter to remove large aggregates. The filtered solution was transferred to a disposable microcuvette (40 µL) and measured for size distribution by collecting data at a 173º measurement angle on a Zetasizer NanoZS instrument at 24.9 ºC (dispersant refractive index = 1.332, and viscosity = 0.9128 cP). Size distribution data obtained from DLS based on intensity (**Figure 3.10**) provide evidence for the presence of fibril aggregates with diameters of 200–600 nm that are comparable to the sizes of aggregates reported in other studies.[120]

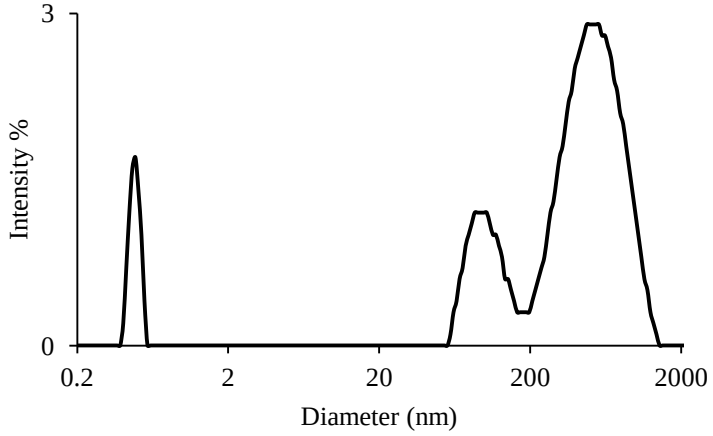

Figure 3.10. Dynamic light scattering distribution data of β-amyloid aggregates (intensity distribution).

Binding studies between conjugate 2.1 and amyloid fibrils

Aliquots (0, 25, 50, and 100 μL) were taken from the stirring stock solution of β-amyloid aggregates and mixed with conjugate **2.1** (0.1 mM, 100 μL). The total volume of each sample was brought to 200 μL with PBS. Samples were vortexed (~5 s) and incubated at ambient temperature with rotation for 3 h. β-Amyloid (0, 25, 50, and 100 μL) was mixed with PBS to a total volume of 200 μL, vortexed (~5 s), incubated with rotation for 3 h, and used as the control. $Gd^{III}DTPA$ (0.1 mM, 100 μL) was used as the non-specific control, and samples with $Gd^{III}DTPA$ were prepared following the same procedure as for conjugate **2.1**. At the end of the incubation T_1 relaxation times were measured for each sample (**Table 3.7**). Measurements were triplicated with independently prepared samples for complex **2.1** and measurements were duplicated for control samples. Fluorescence emission of samples was measured at the end of the relaxation time measurement. Samples were excited at 385 nm with a slit width of ±10 nm.

Table 3.7 β-Amyloid (βA) binding T_1 measurements

	T_1 (ms) at the following ratios of complex to βA*			
Sample	(1:2)	(1:1)	(1:0.5)	(1:0)
2.1/βA (trial 1)	1267	1302	1339	1388
2.1/βA (trial 2)	1265	1298	1395	1375
2.1/βA (trial 3)	1262	1321	1328	1380
GdDTPA/βA (trial 1)	2225	2243	2247	2253
GdDTPA/βA (trial 2)	2232	2247	2243	2253
βA control (trial 1)	3826	3822	3835	3865
βA control (trial 2)	3815	3850	3830	3860

*The concentration of βA in the βA control trials is the same as in the samples containing **2.1** and GdDTPA at the same ratios.

Conclusion

An efficient, small molecular probe for β-amyloid aggregates from non-toxic curcumin and a derivative of a clinically approved contrast agent for MRI was synthesized. In vitro studies demonstrate that curcumin-conjugated contrast agent **2.1** interacts with β-amyloid aggregates resulting in a shortening of T_1 and change in the wavelength and intensity of fluorescence emission. While future studies related to imaging and pharmacokinetic delivery are necessary to evaluate the utility of this work in vivo, the multimodal nature of imaging agent **2.1** is important for Alzheimer's disease related research. In addition, we expect that the facile synthesis of the curcumin-amine linker will be a powerful tool for the synthesis of other curcumin conjugates that are stable in biological environments.

CHAPTER 4. A myelin-specific, multimodal imaging agent for magnetic resonance, optical, and mass spectrometric imaging.

Introduction

The ability to view changes in the brain and peripheral nervous system is of great importance to the study of neurodegenerative diseases and aging,[121–124] and among the components of the nervous system, myelin is a critical target for understanding neuronal anatomy and function.[125–127] Myelin is a characteristic lipid-protein membrane in the nervous system that aids with the proper conduction of nerve impulse. Consequently, nerve cell deterioration caused by inherited or acquired neuropathologies and brain injuries often changes myelinated nerve structures.[125] Hence, effective monitoring of the morphology of myelinated regions of the brain is important in the study of neurodegenerative diseases and therapies for these diseases.

Histology using optical microscopy with chromophoric or fluorophoric stains was the primary method of imaging myelin until recently.[126,127] Advancements in imaging technologies have permitted the use of other modalities for imaging myelin including positron emission tomography (PET) and magnetic resonance imaging (MRI). Although several PET tracers that target myelin have been reported,[122,128,129] the use of PET for imaging myelinated structures in brain is limited because of its low (1–2 mm) resolution.[6,122] Currently, the most promising non-optical imaging method for myelin is MRI.[38,39,122,123,125] The ability to acquire whole brain images using MRI with high resolution (25–100 μm)[6] is important for in vivo imaging and ex vivo pre-clinical research. Various nonconventional and indirect MRI techniques have been investigated for imaging myelin including magnetization transfer, diffusion tensor imaging, T_2

relaxometry, and ultrashort echo time MRI.[123,125] But, the specificity of these methods for myelin is not ideal, and these methods struggle to distinguish changes in myelination from hemorrhages, iron deposits, and changes in the water content of tissue.

Myelin-specific contrast agents provide a way to augment the lack of specificity in myelin imaging; however, the three myelin-specific contrast agents for MRI that have been reported are limited by low relaxivity values.[38,39,81,130] Myelin-specific Gd^{III}-containing small molecules were reported that are similar in efficiency (5.1 mM^{-1} s^{-1}) to nonspecific clinically approved contrast agents.[38,39,130] These contrast agents were able to highlight myelination in MRI via T_1 maps; however, the images acquired with these agents demonstrate the need for contrast agents with higher relaxivities to produce images of myelinated structures with increased signal to noise ratios.[38,39,130] Further, the Cu^{II}-containing myelin-specific histology stain Luxol fast blue MBS (LFB MBS) was reported for imaging of myelinated brains with magnetic resonance spectroscopy.[81] However, LFB MBS did not produce appreciable contrast because of the extremely low efficiency (0.09 mM^{-1} s^{-1}) of the complex as a contrast agent for MRI.[81] Investigation of efficient myelin-specific agents for contrast-enhanced MRI is crucial for effective visualization of changes in brain tissues.

Sensitive measurements of changes in tissue structure require high precision and accuracy, and one way to ensure the reliability of findings is with verification using orthogonal imaging techniques. Furthermore, the ability to combine techniques that produce high resolution structural images with techniques that yield chemical information enables the extraction of multiple types of information from a single tissue sample. Multimodal myelin-specific imaging agents would meet this need by allowing effective visualization of the distribution of myelin and the chemical composition of the agent. In this research, a new multimodal myelin-specific

contrast agents that are more efficient than clinically approved contrast agents for MRI and that can be used with light and near-IR fluorescence microscopies and mass spectrometric imaging were reported. We also report the imaging of myelinated structures in ex vivo samples using our new agents.

Materials and Methods

A detailed description of the synthesis and characterization of Gd^{III}-containing texaphyrins **2.2–2.6** is described in the Chapter 2.

Animals. Animal care and use were in accordance with the National Institutes of Health Animal Care Guidelines and approved by the Wayne State University Institutional Animal Care and Use Committee. Intact brain tissue used for the section- and en bloc-staining techniques were obtained from euthanized C57Bl/6 mice that were bred in-house.[131] Prior to euthanizing, all efforts were made to minimize suffering. The approval from Institutional Animal Care and Approval Committee to handle mice in Prof. Conti Alana's lab is included in Appendix C.

Stain Preparation. *Texaphyrin stain **2.2**:* To a mixture of ethanol (95%, 2 mL) and acetic acid (10%, 100 µL) was added texaphyrin **2.2** (4.4 mg, 0.0045 mmol, 1 equiv). The reaction mixture was heated at 60 °C for 18 h, cooled to ambient temperature, and filtered through a 0.2 µm filter to obtain stain **2.2** as a dark green solution. The stain solution was stored at 4 °C. The concentration of the stain solution was determined by ICP–OES.

*Texaphyrin stain **2.3**:* To a mixture of ethanol (100%, 2 mL) and acetic acid (10%, 100 µL) was added texaphyrin **2.3** (4.0 mg, 0.0048 mmol, 1 equiv) followed by ditolylguanidine (4.7 mg, 0.019 mmol, 4 equiv) dissolved in acetic acid (1 M, 19 µL, 4 equiv). The reaction mixture was filtered through a 0.2 µm filter and heated at 60 °C for 18 h. The solution was cooled to ambient

temperature, and filtered through a 0.2 µm filter to obtain stain **2.3** as a dark green solution. The stain solution was stored at 4 °C. The concentration of the stain solution was determined by ICP–OES.

*Texaphyrin stain **2.4**:* To a mixture of CH_3OH/water (3:2 v/v, 1 mL) was added texaphyrin **2.4** (4.2 mg, 0.0045 mmol, 1 equiv) followed by ditolylguanidine (4.4 mg, 0.018 mmol, 4 equiv) dissolved in acetic acid (1 M, 18 µL, 4 equiv). The reaction mixture was heated at 60 °C for 6 h. The solution was cooled to ambient temperature, and the solvent was removed under reduced pressure. The residue was dissolved in a mixture of ethanol (95%, 2 mL) and acetic acid (10%, 100 µL), and the solution was heated at 60 °C for 14 h. The solution was cooled to ambient temperature and filtered through a 0.2 µm filter to obtain stain **2.4** as a dark green solution. The stain solution was stored at 4 °C. The concentration of the stain solution was determined by ICP–OES.

*Texaphyrin stain **2.5**:* To a mixture of CH_3OH/water (1:1 v/v, 1 mL) was added texaphyrin **2.5** (4.1 mg, 0.0041 mmol, 1 equiv) followed by ditolylguanidine (6.0 mg, 0.025 mmol, 6 equiv) dissolved in acetic acid (1 M, 25 µL, 6 equiv). The reaction mixture was heated at 60 °C for 6 h. The solution was cooled to ambient temperature, and the solvent was removed under reduced pressure. The residue was dissolved in a mixture of ethanol (95%, 2 mL) and acetic acid (10%, 100 µL), and the solution was heated at 60 °C for 14 h. The solution was cooled to ambient temperature and filtered through a 0.2 µm filter to obtain stain **2.5** as a dark green solution. The stain solution was stored at 4 °C. The concentration of the stain solution was determined by ICP–OES.

*Texaphyrin stain **2.6**:* To a mixture of CH_3OH/water (1:2 v/v, 1 mL) was added texaphyrin **2.6** (4.2 mg, 0.0038 mmol, 1 equiv) followed by ditolylguanidine (8.0 mg, 0.033 mmol, 8 equiv) dissolved in acetic acid (1 M, 33 µL, 8 equiv). The reaction mixture was heated at 60 °C for 6 h. The solution was cooled to ambient temperature, and the solvent was removed under reduced pressure. The residue was dissolved in a mixture of ethanol (95%, 2 mL) and acetic acid (10%, 100 µL), and the solution was heated at 60 °C for 14 h. The solution was cooled to ambient temperature and filtered through a 0.2 µm filter to obtain stain **2.6** as a dark green solution. The stain solution was stored at 4 °C. The concentration of the stain solution was determined by ICP–OES.

Tissue Staining. *Tissue Preparation.* Formaldehyde (37% wt/v), Li_2CO_3, ethanol (200 proof), and agarose were purchased from Sigma Aldrich, Acros Organics, Decon Laboratories. Inc., and OmniPur, respectively. Tissues were acquired within 5 min of animal sacrifice and placed in a beaker of 3.7% (wt/v) aqueous formalin solution. Fixed tissue was stored at 4 °C in formalin. Prior to staining, fixed tissues were removed from formalin storage and rinsed with purified water (~10 mL) to remove formalin.

Section-Staining Procedure. Tissue sections (200 µm thick) were obtained from fixed intact tissues using a vibrotome 3000 (MyNeuroLab). For each stain, three tissue sections were stained that provided observation of a diverse assortment of brain regions: 0.50 to 1.54, 0.14 to –0.58, and –1.58 to –2.18 mm from Bregma.[132] Each tissue sample was incubated in staining solution (2–0.8 mM, 0.2 mL) for 5 h at 54 °C. Tissue sections were removed from the staining solution and rinsed by swirling with ethanol (95%, 1 mL, 1 min) followed by water (1 mL, 1 min). Tissue stained with texaphyrin **2.2** were differentiated with a solution of Li_2CO_3 (4.5 mM) in ethanol (65%, 4 mL) for 30 min, three concentrations of ethanol (100, 95, and 70%, 4 mL each)

for 45 min each, and water (4 mL) for 5 min. All differentiations and rinsings were performed on a rotator (Thermo Labquake Tube Shaker/Rotator). Tissues stained with texaphyrins **2.3–2.6** were differentiated with a solution of Li_2CO_3 (4.5 mM) in ethanol (65%, 4 mL) for 1–2 h, rinsed with ethanol (95%, 4 mL, 1 min), and hydrated in water (4 mL, 5 min for complexes **2.3** and **2.4**, 1 min for complexes **2.5** and **2.6**). At the end of the differentiation and hydration, each tissue section was mounted on a microscope slide for imaging.

En bloc-Staining Procedure. Intact mouse brains were incubated in solutions of texaphyrin **2.4** (0.8 mM, 1.8 mL) for 24 h at 54 °C. At the end of the incubation, the brains were rinsed with ethanol (95%, 25 mL, 1 min) then water (25 mL, 1min). The brain tissue was pat dried with tissue paper, and an incision was made using a scalpel along the midline on the dorsal face of the intact brain, such that the incision reached the dorsal third ventricle. Brains were placed in a solution of Li_2CO_3 (11 mM) in ethanol (40%, 25 mL) and the vial containing the brains in the Li_2CO_3 solution was rotated. The solution of Li_2CO_3 was changed after 6 and 24 h, and the differentiation was continued for total of 65 h. At the end of the differentiation, the mouse brain was rinsed with water (25 mL, 1 min) and hydrated in water (25 mL) for 10 min. The hydrated brain was pat dried and suspended in agarose gel (2%) for MR imaging.

Optical Imaging. Optical images were acquired using an Olympus SZX7 (model number SZ2-ILST) microscope (1.25× or 5.6× magnification) with an attached SPOT idea microscope camera (model number 27.2–3.1 MP). Differentiated section-stained mouse brain tissue samples were mounted on microscope slides to obtain images. En bloc-stained mouse brains were sliced (200 μm) using the vibrotome after obtaining MR images, and the slices were mounted on microscope slides to obtain images.

MR Imaging. MR Imaging. MRI scans were performed with a 7 T Varian small animal MRI scanner (299.44 MHz, 7.0 T) equipped with a 12 cm bore magnet and a 38 mm diameter homemade transmit/receive quadrature birdcage coil. Samples included a mouse brain stained with texaphyrin **3** and an unstained control mouse brain suspended in agarose. T_1-maps were acquired at ambient temperature using a T-One by Multiple Read-Out Pulses,[133] which is a Look–Locker sequence.[134] At least one dummy cycle (N pulses followed by T_{relax}) was applied before the start of data acquisition. Inversion of the longitudinal magnetization was accomplished using a non-selective hyperbolic secant adiabatic pulse of duration 12 ms. One phase-encode line of 40 small-tip-angle (approximately10˚ 3-lobe sinc shaped pulses) gradient-echo images (4 ms) was acquired after each such adiabatic inversion (50 ms intervals) for a total recovery time of 3000 ms with a 3 s relaxation interval between each adiabatic inversion. Matrix size = 256×192; 32 mm^2 field-of-view; three image slices at 0.5 mm thickness; and eight averages. Analysis proceeded as described previously,[135] with a modification that is now described. Because the 3 s relaxation time was not sufficient to allow the longitudinal magnetization to re-equilibrate after inversion, the equilibrated magnetization of the sequence was iteratively estimated along with the other model parameters (proton density, T_1, and tip-angle). ImageJ was used to process the R_1-maps. Brightness and contrast were adjusted to 50 and color balance was adjusted to 244. Five regions of interest were used to calculate the percent increase of R_1 in myelin-rich regions with respect to myelin-poor regions in the stained and unstained brains (**Figure B.26**). The difference between the average R_1 values of the regions of interest from myelin-rich and myelin-poor regions were used to calculate percent increase of R_1.

Laser Spray Ionization Vacuum (LSIV) Mass Spectrometric Imaging. Mouse brain tissue (200 μm) mounted on microscope slide was spray coated with the matrix 2-nitrophloroglucinol

(2-NPG) (Alfa Aesar) using an air brush (Iwata). A commercial matrix-assisted laser desorption ionization (MALDI) source of a SYNAPT G2 mass spectrometer (Waters Corporation) was used for the imaging. The intermediate source pressure was 0.16 Torr. The laser used was an Nd:YAG laser (355 nm) in reflection geometry mode with a laser power of 12.5 J cm^{-2} and a firing rate of 200 Hz. Data were acquired in positive ion and sensitivity modes. Laserspray ionization settings were used and are as follows: 0 V on sample plate; 10 V "extraction"; 10 V "hexapole bias"; 5 V "aperture 0". Data were processed using MassLynx version 4.1. Mass spectra were converted to MSI files using a MALDI Imaging Converter. The location of the signal of the complex was mapped using BioMAP 3.8.0.1 from Novartis Institutes for Biomedical Research, Basel, Switzerland.

Results

The design of myelin-specific contrast agents used in this research was inspired by the myelin-specific histology stain LFB MBS (**Figure 4.1**). The structural features of LFB MBS were mimicked to synthesize a ligand with a cavity large enough to encapsulate a Gd^{III} ion for efficient MRI enhancement. The mimic contains a texaphyrin, a ligand that is structurally similar to the phthalocyanine ligand of LFB MBS (**Figure 4.1**). Although it is known that LFB MBS interacts with myelin, the site of interaction is not well established; however, the currently accepted hypothesis assumes that the sulfonate groups of LFB MBS interact with myelin basic protein.[126] To understand the features that are important for interaction with myelin, five Gd^{III}-containing texaphyrins that vary in functional group identity were synthesized (**2.2–2.6** in **Figure 4.1**).

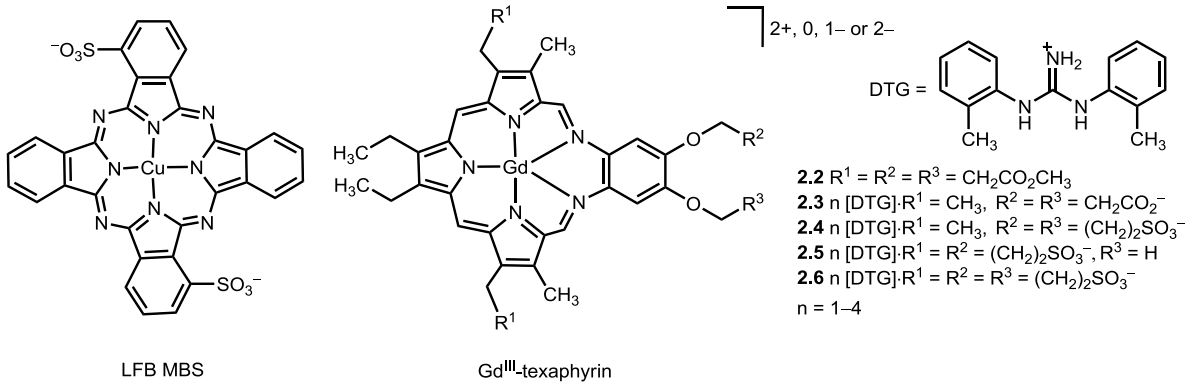

Figure 4.1. Chemical structures of LFB MBS and Gd^{III}-texaphyrin complexes **2.2–2.6**.

The functional groups introduced to the texaphyrin periphery include sulfonates, carboxylates, and methyl esters. Although many texaphyrin derivatives have been reported, texaphyrins **2.2–2.6** were new derivatives. Sulfonates and carboxylates were used to test the importance of the identity of acidic functional groups for interaction with myelin, and methyl esters were used as a control to study the need of acid functional groups. Incorporation of different types and numbers of functional groups into the periphery of texaphyrins resulted in different physicochemical properties including polarity and solubility.

*Solubility of texaphyrins **2.2**–**2.6***

The solubilities of texaphyrins **2.2**–**2.6** after the preparation of stain solutions are described here. Complexes **2.2**, **2.3**, and **2.4** were sparingly soluble in water but soluble in methanol, ethanol, and acetonitrile, while complexes **2.5** and **2.6** were soluble in water. Texaphyrins **2.2** and **2.4–2.6** were soluble in mixtures of water and these organic solvents and solutions of **2.2** and **2.4–2.6** did not yield precipitate after 3 months; however, texaphyrin **2.3**

produced an insoluble precipitate in the presence of 95% ethanol 15 min after dissolution. The use of absolute ethanol avoided the rapid precipitation of **2.3**, but upon storage, precipitation was observed after 2 days. Therefore, stain **2.3** was prepared fresh for each experiment.

*Properties of texaphyrins **2.2**–**2.6** that are important for imaging*

The extended conjugation of texaphyrins produces a characteristic sharp absorption in the visible region that causes the metal complexes to appear dark green in color. All five texaphyrin complexes demonstrated similar absorptions (**Figure B.5**) regardless of the number or type of the functional groups on the side chains. The deep green color of the texaphyrin complexes enabled the visualization with light microscopy similar to the visualization of the blue histology stain LFB MBS. The fluorescence emissions of the five complexes were also similar to each other regardless of functional group identity (**Figures B.6** and **B.7**), exhibiting near-IR emission when excited by 468–492 nm light.

The efficiency of complexes **2.2–2.6** as contrast agents for MRI was determined by measuring their relaxivities at 1.4 T and 37 °C using solvent systems that permit sufficient solubility for the complex. The solvent system that was used for the dissolution of the complex was measured as the blank in each case. All five complexes demonstrated higher relaxivity values than current clinical contrast agents for MRI (**Table 4.1**, **Tables B1–15**, and **Figures B.8–B.22**). Texaphyrin **2.2** had the highest relaxivity (19.5 mM^{-1} s^{-1}) and was similar to other reported texaphyrins with neutral functional group-containing side chains.[136] Texaphyrins **2.3–2.6** that contain negatively charged acidic functional groups in their side chains demonstrated lower relaxivities than **2.2**, but more than 3-fold higher values than clinically approved contrast agents.

Table 4.1. Relaxivity values of texaphyrin complexes **2.2–2.6**.

Gd^{III}-texaphyrin complex	**2.2**	**2.3**	**2.4**	**2.5**	**2.6**
Relaxivity ($mM^{-1} s^{-1}$)	$19.5 \pm 0.1^{*}$	$13.3 \pm 0.2^{*}$	$11.6 \pm 0.1^{\dagger}$	11.3 ± 0.2	11.7 ± 0.1

Relaxivity measured at 1.4 T, 37 °C, and in water or *30% or †50% methanol in water. Results are reported as mean ± standard error of three independently prepared samples.

While the electronic properties of Gd^{III} produce contrast enhancement with MRI, the unique isotopic distribution of Gd^{III} (**Figure B.23**) enables identification of Gd^{III}-containing texaphyrins by mass spectrometry even in the presence of complex mixtures like tissue sections. Hence, the localization of texaphyrins in stained tissue can be mapped using mass spectrometry.

*Staining tissue with texaphyrins **2.2**–**2.6***

The staining of mouse brain tissue was performed by incubating tissue samples (200 µm thick) in stain solutions at 54 °C for 5 h. At the end of the incubation, a marked reduction of the intensity of color of the stain solution was visible, and the mouse brain sections were green. When comparing texaphyrin stains **2.2**–**2.6** to each other, the staining solution of complex **2.2** demonstrated the lowest reduction of color after incubation and resulted in only lightly colored tissue. Tissue sections stained with texaphyrins **2.3**–**2.6** were dark green. To differentiate stained tissue samples, solutions of Li_2CO_3 were used; however, the use of aqueous Li_2CO_3 that is used with LFB MBS[126] led to under-differentiation for tissue samples stained with texaphyrins **2.3** and **2.4** and over-differentiation for texaphyrins **2.5** and **2.6**. An ethanolic Li_2CO_3 solution was selected as the optimal differentiation solution because it demonstrated appreciable differentiation for texaphyrins **2.3**–**2.6**.

Texaphyrin **2.2** that contains methyl esters did not differentiate with aqueous or ethanolic Li_2CO_3. Because of the inability to differentiate myelinated and non-myelinated regions with texaphyrin **2.2**, it was not used for further studies.Texaphyrins **2.3** and **2.4** provided a visible differentiation of myelinated regions from non-myelinated regions, and texaphyrins **2.5** and **2.6** were removed completely from tissue upon exposure to water. The removal of stain with exposure to water likely due to the increased hydrophilicity from presence of three or more negatively charged sulfonate groups and is an undesirable feature for ex vivo staining of myelin. In contrast, texaphyrins **2.3** and **2.4** differentiated with ethanolic Li_2CO_3 and were stable upon exposure to water; thus, texaphyrins **2.3** and **2.4** were found to be viable candidates for staining myelin. Myelin-rich white matter regions demonstrated a green color with respect to myelin-poor surrounding tissues in coronal brain sections with light microscopy when stained with texaphyrins **2.3** and **2.4**. Specifically, the myelin-rich corpus callosum, striations in the caudate putamen, anterior commissure, and mammillothalamic tract appeared green in the optical images (**Figures 4.2**, and **4.3**).

Texaphyrin **2.4** was used for staining intact mouse brains for MRI studies because of its ability to differentiate myelinated structures and the ease of handling without precipitation. When staining intact brains, the optimal incubation time for the diffusion of the texaphyrin was found to be 24–26 h. The diffusion of large molecules like texaphyrins takes more time for thick tissue samples than thin tissue sections. The differentiation time for intact brain was 65 h, and an incision along the mid line of the brain was made prior to differentiation to facilitate the diffusion of Li_2CO_3 into the tissue. The long differentiation times and mechanical opening of tissue were necessary for penetration of ionic Li_2CO_3 through hydrophobic tissue layers.

Differentiated whole mouse brain was used for MR imaging to investigate the ability of texaphyrin **2.4** to act as a myelin-specific contrast agent.

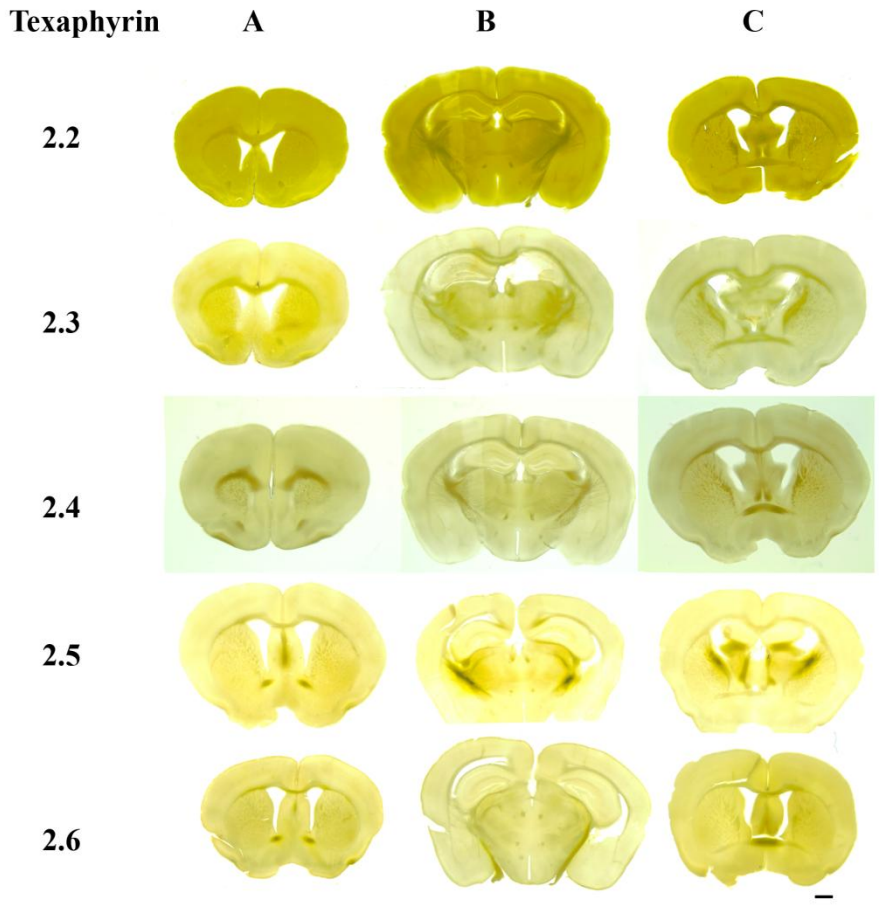

Figure 4.2. Optical images of texaphyrin-stained mouse brain slices. Columns **A–C** contain images of representative mouse brain samples from three different regions of the brain (**A**, 0.50 to 1.54; **B**, –1.58 to –2.18; and **C**, 0.14 to –0.58 mm from Bregma[132]) that were treated with texaphyrin complexes **2.2**–**2.6**. Slice thickness = 200 μm, and scale bar = 1 mm.

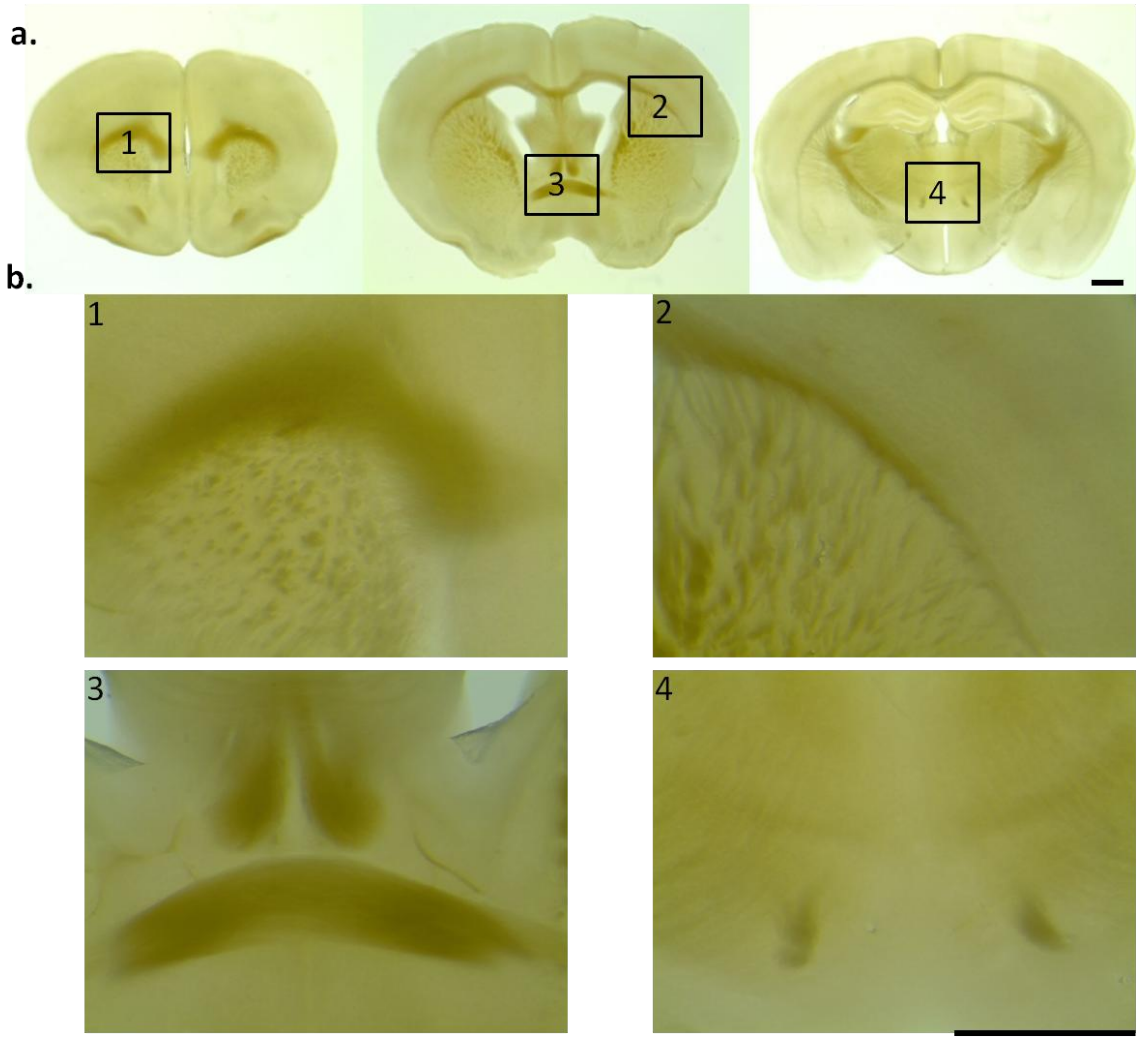

Figure 4.3. Optical images of mouse brain sections stained with texaphyrin **2.4**. Panel **a.** shows representative brain images from 1.54 to –1.82 mm from Bregma.[132] Panel **b.** shows high magnification images of myelinated regions and the magnified area is represented with black squares in panel **a.** Myelin rich regions, namely; forceps minor of the corpus callosum in 1; external capsule and part of the caudate putamen in 2; fornix and anterior commissure anterior part in 3; and the mammillothalamic tract in 4 are highlighted in green. Slice thickness = 200 µm, and scale bars = 1 mm.

*Mass spectrometric imaging of texaphyrin **2.4** stained mouse brain*

The brain sample stained with texaphyrin **2.4** was imaged with LSIV mass spectrometric imaging. Samples for mass spectrometric imaging were prepared by spray coating the brain

sections with the matrix 2-nitrophloroglucinol. Application of 2- nitrophloroglucinol facilitates ionization of the texaphyrin complexes. Expected *m*/*z* for intact texaphyrins were detected in the tissue. The regions with high relative concentrations of texaphyrins corresponded to myelin-rich regions of the brain sample (**Figure 4.4**).

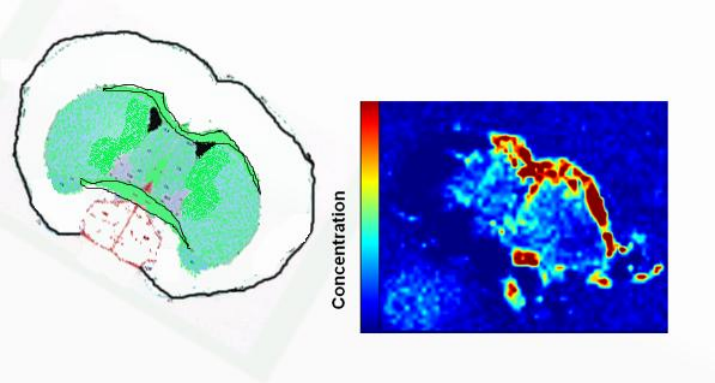

Figure 4.4. Left, Mouse brain atlas corresponding to a matching coronal section with prominent myelin-rich regions highlighted in green (adapted from reference 137); Right, LSIV mass spectrometric imaging of mouse brain sample stained with texaphyrin **2.4**. Relative concentration of the texaphyrin **2.4** in myelin-rich regions is higher with respect to myelin-poor regions in the mass spectrometric image.

*MRI imaging of texaphyrin **2.4** treated mouse brain*

An intact mouse brain stained with texaphyrin **2.4** and an unstained control brain were embedded in agarose prior to MR imaging. The T_1-maps of the mouse brains stained with texaphyrin **2.4** demonstrated a clear deference between myelin-rich (dark) and poor (bright) regions in comparison to the unstained control (**Figure 4.5**, **a** and **b**). Myelin-rich regions of the stained sample were dark because the T_1-relaxation time is shorter (~400 ms) than the myelin poor regions (~650 ms) of the same tissue and the T_1 relaxation time of the control sample (myelin-rich regions ≈ 1000 ms and myelin-poor regions ≈ 1300 ms). The T_1-map was converted into an R_1-map because it is easier for visualization of regions of interest (**Figure 4.5**, **c** and **d**).

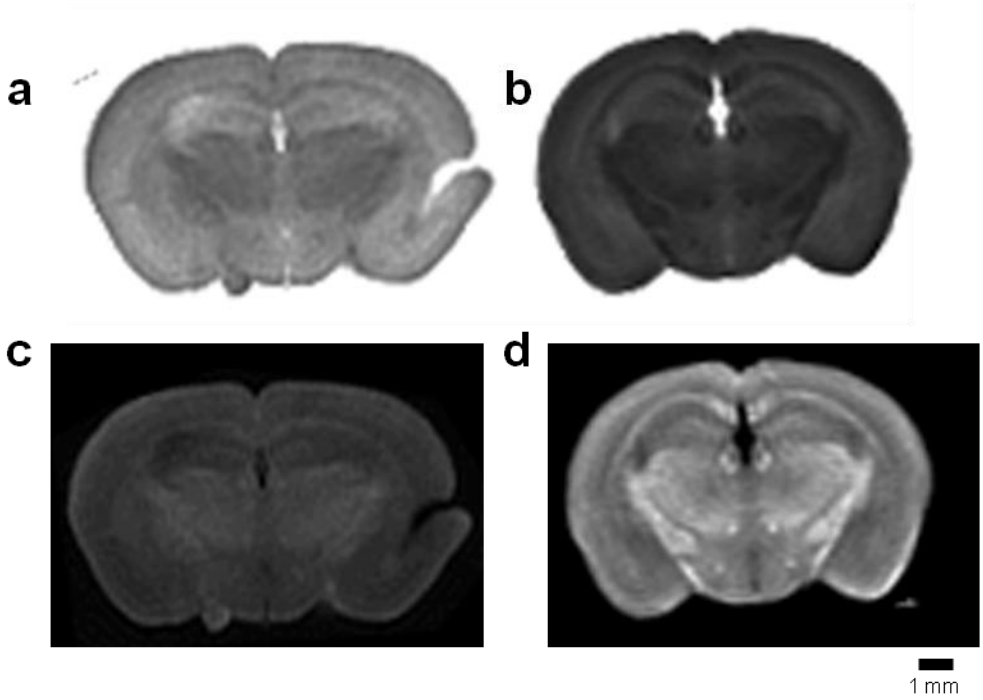

Figure 4.5. Representative T_1- and R_1-maps of coronal sections of mouse brains (–1.58 mm from Bregma)[132]: **a**. T_1-map of unstained control brain; **b**. T_1-map of mouse brain stained with texaphyrin **2.4**; **c**. R_1-map of unstained control brain; and **d**. R_1-map of texaphyrin **2.4** stained mouse brain. Myelin-rich regions of stained brain sample look brighter with respect to the myelin-poor gray matter regions of the tissue, and myelin-rich regions of the control in the R_1-map.

R_1 values represent $1/T_1$, and short T_1 values produce large R_1 values thus, inverting the brightness of the T_1-map. The R_1 value of myelin-rich regions of the stained brain was ~2.6 fold greater than the surrounding myelin-poor tissue while the R_1 value was only ~1.6 fold greater in the myelin rich regions of the unstained control brain. Thus, the myelin-rich regions in R_1-map of stained brain look brighter and are easy to distinguish due to the additional contrast enhancement by texaphyrin **2.4** with respect to the unstained control. At the end of the MR imaging, the brain sample was sectioned and observed with light microscopy and mass spectrometric imaging to verify the MRI and to identify the chemical identity of the Gd^{III}-containing contrast agent after staining (**Figure 4.6** and **Figure B.25**).

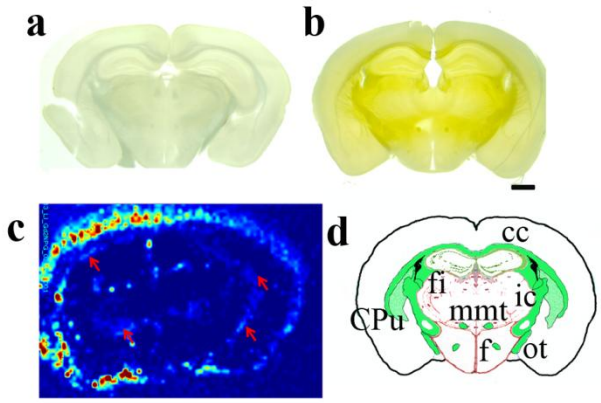

Figure 4.6. Optical and mass spectrometric images of coronal brain sections corresponding to the MR images in **Figure 4.5**. **a.** optical image of unstained control brain; **b.** optical image of brain stained with texaphyrin **2.4**; **c.** mass spectrometric image of brain stained with texaphyrin **2.4**; **d.** mouse brain atlas corresponding to a matching coronal section with prominent myelin-rich regions highlighted in green (adapted from reference 137). In the image cc, CPu, f, fi, ic, mmt, and ot stand for corpus callossum, caudate putamen, fornix, fimbria, internal capsule, mammillothalamic tract, and optic tract, respectively. Red arrows point to the myelin-rich regions of mass spectrometric image. Scale bar = 1 mm.

Discussion

A well known myelin-specific histology stain LFB MBS was used as our structural inspiration because it contains a metal-ligand motif that is amenable to adaptation into a contrast agent for MRI. However, the ligand framework of LFB MBS cannot be directly used for the synthesis of stable Gd^{III}-containing complexes because the cavity size of the phthalocyanine in LFB MBS does not match well with the ionic radius of Gd^{III}.[138] Sessler and co-workers reported the use of expanded porphyrins known as texaphyrins to form stable complexes with lanthanides.[82–84, 93–95] Their studies with Gd^{III}-containing texaphyrins have shown that complexes of these macrocycles are efficient contrast agents for MRI and have higher relaxivities than

clinically approved contrast agents.[136] Knowledge from Sessler's studies helped to realize that texaphyrins have the potential to mimic the structural features of phthalocyanine— including a planar aromatic macrocycle, acidic functional groups, and charge—while forming stable complexes with Gd^{III}. Although, LFB MBS interacts with myelin, the important structural features for interaction are not well established. Therefore, five different texaphyrin complexes that vary in the type and number of functional groups on the side chains were synthesized. This variety was expected to enable on understanding of the structural features that lead to interactions with myelin. The functional groups that were selected included methyl esters, sulfonates, and carboxylates. Because some of these functional groups have not been reported with texaphyrins, synthetic routes to make them had to be devised.

The functional group selection allowed to explore the influence of a variety of properties on staining. Complex **2.2** has an overall charge of +2, and it does not have acidic functional groups; thus, it was designed to test if negative charge or acidic functional groups are crucial for myelin-specific interactions. Complex **2.3** has carboxylate groups and is neutral. This complex is a carboxylate analogue for sulfonate containing texaphyrins and was synthesized to study the necessity of sulfonates as the acidic functional groups. Complexes **2.4**–**2.6** have sulfonate groups and charges of 0, –1, –2, respectively, and these complexes were designed to study the effect of the number of sulfonate groups on interaction with myelin.

Initial staining studies with coronal sections of mouse brain tissue was performed to visualize the interaction of texaphyrins **2.2**–**2.6** with myelinated structures. Brain sections stained with Gd^{III}-containing texaphyrins were differentiated with Li_2CO_3 solutions to remove excess and loosely bound texaphyrins, under the assumption that mild alkali solutions interrupt the interaction between sulfonates and myelin.[126] Because hydrophilic alkali solutions do not enter

the hydrophobic domains of myelin to interrupt the interactions, the stain is retained in myelinated structures.[126] Because of the optical absorptions of texaphyrins, light microscopy was initially used to gauge the interaction of the texaphyrins with myelin. Texaphyrin complexes have a characteristic dark green color due to the absorption of visible light in the 700–750 nm range. Thus, texaphyrins are chromophoric probes similar to LFB MBS. Additionally, the fluorescence emission studies demonstrated a near-IR emission and, consequently, the potential for use as fluorescence probes.

Light microscopy images of mouse brain slices stained with Gd^{III}-containing texaphyrins showed that complexes **2.3** and **2.4** that are less hydrophilic than complexes **2.5** and **2.6** differentiate better and, consequently, highlight myelinated regions in the brain tissue more efficiently than the other three complexes. Texaphyrins **2.5** and **2.6** that have more than two negatively charged functional groups did stain myelin, but the high solubility of these texaphyrins in water interferes with the retention of the stain in myelinated regions. Texaphyrin **2.2** did not highlight myelin and demonstrated non-specific staining of brain tissue. Unlike texaphyrins **2.3**–**2.6**, Li_2CO_3 was not able to remove texaphyrin **2.2** from tissue samples. The observations with staining studies of texaphyrins **2.2–2.6** reveal that the presence of a negatively charged acidic functional group is vital for interaction with myelin. It is assumed that the interaction of LFB MBS and myelin occurs through an acid-base type interaction between the negatively charged sulfonate groups of the stain and positively charged amine residues of the myelin basic proteins.[126] The observations from this research support the presence of this type of interaction because texaphyrin **2.2** with neutral methyl ester groups did not demonstrate myelin-specific staining of brain tissues.

The non-specific labeling observed with texaphyrin **2.2** likely arises because the positively charged molecule interacts with negatively charged lipids in the tissue. Furthermore, maintaining some hydrophobicity seems to be critical to attain desirable staining and differentiation. A possible explanation for observations with texaphyrins **2.5** and **2.6** is that the hydrophilic stain is unable to enter the hydrophobic domains of the myelin sheath. Instead, these molecules might interact with the surface myelin basic proteins, which would make them easily remove upon exposure to water.

To confirm the staining pattern observed with light microscopy and to explore the integrity of the chemical composition of texaphyrins after undergoing staining and differentiation, mass spectrometric imaging was performed with brain slices stained with texaphyrins **2.2**–**2.6**. Although, mass spectrometry has been used as a tool for the characterization of compounds for decades, it has not been used as a tool of imaging until recently.[139] Several promising imaging studies using MALDI and LSIV have been reported for imaging tissues via the detection of proteins or lipids.[139–141] However, the detection of proteins and lipids is often difficult because of the high background present in biological samples. Thus, to confirm the presence of proteins or lipids of interest, a secondary mass spectrometric technique is usually required. But, when non-endogenous material like a contrast agent is being imaged, interference from background is avoided.[142] Because of characteristic mass distribution of Gd^{III} with seven major isotopes (**Figure B.23**), the detection of Gd^{III}-containing texaphyrins in tissue samples is straight forward. The imaging of brain samples stained with complex **2.4** was performed with LSIV mass spectrometry. The presence of intact metal complex in tissue samples indicates the robustness of the metal complex for the staining conditions. The images from brain tissues stained with texaphyrin **2.4** demonstrated high concentration regions that overlapped with

the myelin-rich structures of the mouse brain. Thus, confirming the presence of intact complex in the myelinated structures that were observed with optical microscopy.

From optical microscopy, texaphyrins **2.3** and **2.4** that contain two carboxylates and sulfonates, respectively, demonstrated better staining of myelinated regions in brain tissues than texaphyrins **2.2**, **2.5**, or **2.6**. This observation indicates that the negatively charged functional groups do not need to be sulfonates. However, handling of texaphyrin **2.3** is difficult because of the formation of precipitate upon storage that results likely due to the oligomerization via bridging of carboxylates among Gd^{III}. Consequently, texaphyrin **2.4** was selected as the best myelin-specific texaphyrin of the five complexes for moving to staining of intact brains and observation with MRI.

Texaphyrins **2.2**–**2.6** demonstrated 3.5–4× higher relaxivities than clinically approved contrast agents. These high relaxivities likely result from a combination of slow tumbling due to the size of the molecule and the availability of more than one site for water coordination. Higher relaxivity is desirable for contrast agents because it enables efficient contrast enhancement, which is especially important for detection of fine structures including white matter structures. The relaxivity of methyl ester-containing texaphyrin **2.2** is 1.8–1.5× greater than the sulfonate and carboxylate-containing texaphyrins **2.3**–**2.6**, possibly because the interaction of these negatively charged groups with Gd^{III} causes a reduction of the available sites for water coordination. Ion mobility mass spectrometric studies done with texaphyrin **2.4** have demonstrated two species in the mass plot with same *m*/*z* ratio but different drift times (**Figure B.24**). If negatively charged groups interact with the Gd^{III}, those texaphyrins would have a more compact structure than texaphyrins with free side chains and will result in different drift times.

R_1-mapping of intact mouse brain stained with texaphyrin **2.4** was performed to investigate the contrast enhancing properties of the complex. Myelinated regions of the R_1-map of the brain samples stained with texaphyrin **2.4** demonstrated a faster relaxation rate (2.6-fold) than myelin-poor regions of the stained tissue. The enhancement of R_1 of the myelin-rich regions from the surroundings was only 1.6-fold for the unstained control. Water protons tend to relax faster in the presence of paramagnetic Gd^{III} because of the magnetic inhomogeneity created by the Gd^{III} center. Thus, the increase of the R_1 relaxation rate indicates the presence of Gd^{III}. R_1-maps are useful for visualizing myelinated structures because of the presence of positive contrast enhancement in stained regions.

To validate the observations from MRI studies with intact brains, the brain was sectioned after MR imaging and confirmed the presence of stain with optical microscopy and mass spectrometric imaging. White matter structures appeared green under the light microscope (**Figure 4.6** and **Figure B.25**), and LSIV mass spectrometric imaging of the corresponding brain slice of MRI confirmed that texaphyrin **2.4** was interact and distributed in regions that showed a positive enhancement in R_1-map (**Figure 4.5**). The imaging studies from orthogonal imaging modalities confirmed the ability of texaphyrin **2.4** to diffuse into intact mouse brains, differentiate to be retained specifically in myelinated regions, and to act as a multimodal imaging agent facilitating the visualization of white matter structures and chemical information about the structure of the imaging agent after staining.

Conclusion

Efficient, small molecular probes for myelin were synthesized using a structure-mimicking strategy. Ex vivo studies demonstrated that texaphyrins **2.3** and **2.4** interact with

myelin. The optical and magnetic properties of these texaphyrin complexes allowed the imaging of myelin in brain sections and intact brains using optical microscopy and MRI. Furthermore, the unique isotopic distribution of Gd^{III} facilitated the use of mass spectrometric imaging of myelin to provide chemical information regarding the imaging agent in tissue. The myelin-specific imaging agent **2.4** render the use of MRI, optical, and mass spectrometric imaging to study myelination and demyelination in mouse models of neuropathologies for pre-clinical research.

CHAPTER 5. Conclusions and Future Directions

Conclusions

A multimodal, β-amyloid-targeted contrast agent

A β-amyloid-targeted Gd^{III}-containing complex was synthesized using the conjugation strategy in which a curcumin molecule and a derivative of a clinically approved contrast agent were conjugated using a short linker. The conjugated complex **2.1** demonstrated a higher relaxivity than clinically approved contrast agents for magnetic resonance imaging (MRI). Furthermore, in vitro studies demonstrated that the curcumin-conjugated contrast agent **2.1** interacts with β-amyloid aggregates resulting in a shortening of longitudinal relaxation time. Thus, complex **2.1** has potential to be an efficient, β-amyloid-specific contrast agent for MRI. Additionally, conjugated complex **2.1** exhibits fluorescence, and the both the wavelength and intensity of the emission of complex **2.1** change upon interaction with β-amyloid aggregates in vitro. Thus, this probe is multimodal allowing for validation of the presence of β-amyloid aggregates using orthogonal imaging modalities.

A myelin-specific, multimodal imaging agent for magnetic resonance, optical, and mass spectrometric imaging

Myelin-targeted Gd^{III}-containing complexes were synthesized by mimicking the structural features of a known myelin-specific stain, LFB MBS. The texaphyrin framework was used in this project because it has structural similarities to phthalocyanine and a cavity size that accommodates Gd^{III}. Five different texaphyrins were synthesized by changing the functional groups of the side chains of the texaphyrins. These new complexes contained methyl esters,

carboxylates, and sulfonates. Ex vivo mouse brain samples were stained with these Gd^{III} texaphyrin complexes and imaged using optical microscopy, laser spray ionization vacuum mass spectrometric imaging, and MRI. These ex vivo imaging studies demonstrated that the acid functional groups containing neutral Gd^{III}-containing texaphyrins have affinity toward myelin rich regions in the brain tissue.

Future Directions

*Improvements in synthesis of conjugate **2.1** and modification of the structure for potentially interesting studies*

In the synthesis of conjugate **2.1**, improvements can be made to the synthesis of **2.1d** by using a milder base such as K_2CO_3 instead of NaOMe. Initially, NaOMe was chosen to peroform conjugation at an enolic oxygen; however, phenol can be deprotonated using K_2CO_3, which is milder than NaOMe, and should minimize the formation of multiple conjugation products leading to an increased yield of desired product. Another improvement that can be made in the synthesis is the addition of the isothiocyanate-containing Gd^{III}DTPA, **2.1f,** dropwise to the basic curcumin solution. This will avoid lengthened exposure of the isothiocyanate group to a basic environment and could minimize the potential hydrolysis of isothiocyanate.

The effect of the structure of the conjugate **2.1** on interaction with β-amyloid aggregates is one of the parameter that is important to study. One of the structural features that can be easily changed in conjugate **2.1** is the amine linker length. Another structural feature that can be altered is the conjugation site. The synthesis of conjugates with different linker lengths and different sites of attachment will help in understanding the important factors needed to design more effective β-amyloid-targeted contrast agents. The synthesis of neutral analogues of conjugate **2.1**

is another potentially interesting study. Neutral complexes will enable the penetration of analogues of complex **2.1** through blood brain barrier and facilitate the in vivo imaging. Because the size of amyloid deposits are often microns in diameter, the use of high field MRI for β-amyloid plaque imaging is desirable because high field strength MRI enables high resolution imaging. Synthesis of analogues of **2.1** with metal complexes that have a better relaxivity in high field strengths such as Eu^{II} cryptates is an interesting area of study to obtain contrast enhanced images of β-amyloid deposits at high field strengths.

*Investigation of the ability of conjugate **2.1** to modulate β-amyloid peptide aggregation*

In vitro binding studies that were discussed in Chapter 3 demonstrated the ability of the curcumin moiety in conjugate **2.1** to interact with the pre-formed β-amyloid aggregates. The interaction of curcumin is not limited to labeling of β-amyloid plaques, but also is reported to disrupt the existing β-amyloid deposit and inhibit the formation of β-amyloid oligomers and fibrils. Because of these desirable properties, curcumin is widely studied as a potential therapeutic for Alzheimer's disease. However, the hydrophobic nature of the curcumin molecule renders it insoluble in aqueous solvents limiting its use. Because curcumin conjugate **2.1** is soluble in aqueous solutions, interacts with β-amyloid aggregates similar to free curcumin, and has imaging capabilities with MRI and fluorescence, it would be interesting to study the ability of conjugate **2.1** to modulate the aggregation of β-amyloid. This study would be interesting because it would expand our understanding of the interaction between this multimodal imaging agent and β-amyloid and also our understanding of the positive or negative impact on the function of the curcumin moiety due to conjugation. Additionally, investigation of the molecular properties that are important for in vivo studies of the molecule, including permeability assays, and cell viability assays will give more insight into the use of the molecule.

The ability of **2.1** to modulate the aggregation of β-amyloid peptides can be studied in the presence and absence of metal ions, including Cu^{II} or Zn^{II}, that are relevant in Alzheimer's disease. The formation of aggregates and the morphology of the formed aggregates can be investigated at different time points using gel electrophoresis and transmission electron microscope, respectively.

*Improvements of myelin targeted complexes **2.2–2.6** by changing structural features*

Studies presented in Chapter 4 revealed the necessary structural features of complexes **2.2–2.6** to interact with myelin including acid functional groups. However, another interesting study would be the investigation of the length of the linker between texaphyrin and acid functional group. Because it is assumed that the interaction is taking place between acid functional groups and myelin basic protein, the feasibility of the interaction likely depends on the distance between the acid functional group and the metal ion. By synthesizing texaphyrin complexes containing different linker lengths and performing ex vivo imaging with these stains, the effect of chain length on interaction with myelin could be delineated. Furthermore, based on the relaxivity of complexes **2.2**–**2.6**, it can be assumed that the negatively charged acid functional groups may coordinate to the metal center. This coordination results in a decreased water-coordination number and decreased relaxivity for the complex. By changing the length of side chains and by monitoring the relaxivity values, the interaction between the metal center and acid functional groups can be understood. Furthermore, ^{17}O–NMR studies can be used to determine the water-coordination numbers of the complexes.

Improvements of sample preparation for MR imaging.

Use of agarose gel as the embedding medium for mouse brain imaging with MRI produces lot of background noise because of the water content in the gel. To reduce background noise and to obtain better images, embedding media with minimal water content should be used. By using perflouropolyether (Fomblin, CAS = 69991-67-9) media to embed tissue, background noise in MR image can be reduced.

*Potential applications of texaphyrins **2.3–2.6** in other fields*

Texaphyrin complexes are colored compounds that absorb in the visible region. Unlike previously reported texaphyrins, new complexes **2.3–2.6** contain carboxylate and sulfonate groups in their side chains. These functional groups can potentially be used to anchor texaphyrin complexes on solid surfaces. Hence, the synthesis of these texaphyrins with different metal ions and the investigation of them as dye sensitizers for energy conversion would be an interesting study.

APPENDIX A

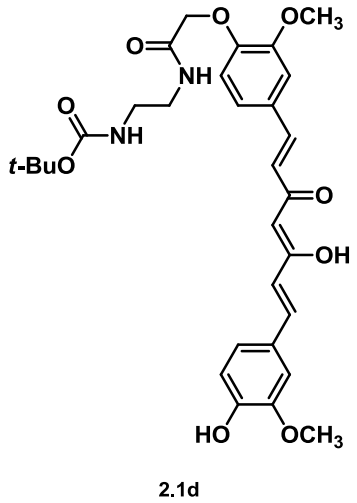

2.1d

^{1}H NMR spectrum

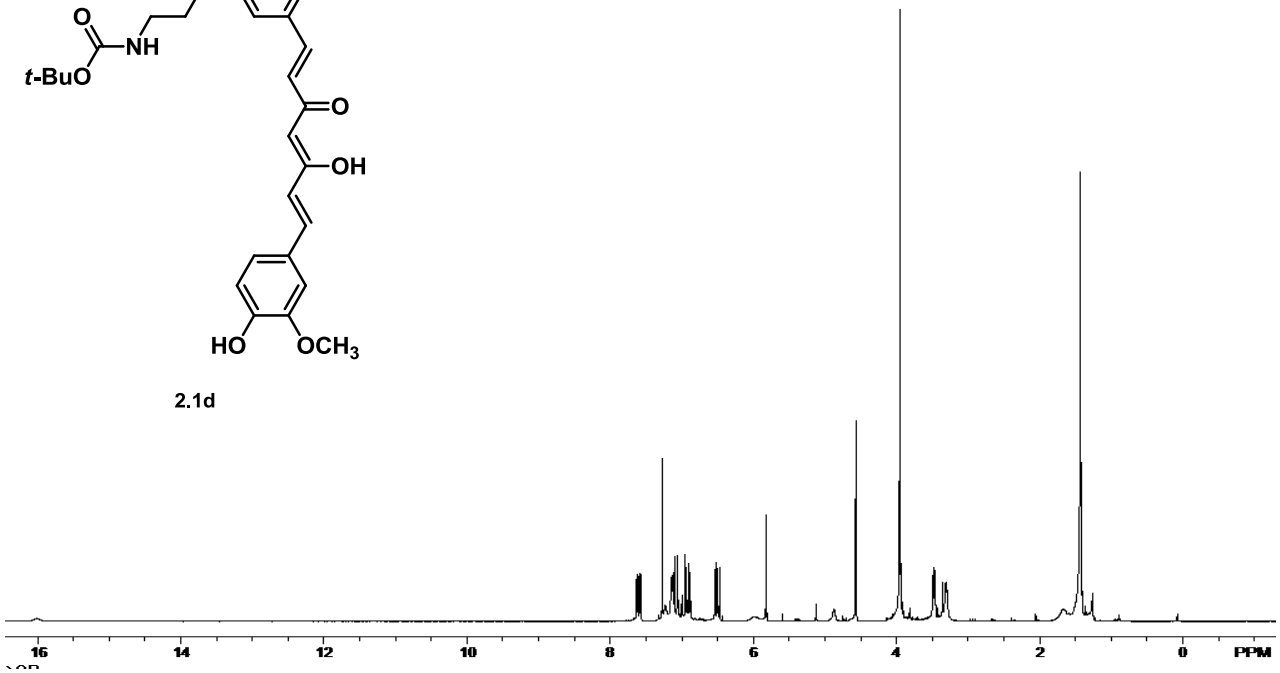

^{13}C NMR spectrum

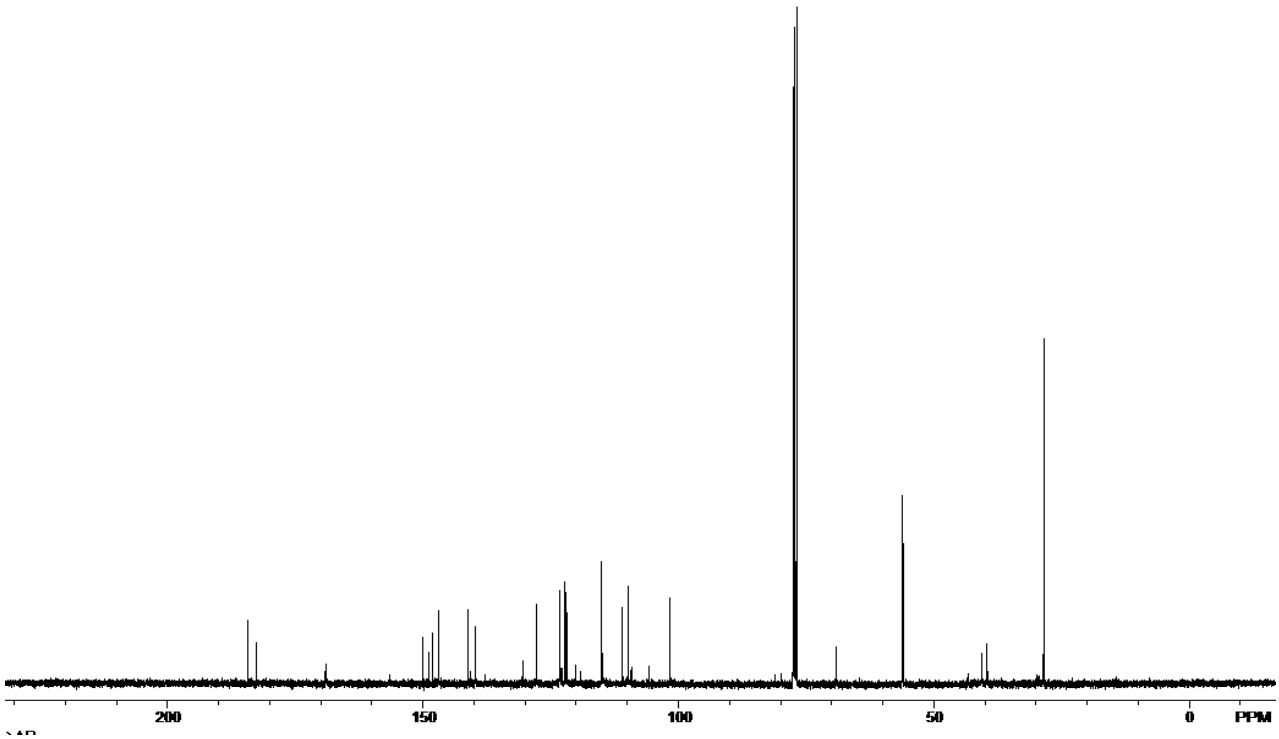

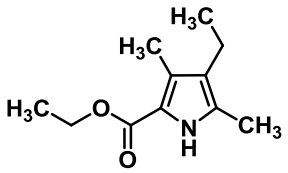

2.3a precursor

^{1}H NMR spectrum

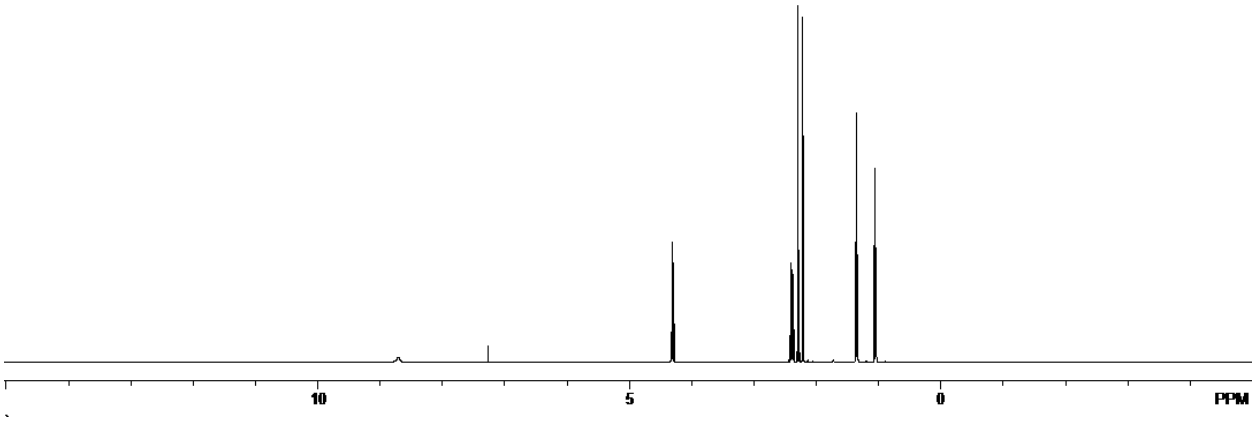

^{13}C NMR spectrum

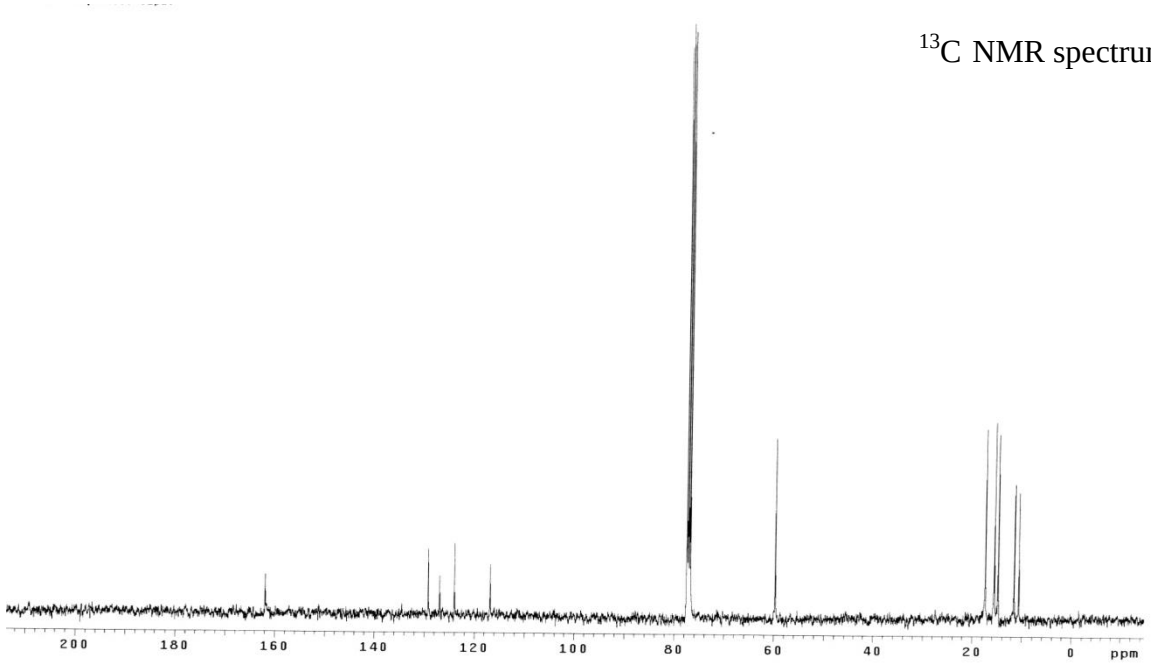

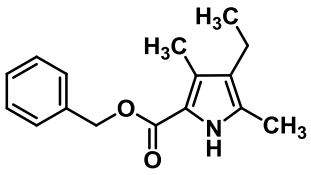

2.3a

^{1}H NMR spectrum

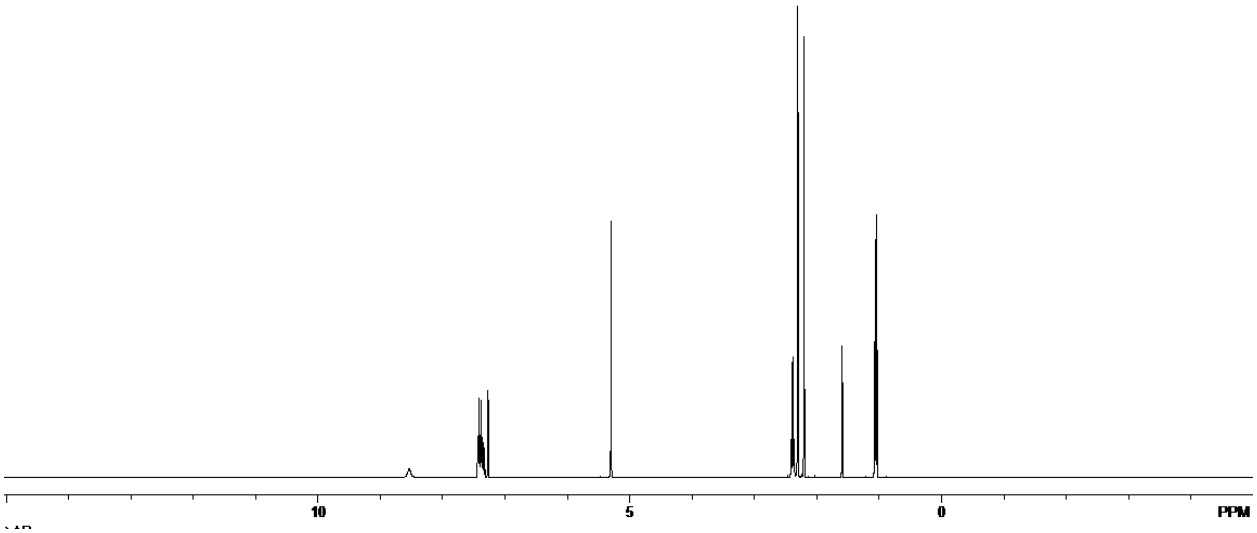

^{13}C NMR spectrum

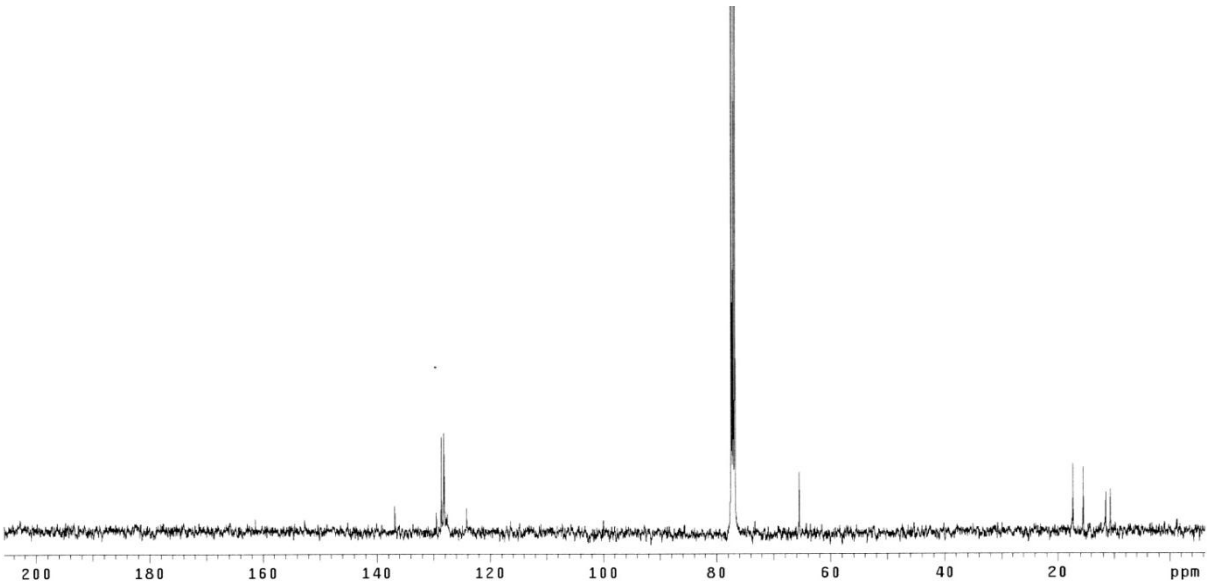

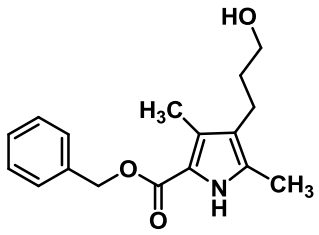

2.4a precursor

^{1}H NMR spectrum

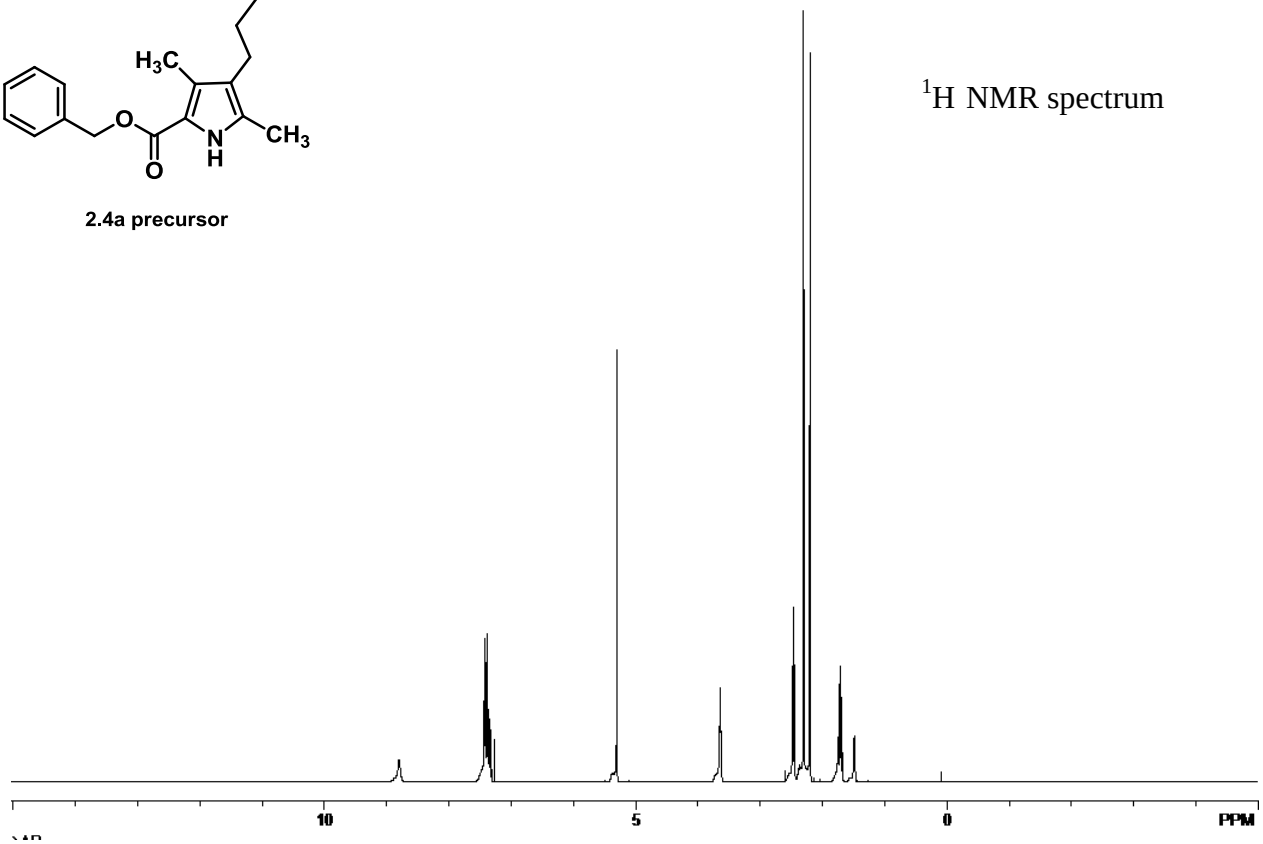

^{13}C NMR spectrum

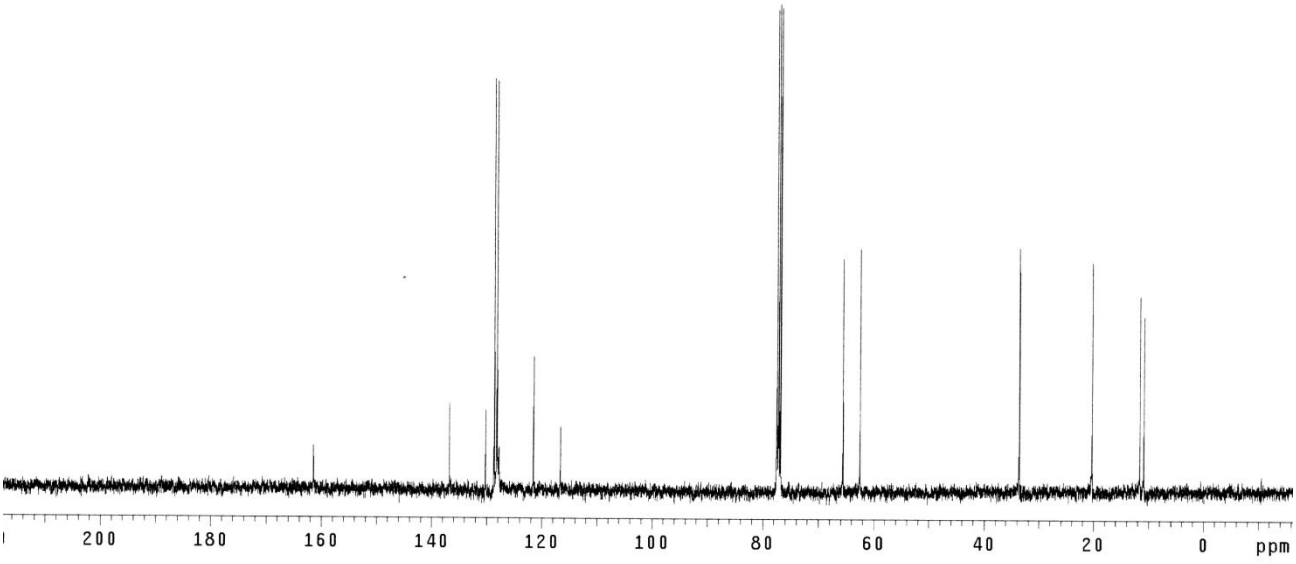

2.4a

^{1}H NMR spectrum

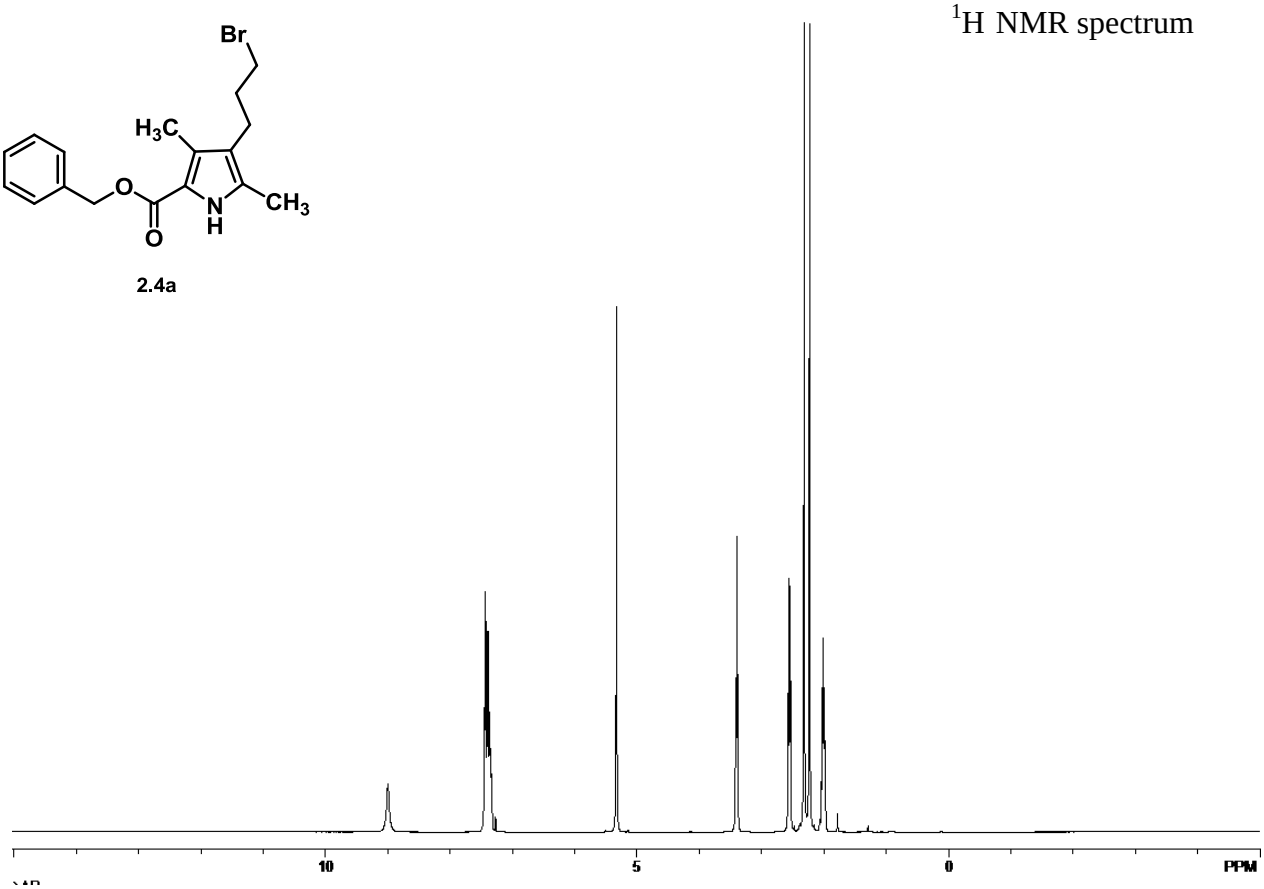

^{13}C NMR spectrum

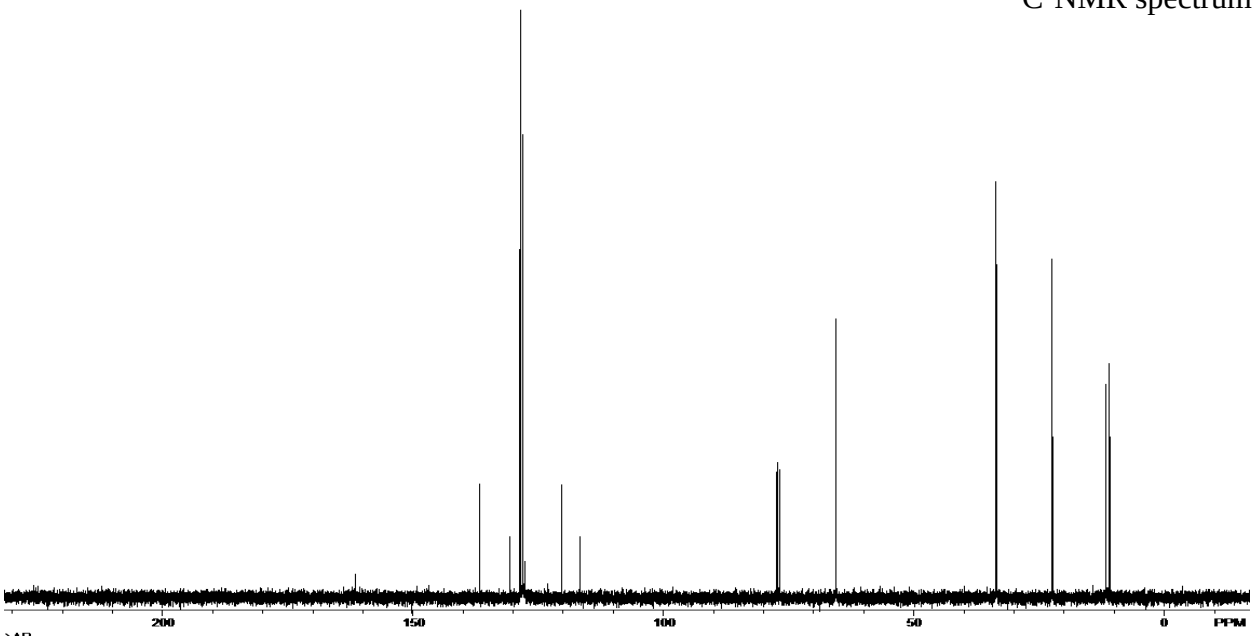

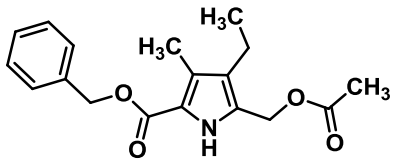

2.3b

^{1}H NMR spectrum

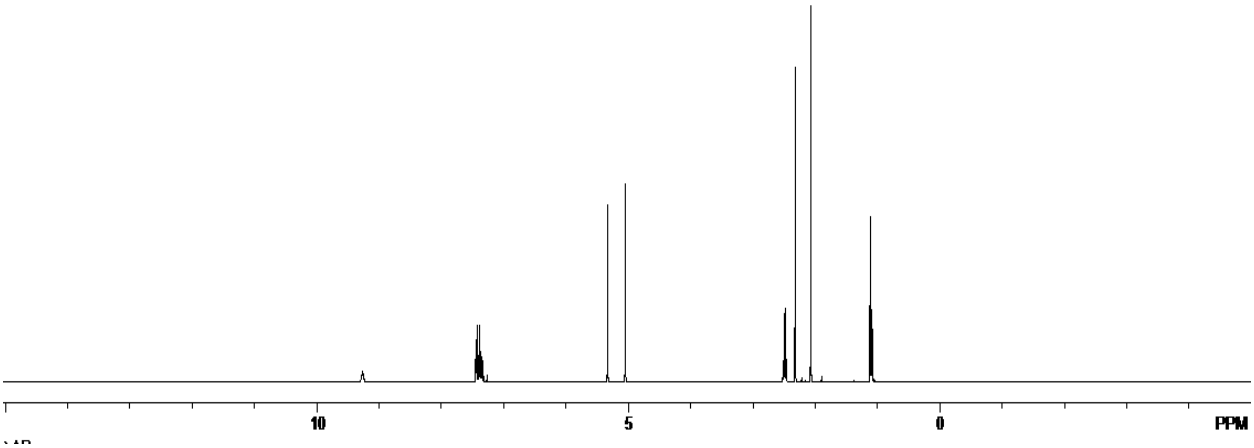

^{13}C NMR spectrum

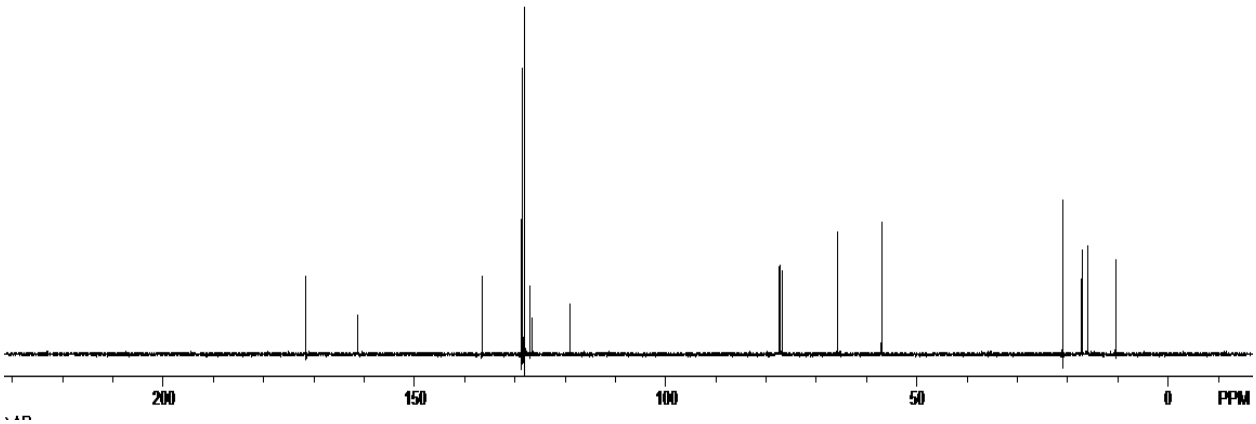

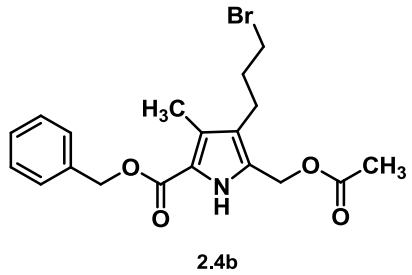

2.4b

^{1}H NMR spectrum

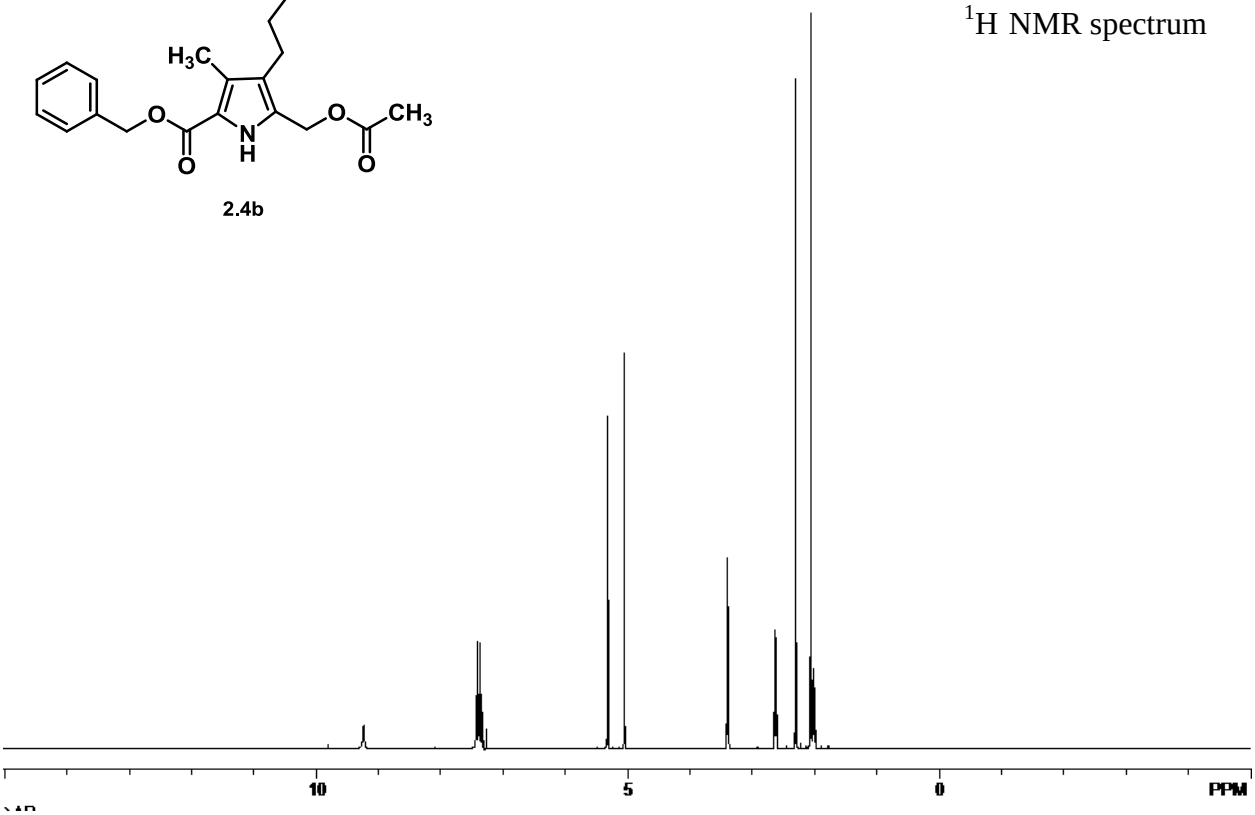

^{13}C NMR spectrum

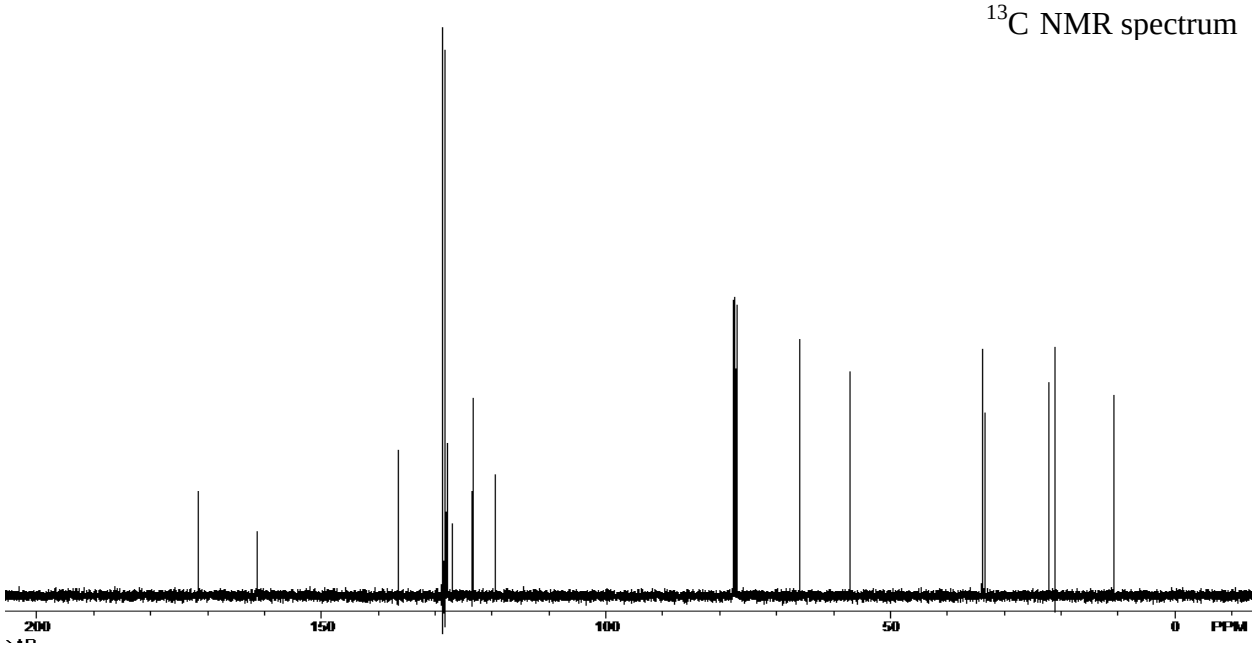

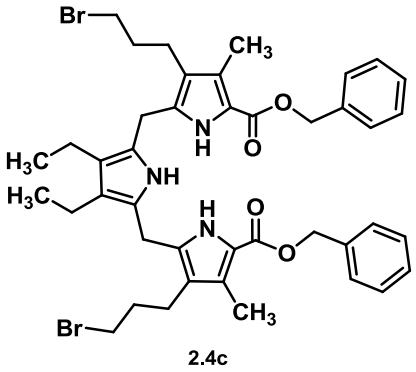

2.4c

^{1}H NMR spectrum

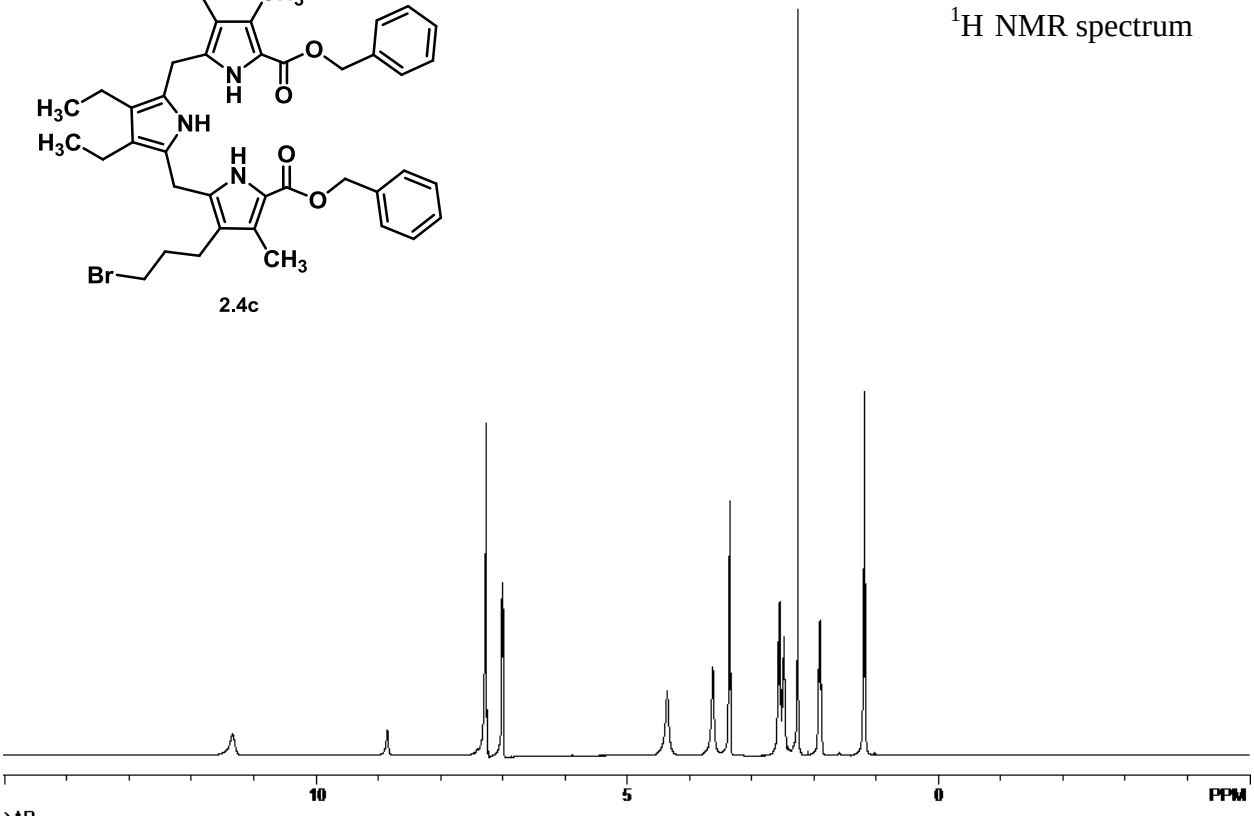

^{13}C NMR spectrum

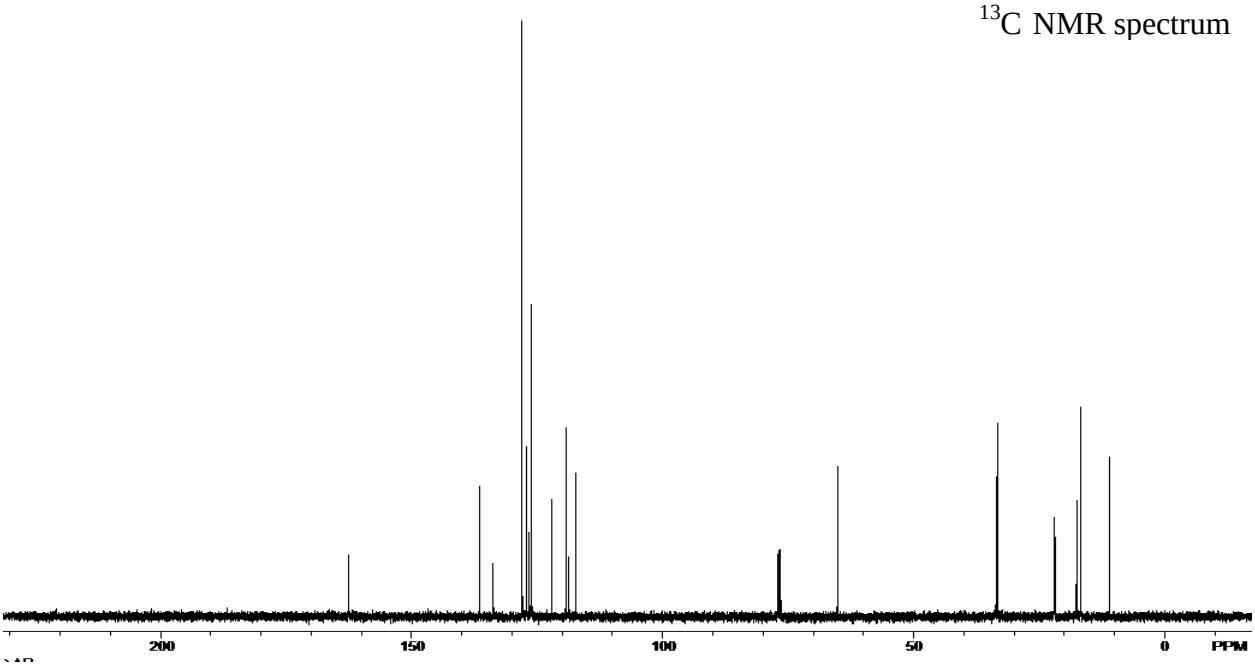

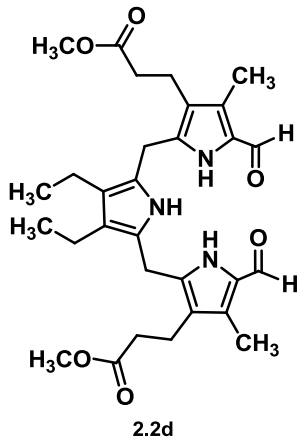

2.2d

^{1}H NMR spectrum

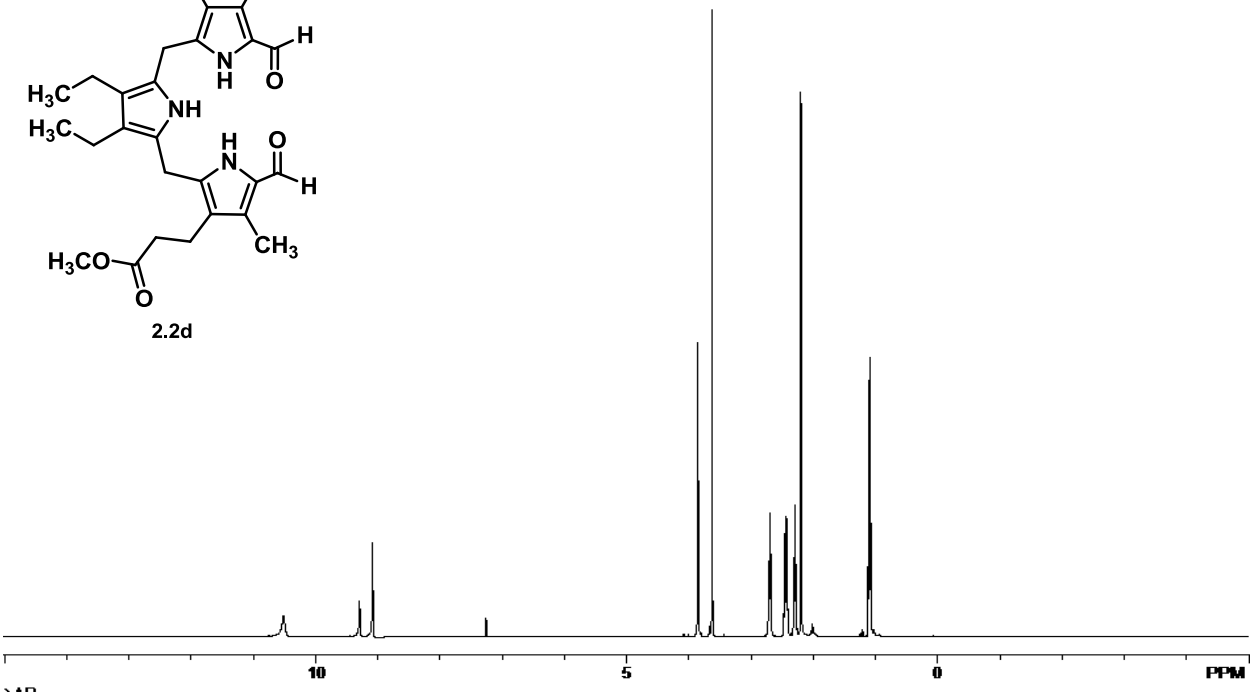

^{13}C NMR spectrum

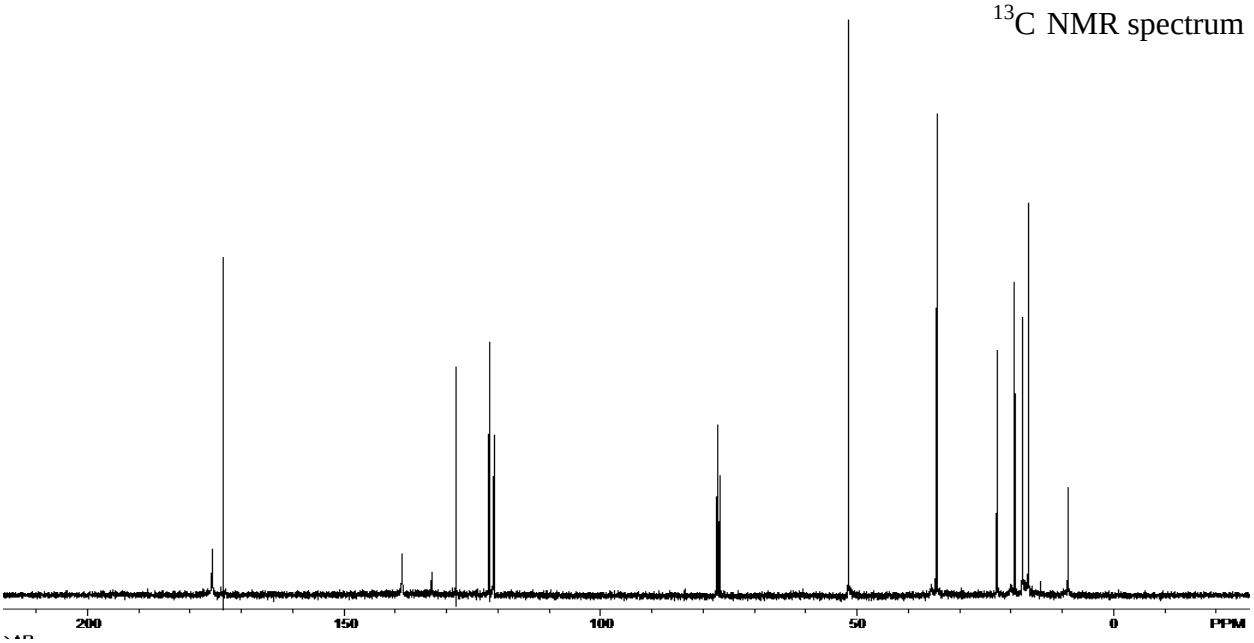

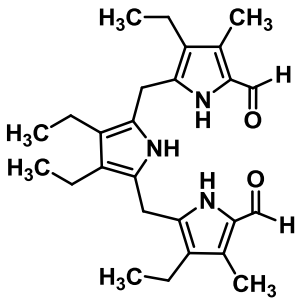

2.3d

^{1}H NMR spectrum

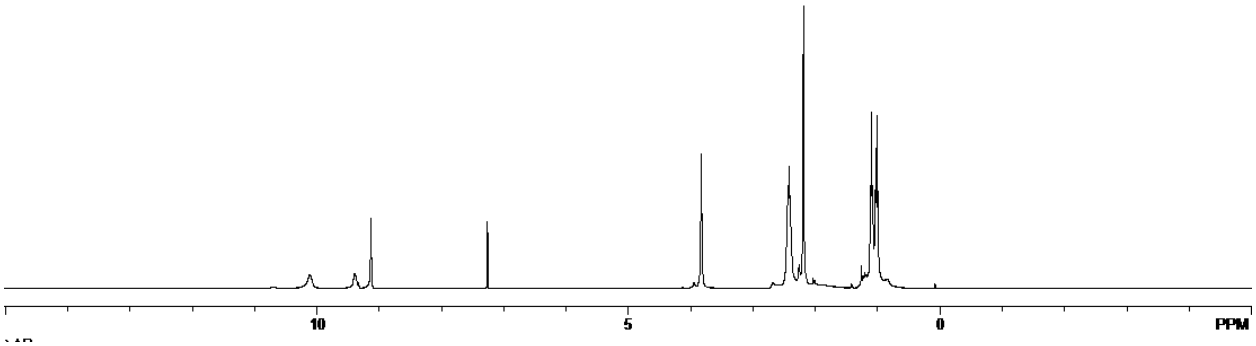

^{13}C NMR spectrum

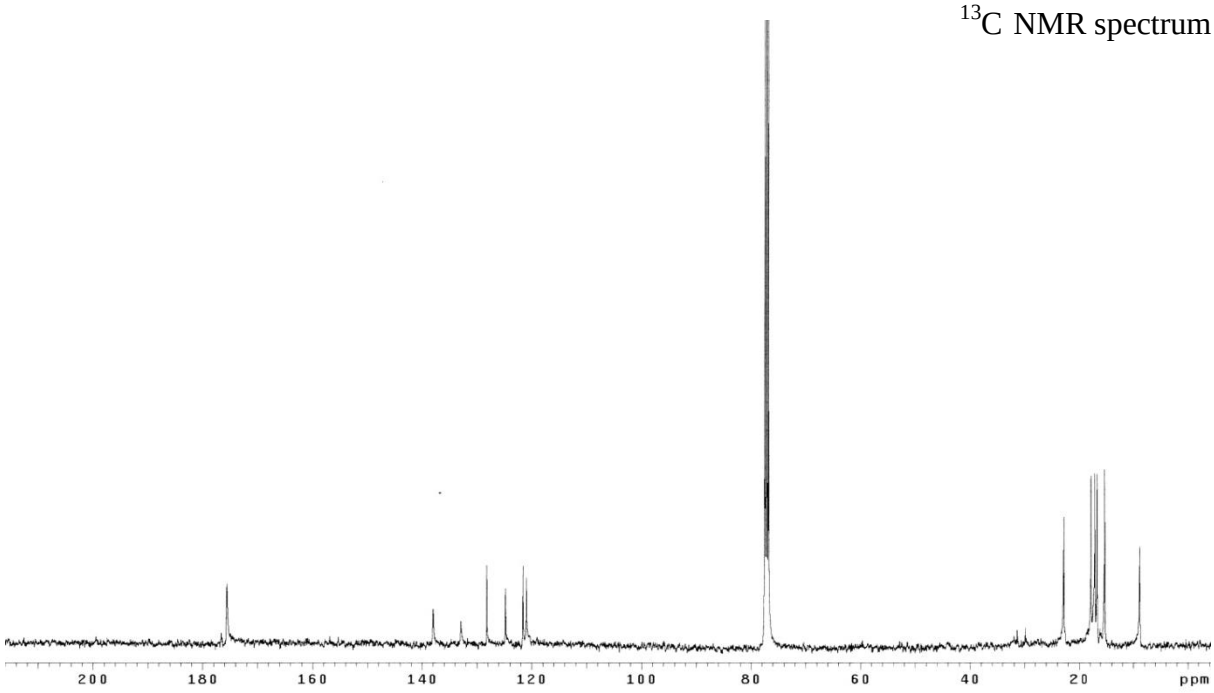

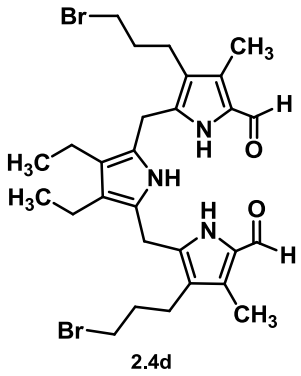

2.4d

^{1}H NMR spectrum

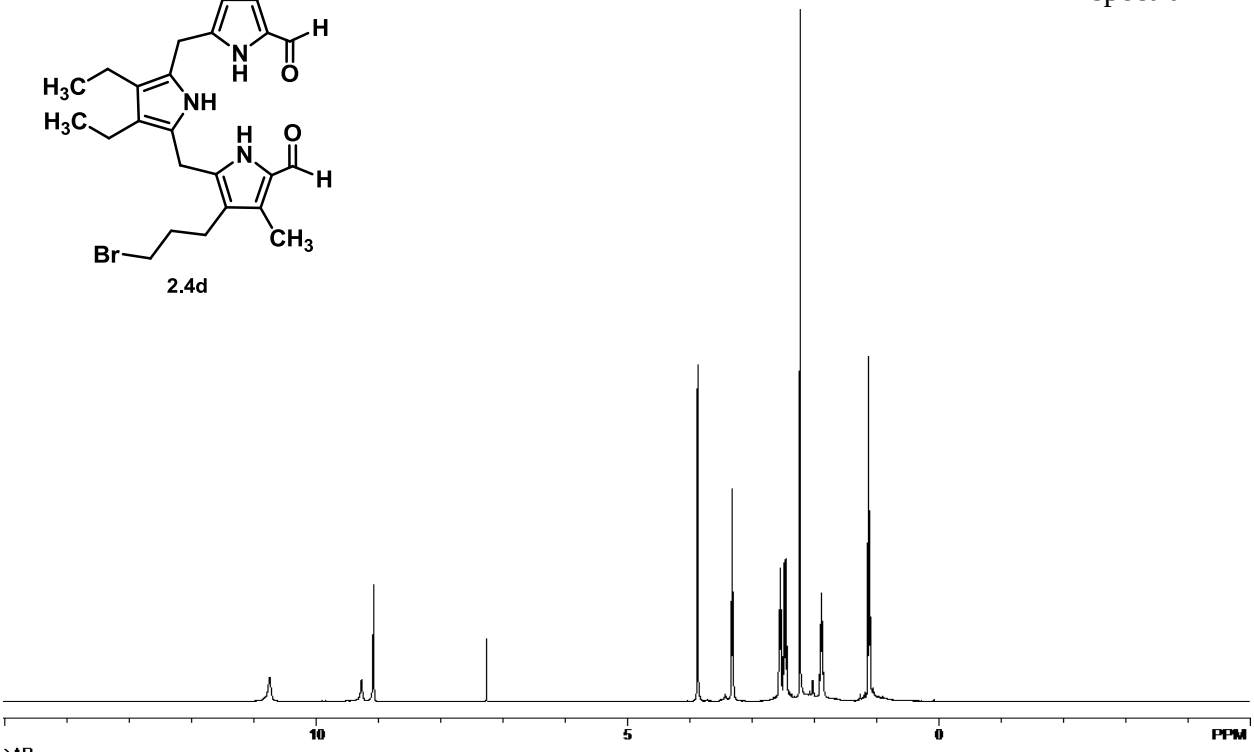

^{13}C NMR spectrum

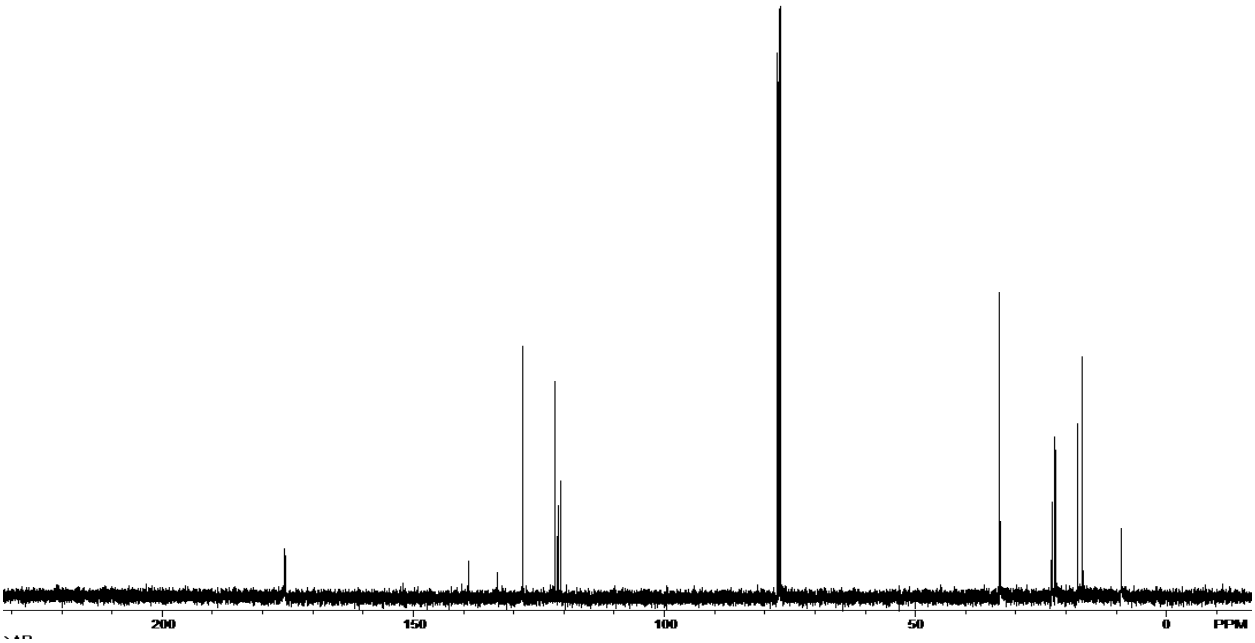

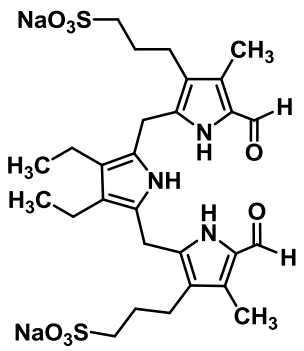

2.5d

^{1}H NMR spectrum

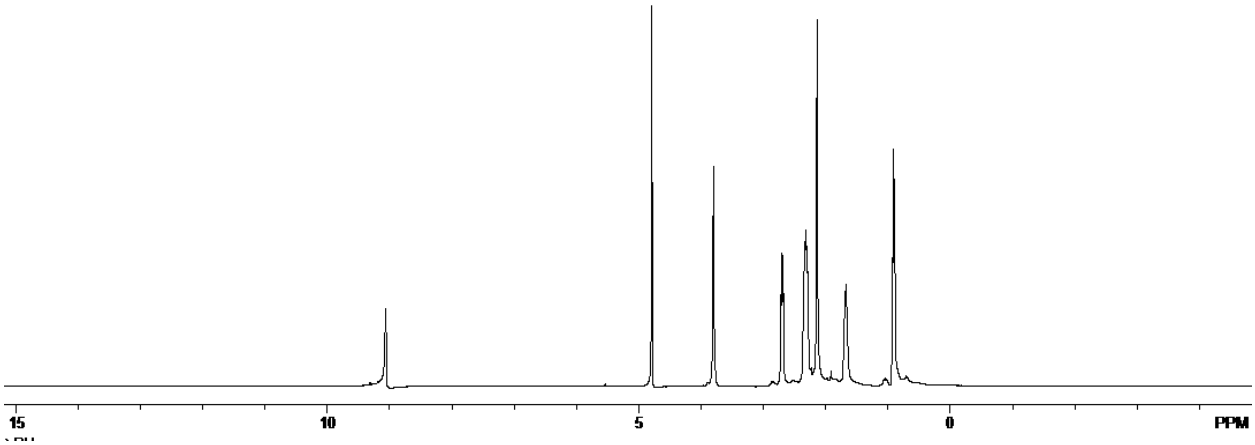

^{13}C NMR spectrum

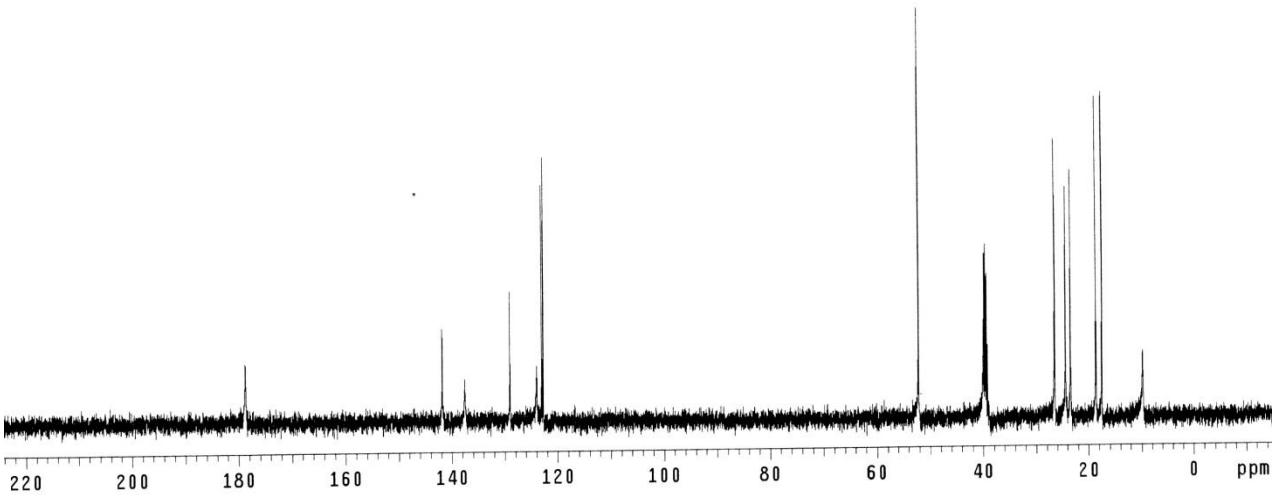

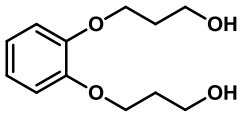

2.2e

^{1}H NMR spectrum

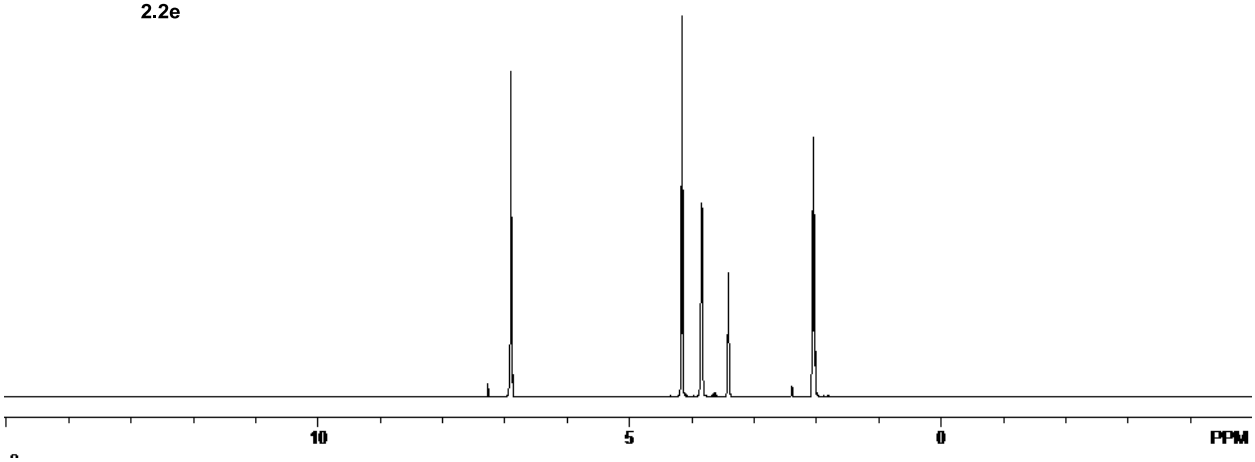

^{13}C NMR spectrum

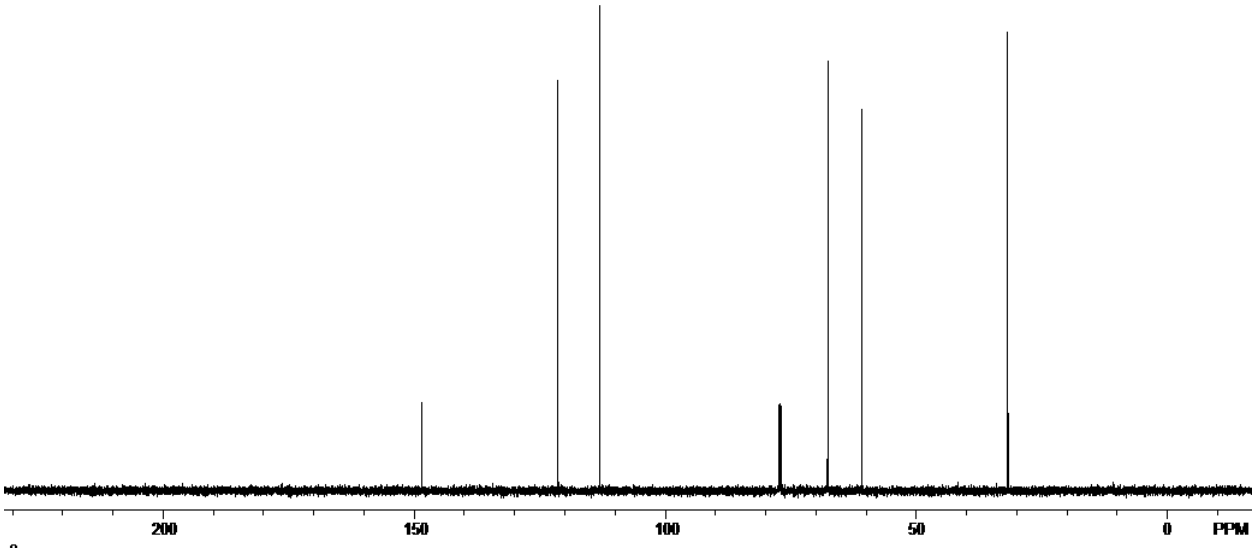

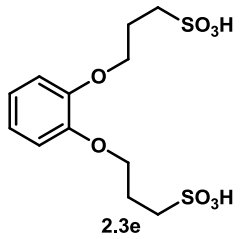

2.3e

^{1}H NMR spectrum

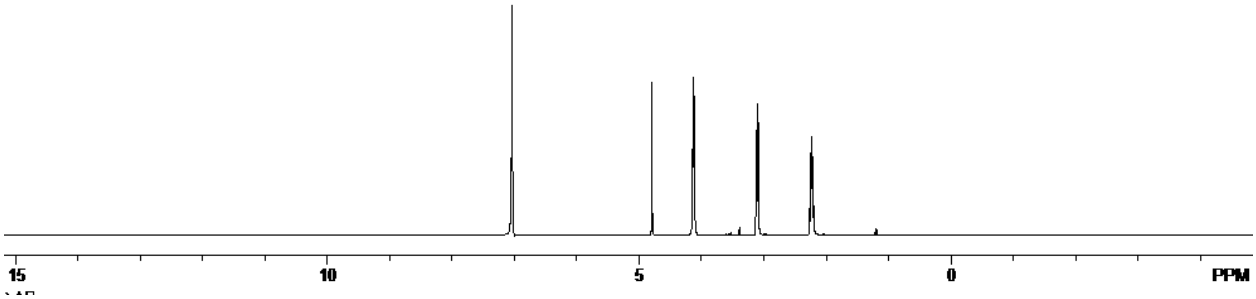

^{13}C NMR spectrum

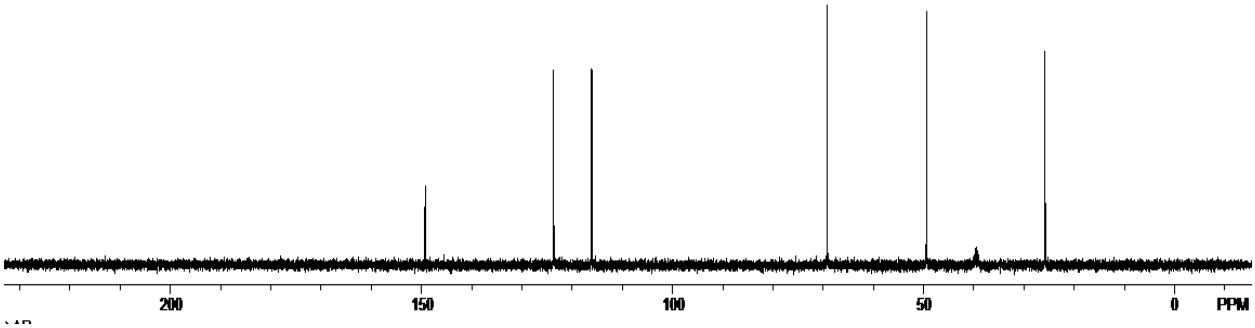

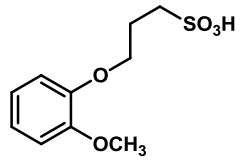

2.4e

^{1}H NMR spectrum

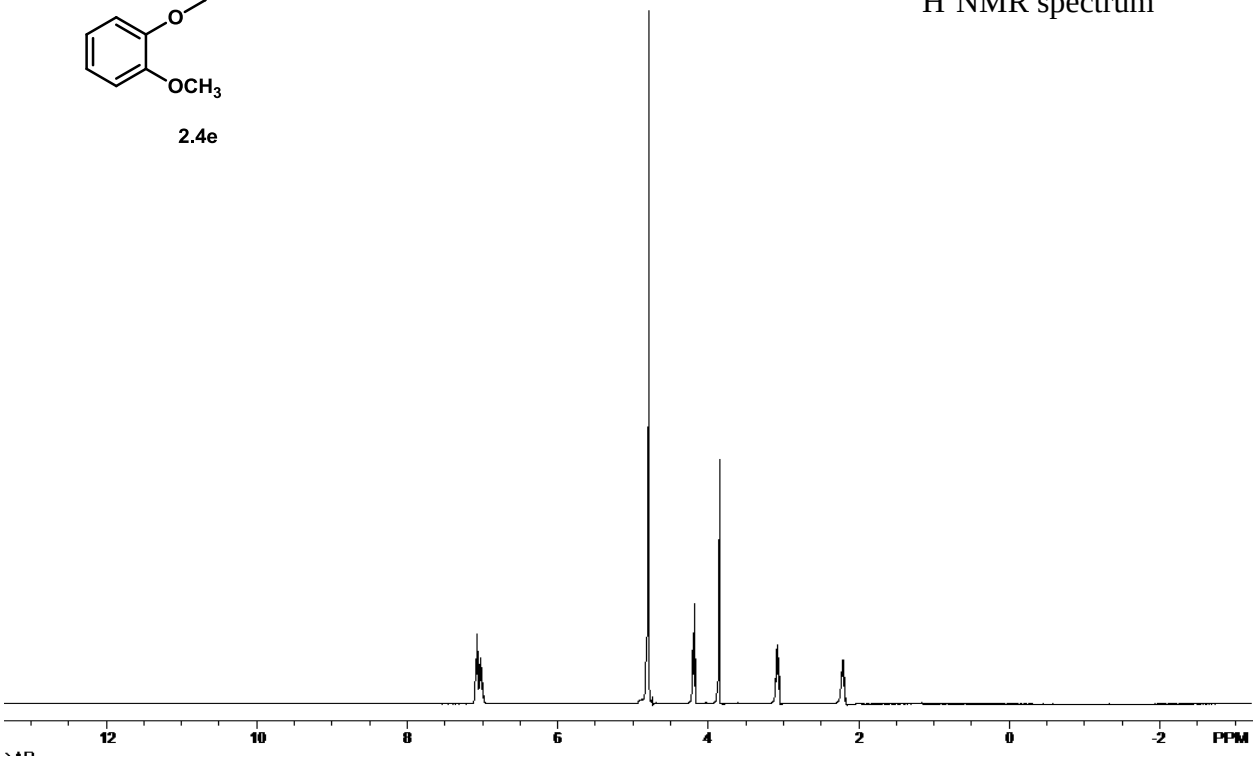

^{13}C NMR spectrum

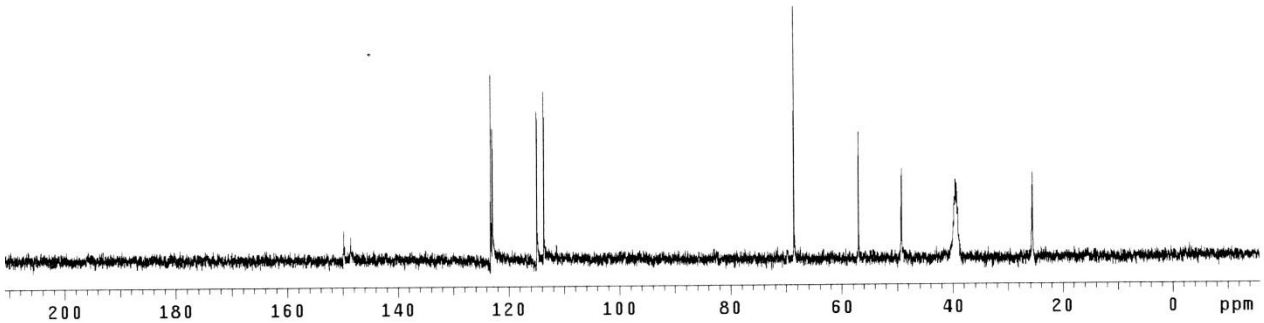

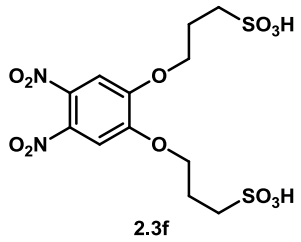

2.3f

^{1}H NMR spectrum

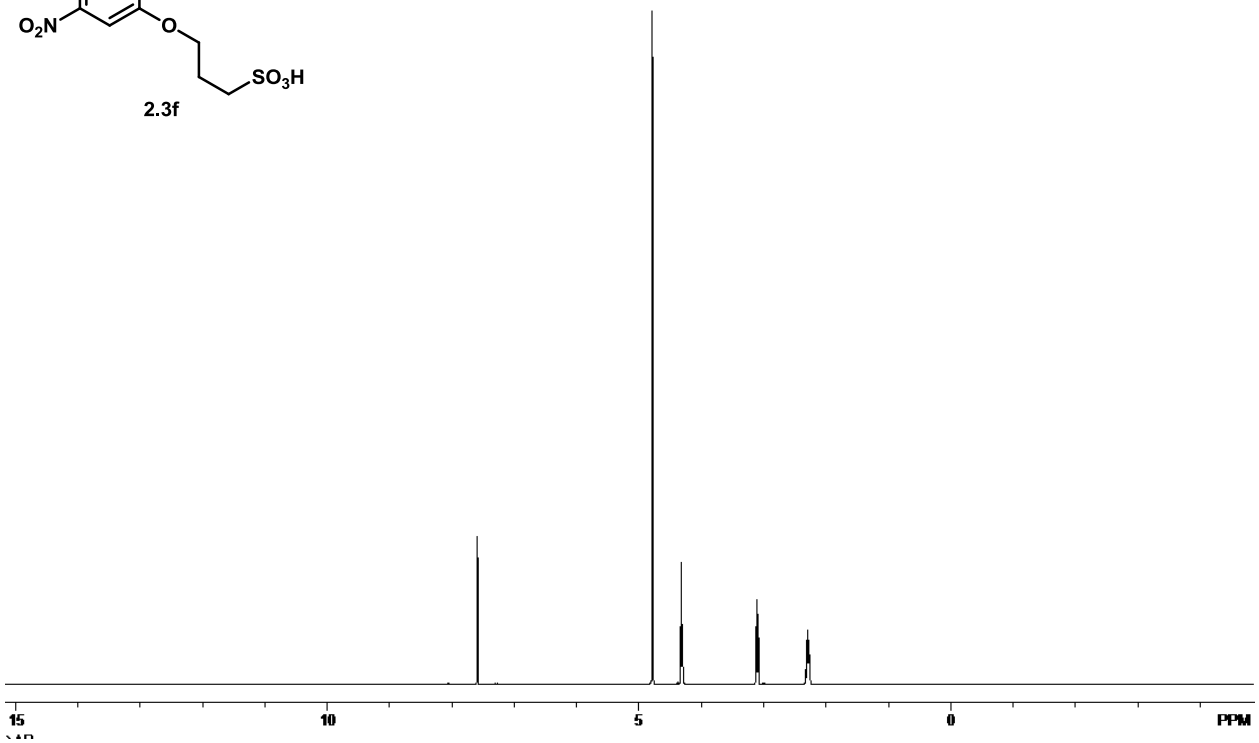

^{13}C NMR spectrum

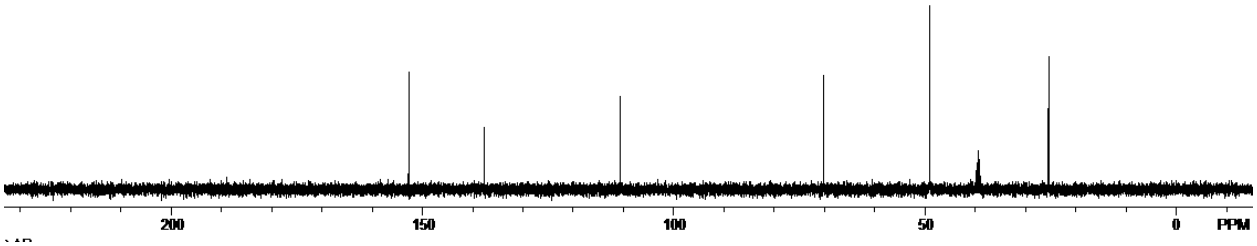

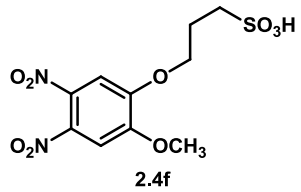

2.4f

^{1}H NMR spectrum

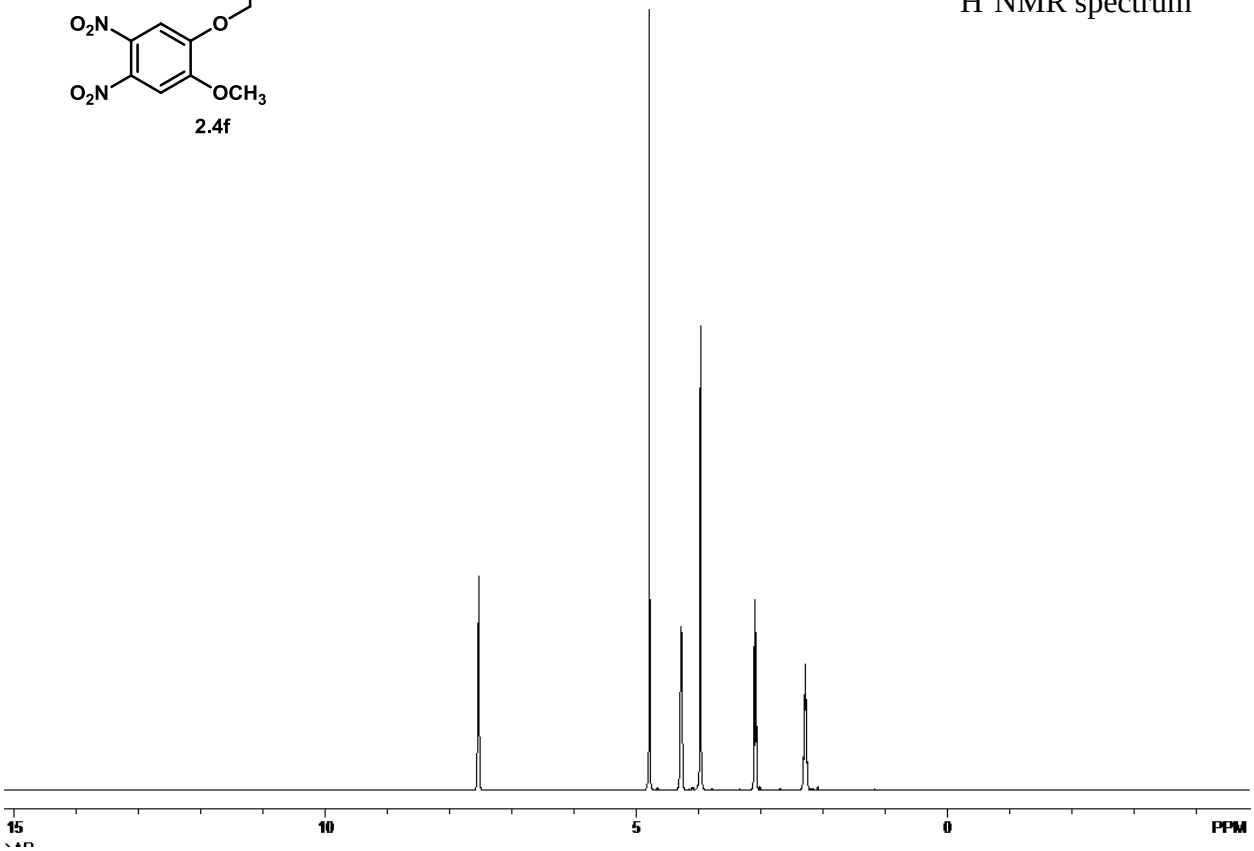

^{13}C NMR spectrum

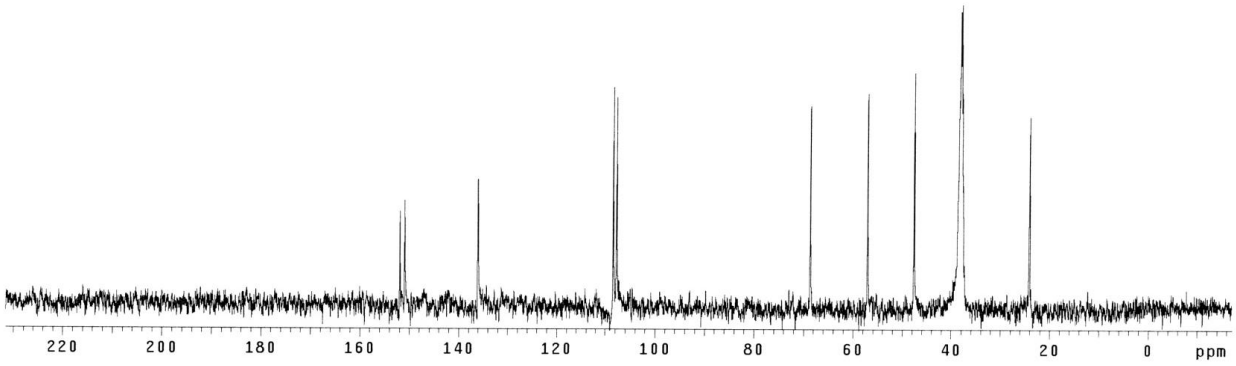

2.2g

^{1}H NMR spectrum

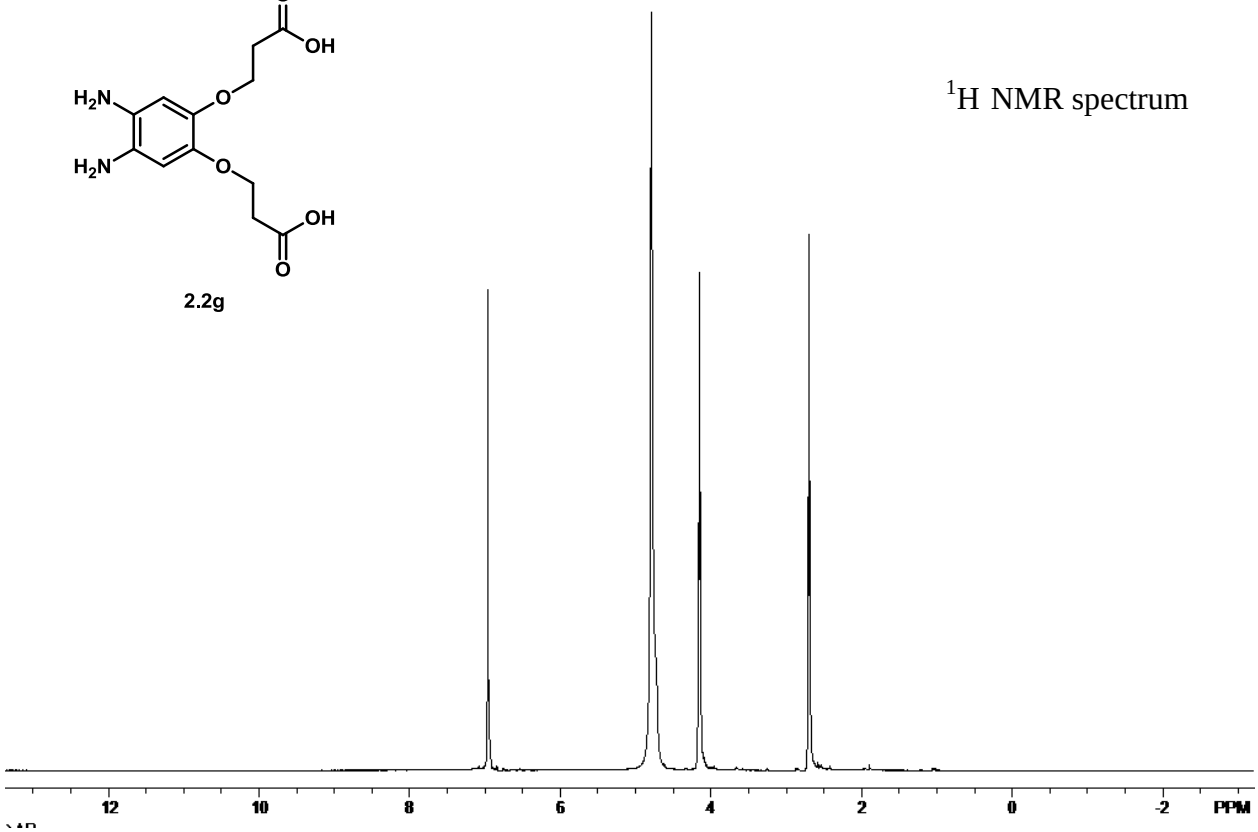

^{13}C NMR spectrum

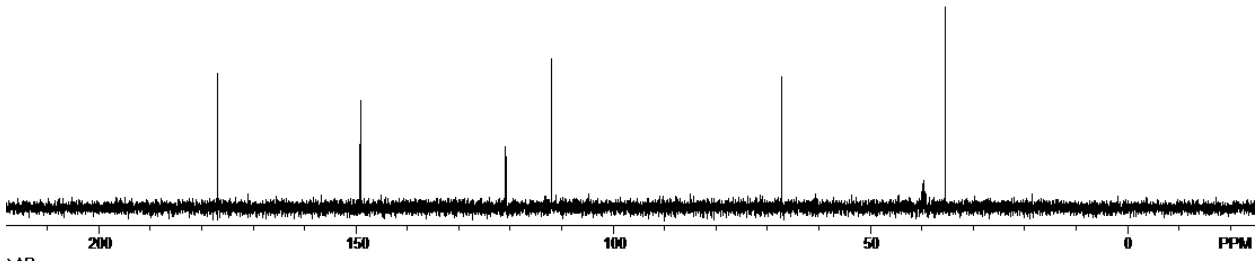

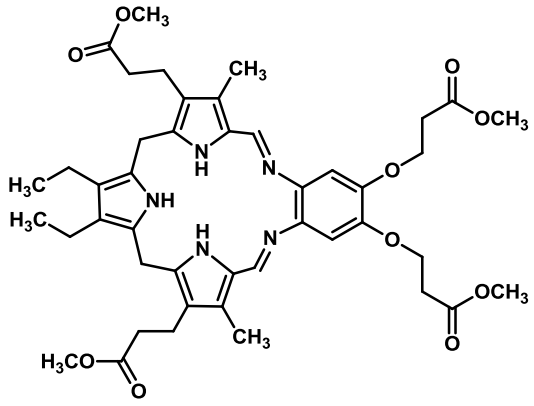

2.2L

^{1}H NMR spectrum

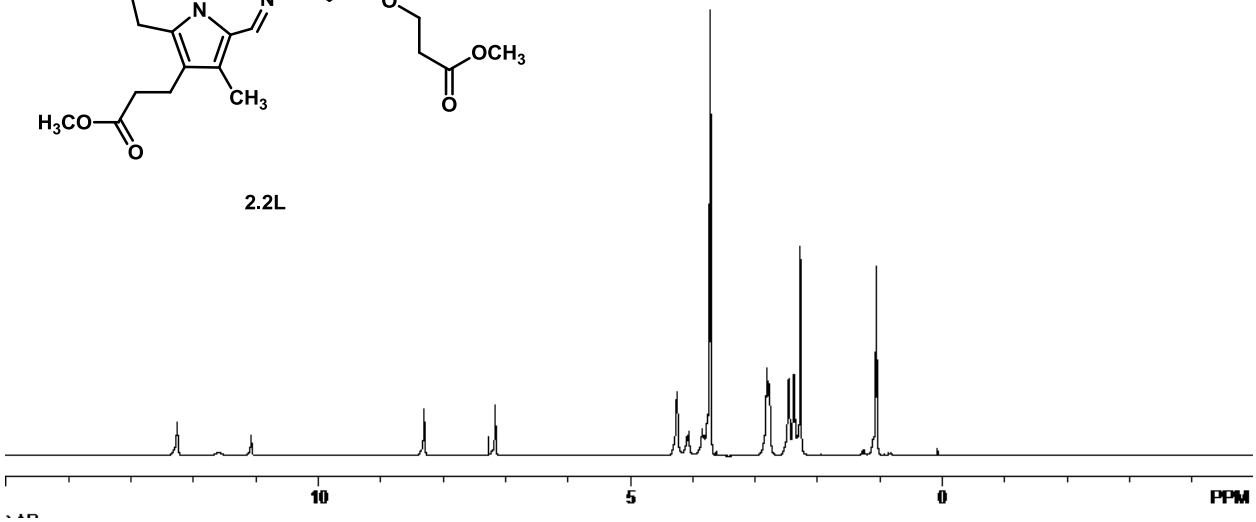

^{13}C NMR spectrum

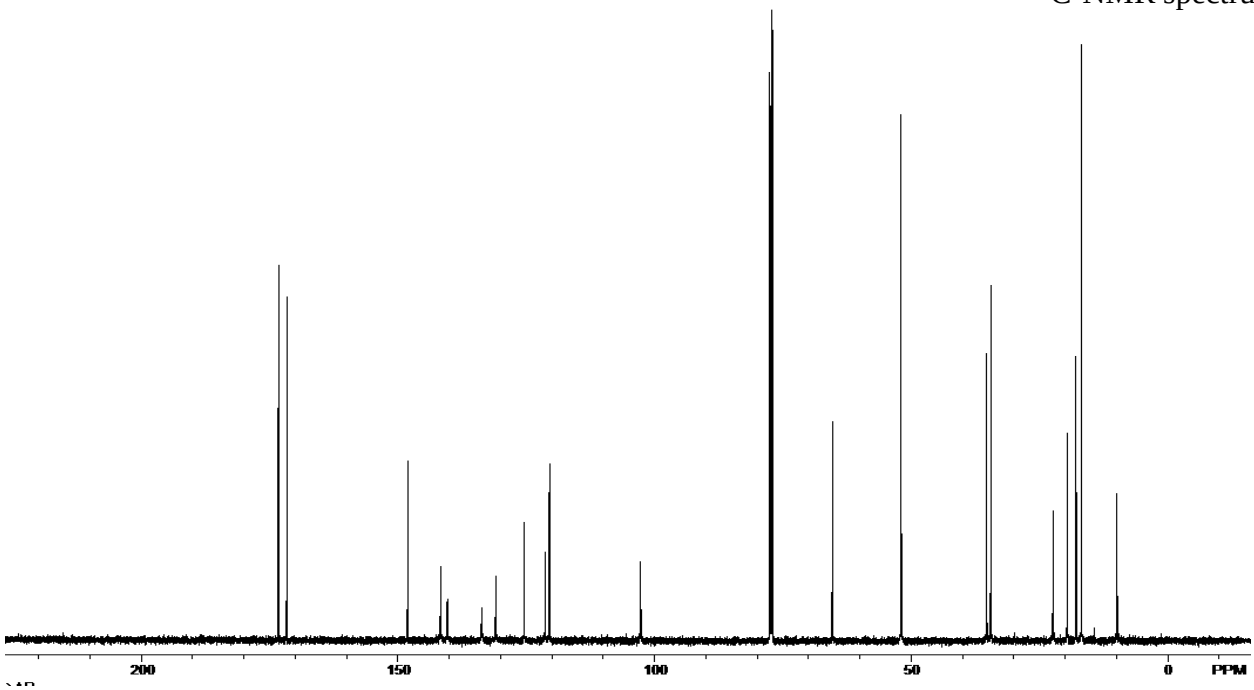

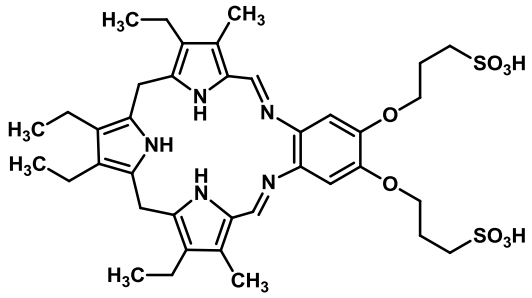

2.4L

^{1}H NMR spectrum

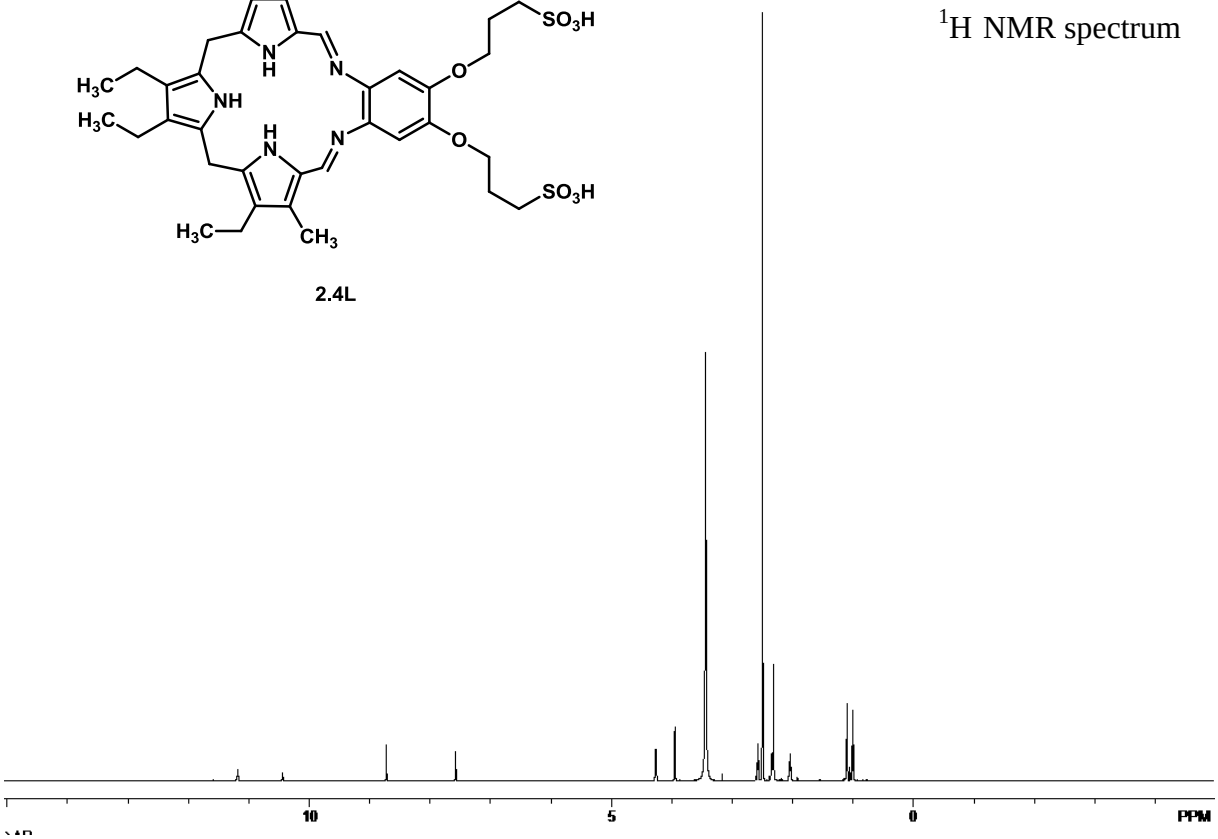

^{13}C NMR spectrum

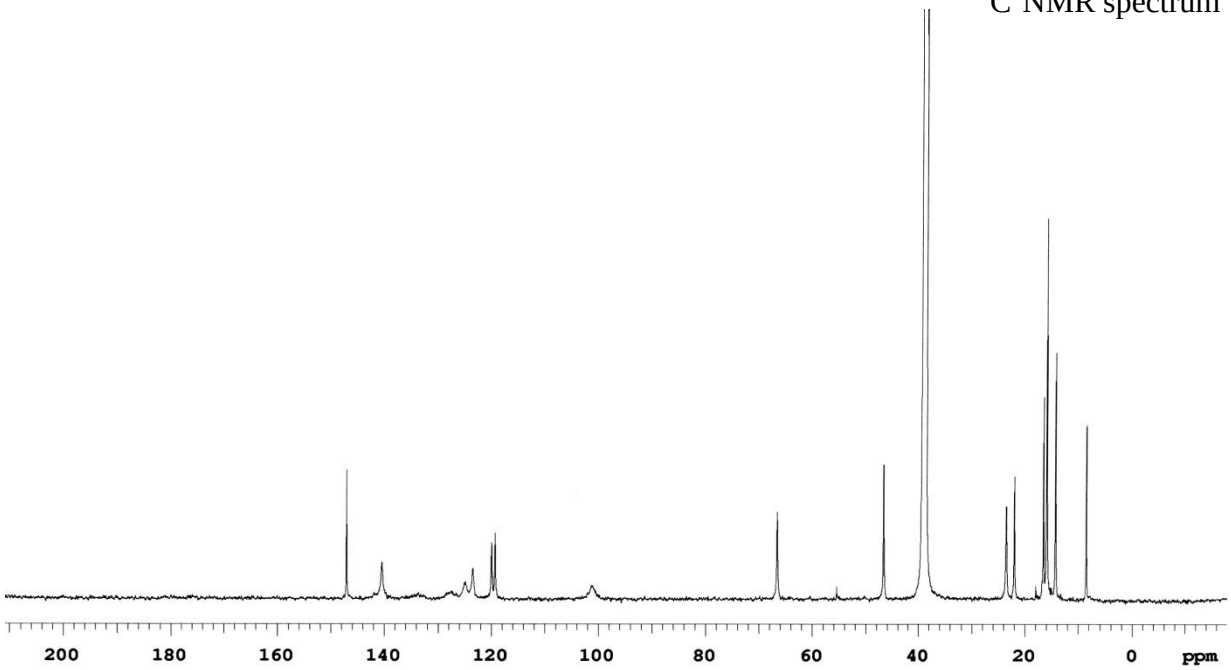

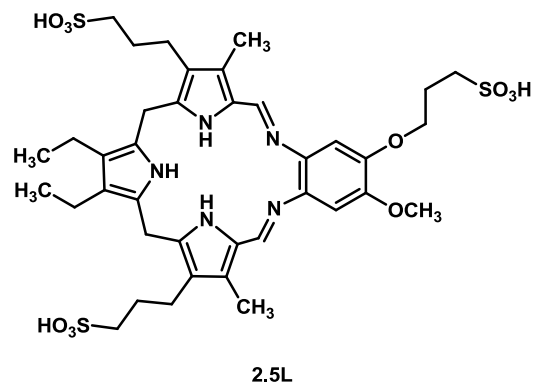

2.5L

^{1}H NMR spectrum

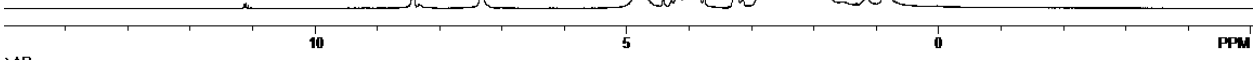

^{13}C NMR spectrum

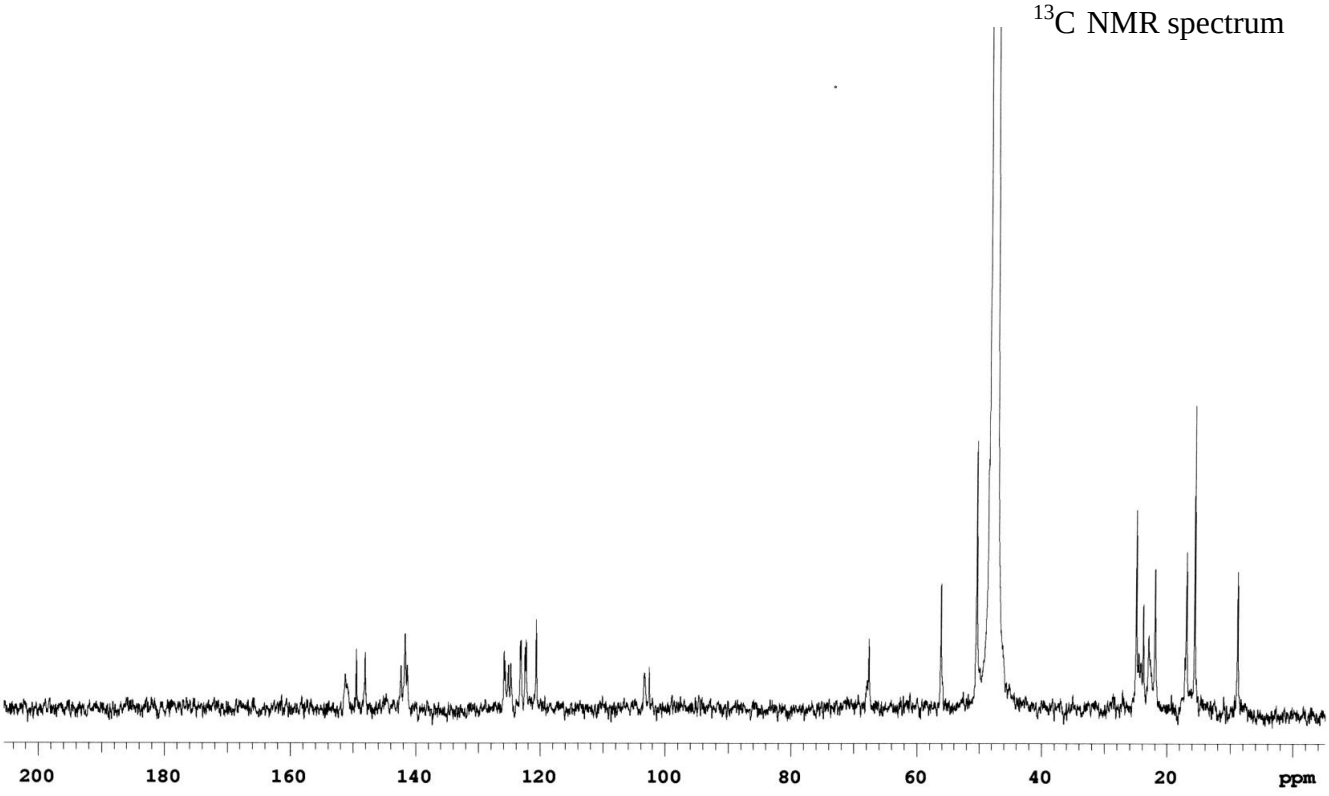

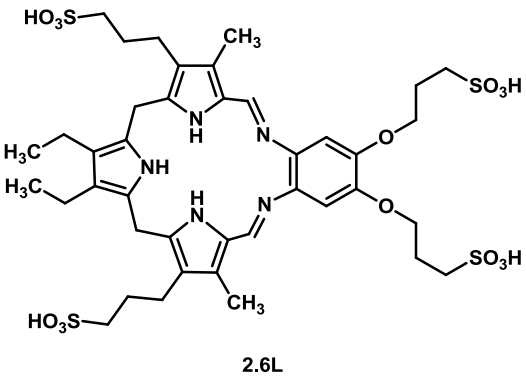

2.6L

^{1}H NMR spectrum

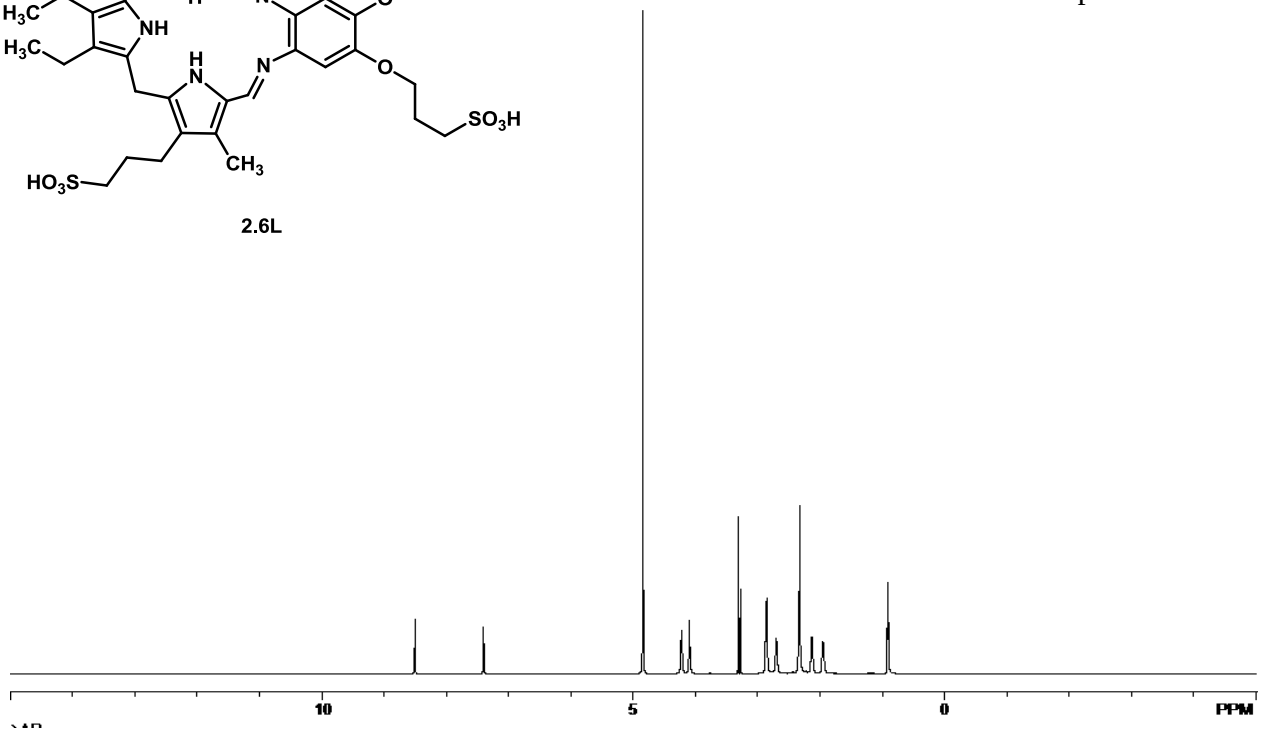

^{13}C NMR spectrum

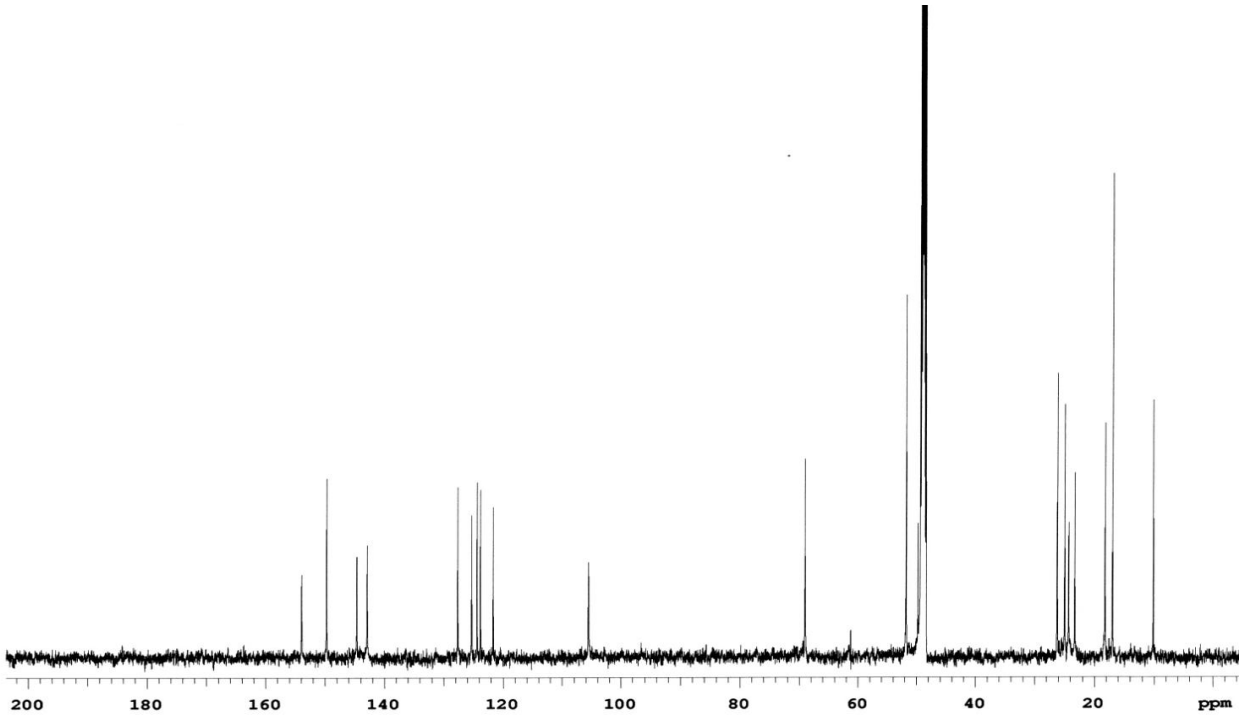

APPENDIX B

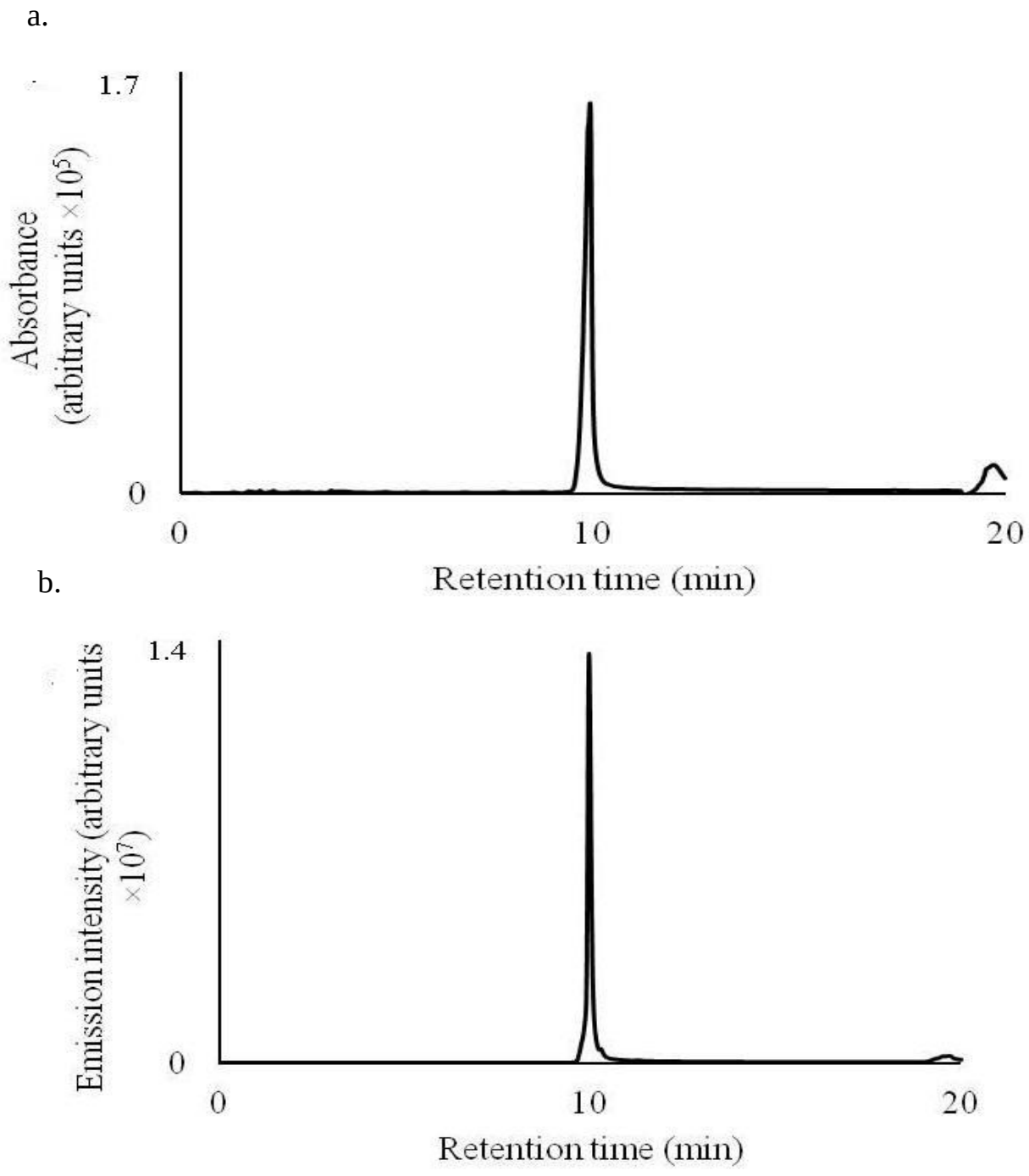

Figure B.1. HPLC Chromatogram of conjugate **2.1**. a. detected using a photodiode array (254 nm trace shown) and b. Detected using a fluorescence detector (λ_{ex} = 395 nm and λ_{em} = 521 nm).

a.

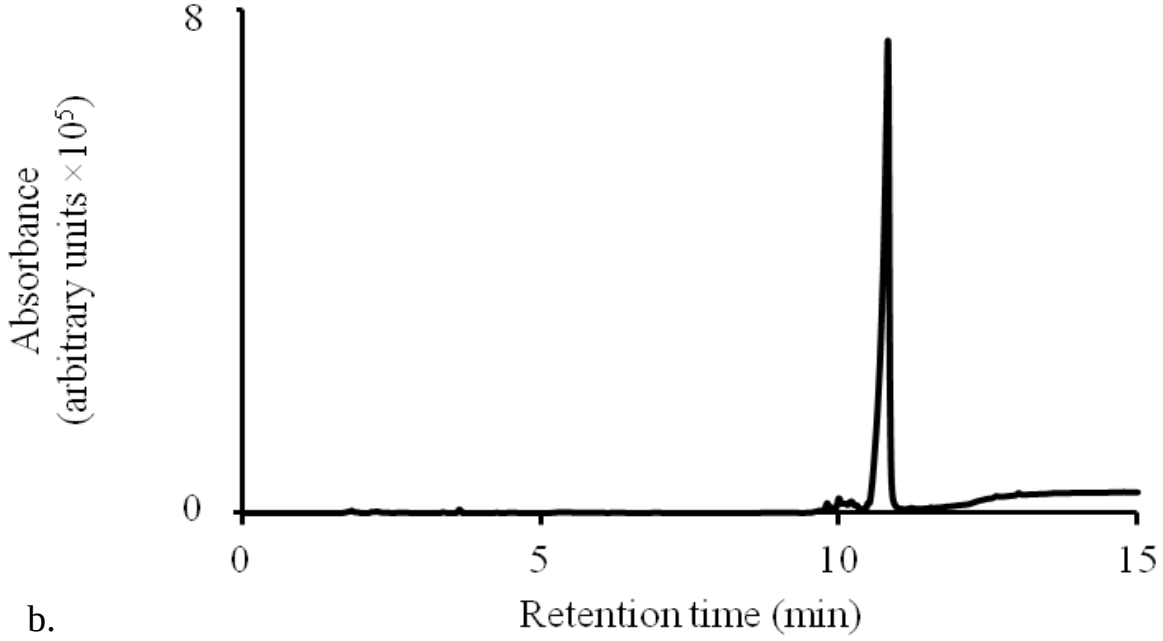

b.

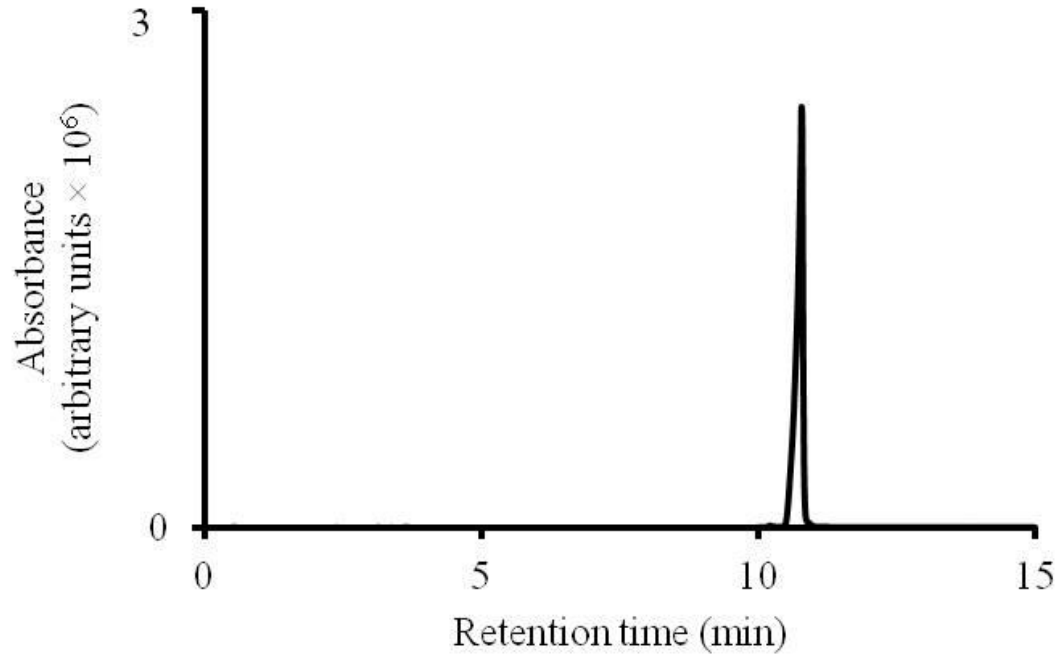

Figure B.2. HPLC Chromatogram of conjugate **2.5**. Detected using a photodiode array: a. 210 nm and b. 476 nm traces shown.

a.

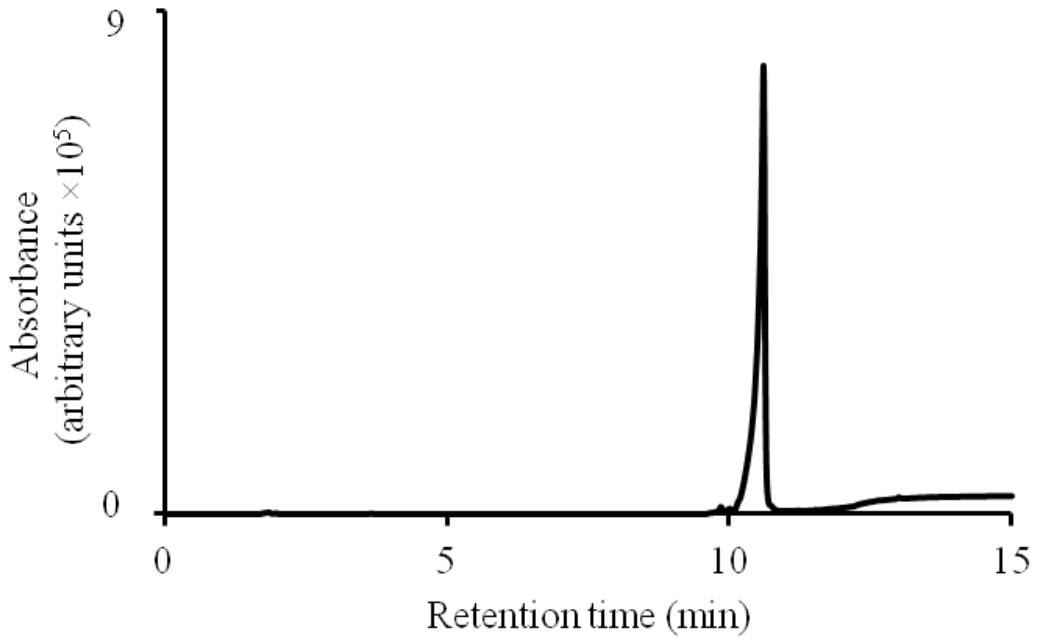

b.

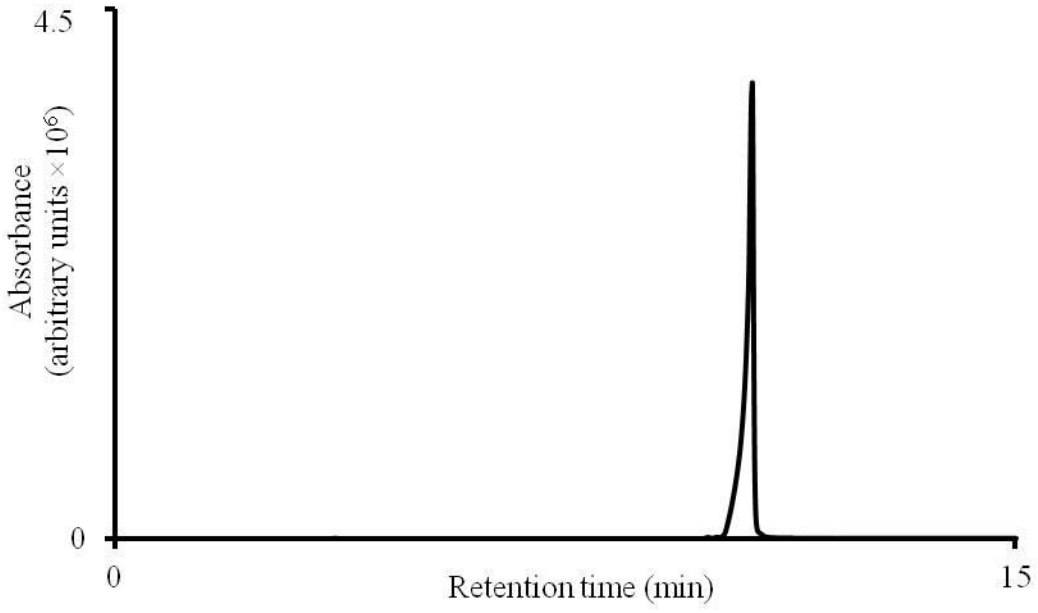

Figure B.3. HPLC Chromatogram of conjugate **2.6**. Detected using a photodiode array: a. 210 nm and b. 476 nm shown.

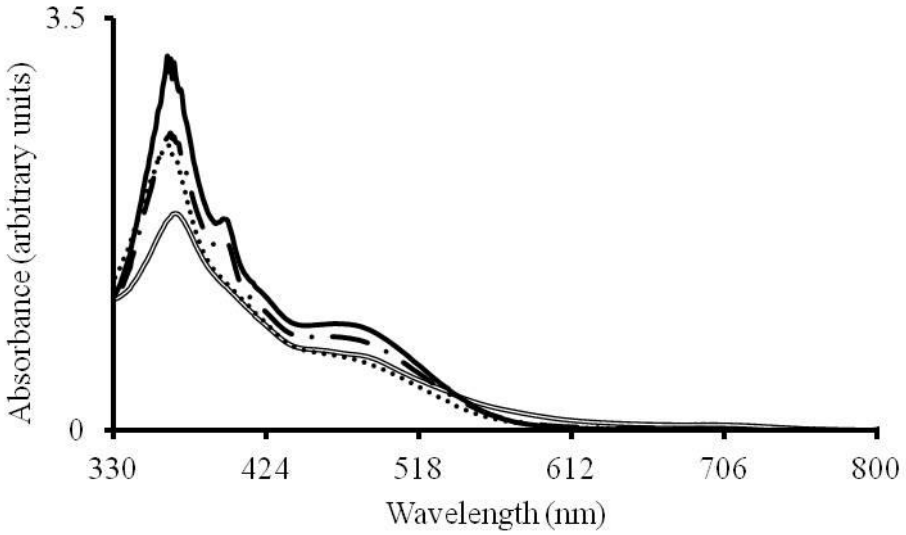

Figure B.4. UV-vis absorption spectra of texaphyrin ligands **2.2L**, **2.4L–2.6L: 2.2L** (…); **2.4L** (=); **2.5L** (· —); and **2.6L** (—).

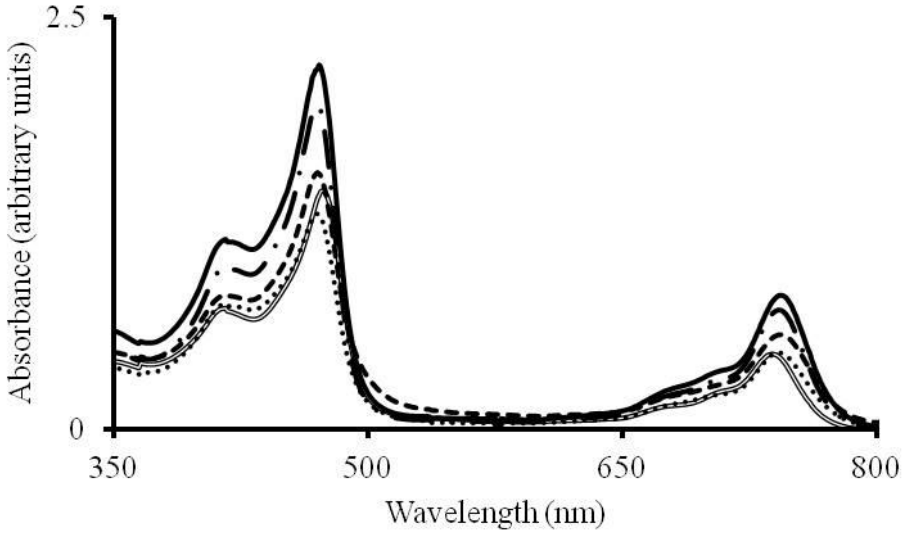

Figure B.5. UV-vis absorption spectra of texaphyrin complexes **2.2–2.6: 2.2** (…); **2.3** (---); **2.4** (=); **2.5** (· —); and **2.6** (—).

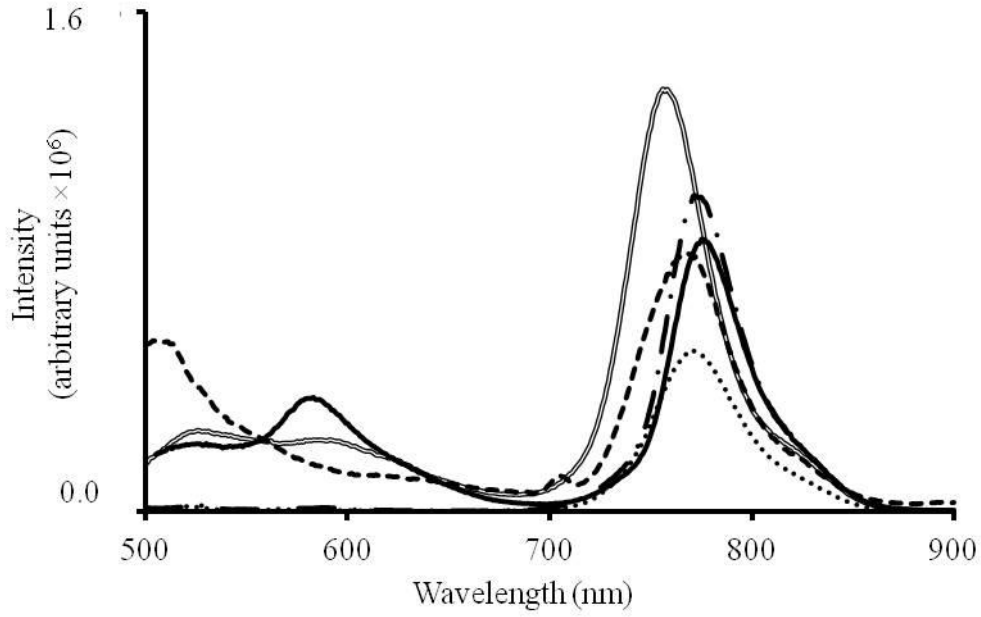

Figure B.6. Emission spectra of texaphyrin complexes **2.2–2.6**: **2.2** (…), λ_{ex} = 485 nm; **2.3** (---), λ_{ex} = 470 nm; **2.4** (=), λ_{ex} = 468 nm; **2.5** (· —), λ_{ex} = 490 nm; and **2.6** (—), λ_{ex} = 492 nm.

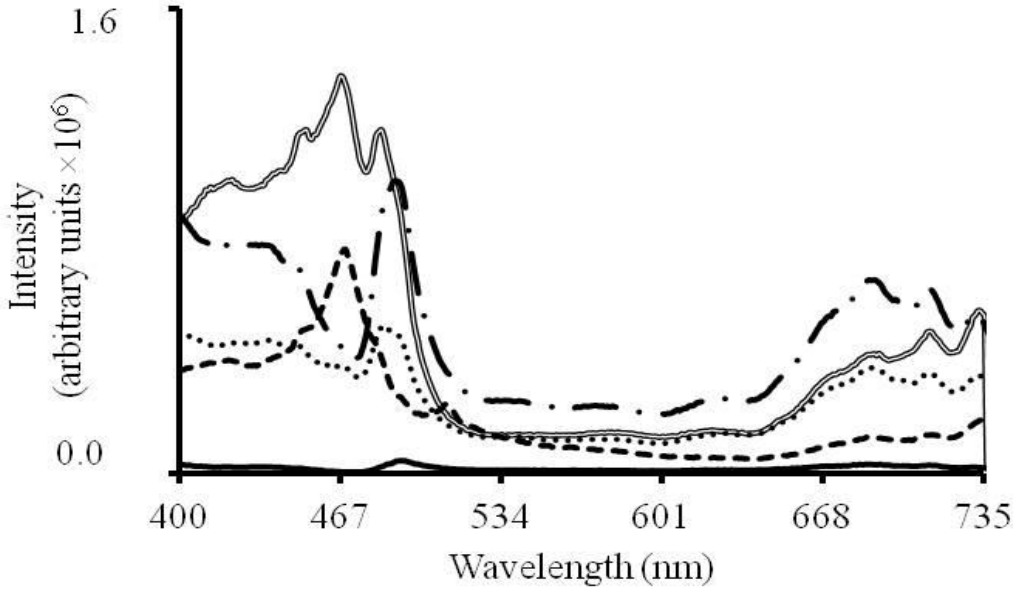

Figure B.7. Excitation spectra of texaphyrin complexes **2.2–2.6**: **2.2** (…), λ_{em} = 772 nm; **2.3** (---), λ_{em} = 767 nm; **2.4** (=), λ_{em} = 757 nm; **2.5** (· —), λ_{em} = 775 nm; and **2.6** (—), λ_{em} = 775 nm.

Table B.1 Texaphyrin **2.2** relaxation time measurements (trial 1).

Concentration (mM)	T_1 (s)	$1/T_1$ (s^{-1})
0.55	0.092	10.9
0.28	0.176	5.68
0.14	0.350	2.86
0.07	0.629	1.59
0.00	2.913	0.340

Table B.2 Texaphyrin **2.2** relaxation time measurements (trial 2).

Concentration (mM)	T_1 (s)	$1/T_1$ (s^{-1})
0.55	0.090	11.1
0.28	0.180	5.71
0.14	0.346	2.87
0.07	0.626	1.60
0.00	2.925	0.350

Table B.3 Texaphyrin **2.2** relaxation time measurements (trial 3).

Concentration (mM)	T_1 (s)	$1/T_1$ (s^{-1})
0.55	0.090	11.1
0.28	0.175	5.56
0.14	0.348	2.89
0.07	0.624	1.60
0.00	2.890	0.340

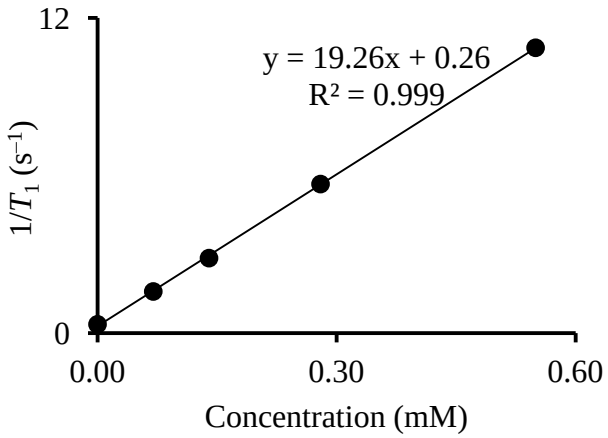

Figure B.8. Relaxivity plot of **2.2** (trial 1).

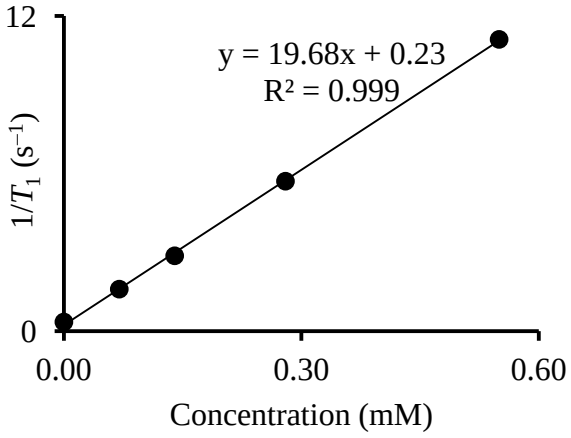

Figure B.9. Relaxivity plot of **2.2** (trial 2).

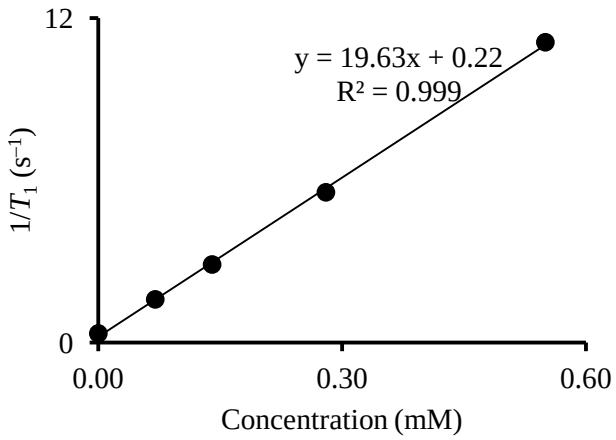

Figure B.10. Relaxivity plot of **2.2** (trial 3).

Table B.4 Texaphyrin **2.3** relaxation time measurements (trial 1).

Concentration (mM)	T_1 (s)	$1/T_1$ (s^{-1})
0.57	0.135	7.41
0.29	0.253	3.95
0.14	0.512	1.95
0.07	0.840	1.19
0.04	2.969	0.340

Table B.5 Texaphyrin **2.3** relaxation time measurements (trial 2).

Concentration (mM)	T_1 (s)	$1/T_1$ (s^{-1})
0.57	0.129	7.75
0.29	0.251	3.98
0.14	0.490	2.04
0.07	0.850	1.18
0.04	2.953	0.340

Table B.6 Texaphyrin **2.3** relaxation time measurements (trial 3).

Concentration (mM)	T_1 (s)	$1/T_1$ (s^{-1})
0.57	0.129	7.75
0.29	0.253	3.98
0.14	0.474	2.04
0.07	0.870	1.18
0.04	2.940	0.340

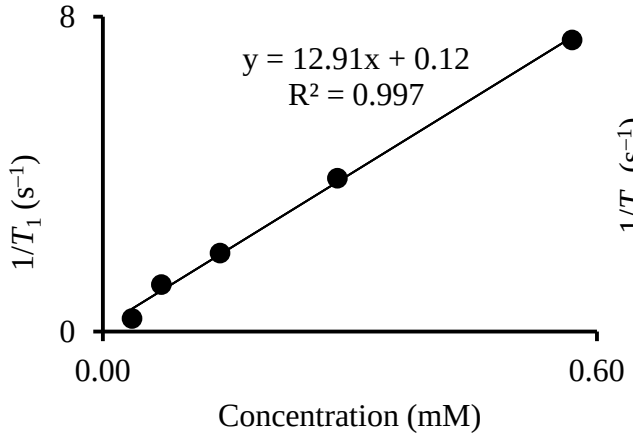

Figure B.11. Relaxivity plot of **2.3** (trial 1).

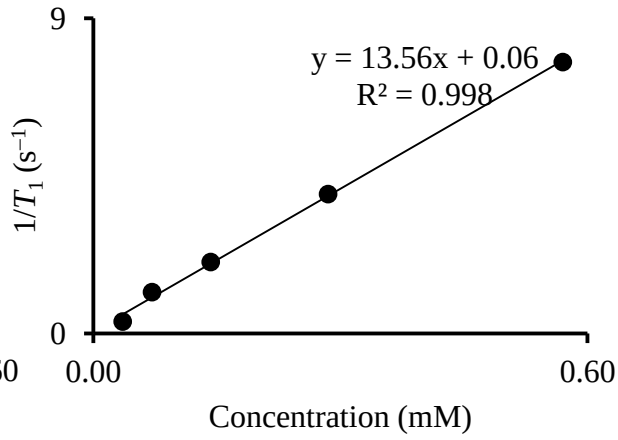

Figure B.12. Relaxivity plot of **2.3** (trial 2).

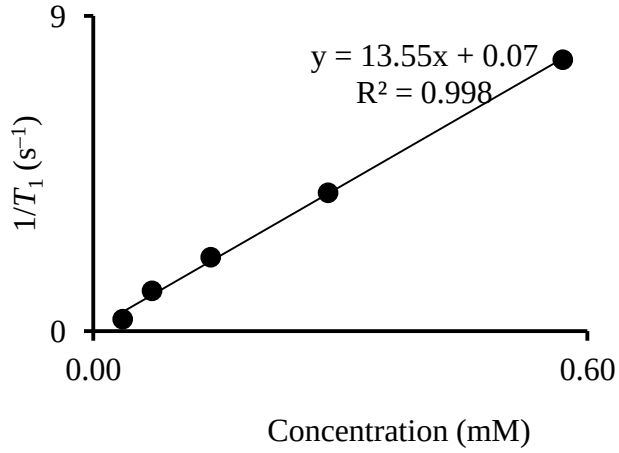

Figure B.13. Relaxivity plot of **2.3** (trial 3).

Table B.7 Texaphyrin **2.4** relaxation time measurements (trial 1).

Concentration (mM)	T_1 (s)	$1/T_1$ (s^{-1})
0.22	0.344	2.91
0.11	0.730	1.37
0.05	1.210	0.83
0.03	1.680	0.60
0.00	2.810	0.360

Table B.8 Texaphyrin **2.4** relaxation time measurements (trial 2).

Concentration (mM)	T_1 (s)	$1/T_1$ (s^{-1})
0.22	0.339	2.95
0.11	0.730	1.37
0.05	1.200	0.83
0.03	1.670	0.60
0.00	2.860	0.350

Table B.9 Texaphyrin **2.4** relaxation time measurements (trial 3).

Concentration (mM)	T_1 (s)	$1/T_1$ (s^{-1})
0.22	0.350	2.86
0.11	0.740	1.35
0.05	1.190	0.84
0.03	1.620	0.62
0.00	2.840	0.350

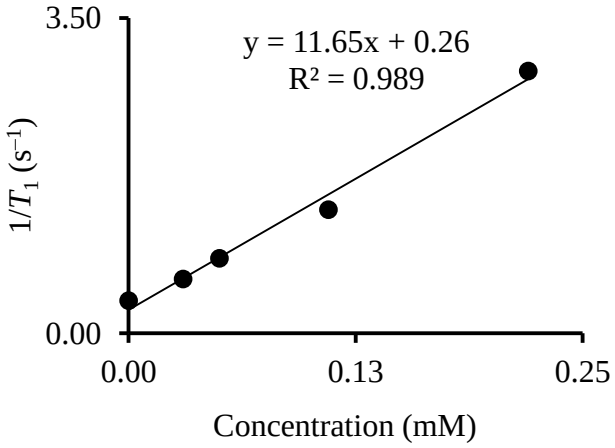

Figure B.14. Relaxivity plot of **2.4** (trial 1).

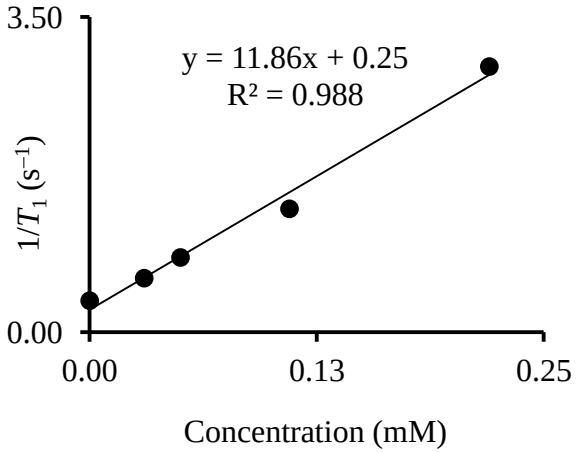

Figure B.15. Relaxivity plot of **2.4** (trial 2).

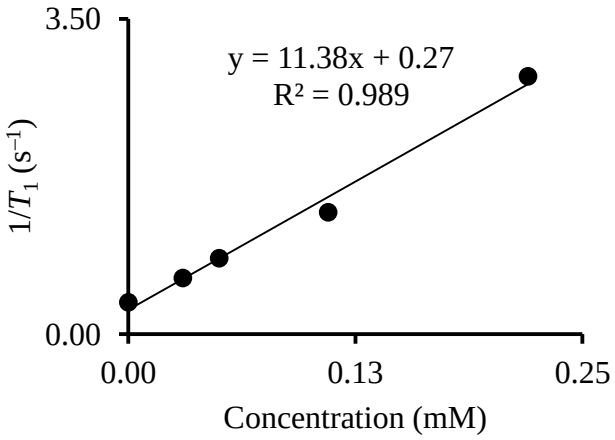

Figure B.16. Relaxivity plot of **2.4** (trial 3).

Table B.10 Texaphyrin **2.5** relaxation time measurements (trial 1).

Concentration (mM)	T_1 (s)	$1/T_1$ (s^{-1})
0.80	0.1093	9.15
0.40	0.2184	4.58
0.20	0.4347	2.3
0.10	0.7392	1.35
0.00	3.8600	0.260

Table B.11 Texaphyrin **2.5** relaxation time measurements (trial 2).

Concentration (mM)	T_1 (s)	$1/T_1$ (s^{-1})
0.80	0.1086	9.21
0.40	0.2200	4.55
0.20	0.4263	2.35
0.10	0.7370	1.36
0.00	3.8610	0.260

Table B.12 Texaphyrin **2.5** relaxation time measurements (trial 3).

Concentration (mM)	T_1 (s)	$1/T_1$ (s^{-1})
0.80	0.1043	9.59
0.40	0.2153	4.64
0.20	0.4244	2.36
0.10	0.7370	1.36
0.00	3.8420	0.260

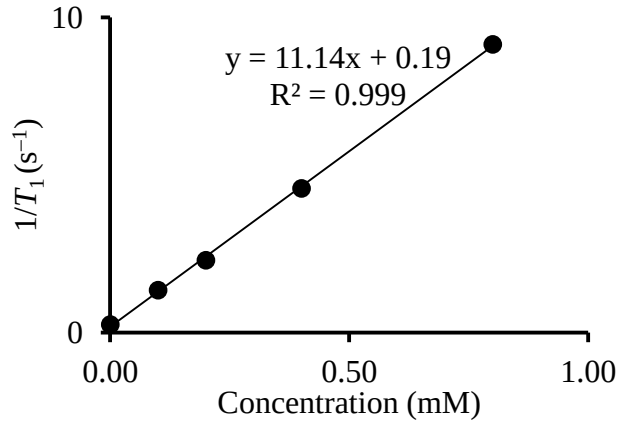

Figure B.17. Relaxivity plot of **2.5** (trial 1).

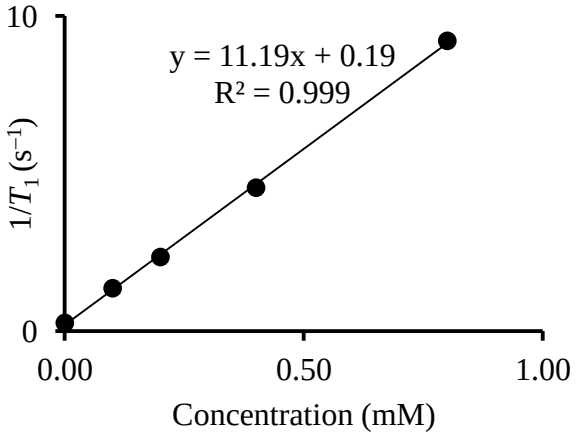

Figure B.18. Relaxivity plot of **2.5** (trial 2).

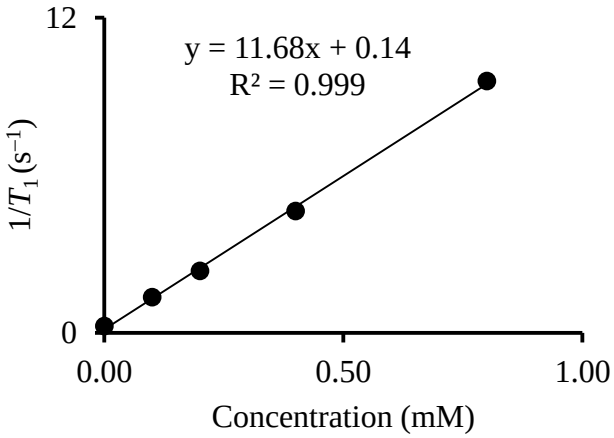

B.19. Relaxivity plot of **2.5** (trial 3).

Table B.13 Texaphyrin **2.6** relaxation time measurements (trial 1).

Concentration (mM)	T_1 (s)	$1/T_1$ (s^{-1})
1.02	0.0830	12.05
0.51	0.1463	6.83
0.26	0.2702	3.70
0.13	0.6137	1.63
0.00	3.8600	0.260

Table B.14 Texaphyrin **2.6** relaxation time measurements (trial 2).

Concentration (mM)	T_1 (s)	$1/T_1$ (s^{-1})
1.02	0.0810	12.35
0.51	0.1456	6.87
0.26	0.2615	3.82
0.13	0.6212	1.61
0.00	3.8610	0.260

Table B.15 Texaphyrin **2.6** relaxation time measurements (trial 3).

Concentration (mM)	T_1 (s)	$1/T_1$ (s^{-1})
1.02	0.0829	12.06
0.51	0.1467	6.82
0.26	0.2636	3.79
0.13	0.6192	1.61
0.00	3.8420	0.260

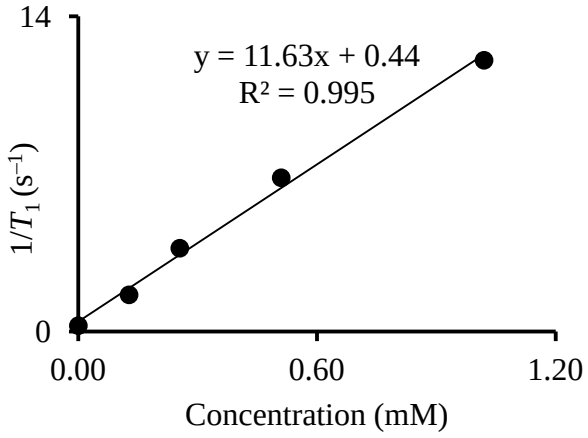

Figure B.20. Relaxivity plot of **2.6** (trial 1).

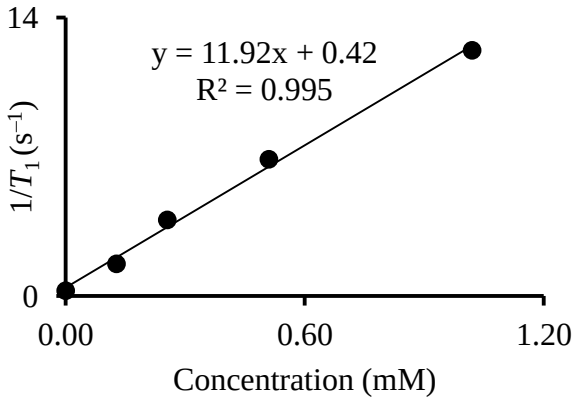

Figure B.21. Relaxivity plot of **2.6** (trial 2).

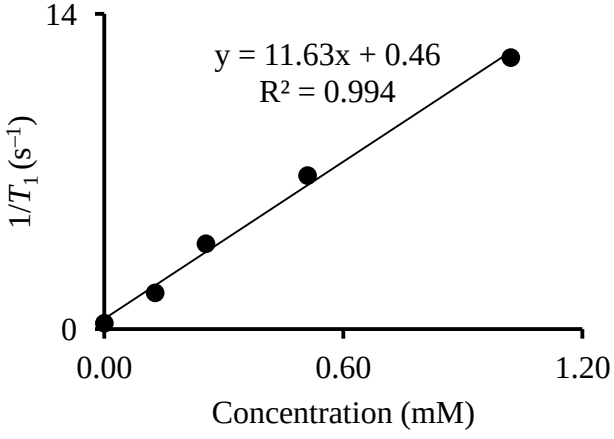

Figure B.22. Relaxivity plot of **2.6** (trial 3).

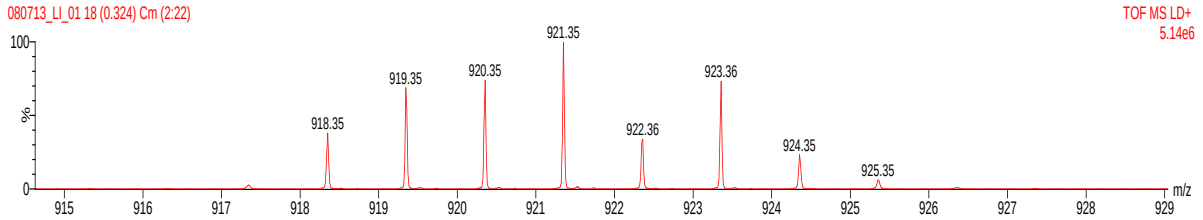

Figure B. 23. Isotopic distribution of texaphyrin **2.4**. The mass spectrum was obtained using LSIV, sample was coated with 2-NPG matrix.

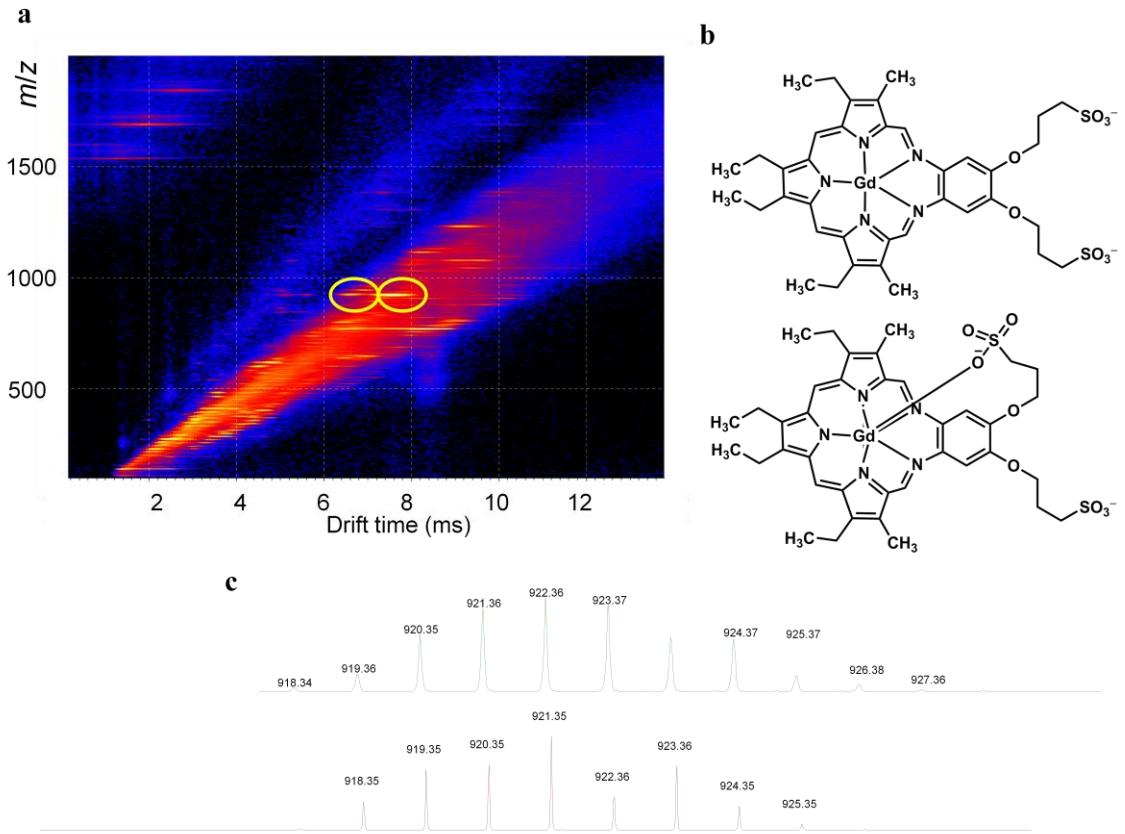

Figure B. 24. Ion mobility mass spectrometric studies of texaphyrin **2.4**. The sample was coated with 2-NPG matrix and mass spectrum was obtained using LSIV. **a** Two dimensional ion mobility plot of drift time vs *m*/*z*. Bright spots highlighted by yellow circles depict the two signals obtained for +1 complex of **2.4** at *m*/*z* 921. **b** Chemical structures of two possible confirmations for texaphyrin **2.4**. **c** Extracted mass spectra for the two signals.

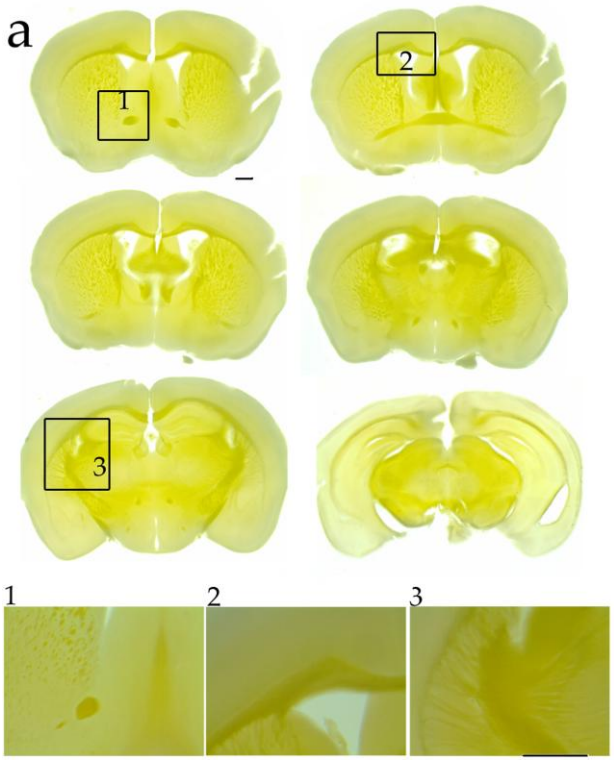

Figure B. 25. Light microscopic images of coronal sections of intact mouse brain stained with texaphyrin **2.4**. The mouse brain was sectioned after obtaining MRI to confirm stain distribution. Panel (**a**) shows representative brain images from 0.62 to –3.40 mm Bregma. Panel (**b**) shows high magnification images of myelinated regions and the magnified area is represented with a black square containing respective number in panel (**a**). Slice thickness = 200 µm, Scale Bars represent 1 mm.

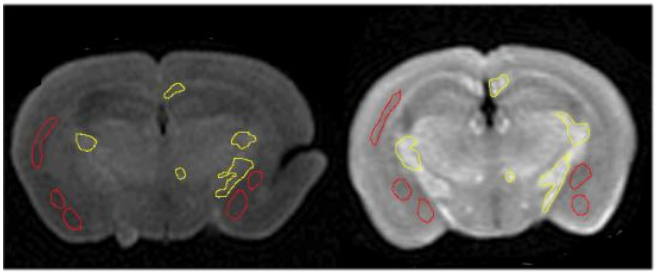

Figure B. 26. R_1-maps of mouse brains stained with texaphyrin **3** and unstained control marked with five regions of interest that were used to calculate the enhancement of relaxation rate. Myelin-rich and myelin-poor regions are marked by yellow and red lines, respectively.

Table B. 16. Values of regions of interest used to calculate enhancement of R_1.

Area	Mean	Min	Max				
0.062	0.002	0.002	0.003	Myelin-rich-Stained			
0.391	0.002	0.002	0.003	Myelin-rich-Stained			
0.031	0.003	0.002	0.003	Myelin-rich-Stained			
0.266	0.003	0.002	0.003	Myelin-rich-Stained	Avg = 0.0026	% increase = 160	Fold increase = 2.6
0.469	0.003	0.002	0.003	Myelin-rich-Stained			
0.188	0.001	0.001	0.001	Myelin-poor-Stained			
0.172	0.001	0.001	0.001	Myelin-poor-Stained			
0.172	0.001	0.001	0.001	Myelin-poor-Stained			
0.281	0.001	0.001	0.001	Myelin-poor-Stained			
0.359	0.001	0.001	0.002	Myelin-poor-Stained	Avg = 0.001		
0.203	8.03E-04	7.24E-04	9.04E-04	Myelin-rich-Unstained control			
0.266	9.58E-04	8.56E-04	0.001	Myelin-rich-Unstained control			
0.25	9.79E-04	8.36E-04	0.001	Myelin-rich-Unstained control			
0.578	8.67E-04	7.19E-04	0.001	Myelin-rich-Unstained control			
0.016	9.43E-04	9.43E-04	9.43E-04	Myelin-rich-Unstained control	Avg = 9.1E-4	% increase = 61.2	Fold increase = 1.61
0.312	6.42E-04	5.98E-04	7.05E-04	Myelin-poor-Unstained control			
0.312	5.28E-04	4.74E-04	5.90E-04	Myelin-poor-Unstained control			
0.219	5.11E-04	4.76E-04	5.70E-04	Myelin-poor-Unstained control			
0.359	5.49E-04	5.24E-04	5.96E-04	Myelin-poor-Unstained control			
0.266	5.92E-04	5.26E-04	6.50E-04	Myelin-poor-Unstained control	Avg = 5.6E-4		

APPENDIX C

This appendix contains permissions to reproduce some of the material in this thesis from Bentham Science Publishers from Vithanarachchi, S. M.; Allen, M. J. *Current Molecular Imaging* **2012,** *1,* 12–25 and from The Royal Society of Chemistry from Vithanarachchi, S. M.; Allen, M. J. *Chem. Commun.* **2013,** *49,* 4148–4150.

This appendix also contains permissions obtained when writing Vithanarachchi, S. M.; Allen, M. J. *Current Molecular Imaging* **2012,** *1,* 12–25.

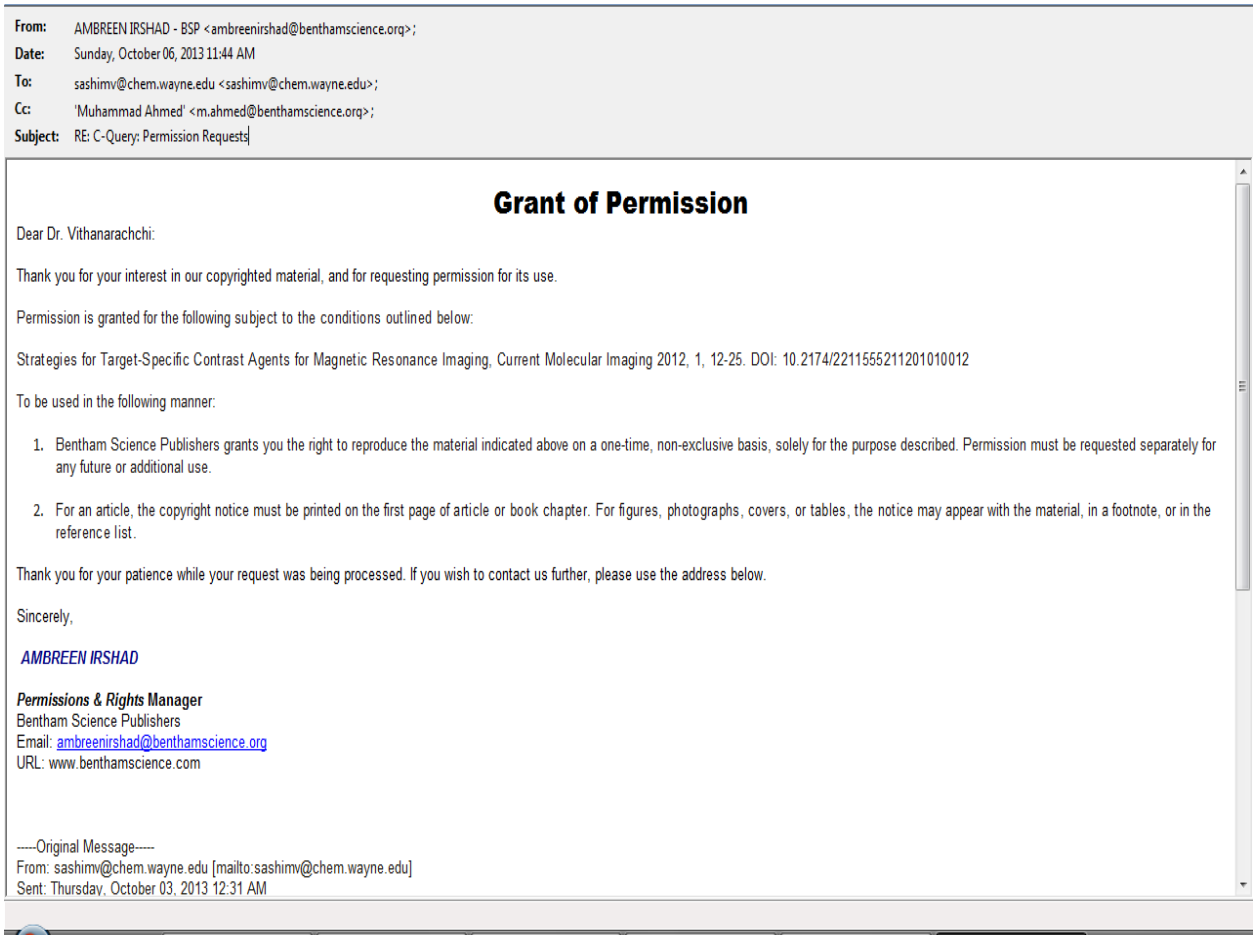

From: AMBREEN IRSHAD - BSP <ambreenirshad@benthamscience.org>;
Date: Sunday, October 06, 2013 11:44 AM
To: sashimv@chem.wayne.edu <sashimv@chem.wayne.edu>;
Cc: 'Muhammad Ahmed' <m.ahmed@benthamscience.org>;
Subject: RE: C-Query: Permission Requests

Grant of Permission

Dear Dr. Vithanarachchi:

Thank you for your interest in our copyrighted material, and for requesting permission for its use.

Permission is granted for the following subject to the conditions outlined below:

Strategies for Target-Specific Contrast Agents for Magnetic Resonance Imaging, Current Molecular Imaging 2012, 1, 12-25. DOI: 10.2174/2211555211201010012

To be used in the following manner:

1. Bentham Science Publishers grants you the right to reproduce the material indicated above on a one-time, non-exclusive basis, solely for the purpose described. Permission must be requested separately for any future or additional use.

2. For an article, the copyright notice must be printed on the first page of article or book chapter. For figures, photographs, covers, or tables, the notice may appear with the material, in a footnote, or in the reference list.

Thank you for your patience while your request was being processed. If you wish to contact us further, please use the address below.

Sincerely,

AMBREEN IRSHAD

***Permissions & Rights* Manager**
Bentham Science Publishers
Email: ambreenirshad@benthamscience.org
URL: www.benthamscience.com

-----Original Message-----
From: sashimv@chem.wayne.edu [mailto:sashimv@chem.wayne.edu]
Sent: Thursday, October 03, 2013 12:31 AM

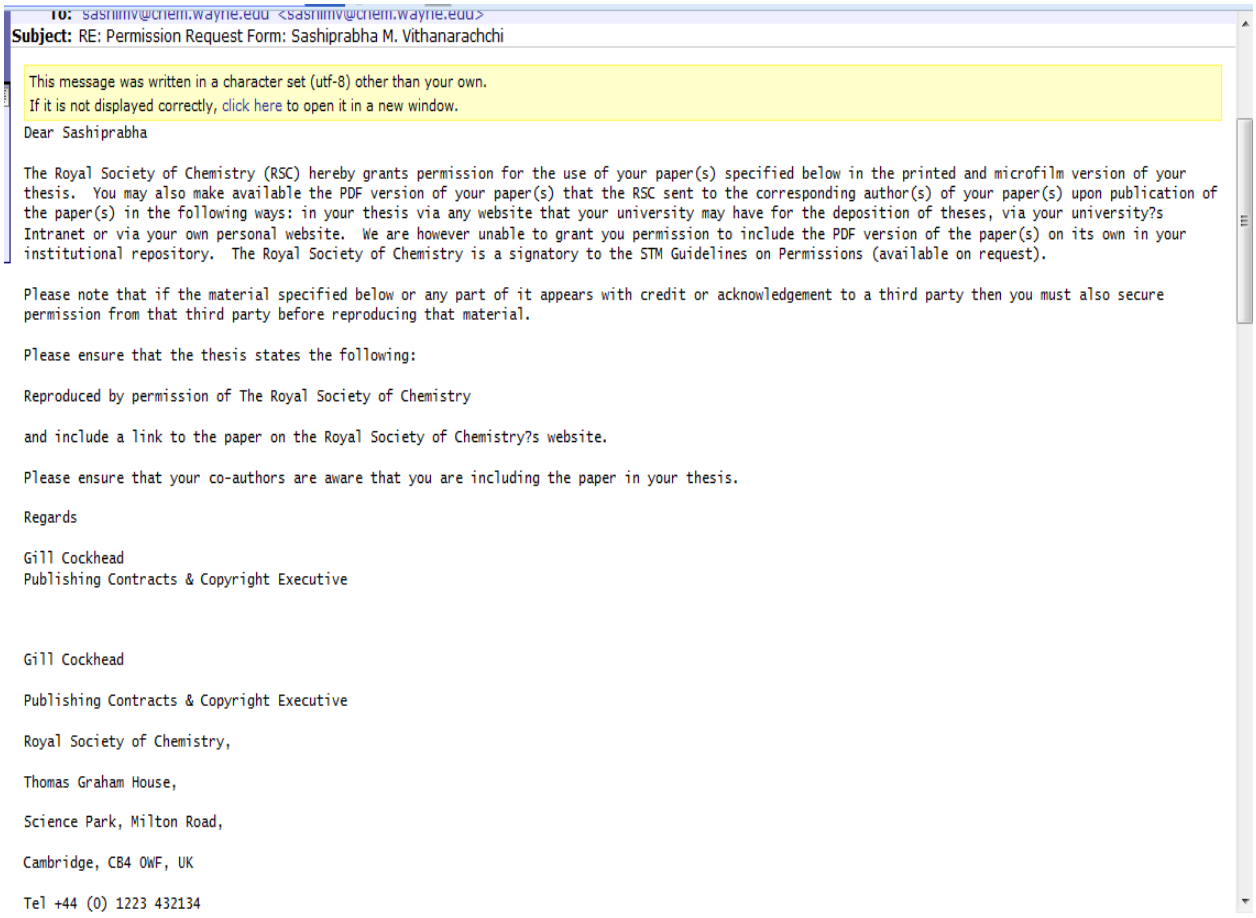

To: sashimv@chem.wayne.edu <sashimv@chem.wayne.edu>

Subject: RE: Permission Request Form: Sashiprabha M. Vithanarachchi

This message was written in a character set (utf-8) other than your own.
If it is not displayed correctly, click here to open it in a new window.

Dear Sashiprabha

The Royal Society of Chemistry (RSC) hereby grants permission for the use of your paper(s) specified below in the printed and microfilm version of your thesis. You may also make available the PDF version of your paper(s) that the RSC sent to the corresponding author(s) of your paper(s) upon publication of the paper(s) in the following ways: in your thesis via any website that your university may have for the deposition of theses, via your university?s Intranet or via your own personal website. We are however unable to grant you permission to include the PDF version of the paper(s) on its own in your institutional repository. The Royal Society of Chemistry is a signatory to the STM Guidelines on Permissions (available on request).

Please note that if the material specified below or any part of it appears with credit or acknowledgement to a third party then you must also secure permission from that third party before reproducing that material.

Please ensure that the thesis states the following:

Reproduced by permission of The Royal Society of Chemistry

and include a link to the paper on the Royal Society of Chemistry?s website.

Please ensure that your co-authors are aware that you are including the paper in your thesis.

Regards

Gill Cockhead
Publishing Contracts & Copyright Executive

Gill Cockhead

Publishing Contracts & Copyright Executive

Royal Society of Chemistry,

Thomas Graham House,

Science Park, Milton Road,

Cambridge, CB4 0WF, UK

Tel +44 (0) 1223 432134

Title: An Intein-Mediated Site-Specific Click Conjugation Strategy for Improved Tumor Targeting of Nanoparticle Systems
Author: Drew R. Elias,Zhiliang Cheng,Andrew Tsourkas
Publication: Small
Publisher: John Wiley and Sons
Date: Nov 5, 2010

Order Completed

Thank you very much for your order.

This is a License Agreement between Sashiprabha Vithanarachchi ("You") and John Wiley and Sons ("John Wiley and Sons"). The license consists of your order details, the terms and conditions provided by John Wiley and Sons, and the payment terms and conditions.

Get the printable license.

License Number	2870900360136
License date	Mar 16, 2012
Licensed content publisher	John Wiley and Sons
Licensed content publication	Small
Licensed content title	An Intein-Mediated Site-Specific Click Conjugation Strategy for Improved Tumor Targeting of Nanoparticle Systems
Licensed content author	Drew R. Elias,Zhiliang Cheng,Andrew Tsourkas
Licensed content date	Nov 5, 2010
Start page	2460
End page	2468
Type of use	Journal
Requestor type	University/Academic
Is the reuse sponsored by or associated with a pharmaceutical or medical products company?	no
Format	Print and electronic
Portion	Figure/table
Number of figures/tables	2
Original Wiley figure/table number(s)	2
Will you be translating?	No
Circulation	100000
Order reference number	
Title of new article	Strategies for Targeted Contrast agents for Magnetic Resonance Imaging
Publication the new article is in	Cuurent Molecular Imaging
Publisher of new article	Bentham Science Publishers
Author of new article	Sashiprabha M. Vithanarachchi and Matthew J. Allen
Expected publication date of new article	Sep 2012
Estimated size of new article (pages)	12
Total	0.00 USD

WAYNE STATE UNIVERSITY

INSTITUTIONAL ANIMAL
CARE AND USE COMMITTEE
87 E. Canfield, Second Floor
Detroit, MI 48201-2011
Telephone: (313) 577-1629
Fax Number: (313) 577-1941

ANIMAL WELFARE ASSURANCE # A 3310-01

PROTOCOL # A 06-04-12

Protocol Effective Period: August 1, 2012 – June 30, 2015

TO: Dr. Alana Conti
Neurosurgery
11R-B4250 Veterans Administration Medical Center

FROM: Lisa Anne Polin, Ph.D.
Chairperson
Institutional Animal Care and Use Committee

SUBJECT: Approval of Protocol # A 06-04-12

"Effects of Adenylyl Cyclases 1 and 8 on Neuronal Sensitivity to Ethanol- VAMC"

DATE: August 1, 2012

Your animal research protocol has been reviewed by the Wayne State University Institutional Animal Care and Use Committee, and given final approval for the period effective **August 1, 2012** through **June 30, 2015**. The listed source of funding for the protocol is **NIH (NIAAA)**. The species and number of animals approved for the duration of this protocol are listed below.

Species	Strain	Qty.	USDA Cat.
MICE	C57Bl/6J, male, 2-3 mos. To be used as breeders only.	10	B
*To be purchased			
MICE	C57Bl/6J, male, 2-14 mos. (existing breeders)	10	B
MICE	C57Bl/6J, female, 2-8 mos. (existing breeders)	20	B
MICE	AC1/8KO, male, 2-14 mos. (existing breeders)	10	B
MICE	AC1/8KO, female, 2-8 mos. (existing breeders)	20	B
**To be transferred from WSU protocol #A 07-01-09			
MICE	C57Bl/6J, male- anticipated breeders	20	B
MICE	C57Bl/6J, female- anticipated breeders	100	B
MICE	AC1/8KO, male- anticipated breeders	20	B
MICE	AC1/8KO, female- anticipated breeders	100	B
MICE	C57Bl/6J, male- culled	208	B
MICE	C57Bl/6J, female- culled	209	B
MICE	AC1/8KO, male- culled	202	B
MICE	AC1/8KO, female- culled	201	B
MICE	C57Bl/6J, male- experimental	2085	C
MICE	C57Bl/6J, female- experimental	2085	C
MICE	AC1/8KO, male- experimental	2015	C
MICE	AC1/8KO, female- experimental	2015	C
***To be bred in-house			

Be advised that this protocol must be reviewed by the IACUC on an annual basis to remain active. Any change in procedures, change in lab personnel, change in species, or additional numbers of animals requires prior approval by the IACUC. Any animal work on this research

protocol beyond the expiration date will require the submission of a new IACUC protocol form and full committee review.

The Guide for the Care and Use of Laboratory Animals is the primary reference used for standards of animal care at Wayne State University. The University has submitted an appropriate assurance statement to the Office for Laboratory Animal Welfare (OLAW) of the National Institutes of Health. The animal care program at Wayne State University is accredited by the Association for Assessment and Accreditation of Laboratory Animal Care International (AAALAC).

REFERENCES

1. Rahmim, A.; Zaidi, H. *Nucl. Med. Commun.* **2008,** *29,* 193–207.

2. Filippucci, E.; Iagnocco, A.; Meenagh, G.; *Clin. Exp. Rheumatol.* **2006,** *24,* 1–5.

3. Morawski, A. M.; Lanza, G. A.; Wickline, S. A. *Curr. Opin. Biotechnol.* **2005,** *16,* 89–92.

4. Wang, L. V.; Hu, S. *Science* **2012,** *335,* 1458–1462.

5. Ntziachristos, V. *Nat. Methods* **2010,** *7,* 603–614.

6. Skotland, T. *Contrast Media Mol Imaging* **2012,** *7,* 1–6.

7. Tóth, É.; Helm, L.; Merbach, A. E. Relaxivity of gadolinium (III) complexes: Theory and Mechanism. In: Merbach AE, Tóth É, Eds. The chemistry of contrast Agents in medical magnetic resonance imaging, John Wiley & Sons: Chinchester, UK **2001**, pp. 45–119.

8. Artemov, D.; Bhujwalla, Z. M.; Bulte, J. W. M. *Curr. Pharm. Biotechno.* **2004**, *5,* 485–494.

9. Major, J. L.; Meade, T. J. *Acc. Chem. Res.* **2009,** *42,* 893–903.

10. Lauffer, R. B.; Grief, W. L.; Stark, D. D.; Vincent, A. C.; Saini, S.; Wedeen, V. J.; Brady, T. J. *J. Comput. Assist. Tomogr.* **1985,** *9,* 431–438.

11. Unger, E. C.; Totty, W. G.; Neufeld, D. M.; Otsuka, F. L.; Murphy, W. A.; Welch, M. S.; Connett, J. M.; Philpott, G. W. *Invest. Radiol.* **1985,** *20,* 693–700.

12. Artemov, D. *J. Cell Biochem.* **2003,** *90,* 518–524.

13. Weinmann, H-J.; Ebert, W.; Misselwitz, B.; Schmitt-Willich, H. *Eur. J. Radiol.* **2003,** *46*, 33–44.

14. Peng, X-H.; Qian, X.; Mao, H.; Wang, A. Y.; Chen, Z. (G).; Nie, S.; Shin, D. M. *Int. J. Nanomed.* **2008,** *3*, 311–321.

15. Tan, M.; Lu, Z. *Theranostics* **2011,** *1*, 83–101.

16. Kozlowska, D.; Foran, P.; MacMahon, P.; Shelly, M. J.; Eustace, S.; O'Kennedy, R. *Adv. Drug Delivery Rev.* **2009,** *61*, 1402–1411.

17. Bellin, M-F.*Eur. J. Radiol.* **2006,** *60*, 314–323.

18. Gallagher, F. A. *Clin. Radiol.* **2010,** *65*, 557–566.

19. Averill, D. J.; Garcia, J.; Siriwardena-Mahanama, B. N.; Vithanarachchi, S. M.; Allen, M. J. *J. Vis. Exp.* **2011,** *53*, e2844: Available from: http://www.jove.com/video/2844/.

20. Villaraza, A. J. L.; Bumb, A.; Brechbiel, M. *Chem. Rev.* **2010,** *110*, 2921–2959.

21. Caravan, P. *Acc. Chem. Res.* **2009,** *42*, 851–862.

22. Sukerkar, P. A.; MacRenaris, K. W.; Meade, T. J.; Burdette, J. E. *Mol. Pharmaceutics* **2011,** *8*, 1390–1400.

23. Pais, A.; Gunanathan, C.; Margalit, R.; Biton, I. E.; Yosepovich, A.; Milstein, D.; Degani, H. *Cancer Res.* **2011,** *71*, 7387–7397.

24. Rohrer, M.; Bauer, H.; Mintorovitch, J.; Requardt, M.; Weinmann, H-J. *Invest. Radiol.* **2005,** *40*, 715–724.

25. Klink, A.; Lancelot, E.; Ballet, S.; Vucic, E.; Fabre, J-E.; Gonzalez, W.; Medina, C.; Corot, C.; Mulder, W. J. M.; Mallat, Z.; Fayad, Z. A. *Arterioscler Thromb. Vasc. Biol.* **2010,** *30*, 403–410.

26. Verwilst, P.; Eliseeva, S.V.; Carron, S.; Elst, L. V.; Burtea, C.; Dehaen, G.; Laurent, S.; Binnemans, K.; Muller, R. N.; Parac-Vogt, T. N.; De Borggraeve, W. M. *Eur. J. Inorg. Chem.* **2011,** 3577–3585.

27. Park, J-A.; Lee, J-J.; Jung, J-C.; Yu, D-Y.; Oh, C.; Ha, S.; Kim, T-J.; Chang, Y. *ChemBioChem.* **2008,** *9*, 2811–2813.

28. Lawler, J.; Hynes, R. O. *Blood* **1989,** *74*, 2022–2027.

29. Kalber, T. L.; Kamaly, N.; So, P-W.; Pugh, J. A.; Bunch, J.; McLeod, C. W.; Jorgensen, M. R.; Miller, A. D.; Bell, J. D. *Mol. Imaging Biol.* **2011,** *13*, 653–662.

30. Wang, Z. J.; Boddington, S.; Wendland, M.; Meier, R.; Corot, C.; Daldrup-Link, H. *Pediatr. Radiol.* **2008,** *38*, 529–537.

31. Qiao, J.; Li, S.; Wei, L.; Jiang, J.; Long, R.; Mao, H.; Wei, L.; Wang, L.; Yang, H.; Grossniklaus, H. E.; Liu, Z-R.; Yang, J. J. *PLoS ONE* **2011,** *6*, e18103: Available from: http://www.plosone.org/pone.0018103.

32. Caravan, P.; Cloutier, N. J.; Greenfield, M. T.; Mcdermid, S. A.; Dunham, S. U.; Bulte, J. W. M.; Amedio, Jr. J. C.; Looby, R. J.; Supkowski, R. M.; Horrocks, Jr. W. D.; Mcmurry, T. J.; Lauffer, R. B. *J. Am. Chem. Soc.*, 2002, **124**, 3152.

33. Aime, S.; Botta, M.; Crich, S. G.; Giovenzana, G. B.; Pagliarin, R.; Piccinini, M.; Sisti, M.; Terreno, E. *J. Biol. Inorg. Chem.* **1997,** *2*, 470–479.

34. Ye, F.; Jeong, E-K.; Jia, Z.; Yang, T.; Parker, D.; Lu, Z-R. *Bioconjugate Chem.* **2008,** *19,* 2300–2303.

35. Poduslo, J. F.; Wengenack, T. M.; Curran, G. L.; Wisniewski, T.; Sigurdsson, E. M.; Macura, S. I.; Borowski, E. J.; Jack, Jr., C. R. *Neurobiol. Dis.* **2002,** *11,* 315–329.

36. Poduslo, J. F.; Curran, G. L.; Peterson, J. A.; McCormick, D. J.; Fauk, A. H.; Khan, M. A.; Wengenack, T. M. *Biochemistry* **2004,** *43,* 6064–6075.

37. Koronyo-Hamaoui, M.; Koronyo, Y.; Ljubimov, A. V.; Miller, C. A.; Ko, M. K.; Black, K. L.; Schwartz, M.; Farkas, D. L. *Neuroimage* **2011,** *54,* S204–217.

38. Frullano, L.; Wang, C.; Miller, R. H.; Wang, Y. *J. Am. Chem. Soc.* **2011,** *133,* 1611–1613.

39. Frullano, L.; Zhu, J.; Wang, C.; Wu, C.; Miller, R. H.; Wang, Y. *J. Med. Chem.* **2012,** *55,* 94–105.

40. Overoye-Chan, K.; Koerner, S.; Looby, R. J.; Kolodziej, A. F.; Zech, S. G.; Deng, Q.; Chasse, J. M.; McMurry, T. J.; Caravan, P. *J. Am. Chem. Soc.* **2008,** *130,* 6025–6039.

41. Spuentrup, E.; Katoh, M.; Weithoff, A. J.; Parsons, Jr., E. C.; Botnar, R. M.; Mahnken, A. H.; Günther, R. W.; Buecker, A. *Am. J. Respir. Crit. Care Med.* **2005,** *172* 494–500.

42. Stracke, C. P.; Katoh, M.; Weithoff, A. J.; Parsons, E. C.; Spangenberg, P.; Spüntrup, E. *Stroke* **2007,** *38,* 1476–1481.

43. Caravan, P.; Das, B.; Dumas, S. Epstein, F. H.; Helm, P. A.; Jacques, V.; Koerner, S.; Kolodziej, A.; Shen, L.; Sun, W. C.; Zhang, Z. *Angew. Chem. Int. Ed.* **2007,** *46,* 8171–8173.

44. Helm, P. A.; Caravan, P.; French, B. A.; Jacques, V.; Shen, L.; Xu, Y.; Beyers, R. J.; Roy, R. J.; Kramer, C. M.; Epstein, F. H. *Radiology* **2008,** *247,* 788–796.

45. Ke, T.; Jeong, E-K.; Wang, X.; Feng, Y.; Parker, D. L.; Lu, Z-R. *Int. J. Nanomed.* **2007,** *2,* 191–199.

46. Zarabi, B.; Borgman, M. P.; Zhuo, J.; Gullapalli, R.; Ghandehari, H. *Pharm. Res.* **2009,** *26,* 1121–1129.

47. Gustafsson, B.; Youens, S.; Louie, A. Y. *Bioconjugate Chem.* **2006,** *17,* 538–547.

48. Konda, S. D.; Aref, M.; Wang, S.; Brechbiel, M.; Weiner, E. C. *Magn. Reson. Mater. Phys. Biol. Med.* **2001,** *12,* 104–113.

49. Zhang, W-L.; Li, N.; Huang, J.; Luo, S-F.; Fan, M-X.; Liu, S-Y.; Muir, B.; Yu, J-H. *J. Appl. Polym. Sci.* **2011,** *121,* 3175–3184.

50. Swanson, S. D.; Kukowska-Latallo, J. F.; Patri, A. K.; Chen, C.; Ge, S.; Cao, Z.; Kotlyar, A.; East, A. T.; Baker, J. R. *Int. J. Nanomed.* **2008,** *3,* 201–210.

51. Bui, T.; Stevenson, J.; Hoekman, J.; Zhang, S.; Maravilla, K.; Ho, R. J. Y. *PLoS ONE* **2010,** *5,* e13082: Available from: http://www.plosone.org/pone.0013082.

52. Kim, T.; Momin, E.; Choi, J.; Yuan, K.; Zaidi, H.; Kim, J.; Park, M.; Lee, N.; McMahon, M. T.; Quinones-Hinojosa, A.; Bulte, J. W. M.; Hyeon, T.; Gilad, A. A. *J. Am. Chem. Soc.* **2011,** *133,* 2955–2961.

53. Warsi, M. F.; Adams, R. W.; Duckett, S. B.; Chechik, V. *Chem. Commun.* **2010,** *46,* 451–453.

54. Schmieder, A. H.; Winter, P. M.; Caruthers, S. D.; Harris, T. D.; Williams, T. A.; Allen, J. S.; Lacy, E. K.; Zhang, H.; Scott, M. J.; Hu, G.; Robertson, J. D.; Wickline, S. A.; Lanza, G. M. *Magn. Reson. Med.* **2005,** *53,* 621–627.

55. Schmieder, A. H.; Caruthers, S. D.; Zhang, H.; Williams, T. A.; Robertson, J. D.; Wickline, S. A.; Lanza, G. M. *FASEB J.* **2008,** *22,* 4179–4189.

56. Tan, M.; Wu, X.; Jeong, E-K.; Chen, Q. Lu, Z-R. *Biomacromolecules* **2010,** *11,* 754–761.

57. Ghaghada, K. B.; Ravoori, M.; Sabapathy, D.; Bankson, J.; Kundra, V.; Annapragada, A. *PLoS ONE* **2009,** *4*, e7628: www.plosone.org/

58. Nam, T.; Park, S.; Lee, S-Y.; Park, K.; Choi, K.; Song, I. C.; Han, M. H.; Leary, J. J.; Yuk, S. A.; Kwon, I. C.; Kim, K.; Jeong, S, Y. *Bioconjugate Chem.* **2010,** *21,* 578–582.

59. Ayyagari, A. L.; Zhang, X.; Ghaghada, K. B.; Annapragada, A.; Hu, X.; Bellamkonda, R. V. *Magn. Reson. Med.* **2006,** *55,* 1023–1029.

60. Tan, M.; Wu, X.; Jeong, E-K.; Chen, Q.; Parker, D. L.; Lu, Z-R. *Mol. Pharmaceutics* **2010,** *7,* 936–943.

61. Pan, D.; Senpan, A.; Caruthers, S. D.; Williams, T. A.; Scott, M. J.; Gaffney, P. J.; Wickline, S. A.; Lanza, G. M. *Chem. Commun.* **2009,** 3234–3236.

62. Liu, W.; Dahnke, H.; Jordan, E. K.; Schaeffter, T.; Frank, J. A. *NMR Biomed.* **2008,** *21,* 242–250.

63. Rasaneh, S.; Rajabi, H.; Babaei, M. H.; Akhlaghpoor, S. *J. Nanopart. Res.* **2011,** *13,* 2285–2293.

64. Elias, D. R.; Cheng, Z.; Tsourkas, A. *Small* **2010,** *6,* 2460–2468.

65. Yang, L.; Peng, X-H.; Wang, Y. A.; Wang, X.; Cao, Z.; Ni, Z.; Karna, P.; Zhang, X.; Wood, W. C.; Gao, X.; Nie, S.; Mao, H. *Clin. Cancer Res.* **2009,** *15,* 4722–4732.

66. Zou, P.; Yu, Y.; Wang, Y. A.; Zhong, Y.; Welton, A.; Galban, C.; Wang, S.; Sun, D. *Mol. Pharmaceutics* **2010,** *7,* 1974–1984.

67. Serkova, N. J.; Renner, B.; Larsen, B. A.; Stoldt, C. R.; Hasebroock, K. M.; Bradshaw-Pierce, E. L.; Holers, W. M.; Thurman, J. M. *Radiology* **2010,** *255,* 517–526.

68. Sargsyan, S. A.; Serkova, N. J.; Renner, B.; Hasebroock, K. M.; Larsen, M.; Stoldt, C. R.; McFann, K.; Pickering, M. C.; Thurman, J. M. *Kidney Int*. **2012,** *81,* 152–159.

69. Ni, Y. *Curr. Med. Imaging Rev.* **2008,** *4,* 96–112.

70. Zhang, Z.; He, R.; Yan, K.; Guo, K-N.; Lu, Y-G.; Wang, X-X.; Lei, H.; Li, Z-Y. *Bioorg. Med. Chem. Lett.* **2009,** *19,* 6675–6678.

71. Lee, T.; Zhang, X.; Dhar, S.; Fass, H.; Lippard, S. J.; Jasanoff, A. *Chem. Biol.* **2010,** *17,* 665–673.

72. Shahbazi-Gahrouei, D. *J. Res. Med. Sci.* **2006,** *11,* 217–223.

73. Shahbazi-Gahrouei, D.; Williams, M.; Rizvi, S.; Allen, B. J. *J. Magn. Reson. Imaging* **2001,** *14,* 169–174.

74. Lyon, R. C.; Faustino, P. J.; Cohen, J. S.; Katz, A.; Mornex, F.; Colcher, D.; Baglin, C.; Koenig, S. H.; Hambright, P. *Magn. Reson. Med.* **1987,** *4,* 24–33.

75. Frias, J. C.; Williams, K. J.; Fisher, E. A.; Fayad, Z. A. *J. Am. Chem. Soc.* **2004,** *126,* 16316–16317.

76. Cormode, D. P.; Skajaa, T.; van Schooneveld, M. M.; Koole, R.; Jarzyna, P.; Lobatto, M. E.; Calcagno, C.; Barazza, A.; Gordon, R. E.; Zanzonico, P.; Fisher, E. A.; Fayad, Z. A.; Mulder, W. J. M. *Nano Lett*. **2008,** *8,* 3715–3723.

77. Ohta, E.; Takiyama, Y. *Neurology Research International* **2012,** *2012,* Article ID 197438: Available from: http://www.hindawi.com/journals/nri/2012/197438/

78. Uchida, M.; Terashima, M.; Cunningham, C. H.; Suzuki, Y.; Willits, D. A.; Willis, A. F.; Yang, P. C.; Tsao, P. S.; McConnell, M. V.; Young, M. J.; Douglas, T. *Magn. Reson. Med.* **2008,** *60,* 1073–1081.

79. Bennett, K. M.; Zhou, H.; Sumner, J. P.; Dodd, S. J.; Bouraoud, N.; Doi, K.; Star, R. A.; Koretsky, A. P. *Magn. Reson. Med.* **2008,** *60,* 564–574.

80. Kluver, H.; Barrera, E. *J. Neuropathol. Exp. Neurol.* **1953,** *12,* 400–403.

81. Blackwell, M. L.; Farrar, C. T.; Fischl, B.; Rosen, B. R. *NeuroImage* **2009,** *46,* 382–393.

82. Young, S. W.; Sidhu, M. K.; Quing, F.; Muller, H. H.; Neuder, M.; Zanassi, G.; Mody, T. D.; Hemmi, G.; Dow, W.; Mutch, J. D.; Sessler, J. L.; Miller, R. A. *Invest. Radiol*. **1994,** *29*, 330–338.

83. Arambula, J. F.; Preihs, C.; Borthwick, D.; Magda, D.; Sessler, J. L. *Anti-Cancer Agents Med. Chem.* **2011,** *11*, 222–232.

84. Geraldes, C. F. G. C.; Sherry, A. D.; Vallet, P.; Maton, F.; Muller, R. N.; Mody, T. D.; Hemmi, G.; Sessler, J. L. *J. Magn. Reson. Imaging* **1995,** *5*, 725–729.

85. Thomas, S. R.; Khuntia, D. *Expert Opin. Drug. Discov.* **2011,** *6*, 195–203.

86. Yang, J. J.; Yang, J.; Wei, L.; Zurkiya, O.; Yang, W.; Li, S.; Zou, J.; Zhou, Y.; Maniccia, A. L. W.; Mao, H.; Zhao, F.; Johnson, J.; Hu, X.; Krogstad, E.; Liu, Z-R. *J. Am. Chem. Soc.* **2008,** *130*, 9260–9267.

87. Anand, P.; Kunnumakkara, A. B.; Newman, R. A.; Aggarwal, B. B. *Mol. Pharm.* **2007,** *4*, 807–817.

88. Porat, Y.; Abramowitz, A.; Gazit, E. *Chem. Biol. Drug Des.* **2006,** *67*, 27–37.

89. Fadda, A. A.; Latif, E.A.; El-Mekaway, R. E.; *Europ. J. Med. Chem.* **2009,** *44*, 1250–1256.

90. Fanning, A. M.; Plush, S. E.; Gunnlaugsson, T. *Chem. Commun.* **2006,** 3791–3793.

91. Clasen, R. A.; Simon, R. G.; Scott, R.; Pandolfi, S.; Liang, I.; Lesak, A. *J. Neuropathol. Exp. Neurol*. **1973**, *32*, 271–283.

92. Kiernan, J. A. *J. Histotechnol.* **2007,** *30*, 87–106.

93. (a) Sessler, J. L.; Hemmi, G. V.; Mody, T. D.; Murai, T.; Burrell, A.; Young, S. W. *Acc. Chem. Res.* **1994**, *27*, 43–50. (*b*) Guldi, D. M.; Mody, T. D.; Gerasimchuk, N. N.; Magda, D.; Sessler, J. L. *J. Am. Chem. Soc.* **2000,** *122,* 8289–8298.

94. Sessler, J. L.; Johnson, M. R.; Lynch, V. *J. Org. Chem.* **1987,** *52,* 4394–4397.

95. Sessler, J. L.; Mody, T. D.; Hemmi, G. W.; Lynch, V. *Inorg. Chem.* **1993,** *32,* 3175–3187.

96. Smith, K. M.; Pandey, R. K. *Tetrahedron* **1984,** *40,* 1749–1754.

97. Lash, T. D.; Mani, U. N.; Lyons, E. A.; Thientanavanic, P.; Jones, M. A.; *J. Org Chem.* **2003**, *64*, 478-487.

98. Kyba, E. P.; Davis, R. E.; Hudson, C. W.; John, A. M. *J. Am. Chem. Soc.* **1981,** *103,* 3868–3875.

99. (*a*) Gorman, P.M.; Yip, C. M.; Fraser, P. E.; Chakrabartty, A. *J. Mol. Biol.* **2003,** *325,* 743; (*b*) Näslund, J.; Haroutunian, V.; Mohs, R.; Davis, K. L.; Davies, P.; Greengard, P.; Buxbaum, J. D.; *J. Am. Med. Assoc.* **2000,** *283,* 1571.

100. Yang, F.; Lim, G. P.; Begum, A. N.; Ubeda, O. J.; Simmons, M. R.; Ambegaokar, S. S.; Chen, P.; Kayed, R.; Glabe, C. G.; Frautschy, S. A.; Cole, G. M. *J. Biol. Chem.* **2005,** *280,* 5892.

101. Garcia-Alloza, M.; Borrelli, L. A.; Rozkalne, A.; Hyman, B. T.; Bacskai, B. J. *J. Neurochem.* **2007,** *102,* 1095.

102. Ono, K.; Hasegawa, K.; Naiki, H.; Yamada, M. *J. Neurosci. Res.* **2004,** *75,* 742.

103. Ryu, E. K.; Choe, Y. S.; Lee, K.-H.; Choi, Y.; Kim, B.-T. *J. Med. Chem.* **2006,** *49,* 6111.

104. Klunk, W. E.; Wang, Y.; Huang, G.-F.; Debnath, M. L.; Holt, D. P.; Mathis, C. A. *Life Sciences* **2001,** *69,* 1471.

105. (a) Skovronsky, D. M.; Zhang, B.; Kung, M.-P.; Kung, H. F.; Trojanowski, J. Q.; Lee, V. M.-Y. *Proc. Natl. Acad. Sci. USA,* **2000,** *97,* 7609. (b) Solbach, C.; Uebele, M.; Reischl, G.; Machulla, H.-J. *Appl. Radiat. Isot.* **2005,** *62,* 591. (*c*) Ono, M.; Ikeoka, R.; Watanabe, H.; Kimura, H.; Fuchigami, T.; Haratake, M.; Saji, H.; Nakayama, M. *ACS Chem. Neurosci.* **2010,** *1,* 598; (*d*) Cui, M.; Ono, M.; Kimura, H.; Liu, B.; Saji, H. *Bioorg. Med. Chem. Lett.* **2011,** *21,* 4193; (*e*) Sumbria, R. K.; Boado, R. J.; Pardridge, W. M. *Bioconjugate Chem.* **2012,** *23,* 1318.

106. (*a*) Benveniste, H.; Einstein, G.; Kim, K. R.; Hulette, C.; Johnson, G. A. *Proc. Natl. Acad. Sci. USA* **1999,** *96,* 14079; (*b*) Borthakur, A.; Gur, T.; Wheaton, A. J.; Corbo, M.; Trojanowski, J. Q.; Lee, V. M.-Y.; Reddy, R. *J. Magn. Reson.* **2006,** *24,* 1011; (*c*) Dhenain, M.; Delatour, B.; Walczak, C.; Volk, A. *Magn. Reson. Med.* **2006,** *55,* 687; (*d*) Zhang, J.; Yarowsky, P.; Gordon, M. N.; Carlo, G. D.; Munireddy, S.; van Zijl, P. C. M.; Mori, S. *Magn. Reson. Med.* **2004,** *51,* 452; (*e*) Helpern, J. A.; Lee, S.-P.; Falangola, M. F. ; Dyakin, V. V.; Bogart, A.; Ardekani, B.; Duff, K.; Branch, C.; Wisniewski, T.; de Leon, M. J.; Wolf, O.; O'Shea, J.; Nixon, R. A. *Magn. Reson. Med.* **2004,** *51,* 794; (*f*) Braakman, N.; Matysik, J.; van Duinen, S. G.; Verbeek, F.; Schliebs, R.; de Groot, H. J. M.; Alia, A. *J. Magn. Reson.* **2006,** *24,* 530; (*g*) Jack Jr., C. R.; Garwood, M.; Wengenack, T. M.; Borowski, B.; Curran, G. L.; Lin, J.; Adriany, G.; Gröhn, O. H. J.; Grimm, R.; Poduslo, J. F. *Magn. Reson. Med.* **2004,** *52,* 1263.

107. (*a*) Sigurdsson, E. M.; Wadghiri, Y. W.; Mosconi, L.; Blind, J. A.; Knudsen, E.; Asuni, A.; Scholtzova, H.; Tsui, W. H.; Li, Y.; Sadowski, M.; Turnbull, D. H.; de Leon, M. J.; Wisiniewski, T. *Neurobiol. Aging* **2008,** *29,* 836; (*b*) Yang, J.; Wadghiri, Y. Z.; Hoang, D. M.; Tsui, W.; Sun, Y.; Chung, E.; Li, Y.; Wang, A.; de Leon, M.; Wisniewski, T.

NeuroImage **2011,** *55,* 1600; (*c*) Larbanoix, L.; Burtea, C.; Laurent, S.; Leuven, F. V.; Toubeau, G.; Elst, L. V.; Muller, R. N. *Neurobiol. Aging* **2010,** *31,* 1679.

108. Ramakrishnan, M.; Wengenack, T. M.; Kandimalla, K. K.; Curran, G. L.; Gilles, E. J.; Ramirez-Alvarado, M.; Lin, J.; Garwood, M.; Jack Jr. C. R.; Poduslo, J. F. *Pharmaceut. Res.* **2008,** *25,* 1861.

109. Li, S.; He, H.; Cui, W.; Gu, B.; Li, J.; Qi, Z.; Zhou, G.; Liang, C.-M.; Feng, X.-Y. *Anat. Rec.* **2010,** *293,* 2136.

110. (*a*) Higuchi, M.; Iwata, N.; Matsuba, Y.; Sato, K.; Sasamoto, K.; Saido, T. C. *Nat. Neurosci.* **2005,** *8,* 527; (*b*) Sato, K.; Higuchi, M.; Iwata, N.; Saido, T. C.; Sasamoto, K. *Eur. J. Med. Chem.* **2004,** *39,* 573; (*c*) Flaherty, D. P.; Walsh, S. M.; Kiyota, T.; Dong, Y.; Ikezu, T.; Vennerstrom, J. L. *J. Med. Chem*. **2007,** *50,* 4986; (*d*) Amatsubo, T.; Morikawa, S.; Inubushi, T.; Urushitani, M.; Taguchi, H.; Shirai, N.; Hirao, K.; Kato, M.; Morino, K.; Kimura, H.; Nakano, I.; Yoshida, C.; Okada, T.; Sano, M.; Tooyama, I. *Neurosci. Res.*, **2009,** *63,* 76.

111. Vithanarachchi, S. M.; Allen, M. J. *Curr. Mol. Imaging* **2012,** *1*, 12–25.

112. (*a*) Ferrari, E.; Pignedoli, F.; Imbriano, C.; Marverti, G.; Basile, V.; Venturi, E.; Saladini, M. *J. Med. Chem.* **2011,** *54,* 8066; (*b*) Lenhart, J. A.; Ling, X.; Gandhi, R.; Guo, T. L.; Gerk, P. M.; Brunzell, D. H.; Zhang, S. *J. Med. Chem.* **2010,** *53,* 6198; (*c*) Qiu, X.; Du, Y. Lou, B.; Zuo, Y.; Shao, W.; Huo, Y.; Huang, J.; Yu, Y.; Zhou, B.; Du, J.; Fu, H.; Bu, X. *J. Med. Chem.* **2010,** *53,* 8260; (*d*) Kim, M. K.; Jeong, W.; Kang, J.; Chong, Y. *Bioorg. Med. Chem.* **2011,** *19,* 3793; (*e*) Qiu, X.; Liu, Z.; Shao, W.-Y.; Liu, X.; Jing, D.-P.; Yu, Y.-J.; An, L.-K.; Huang, S.-L. ; Bu, X.-Z.; Huang, Z.-S.; Gu, L.-Q. *Bioorg. Med. Chem.* **2008,** *16,* 8035.

113. Amolins, M. W. ; Peterson, L. B.; Blagg, B. S. J. *Bioorg. Med. Chem.* **2009,** *17*, 360.

114. (*a*) Lin, L.; Shi, Q.; Su, C.-Y.; Shih, C. C.-Y.; Lee, K.-H. *Bioorg. Med. Chem.* **2006,** *14*, 2527; (*b*) Simoni, D.; Rizzi, M.; Rondanin, R.; Baruchello, R.; Marchetti, P.; Invidiata, F. P.; Labbozzetta, M.; Poma, P.; Carina, V.; Notarbartolo, M.; Alaimo, A.; D'Alessandro, N. *Bioorg. Med. Chem. Lett.* **2008,** *18*, 845; (*c*) Arezki, A.; Brulé, E.; Jaouen, G. *Organometallics* **2009,** *28*, 1606; (*d*) Changtam, C.; de Koning, H. P.; Ibrahim, H.; Sajid, M. S.; Gould, M. K.; Suksamrarn, A. *Eur. J. Med. Chem.* **2010,** *45*, 941; (*e*) Bao, Z.; Wang, S.; Shi, W.; Dong, S.; Ma, H. *J. Proteome. Res.* **2007,** *6*, 3835; (*f*) Zambre, A. P.; Kulkarni, V. M.; Padhye, S.; Sandur, S. K.; Aggarwal, B. B. *Bioorg. Med. Chem.* **2006,** *14*, 7196; (g) Shi, W.; Dolai, S.; Rizk, S.; Hussain, A.; Tariq, H.; Averick, S.; L'Amoreaux, W.; El Idrissi, A.; Banerjee, P.; Raja, K. *Org. Lett.* **2007,** *9*, 5461; (h) Singh, R. K.; Rai, D.; Yadav, D.; Bhargava, A.; Balzarini, J.; De Clercq, E. *Eur. J. Med. Chem.* **2010,** *45*, 1078.

115. Zalipsky, S. *Adv. Drug Deliv. Rev.* **1995,** *16*, 157.

116. Tønnesen, H. H.; Karlsen, J.; van Henegouwen, G. B. *Z. Lebensm. Unters. Forsch.* **1986,** *183*, 116.

117. (*a*) Garcia, J.; Allen, M. J. *Inorg. Chim. Acta.* **2012,** *393*, 324–327.

118. (*a*) Hudson, S. A.; Ecroyd, H.; Kee, T. W.; Carver, J. A. *FEBS J.* **2009,** *276*, 5960; (*b*) Yanagisawa, D.; Taguchi, H.; Yamamoto, A.; Shirai, N.; Hirao, K.; Tooyama, I.; *J. Alzheimers Dis.* **2011,** *24*, 33.

119. Hasegawa, K.; Yamaguchi, I.; Omata, S.; Gejyo, F.; Naiki, H. *Biochemistry* **1999,** *38*, 15514.

120. Plakoutsi, G.; Bemporad, F.; Calamai, M.; Taddei, N.; Dobson, C. M.; Chiti, F. *J. Mol. Biol.* **2005,** *351*, 910.

121. Tabrizi, S. *J. Neurol. Neurosurg. Psychiatry* **2006**, 77: 284

122. Stankoff, B. et al. *Proc. Natl. Acad. Sci. USA* **2006,** *103*, 9304–9309.

123. Wilhelm, M. J. et al. *Proc. Natl. Acad. Sci. USA* **2012,** *109*, 9605–9610.

124. Ragan, T. et al. *Nat. Methods.* **2012,** *9*, 255–258.

125. Laule, C. et al. *Neurotherapeutics* **2007**, *4*, 460–484.

126. Kiernan, J. A. *Histotechnol.* **2007,** *30*, 87–106.

127. Wu, C. et al. *J. Histochem. Cytochem.* **2006,** *54*, 997–1004.

128. Stankoff, B. et al. *Ann. Neurol.* **2011**, *69*, 673–680.

129. Wu, C. et al. *Ann. Neurol.* **2013,** *74*, 688–698.

130. Frullano, L.; Zhu, J.; Miller, R. H.; Wang, Y. *J. Med. Chem.* **2013,** *56*, 1629–1640.

131. Conti, A. C. et al. *PLoS One* **2009**, *4*, e5697.

132. Paxinos, G.; Franklin, K. B. J. The Mouse Brain: In Stereotaxic Coordinates. Second ed. San Diego: Academic Press, **2001**.

133. Brix, G.; Schad, L. R.; Deimling, M.; Lorenz, W. J. *Magn. Reson. Imaging.* **1990,** *8*, 351–356.

134. Look, D. C.; Locker, D. R. *Rev. Sci. Instrum.* **1970,** *41*, 250–251.

135. Gelman, N.; Ewing, J. R.; Gorell, J. M.; Spickler, E. M.; Solomon, E. G. *Magn. Reson. Med.* **2001,** *45*, 71–79.

136. Young, S. W.; Fan, Q.; Kunis, D. M.; Steinberg, G. K. *Invest. Radiol.* **1996,** *31*, 353–358.

137. Images adapted from the Allen Institute for Brain Science website. Allen Brain Reference Atlas. Available from: http://mouse.brain-map.org/experiment/thumbnails/100048576?image_type=atlas.

138. Sleven, J.; Görller-Walrand, C.; Binnemans, K. *Mater. Sci. Eng.* **2001,** *18*, 229–238.

139. Walch, A.; Rauser, S.; Deininger, S-O.; Hofler, H. *Histochem. Cell. Biol.* **2008,** *130*, 421–434.

140. Ceuppens, R.; Dumont, D.; Van Brussel, L.; Van de Plas, B.; Daniels, R.; Noben, J-P.; Verhaert, P.; Van der Gucht, E.; Robben, J.; Clerens, S.; Arckens, *Int. Natl. J. Mass. Spect.* **2007,** *260*, 185–194.

141. Inutan, E.D.; Wager-Miller, J.; Mackie, K.; Trimpin, S. *Anal. Chem.* **2012,** *84*, 9079–9084.

142. Managh, A. J.; Edwards, S. L.; Bushell, A.; Wood, K. J.; Geissler, E. K.; Hutchinson, J. A.; Hutchinson, R. W.; Reid, H. J.; Sharp, B. L. *Anal. Chem.* **2013,** *85*, 10627–10634.

ABSTRACT

SYNTHESIS AND CHARACTERIZATION OF NEW Gd^{3+}-CONTAINING COMPLEXES AS POTENTIAL TARGETED CONTRAST AGENTS FOR MAGNETIC RESONANCE IMAGING.

by

SASHIPRABHA MANJARI VITHANARACHCHI

May 2014

Advisor: Dr. Matthew John Allen

Major: Chemistry (Inorganic)

Degree: Doctor of Philosophy

The focus of the research described in this thesis is the study of chemistry relevant to target-specific contrast agents for magnetic resonance imaging (MRI). MRI is a widely used technique in diagnostic medicine and biomedical research to obtain anatomical and physiological details of soft tissues. Contrast agents are used to enhance the contrast of MR images by causing changes to the chemical environment of water molecules. Clinically approved Gd^{III}-containing contrast agents for MRI are non-specific, and consequently, have limited utility. Target-specific contrast agents represent one way to circumvent this limitation. In the research described in this thesis, myelin and β-amyloid aggregates were selected as targets because they are important in diagnosing neurological diseases. The myelin-targeted complexes were designed to mimic the structural features of a known myelin-specific histology stain, and ex vivo mouse-brain staining method was developed to test these complexes. Ex vivo staining studies (optical, MRI, and mass spectrometry imaging) demonstrated the ability of these complexes to interact with the myelinated regions in mouse brain tissue. Additionally, a β-amyloid-targeted agent was synthesized by conjugating a Gd^{III}-containing complex to curcumin. The binding ability of this

complex with in vitro β-amyloid peptide aggregates was studied using relaxation time and fluorescence measurements. This dissertation presents the synthesis, characterization, and in vitro and ex vivo imaging of these complexes. The studies using these paramagnetic metal complexes have the potential to enable a reliable method to observe structural changes in the brain.

AUTOBIOGRAPHICAL STATEMENT

Education

Wayne State University, Detroit, MI, USA: Chemistry, Ph.D (August 2008–January 2014)

University of Colombo, Colombo, Sri Lanka: Chemistry, B.Sc. (September 2002–August 2006)

Fellowships and Awards

Wenner-Gren fellowship for post doctoral studies in Uppsala University, Sweden: December 2013

Summer 2013 Dissertation Fellowship: May 2013–August 2013

ACS Division of Inorganic Chemistry Travel Award: 2012 (Nationally competitive award)

American Foundation for Aging Research (AFAR) Fellowship: December 2010–November 2011 (Nationally competitive award)

Dharmachandra & Tamarasa Gunawardhana Memorial Gold Medal for Analytical Chemistry awarded by the senate of the University of Colombo, Sri Lanka on the results of the B.Sc. special degree in chemistry: August 2006

Merit award for the inter-university chemistry competition by the Sri Lankan section of the Royal Society of Chemistry: 2006

Research Experience

Wayne State University August 2008–December 2013 (Graduate Student)
Advisor: Dr. Matthew J. Allen
Synthesis and characterization of new Gd^{3+}-containing complexes as targeted contrast agents for magnetic resonance imaging

University of Colombo January 2005–June 2006 (Undergraduate Student)
Advisor: Dr. Sujatha Hewage
Development and improvement of biodegradable cowpea protein polymer film

Publications

Vithanarachchi, S. M.; Allen, M. J. A Multimodal, β-Amyloid-Targeted Contrast Agent. *Chem. Commun.* **2013,** *49,* 4148–4150.

Vithanarachchi, S. M.; Allen, M. J. Strategies for Target-Specific Contrast Agents for Magnetic Resonance Imaging. *Current Molecular Imaging,* **2012,** *1,* 12–25. (Review article)

Averill, D. J.;* Garcia, J.;* Siriwardena-Mahanama, B. N.;* **Vithanarachchi**, **S. M**.;* Allen, M. J. Preparation, Purification, and Characterization of Lanthanide Complexes for Use as Contrast Agents for Magnetic Resonance Imaging. *J. Vis. Exp.* **2011,** *53,* e2844. (* co-first author)

Hewage, S.; **Vithanarachchi, S. M.** Preparation and characterization of biodegradable polymer films from cowpea (*Vigna unguiculata*) protein isolate. *J. Natn. Sci. Foundation Sri Lanka* **2009,** *37,* 53–59.

Stiff, S. J.;* **Vithanarachchi, S. M.**;* Newman, B. D.; Mack, D. T.; Allen, M. J.; Mathews, T. A. An En Bloc Staining Method for Macrostructure Identification in the Mouse Brain. *Submitted for publication* (*co-first author)

Vithanarachchi, S. M.; Allen, M. J. A myelin-specific, multimodal imaging agent for magnetic resonance, optical, and mass spectrometric imaging. *In preparation*

Presentations

244th American Chemical Society National Meeting & Exposition. Philadelphia, PA. August 19–23, 2012; Poster Abstract INOR-212.

Ohio Inorganic Weekend 2011. University of Cincinnati, Cincinnati, OH. October 28–29, 2011; Talk.

Ohio Inorganic Weekends 2013, 2012, 2010, and 2009; Posters.

Annual Chemistry Graduate Research Symposium 2013, 2012, 2011, 2010, and 2009. Wayne State University, Detroit, MI; Posters

Graduate Exhibition 2012. Wayne State University, Detroit, MI. March 6, 2012; Poster.

Proteases and Cancer Program Annual Retreat 2011. Wayne State University, Detroit, MI. December 1, 2011; Poster.

Chemtech 2007, International Conference. Bandaranaike Memorial Conference Hall, Colombo, Sri Lanka. June 20–23, 2007; Poster.